BROWNLEE, Roger Grant.
Ph.D. August 1971

The University of Sydney

MEMORANDUM TO MISS PAMELA GREEN,
RARE BOOK LIBRARIAN,
FISHER LIBRARY.

I enclose the original copy of the thesis submitted by Mr. R. G. Brownlee, who has fulfilled the requirements for the degree of Doctor of Philosophy.

R. B. Fisher
Acting Registrar

SM:DS:S
9.6.71.
Enc.

A DIRECTIONAL ANALYSIS OF VERY HIGH ENERGY EXTENSIVE AIR SHOWERS.

Ph.D. Thesis R.G. Brownlee

A 40 km^2 array of liquid scintillators, each of area 6 m^2 and located near Narrabri N.S.W., has been used to detect the muon component of extensive air showers with primary energy greater than 10^{17}ev.

The fast timing method, with an uncertainty of 70 to 80 nsecs, has been used to determine shower arrival directions to within 5^0. The timing signal is relayed, via a U.H.F. radio link, from a central clock.

The present analysis is based on 2659 events with primary energy greater than 10^{17}ev. Of these, 808 have primary energy greater than 10^{18}ev, 87 have primary energy greater than 10^{19}ev and 8 have primary energy greater than 10^{20}ev.

The celestial arrival direction distributions appear to be isotropic in each energy range.

No point sources of high energy cosmic radiation from the southern celestial sky are apparent. In particular, no direct correlation with pulsar directions, has been observed. However, a pulsar production mechanism may explain the observed, isotropic flux of high energy cosmic rays, if the primaries are iron

nuclei or heavier and the galactic magnetic field strength is greater than 10^{-6} gauss.

The flux of high energy cosmic radiation from the direction of the local galactic spiral arm is in accordance with an isotropic distribution.

The curvatures of the muon shower fronts of 723 showers have been investigated as a sideline to the determination of accurate arrival directions. The results are in good agreement with those of the Haverah Park array. No variation of curvature with shower size is evident and a constant height of origin of 4 km is indicated.

The curvature and zenith angle of an individual, highly inclined shower, have been used for an estimate of geomagnetic splitting of the shower front. The primary energy of this event may be greater than 10^{21}ev.

A DIRECTIONAL ANALYSIS OF VERY HIGH ENERGY EXTENSIVE AIR SHOWERS.

by

R.G. BROWNLEE

A THESIS SUBMITTED TO THE UNIVERSITY OF SYDNEY FOR THE DEGREE OF DOCTOR OF PHILOSOPHY.

DECEMBER, 1970.

CONTENTS

ACKNOWLEDGEMENTS.

The work described in this thesis was carried out by the author as a member of the Falkiner Nuclear Department within the School of Physics, University of Sydney. During this time he was supported by a Commonwealth Research Studentship and by a Teaching Fellowship from the University of Sydney.

The author wishes to express his sincere thanks to his supervisor, Prof. C.B.A. McCusker for his encouragement and many helpful suggestions.

The author would also like to thank Assoc. Prof. M.M. Winn for his constant guidance and the late Dr. M.H. Rathgeber for his willing assistance. He also thanks all other members of the group and in particular Dr. L.S. Peak and Dr. L. Goorevich for their valuable suggestions and criticisms.

For the running and maintenance of the array, the author would like to thank Dr. M.J. Ryan and Mr. P. Kohn.

The author would like to thank Prof. H. Messel for the excellent facilities provided, including access to a large KDF9 computer within the School of Physics. He would also like to thank the Science Research

Foundation of the University of Sydney, the Australian Research Grants Committee and the United States Air Force Office of Scientific Research for the financial support of this work.

Finally he would like to thank Patricia Kelly for her keen perseverance in the typing of this thesis.

CONTRIBUTION OF THE AUTHOR.

The transmission and reception of the timing information as illustrated in chapter 3 was the responsibility of the author. The design and testing of the U.H.F. receiver system was also the work of the author, who in collaboration with Assoc. Prof. M.M. Winn participated in the design and testing of the U.H.F. transmission system.

The author, amongst others, has contributed to the fast timing measurements and the work in chapter 4, unless otherwise stated, is that of the author. In particular the investigation of phenomena affecting the transmission and reception of the timing signal (sections 4.8 and 4.9). The analysis of array symmetry and timing fluctuations in highly inclined showers (sections 4.13 and 4.14) is entirely the work of the author.

An already existing basic shower front analysis program was modified by the author to become part of the routine SUGAR system, such that accurate shower direction and curvature information can be read directly from magnetic tape.

The analysis of shower arrival directions and muon shower front curvature as depicted in chapters 5 and 6, is the work of the author as are the conclusions reached.

CHAPTER 1

HIGH ENERGY COSMIC RADIATION.

1.1 INTRODUCTION.

The desire to pinpoint an origin for cosmic radiation has led many workers to investigate its sidereal variation. The first reported sidereal variation was made in 1923 by the German physicists W. Kolhörster and G.V. Salis. Using crude apparatus at altitudes between 2300m and 3500m on the Jungfrau in Switzerland, they reported a maximum in their ionisation measurement when the Milky Way crossed their zenith. On repeating his experiment in 1924, Kolhörster obtained a similar result. However, other workers (Millikan and Cameron 1928, Hoffmann 1925) were unable to duplicate his results, and obtained no anisotropy.

Since that time we have come to realise the affect of galactic and extragalactic magnetic fields on the primary radiation. All primaries with energy less than 10^{15}ev are easily contained within the galaxy. At energies in excess of 10^{17}ev, if the primaries are protons, their containment becomes more difficult.

If an anisotropy in the arrival directions of cosmic radiation exists, it will be only in the very high energy end of the spectrum, since it is only these primaries that are relatively unaffected by magnetic fields and possibly retain some *memory* of their origin. Such primaries can only be observed indirectly via the

extensive air showers they create in the atmosphere.

Using 15 vertical planes of sonic ranging spark chambers triggered by water-filled Cerenkov counters in the large underground cosmic ray detector of the University of Utah (Davis et al 1970), the arrival directions of more than 100,000 showers with energy in the range 2.5×10^{13} to 10^{15}ev have been investigated. The corresponding energies of the muons detected underground are greater than 7.5×10^{11}ev and the angular resolution, including scattering and machine errors, is less than 1^{0}. Over the declination band $-20^{0} < \delta < 80^{0}$, they found no evidence for anisotropy outside normal statistical fluctuations.

Efimov et al (1968), using a small array of G-M counters, each of area 1 m^2 and separated in groups by 57m, have observed 4.5×10^{7} showers with energy $\sim 10^{14}$ev and 5.2×10^{6} showers with energy $\sim 10^{15}$ev. If a sidereal anisotropy exists in this range, then they find it must have an amplitude less than 0.1%.

For showers of energy $\sim 8 \times 10^{15}$ev, Rothwell et al (1956), using an array of 4 cloud chambers triggered by a double coincidence between 2 groups of G-M counters 20m apart, searched for localised sources of cosmic rays in the declination band $10^{0} < \delta < 90^{0}$. The angular resolution of their detector was approxim-

ately 5^{0}. Out of 1100 showers no sources of cosmic radiation at this energy, were found. Using the Culham array at Harwell, Cranshaw and Galbraith (1957) have shown that for showers of energy $\sim 10^{16}$ev, any sidereal variation has amplitude less than 1%. At Manchester, Crawshaw and Elliot (1955) found no evidence for a sidereal daily variation for air showers with energy as high as 10^{17}ev. The results of a harmonic analysis gave amplitudes of the first harmonics for showers at 2×10^{16}ev and 10^{17}ev as 1.7 ± 2.5% and 7.5 ± 6% respectively.

At higher energies large airshower arrays have extended observations greatly (ref. section 5.2), in particular the Haverah Park array which based on an analysis of 22,000 selected showers (Blake et al 1968) with a mean energy of 5×10^{17}ev, have found no deviation from isotropy greater than 3%. For the same energy and based on $\sim$ 1300 showers and for 63 showers of mean energy 3×10^{18}ev, the Volcano Ranch array (Linsley et al 1962) also found no claim for anisotropy in their arrival direction distributions.

Preliminary results of the SUGAR array (Brownlee et al 1969b) have found no evidence for an anisotropy of cosmic radiation with energy as high as 10^{19}ev.

At the time of the Calgary conference on cosmic rays, about thirty point sources of cosmic x-rays had been recorded, (Hayakawa 1967). Of these only 5 were generally accepted, these being Sco X-1, Sco X-2, Cyg X-1, Cyg X-2 and Tau X-1. The Crab nebula, pulsar NP 0532, is also thought to produce pulsed x-radiation (Bradt et al 1969), and possibly pulsed γ-radiation (Vasseur et al 1970). Evidence has also been found for a point source of cosmic gamma radiation in Sagittarius, close to the galactic centre (Frye et al 1969). These regions may also provide sources of some of the observed high energy primaries.

1.2 PRIMARY PRODUCTION MECHANISMS.

In the following section a brief review of some of the more likely, as well as a few unlikely explanations for the production of very high energy primary cosmic radiation is given. Special attention is given to the prediction that pulsars, believed to be rapidly spinning neutron stars, can in the limit produce cosmic rays with energy of the order 10^{21}ev.

1.2.1 EARLY MODELS.

From the time of recognition that the Earth is being bombarded by a penetrating radiation (Hess 1912), many people have tried to explain its origin.

Early models of origin included the possibility that the penetrating radiation is a terrestial effect and could be produced by the acceleration of electrons in the electric fields of thunderstorms (Halliday 1941) or by the electric fields created between the Earth and polarised water molecules in the stratosphere (Holmes 1937).

The majority of workers tended however to favour a cosmic origin of the radiation, either in stellar bodies or in interstellar space. Early theories ranged from the creation of cosmic radiation by the annihilation of matter (Jeans 1931) to the acceleration of dust particles by supernovae (Spitzer 1950).

As early as 1929, W. Bothe and W. Kolhörster suggested that cosmic radiation was corpuscular and was accelerated by interstellar or intergalactic fields of force ranging over enormous distances.

Fermi (1949) postulated what is today still one of the favourite acceleration mechanisms of charged particles in the cosmic ray beam. He considered the interactions between these particles and the *wandering* interstellar magnetic fields. These fields he assumed to be irregular and their affect on an incident charged particle would be to reflect or *mirror* them. Head on

collisions resulting in a net gain of energy by the particle of

$$dw = B^2 w$$

where w equals the energy (including rest energy) of the particle and B is the velocity of the wandering magnetic cloud in units of the velocity of light. After N collisions, a particle starting with non-relativistic energy will attain an energy

$$w = Mc^2 \exp(B^2 N)$$

An overtaking collision will result in a loss of energy, but these collisions occur statistically less than head on collisions, the net result being a gain in energy for a charged particle suffering sufficient collisions.

In order to compensate for absorption losses, protons require an injection energy of greater than 200 Mev. Because of their large ionisation losses, heavier primaries require much larger injection energies. An α-particle requiring about 1 Gev and an iron nucleus about 300 Gev.

Fermi estimated the distance between collisions to be of the order of a light year and the average velocity of the magnetic clouds to be $\sim$ 30 km sec^{-1}.

Burbidge and Hoyle (1964) have postulated a mechanism whereby violent events in galactic nuclei eject relativistic streams of charged particles into extragalactic space. Associated with these particles are relativistic magnetic fields which interact with already existing cosmic ray particles. The effect is a Fermi type acceleration process where the collisions are predominantly head on and due to the high magnetic field velocities, the energy gain is particularly large.

If the extragalactic field is assumed to be 10^{-8} gauss, a region of extent > 10 Mpc, the size of a *supercluster* (Abell 1962), is sufficient to contain protons of energy 10^{20}ev.

Greisen (1965) has considered the combined affect of spatial size and magnetic field strength imposed on a body which is to be capable of accelerating and containing high energy cosmic rays.

The two limiting factors are:-

(a) the radius of the trapped particle, assumed here to be a proton, given by

$$\rho = \frac{300E}{B} \text{ cm}$$

where E is the energy of the proton in electron volts and B the strength of the trapping magnetic field in gauss and

(b) the loss of energy by synchrotron radiation. The relative loss of energy per radian for a proton in a uniform magnetic field is (Ginzburg and Syrovatsky 1964)

$$\frac{\Delta E}{E} = \frac{2}{3} E^2 B \frac{e\beta^2}{(Hc^2)^4}$$

For the proton to be contained requires the size of the source $R >> \rho$, and for it to not lose energy requires the synchrotron energy loss to be much less than one. Assuming $R \geq 30\rho$, Greisen puts a limit on the size of the source region as

$$R > 10^{-13} \gamma^3 \text{ cm}$$

where γ is the Lorentz factor. The restriction on the magnetic field strength is

$$B < 10^{21} \gamma^{-2} \text{ gauss.}$$

For a 10^{21}ev proton this implies that $B < 10^{-3}$ gauss.

The restriction on source size is $R > 30$ pc for protons with energy 10^{20}ev and $R > 30$ kpc for protons with energy 10^{21}ev. For energies in excess of 10^{21}ev, no structure in the universe large enough to contain and accelerate protons, has yet been observed.

The total magnetic energy of the source, must be comparable to the particle energy density in the source

volume. For a total magnetic energy of

$$W_B = \frac{B^2}{4\pi} \frac{4}{3} \pi R^3$$

and following the method of Greisen, this implies that

$$W_B >> 300\ \gamma^5 \text{ ergs}$$

A 10^{19}ev proton then requires $W_B >> 10^{52}$ ergs which is typical of galactic energies, while a 10^{21}ev proton requires $W_B >> 10^{62}$ ergs which is far larger than the energy content of the strongest radio source.

The discovery of the universal 3^{o}K blackbody radiation (ref. section 1.6) limits source distances to within 10 Mpc for protons of energy 3×10^{20}ev. This distance contains the region of the local *supercluster* which contains about 10,000 galaxies.

The existence of supernovae within our galaxy, have led people to speculate the possibility of a galactic origin for cosmic radiation. Colgate and White (1963) calculate that for a type 2 supernova explosion of a star of 10 solar masses, 10^{51} ergs of cosmic radiation can be ejected. The upper limit for the energy delivered to a particle by the shock acceleration is 3×10^{16}ev for a radiation shock and 2×10^{19}ev for a plasma oscillation shock. Assuming an injection of 10^{51} ergs of cosmic

radiation for each type 2 supernova explosion in the galaxy, and a cosmic ray lifetime of 2×10^8 years, Colgate and White calculate that one large type 2 supernova explosion every 10^4 years would be sufficient to maintain the cosmic ray energy density present in the galaxy.

1.2.2 PULSARS.

The discovery in 1968 of accurate periodic radio pulses which move sidereally across the sky (Hewish et al 1968) has posed many difficulties as to how they arise. If the pulses originate from the rotation of a solid body, periods much less than one second are required.

An object which could possibly fulfill this condition is a neutron star; the hypothetical remnant of a collapsed supernova (Gold 1968). The diameter of a neutron star is thought to be 6 - 10 km, and due to its high electrical conductivity, its magnetic decay time is of the order of 10^7 to 10^8 years. Periods of the order of 1 msec are quite feasible for such a body.

According to Gold (1970), a star that rotates 10 times per solar year would, after collapsing by a factor of 10^5 to become a neutron star, have a rotational period of 3×10^{-4} secs. Since angular momentum is

conserved in the collapse, the rotational kinetic energy would increase by 10^{10} to become of the order of 10^{52} ergs. For the same star, the conservation of magnetic flux during the collapse would increase the surface field by a factor of 10^{10} also. In this way surface field strengths of 10^{12} to 10^{13} gauss would not be uncommon for a neutron star.

This rotating neutron star or *pulsar* can now be thought of as containing a rapidly co-rotating magnetosphere. At the critical radius, where $\omega r = c$ the speed of light, the magnetic field strength is still quite large. The electrodynamics of such a relativistic magnetosphere are not clearly understood, however it is feasible that such a system could radiate vast amounts of energy, both electromagnetic and particle in form.

The association of pulsars with supernovae remnants has been confirmed for two cases. One is the 89 msec Vela pulsar (Large et al 1968) and the other is the 33 msec Crab pulsar (Staelin and Reifenstein 1968). Slower pulsars are likely to be much older and any supernova remnant would have long vanished.

The slowing down of at least seven pulsars has been observed, and in the case of the Crab pulsar the rate is one part in 2400 per year (Richards 1968).

Gold (1969) has suggested that as a pulsar slows down, it spins off relativistic particles, thus providing a fast electromagnetic process for the production of cosmic rays. On the assumption that the Crab pulsar has mass equal to one solar mass and diameter 7 km, then with the present period of 33 msec, the rotational energy is 10^{49} ergs. The observed rate of spin down implies that energy is being radiated at the rate of 2×10^{38} erg sec^{-1} A vast quantity of this radiation, in the form of a relativistic plasma, being flung out of the magnetosphere at the critical radius.

Extrapolating back to the creation of the Crab pulsar results in an initial period $\sim$ 1 msec, corresponding to an initial amount of rotational energy of 10^{52} ergs. At the rate of one such supernova per 100 years, a flux of cosmic rays of 3×10^{42} erg sec^{-1} could easily be injected into the galaxy (Gold 1969).

Goldreich (1969) has proposed a simple physical model for a pulsar. He assumes that the axis of rotation of a neutron star is parallel to the magnetic dipole axis. Such a model cannot account for pulsed electromagnetic radiation, this requires a tilt between the two axes (Komesaroff 1970).

In Goldreich's model, the pulsar has a very thin plasma for an atmosphere. Particles are swept along the

polar field lines which extend beyond the critical radius, and achieve kinetic energies

$$E = \frac{10^{13}\ Z\ R^3\ B}{P^2}\ ev$$

and escape to infinity. Here R is the stellar radius in units of 10^6 cm, B is the surface field in units of 10^{12} gauss, Z is the charge on the particle and P is the period of the pulsar.

For the Crab pulsar, the present conditions would accelerate particles upto 3×10^{16}ev. With periods as short as 1 msec, energies as high as 10^{20}ev are possible.

Gunn and Ostriker (1969) have made a detailed analysis of emission of cosmic radiation from the Crab pulsar. In their model, the pulsar's magnetic and spin axes are at right angles. They find that for a particle with atomic number A and charge Ze, injected with small energy into the pulsar's co-rotating magnetosphere, a maximum energy (fig. 1.1)

$$E_M = 1.71 \times 10^{15}\ A^{\frac{1}{3}}\ Z^{\frac{2}{3}} \left(\frac{\Omega}{200}\right)^{\frac{4}{3}} \left(\frac{B}{10^{12}}\right)^{\frac{2}{3}}\ ev$$

can be obtained.

The mass of the Crab is assumed to be 1.4 solar

FIGURE 1.1

Energy as a function of angular velocity for a proton (P) and fully ionised iron nucleus (FE), as is obtained from the Gunn and Ostriker model of the Crab pulsar NP 0532.

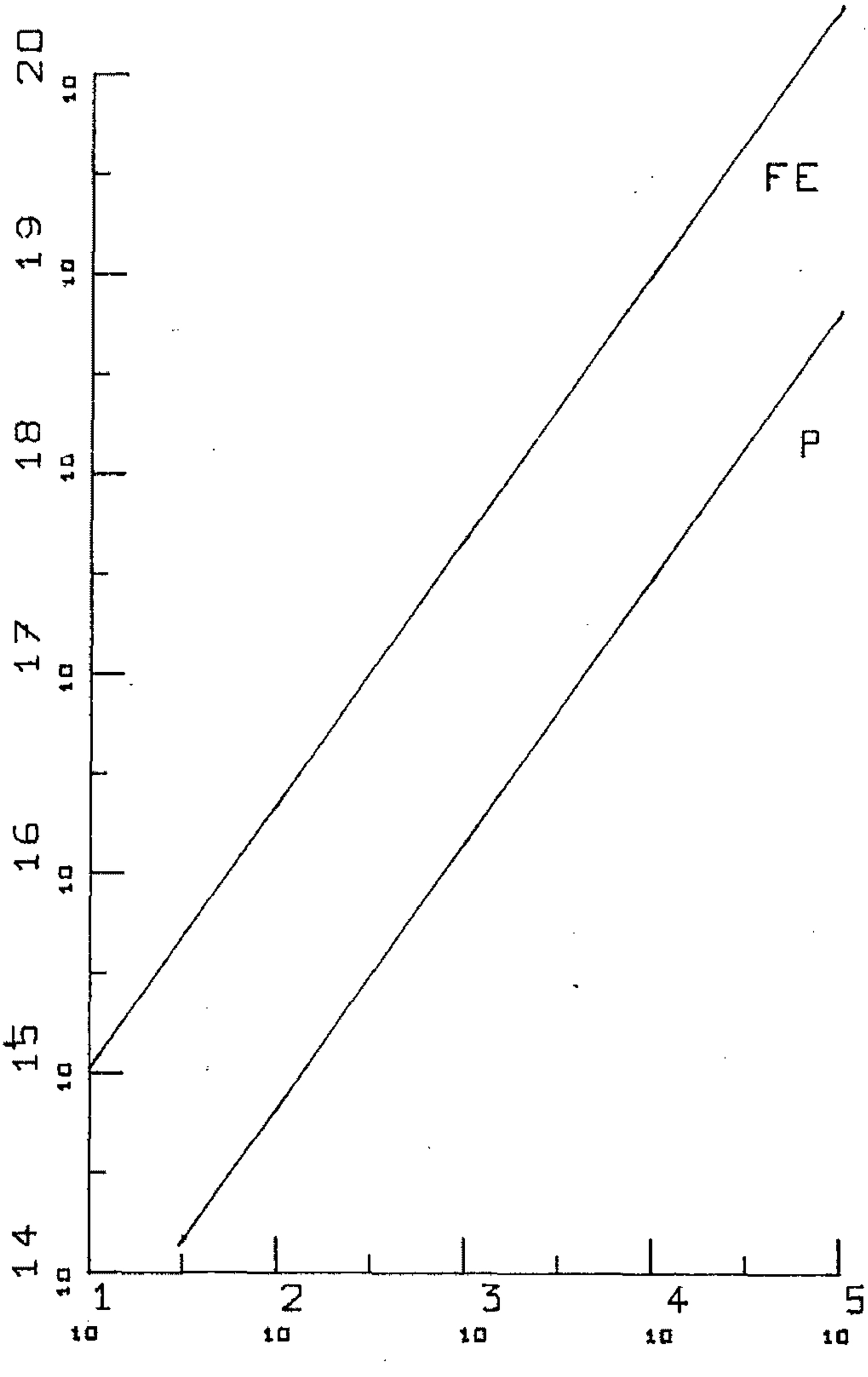
FE
P
E_P (EV)
20
19
18
17
16
15
14
10
1
2
3
4
5
ANG VEL (RAD/SEC)

masses and its surface magnetic field to be 10^{12} gauss.

The exponent of the differential energy spectrum of the radiation is -2.5, which is not far different from that observed (ref. section 1.7).

For the Crab pulsar at present, (i.e. 916 years after its creation), $\Omega \sim 200$ rads sec^{-1}. The maximum energy attainable by a proton is then 1.6×10^{15}ev and that attainable by a fully ionised iron nucleus is 5.5×10^{16}ev. The energy suppliable to electrons is $\sim 2 \times 10^{13}$ev which is sufficient to explain the present synchroton radiation from the Crab Nebula.

Extrapolating to time $t = 0$, $\Omega = 1.03 \times 10^{4}$ rad sec^{-1}. During the short period of time that the pulsar rotates with this angular velocity, protons may acquire energies as high as 3×10^{17}ev and iron nuclei energies as high as 1×10^{19}ev.

Assuming the density of particles in the magnetosphere is as given by Goldreich (1969), the flux of particles from the Crab pulsar is given by

$$\eta = 2.7 \times 10^{33} \left(\frac{\Omega}{200}\right)^2 \frac{B}{10^{12}} \left(\frac{r}{10^6}\right)^3 \text{ particles sec}^{-1}$$

where r is the stellar radius.

Initially the flux of cosmic radiation from the Crab pulsar was 3×10^{37} particles sec^{-1}. Now the

flux should be $\sim 10^{34}$ particles sec^{-1}.

Stretching the theory of Gunn and Ostriker to the limit where the radius of the star is at the Schwarzchild limit, the maximum energy obtainable by a proton is $\sim 10^{21}$ev.

The latest observations of the electromagnetic radiation emitted from pulsars and in particular, the presence of *marching* sub-pulses (Cole 1970), indicate that the processes underlying pulse production are very likely to be extremely complex.

It logically follows that cosmic ray acceleration mechanisms would also be complex, making theories like that of Gunn and Ostriker only a very rough guess to the true nature of the processes involved.

1.2.3 QUASARS.

Quasars are still the least understood astronomical phenomena. According to red shift measurements they are the most distant objects yet found in our universe. Luminosity measurements imply that vast sources of energy must be available.

One attempt to explain the energy output of quasars which can also be extended to the nuclei of some galaxies, has been put forward by Bahcall et al (1970). Based on the existence of fractionally charged particles

called quarks, which have been predicted by Murray Gell-Mann (1964) and evidence for which has recently been reported (McCusker and Cairms 1969, Cairns et al 1969, Chu et al 1970), this theory predicts that quasars obtain their energy by *quark-fusion* . Assuming a mass of 10^{10} solar masses for a typical quasar and an energy release of $\sim M_q c^2$ from each q-q interaction, they can explain a luminosity of 10^{46} ergs sec^{-1} if the quarks burn at 2×10^6 ^oK.

The presence of quark electron atoms if they exist, could be verified by looking for their predicted recombination lines which occur mostly in the strong infra-red region of the spectrum. Infra-red astronomy in this way may reveal the location of high energy cosmic ray sources. Because of the distances of galactic nuclei and further still quasars, this may be the only way of finding cosmic ray sources.

Extending the concept of pulsar radiation to great limits, Piddington (1970) assumes that quasars are large rapidly rotating bodies. He is able to produce energy at the rate of 4×10^{48} ergs sec^{-1} or 10^{61} ergs over a period of 10^5 years. Owing to the lack of understanding and complexity of normal pulsars, it is unlikely that their properties can be simply extrapolated to explain phenomena of the same scale

as quasars.

The main objection to quasars as a source of our high energy cosmic rays, is the attenuation of the particles by the universal blackbody radiation (ref. section 1.6). The fact that no cosmic ray cutoff has been observed above the predicted value (Brownlee et al 1969a) may imply that no such attenuation occurs, or that the sources of our observed energetic primaries occur within our *supercluster*. Possibly in bodies like Centaurus A, the strong radio source. In either way any sense of direction will be lost due to magnetic deflection over the distances involved.

1.3 EXTENSIVE AIR SHOWERS.

The observed flux of high energy cosmic radiation is very small, one primary of energy > 10^{20}ev strikes each square mile of atmosphere per year.

In order to observe such a low flux of cosmic radiation, we look instead at the shower of secondary particles initiated in the atmosphere by the primary. Such a shower, called an extensive air shower, consists of a disc of upto a mile in diameter by the time it reaches the ground. In this way, instead of intercepting a primary particle whose diameter is typically 10^{-12}cm, we intercept the E.A.S. produced by the primary,

whose diameter is typically 10^5 cm. The atmosphere acts as a spatial amplifier with gain $\sim 10^{17}$ times.

Observations made by sampling the shower front can be extrapolated via a knowledge of nuclear interaction theory, to describe the properties of the primary particle. For a primary proton, the most abundant primary particle, the interaction mean free path in air is 80 g cm^{-2} which corresponds to 12 interaction lengths in a vertical atmosphere. The height of the first interaction is subject to fluctuation but on the average occurs about 18 km above sea level.

The cascade produced as the proton descends through the atmosphere can be divided into three categories. The first being the nuclear cascade which is confined close to the core and consists of strongly interacting particles. Secondly is the electromagnetic component which is initiated by high energy γ-rays from the nuclear cascade and consists of γ-rays and electrons. This cascade quickly reaches a maximum developement and then becomes absorbed into the atmosphere. On reaching the ground the remainder of the electromagnetic cascade is easily stopped by a few metres of earth. Thirdly there is the penetrating or muon component of the air shower. The muons originate from the decay of

charged pions generated in the nuclear cascade. The muons carry away most of the decay energy and their atmospheric absorption is small, so virtually all of them reach sea level.

The total number of particles generated in an air shower depends on the zenith angle and energy of the primary particle. However for air showers of energy $\sim 10^{17}$ev, the number of muons is generally $\sim 10^{6}$ particles at sea level.

1.4 METHODS OF SHOWER DETECTION.

Because of the low rate of very high energy E.A.S. created in the atmosphere, large area detectors are required to maximise the probability of recording them. The probability of recording such an air shower increases with the effective area of the detector.

A straight forward way of detecting E.A.S.is by intercepting samples of the shower front using particle detectors spread over a large area on the ground. The only limitation to this technique is the correlation of distant detectors. The method suggested by McCusker and Winn (1963) has overcome this problem and proved successful in the running of the SUGAR array.

There are several methods of detecting E.A.S. which do not involve intercepting the particles of the

shower disc. These methods rely on observing the electromagnetic radiation produced by the charged particles of the shower front as it descends through the Earth's atmosphere and magnetic field.

The Cerenkov light emitted by E.A.S. was first recorded by Galbraith and Jelley (1953). Recently, Bosia et al (1970) have recorded multiple Cerenkov pulses from air showers. The probability of being due to instrumental effects or the simultaneous arrival of low energy air showers, they claim to be $< 10^{-6}$. The observation of these multiple Cerenkov pulses, they also claim, indicate a possible structure of shower development or the presence of a massive particle of mass 10 Gev and energy $\sim 10^{12}$ev.

Attempts to use the atmosphere as a scintillator and observe E.A.S. by the atmospheric fluorescense they produce have also been tried (Bunner et al 1968). So far no outstanding success has been met, the principal reason being the low level of light output generated by each shower.

Using the lower frequency end of the electromagnetic spectrum, several workers have observed radio pulses from air showers. The major source of this radiation being due to the passage of the geomagnetically separated particles of the shower front through the

Earth's magnetic field. Correlations between shower parameters derived from particle detectors and radio pulse measurements (Prescott and Hough 1970, Allan et al 1970) have recently been reported.

1.5 PRIMARY COMPOSITION.

The primary composition at low energies has been well determined by direct observation of primary tracks in nuclear emulsions (Waddington 1960). The ratio $p:\alpha:Z\geq 3$ based on Sydney results for primaries with the same total energy ($10^{12} < E < 10^{15}$ev) is 2.2:1:3.2. Until recently the heaviest primary observed has been iron (Z=26), however Fowler et al (1967) also using nuclear emulsions at balloon altitudes have found primaries with $Z > 30$. Using the magnetic field of the Earth to help eliminate slow iron nuclei and interspersing their emulsions with lead to help reject slow heavily ionising particles, they have found elements in the primary cosmic ray beam upto $Z = 92$ with an error of ±4%.

At higher energies than can be studied with nuclear emulsions, the composition of the primary beam has been investigated using multicored showers (Bray et al 1965). By comparing observed core structure with a Monte Carlo model (McCusker et al 1969a) which indicate

that proton primaries produce single cored showers at least 90% of the time, Bakich et al (1970) have shown that at 10^{15}ev protons constitute about 60% of all showers, the rest being due to heavier primaries. At higher energies the results indicate that the proportion of proton primaries become less.

Above 10^{18}ev little is known about the composition. Linsley and Scarsi (1962) suggest a *metagalactic* flux of protons, heavier muclei being broken up by photodisintegration before reaching the Earth.

1.5.1 HEAVY PRIMARIES.

Primaries of mass greater than that of a proton are likely to produce extensive air showers with a higher $\frac{\mu}{e}$ ratio than for proton showers. Such showers are called *muon rich*.

Observations of the arrival directions of muon rich air showers (Matano et al 1965) with shower size $10^6 \leq \bar{N} < 10^7$ particles, indicate an as yet unestablished decrease of events between right ascension 15 hr and 21 hr. The definition of a muon rich shower taken by the Tokyo group, is one in which the muons constitute at least 60% of the total number of shower particles. Such showers constitute 6% of all showers recorded by them.

A harmonic analysis on a total of 219 muon rich air showers, which represents the sum of several earlier results, yields an amplitude of 30 ± 8%. The Tata group (Chatterjee et al 1968) have observed a similar trend in their muon rich air showers, observing a *dark region* between 15 hr and 21 hr in right ascension. By using a chi-squared test on their data, they attribute a probability of less than 3% that their distribution is isotropic. The latitudes of the Tokyo and Tata arrays are 36^{o}N and 11^{o}N respectively.

1.6 THE BLACKBODY BACKGROUND RADIATION.

The discovery by Penzias and Wilson (1965) of an intense isotropic microwave radiation at 7.35 cm wavelength was later confirmed at 3.2 cm (Roll and Wilkinson 1966) and shown to correspond to a blackbody thermal radiation at 3.0 ± 0.5 ^{o}K. This radiation is believed by some to be the sea of photons produced by a primeval-fireball creation of the universe (Dicke et al 1965), and cooling due to the adiabatic expansion of the universe.

Greisen (1966) shows that if such a flux of thermal photons is universal, then a cutoff in the cosmic ray energy spectrum should occur above 3×10^{19}ev.

For an equivalent blackbody temperature of 3 ^{o}K,

the photon density is 548 cm^{-3} and the mean photon energy is 7.0×10^{-4}ev. The threshold energy for protons on photons of this energy is 10^{20}ev with a mean cross-section of $\sim$ 200 μb, the interaction being

$$p + \gamma \rightarrow N + \pi$$

The distance scale for loss of energy is $\sim 4 \times 10^{25}$ cm, or $\sim$ 10 Mpc. If the particle is a heavy primary rather than a proton the distance scale is severely reduced by photodisintegration.

The net effect on the cosmic ray energy spectrum is that below 3×10^{19}ev the photo-pion reaction has negligble effect however above this energy the inter-action cross section rises rapidly and if cosmic ray sources are more distant than 10 Mpc, the spectrum should drop steeply.

Rocket borne observations in the region 0.4 to 1.3 mm wavelengths, of the thermal radiation, (Shivanandan et al 1968) imply that the intensity of the radiation is greater than expected and possibly corresponds to an equivalent blackbody of temperature $8.3 \begin{smallmatrix}+2.2\\-1.3\end{smallmatrix}$ ^{o}K. If this result is correct, then the observed radiation may not follow a blackbody distribution and may not be universal, thus removing the neccessity for a cutoff in the energy spectrum.

1.7 THE PRIMARY ENERGY SPECTRUM.

More than any other aspect of the primary cosmic radiation, the primary energy spectrum provides the greatest potential for interpretation. From it can be drawn inferences of the primary composition and conclusions of astrophysical significance regarding the origin of cosmic rays. The integral spectrum as represented in fig. 1.2 consists of three regions:-

(a) $E_p < 2 \times 10^{15}$ev.

In this region the slope of the spectrum is -1.7. The composition is believed to be the same as has been measured at lower energies in nuclear emulsions.

(b) $2 \times 10^{15}\text{ev} < E_p < 5 \times 10^{18}\text{ev}$.

The slope in this region steepens to -2.1. The steepening of the slope has been explained (McCusker 1965) by assuming that primaries are produced with the same percentage composition as indicated by the region $E_p < 2 \times 10^{15}$ev. Above 2×10^{15}ev (the *knee*), protons are no longer contained by the galaxy and drop out. As energy increases the heavier elements are successively removed by this rigidity cutoff until at 5×10^{18}ev the iron primaries start to drop out.

FIGURE 1.2

Integral Primary Energy Spectrum

$E_P > 10^{11}$ev.

(Brownlee et al 1969a)

Integral Energy Spectrum

Mc Donald
Slope --1·5

Slope
-1·7

McCusker + Peak

Greisen

Jauncey

Jauncey

Slope 2·0-2·1

Greisen

Assuming
Cu. Primaries

Sydney

Slope-1·1

Volcano
Ranch

Log Intensity
(Per Metre²
Per Second
Per Steradian)

Log E₀ (Electron Volts)

(c) $E_p > 5 \times 10^{18}$ev.

In this region past statistics have been poor. The results of the Volcano Ranch array indicate that the spectrum flattens again with a slope of -1.6 This flattening according to Linsley and Scarsi (1962) represents a flux of meta-galactic protons. Early results of the SUGAR array (Brownlee et al 1969a) as depicted in fig. 1.2, also note a flattening of the spectrum. The slope being flatter and equal to -1.1.

Hillas (1968) explains the form of the energy spectrum by supposing that cosmic ray sources were much stronger in the past than at present and that reactions with a universal microwave radiation should have led to a much greater energy loss, with lower threshold energies in the past. The presence of an *ankle* at 5×10^{18}ev could be due to this interaction and not a transition from galactic to extragalactic cosmic rays as suggested by Linsley and Scarsi (1962).

Unpublished results on the energy spectrum and based on 2983 events recorded by the SUGAR array, indicate that the presence of an *ankle* in the energy spectrum (fig. 1.2) at 5×10^{18}ev maybe an array boundary effect.

CHAPTER 2

THE SUGAR ARRAY.

2.1 THE SUGAR SYSTEM.

Due to the low flux of cosmic ray primaries and hence air showers, with energy greater than 10^{19}ev, it is necessary to build a large area detector if a significant number of showers are to be recorded in this range. Such a system is faced with the problem of recording coincidences between widely separated detectors. The inter station spacings involved make the use of cables virtually impossible, owing to bandwidth limitations. Also the cost of extensions to the array is very non linear. In a system such as SUGAR, it costs a fixed amount to install each station, independent of the number of stations. The SUGAR system is unique (McCusker and Winn 1963, Brownlee et al 1968a) in so far as each station is autonomous, i.e. each event is recorded locally on magnetic tape. The timing of an event is supplied by a common clock pattern which is transmitted to each station and recorded along with each event. All information is recorded in digital form. Coincidences are sorted out of the many hundreds of local events by feeding the magnetic tapes from each station into a large English Electric KDF9 digital computer. This sorting is generally done about ten days after the actual events have been recorded.

The requirements that need to be met by a site

on which a giant air shower experiment such as SUGAR, is to be built, are quite stringent. The land must be reasonably flat over an area of approximately 100 km^2 and must have access roads to enable easy servicing and maintenance of stations. The area must be reasonably private and remote to prevent possible tampering with equipment and to minimize electrical interference.

2.2 LOCATION OF THE ARRAY.

The site chosen for the SUGAR experiment is the Pilliga state forest fifteen miles south of Narrabri, New South Wales. Narrabri is located 350 miles north west of Sydney at latitude $30^{o}31'$ south and longtitude $149^{o}38'$ east and at an altitude of 280m above sea level. Over the area of the array the land deviates no more than ±7m from a plane, and forestry commission roads permeate the whole forest. The only inhabitants are a few timbercutters and the land is rent free.

The array itself is situated at the northern end of the forest. Located 2 miles north of the north east corner of the array is the timing transmitter, the laboratory and living quarters for permanent university staff who service and maintain the array.

At the time of writing the array is composed of 34 stations spread over an area of 38 km^2 with a geometry

as depicted by fig. 2.1. With this geometry the array is sensitive to air showers with energy greater than 10^{17}ev.

2.3 EXTENSIONS TO THE ARRAY.

Installing of a further 26 stations is at present underway. This will increase the area to about 87 km^2. With this area and using our present energy spectrum (ref. section 1.7), we will expect $\sim$ 5 showers per year having an energy greater than 10^{20}ev.

Located midway between stations 12 and 15 (fig. 2.1) and connected by coaxial cables, is a small array of 6 spark chambers, each of area 0.25 m^2. These spark chambers are triggered in coincidence with stations 12 and 15 (at the one particle level), and record both the muon and electron component of the air shower.

2.4 DESCRIPTION OF A STATION.

Each sugar station is an autonomous unit, the only common link between stations is the reception of timing information from the central timing transmitter.

A station consists of two tanks containing liquid scintillator and separated by 50m in the north south direction. Both tanks are buried, with the scintillator about 2m below the surface of the ground (fig. 2.2).

FIGURE 2.1

Map Of The SUGAR Array.

o Present Stations

x Extensions To The Array

e Electron Detector

Station marked 32 refers to section 3.4.3

Timing
Transmitter

+

N

scale 0 1 2 3 4 5

km

In this way only muons with energy greater than a threshold energy of (0.75 ± 0.15) secθ Gev (θ is the zenith angle of incoming particles) are detected, and except very near the core, the electromagnetic and nuclear component is shielded out.

The tanks which are made of steel, are connected by an underground pipe which carries signal cables. Each tank consists of a conical section 1.2m high opening out to a diameter of 2.7m at the base. A 1.8m high cylindrical section having a diameter of 0.6m is attached to the top. The whole tank sits on a concrete base in a hole about 3m deep.

The base area of 6 m^2 of each tank is covered by 600 litres of Shellsol A solvent containing 3gm/litre of p-terphenyl scintillator and 0.01 gm/lite of POPOP wavelength shifter, the average depth being 10 cm.

A single photomultiplier tube is mounted at the top of the conical section about 1m from the scintillator. To obtain a uniform light response from the edges to the centre (Ryan 1968), the base is dished so that the central depth of scintillator fluid is about 6 cm and the depth at the edges is about 15 cm.

To compromise between good particle resolution and fast timing response, a 17 cm diameter photomultiplier tube type EMI 9623B has been used. This tube

FIGURE 2.2

A SUGAR Station.

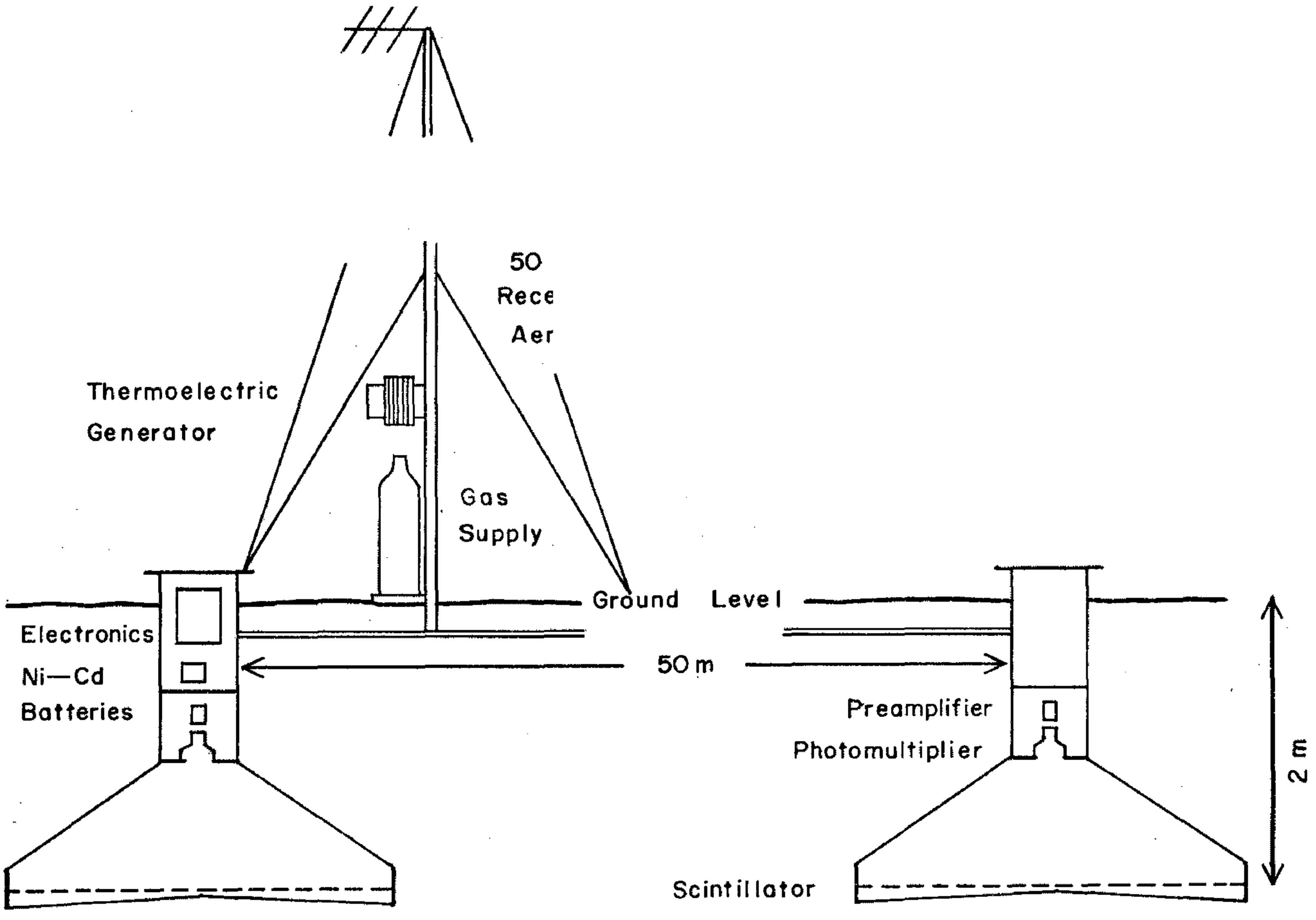
50
Rece
Aer
Thermoelectric
Generator
Gas
Supply
Ground Level
Electronics
Ni—Cd
Batteries
50 m
Preamplifier
Photomultiplier
2 m
Scintillator

enables the single particle level of background cosmic radiation to just be resolved, and gives satisfactory timing accuracy.

Above the photomultiplier in one tank, are stored the batteries and the station's electronics, the electronics being entirely transistorised. Associated with each station is an aerial mast for the reception of the station's timing information. This is located near to one of the scintillators.

In many stations the batteries are Nickel Cadmium cells, and are continuously charged by a thermo-electric generator. The other stations are powered by lead acid batteries which need charging every week. In time the whole array will be run on thermo-electric generators, thus reducing servicing time.

2.5 PARTICLE DETECTION.

The photomultiplier output current pulse is integrated on a capacitor which decays exponentially through a resistor. This exponential pulse is then amplified by a fast risetime logarithmic amplifier of gain 50 (Suga et al 1961). This amplifier provides an output pulse whose length is proportional to the logarithm of the input pulse height, independent of the degree of overload. Cables from the preamplifiers pass through

a light tight septum and connect to the main electronics located in one of the tanks. This tank also contains an extra 50m of cable to compensate for the delay of the signal from the other tank.

At the electronics, the signal is again amplified by 50 and discriminated. The transmission cable, whose impedance is 50 Ω, is terminated and hence a 3 dB loss is introduced. The overall gain of the preamplifier system being 1250.

The pulse length l is given by

$$l = RC \ln \left(\frac{V}{V_0}\right)$$

RC = 3 μsec and V_0 is the discriminator voltage. The pulse lengths of both channels are digitized at 10 MHZ and stored. Fig. 2.3 is a block diagram of the system.

The discriminator level is set such that a three particle response detected in each tank, produces a coincidence (a highly inclined single particle owing to increased path length in the scintillator, can give a three particle response). In this way the number of local events is minimized and the sensitivity of the stations to the low particle densities on the fringes of large air showers is maintained.

The two discriminator outputs trigger two 350 nsec

FIGURE 2.3

Electronics Block Diagram.

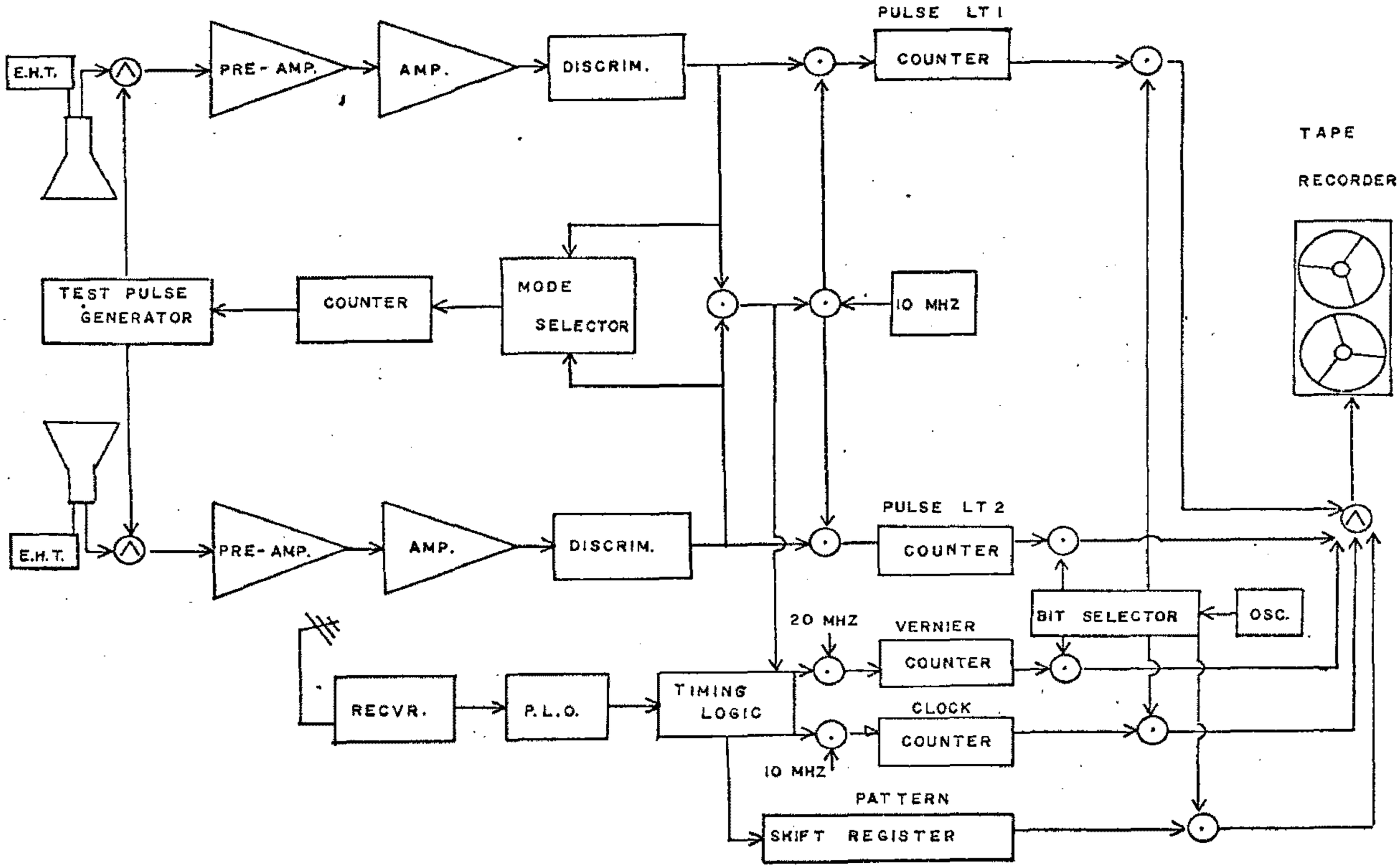
E.H.T.
PRE-AMP.
AMP.
DISCRIM.
PULSE LT 1
COUNTER
TAPE
RECORDER
TEST PULSE
GENERATOR
COUNTER
MODE
SELECTOR
10 MHZ
E.H.T.
PRE-AMP.
AMP.
DISCRIM.
PULSE LT 2
COUNTER
20 MHZ
VERNIER
COUNTER
BIT SELECTOR
OSC.
RECVR.
P.L.O.
TIMING
LOGIC
CLOCK
COUNTER
10 MHZ
PATTERN
SHIFT REGISTER

monostables which in turn trigger a coincidence whenever the two pulses are within 350 nsecs of each other. This enables recording of horizontal showers whose transit time between tanks can be of the order of 170 nsecs.

The coincidence pulse switches on the temporary power supply (most of the electronics is off between events to conserve power), and initiates the timing logic.

The coincidence output, which is the overlap between the monostable pulses, is stretched by a factor of ten, digitised, and stored. One storage bit records which pulse came first, this tells which tank to use in subsequent analysis of the timing of the shower front. The output also gives the time difference between the two channels.

2.6 RECORDING OF ARRIVAL TIME.

Each station continually receives a timing pattern, generated by a crystal controlled digital clock and transmitted on a 397.25 MHZ carrier wave from the base station (ref. chapter 3).

The pattern is a 48 bit word (fig. 2.4a) and is of length 80.5 μsecs (2^{-30} days). Each bit occupies a time of 840 nsecs with a *1* turning the carrier off and a *0* leaving it on. Bits are separated by logical zeros

of length 830 nsecs. The end of each word is marked by setting the two most significant bits and the space between them equal to *ones*. This is called the long pulse. Each 48 bit word expresses the time to within 80.5 μsecs, and each word will repeat itself every $2^{-30} \times 2^{46}$ days (or 180 years).

Owing to there being long gaps of upto 76 μsecs in the timing pattern, a local crystal oscillator is phase locked onto the receiver output. Its period is the same as the bit period (∿1.6 μsec) and its output is called the clock signal. The jitter in the clock oscillator is about ± 10 nsecs.

To obtain a timing accuracy of 50 nsecs, an unsynchronised 20 MHZ crystal oscillator is used to interpolate between the clock pulses. This oscillator is also halved and used for the 10 MHZ digitalisation.

When an event occurs, the number of vernier pulses until the second clock pulse after the eighth vernier pulse is recorded. The number of clock pulses until the next long pulse is counted, and finally the next pattern is shifted into a 48 bit integrated circuit shift register.

FIGURE 2.4

(a) The receiver pattern.

(b) The phase locked oscillator.

(c) The overlap between (a) and (b). The ratio (c)/(a) is kept constant.

(d) The long pulse.

(e) The event pulse.

(f) The vernier pulses.

(g) The clock pulses.

(h) The signal for the next pattern to be read into the shift register.

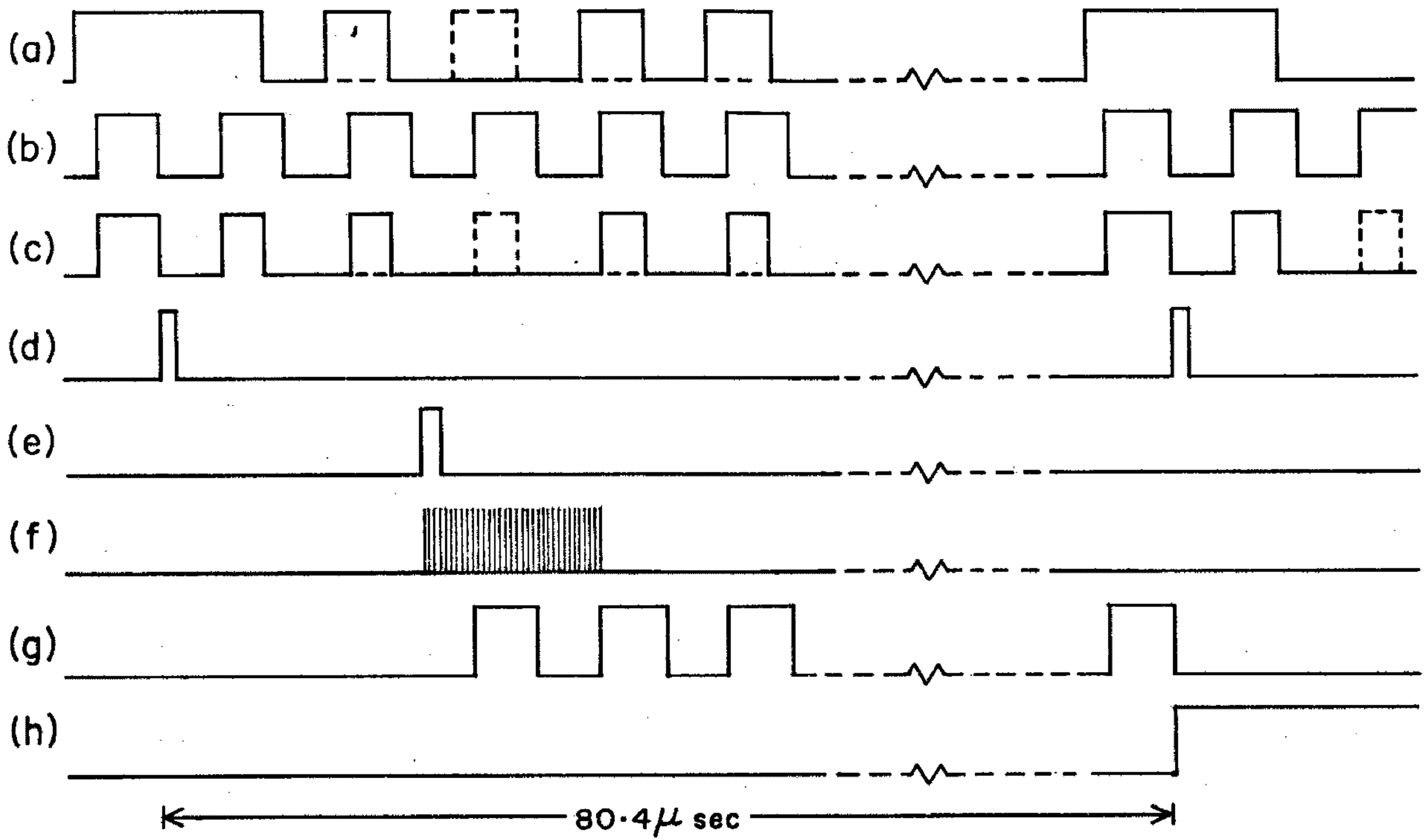
(a)
(b)
(c)
(d)
(e)
(f)
(g)
(h)
80·4μ sec

2.7 RECORDING AN EVENT.

The information from each event is stored in scalers and shift registers. This information is readout serially and in triplicate (to enable lost bits to be recovered by a majority decision) onto a ¼ inch magnetic tape. Each recording of the event uses 96 bits, which are divided into:-

9 bits	station number
3 bits	type of event and simulator type
6 bits	vernier count
6 bits	clock count
6 bits	time difference
9 bits	pulse length channel 2
9 bits	pulse length channel 1
48 bits	timing pattern

Each event, of which there are 12 per hour paralyses a station for about 10 secs.

2.8 SIMULATED EVENTS.

Apart from recording real events, a station also records simulated events. There are four possible simulator pulse heights, each stable to better than 0.2%. A simulated event is generated after every 2^{12} and after every 2^{17} real pulses have been counted. In this way, the rates and pulse height calibration for each

channel can be checked over the range of the system. A background count of 30 particles sec^{-1} is equivalent to discriminating at the 3 particle level.

The tapes are collected at approximately weekly intervals from all the stations, and sent by rail to Sydney for data reduction analysis, after which they are returned, erased and used again on stations.

2.9 DATA ANALYSIS.

All the ¼ inch tapes from any one week's run are transcribed onto one or more 1 inch magnetic tapes. Each 1 inch tape holds about 35,000 events, and one week's running of the array yields about 70,000 events. At the same time a format check is made of the original recording of each 6 bit character and another character of 6 bits is set indicating whether or not this format is correct and if not, where it is in error. After each event, now consisting of 96 characters, a terminator is set. These tapes are then transcribed offline onto a standard KDF9 computer tape via a Continous Data Input Buffer.

The raw data is analysed by four analysis programs:-

(1) Decoding of raw information - CHUNK I

(2) Coincidence detection - CHUNK II

(3) Basic shower analysis - CHUNK III

(4) Direction and curvature analysis - CHUNK IV

2.10 DECODING OF RAW INFORMATION.

CHUNK I

The decoding of the raw information that has now been assembled, is done by a program called CHUNK I.

CHUNK I looks through the recorded information and for each event, checks the three separate recordings of that event. If all three recordings are internally consistent or a majority descision can be made, the event is accepted otherwise it is discarded.

For each accepted event, the time of the event is calculated

$$t_i = T - v\tau_v - c\tau_c + r_i$$

t_i time of event at ith station

T time of next pattern after the coincidence

c, τ_c number and period of clock counts

v, τ_v number and period of vernier counts

r_i signal transmission time to station i

Also the particle number in each tank is calculated. This information together with the station number, event number and the original event data, is recorded onto another computer tape.

2.11 COINCIDENCE DETECTION.

CHUNK II

The next step in the analysis is the sorting of events which involve three or more stations. To do this the CHUNK I output is analysed by another program called CHUNK II. This program looks for events which occur within ± 80.4 μsecs (or ± one clock pattern) of each other. All events triggering three or more stations have the following information output onto 8-channel paper tape.

(1) coincidence event number.

(2) multiplicity (number of stations triggered)

(3) time of event

and for each station in the coincidence

(a) relative time of triggering in nsecs.

(b) particle number in each tank

(c) pulse length out of each scintillator

(d) time difference in nsecs.

Coincidences involving only two stations are printed on the line printer, but are generally not used in further analysis.

On the average we expect approximately 40 events with multiplicity greater than 3 per week.

2.12 BASIC SHOWER ANALYSIS.

CHUNK III

This program performs the basic analysis of SUGAR events. For each event, the triggering times of each station are corrected for phase and pulse height (ref. chapter 4), and assuming the array to be flat, a least squares plane fit is made to the shower front. The direction cosines of this plane provide an estimate, to within $\sim 5^{o}$, of the local arrival direction. The shower's celestial co-ordinates are estimated, however, in the investigation of arrival direction distributions more accurate angle determinations are used. The local direction provides a first step in finding the shower core position and muon number.

2.12.1 CORE POSITION AND SHOWER SIZE.

In determining the shower size and core position, a structure function based on SUGAR results is used (Fisher 1970, Brownlee et al 1969c). The structure function is basically a Greisen structure function, but with the exponent of the second term being variable and a function of zenith angle

$$\rho(\mu) = k\ A\ r^{-0.75} \left(\frac{r}{320} + 1\right)^{-\alpha}$$

$$\alpha = 1.5 + 1.86\cos\theta$$

The core position and muon shower size are determined by a maximum likelihood method (Goorevich 1969). Should any station in an event register more than 4000 particles in either tank, then no core search is made. Instead the core is assumed to have landed on the tank with the largest response. Also the response of the tank, being unreliable owing to possible saturation of the electronics, is not used in estimating the muon shower size.

The error in muon shower size for all showers is approximately 10% and the error in core position in the shower plane (fig. 2.5) is approximately 40m. These errors represent fluctuations of one standard deviation away from the maximum likelihood value.

2.12.2 ENERGY ESTIMATION.

An estimate of the primary energy is made based on a Monte Carlo calculation (McCusker et al 1969b). The primary energy being given by

$$y = 21.80 - 2.26w + 2.20w^2 + (1.21 - 0.16w)x$$

where $y = \ln(E)$ — E is energy in Gev.

$x = \ln(N_\mu/10^7)$ — N_μ is muon shower size

$w = \ln(\sec\theta)$ — θ is zenith angle.

The estimate is valid in the range 10^{17}ev $< E < 10^{20}$ev and $\theta \leq 70^0$. The error in the estimate is about 10%.

FIGURE 2.5

Core Position Error Distribution.

Mean Error = 39m.

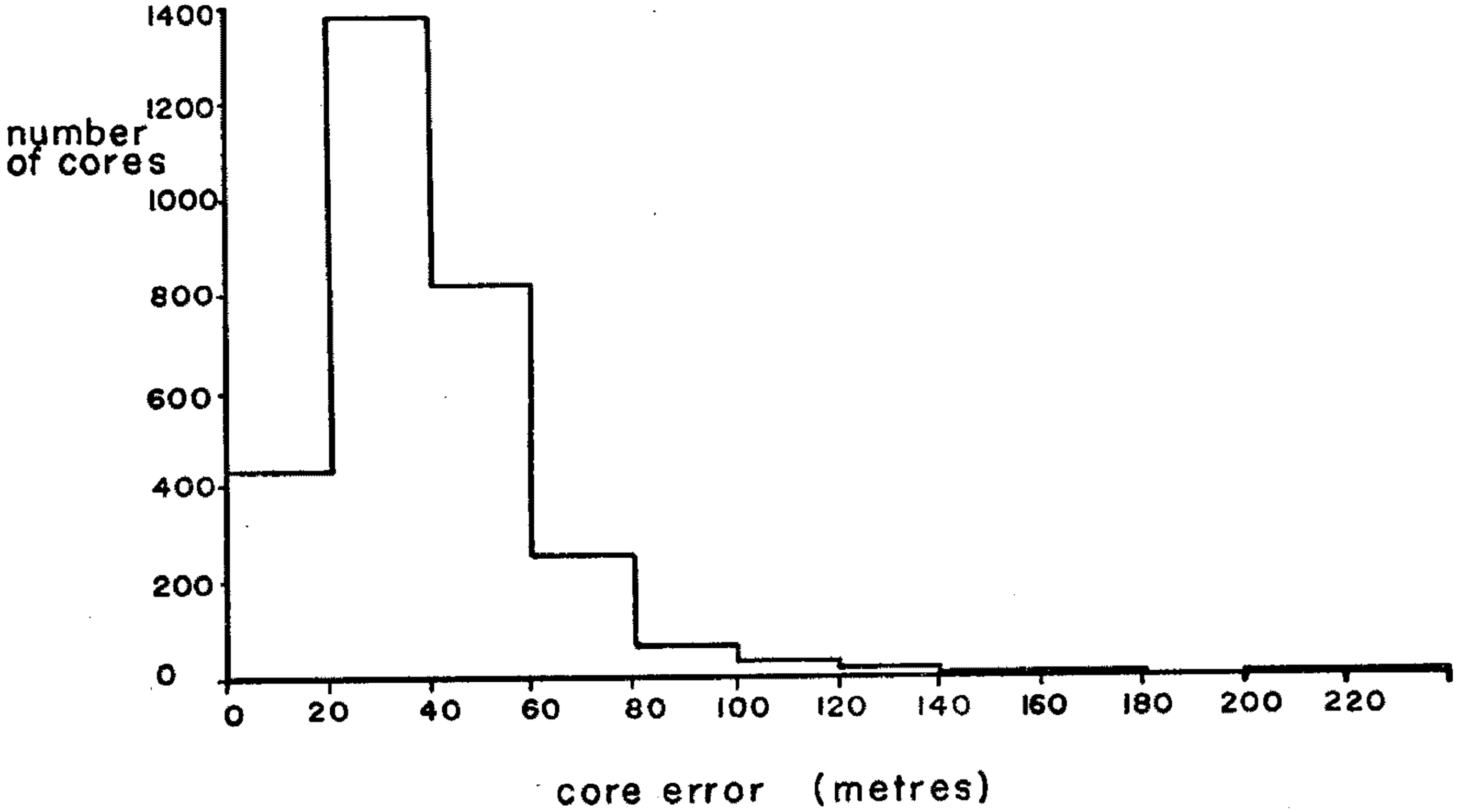
number of cores
1400
1200
1000
800
600
400
200
0
0
20
40
60
80
100
120
140
160
180
200
220
core error (metres)

All CHUNK III results are permanently stored along with the basic CHUNK II output on one magnetic tape, for access in further analysis.

2.13 DIRECTION AND CURVATURE ANALYSIS.

CHUNK IV

This program recalculates shower arrival directions allowing for shower front curvature (ref. appendix). At the same time errors in timing, local and celestial co-ordinates and curvature are calculated. The new angle measurements are used to overwrite the original CHUNK III angle measurements (with a marker to indicate that the results came from CHUNK IV).

Curvature measurements and errors are also added to the CHUNK III magnetic tape.

Having accurately determined shower directions, CHUNK III is rerun, this time using these accurate directions rather than the original plane fit directions. A new core is found, a new muon shower size is found and a new estimate of the primary energy is made.

With this new core position CHUNK IV (which relies on a knowledge of core position), is rerun and the shower directions are refined further.

CHUNK IV directions generally differ by no more than a few degrees from CHUNK III directions. And only

in rare circumstances are the deviations greater than 10^{o}.

Recalculation of CHUNK IV with a new core only creates a significant difference if the original core positioning is uncertain. This is generally the case only in a few very inclined showers.

APPENDIX.

A cosmic ray air shower front can be roughly approximated by a plane which is at right angles to the direction of travel of the air shower, and travelling at almost the speed of light. A second and more accurate treatment is to consider the air shower front as being spherical and expanding from the point of origin with almost the velocity of light. The radius of the sphere being time dependent.

The method of estimating the relative parameters for each of the above cases, is to do a least squares fit of the required surface to the corrected timing measurements at each station (ref. chapter 4).

(1) Plane Fit.

The equation of any plane is given by

$$lx + my + nz = p$$

where l, m and n are the direction cosines of the plane, and p it's perpendicular distance from the origin. If v is the velocity of the plane then

$$p = p_o - vt$$

where p_o is the perpendicular distance when the time $t = 0$.

If each of the N triggered stations have position co-ordinates (a_i, b_i, c_i) and triggering time t_i, then we

can form a set of least squares equations. To simplify matters, we work in a centre of mass system, i.e.

$$\sum a_i = \sum b_i = \sum c_i = \sum t_i = 0$$

hence $p_o = 0$.

The least squares equations are found by minimising

$$S = \sum \{vt_i + la_i + mb_i + nc_i\}^2$$

with respect to l and m, assumed to be independent and normally distributed. n is related to l and m by

$$n^2 + l^2 + m^2 = 1$$

The least squares equations are given by

$$\frac{\partial S}{\partial l} = 0 \quad \text{and} \quad \frac{\partial S}{\partial m} = 0$$

For N=3 the fit is exact. For N>3 an iterative solution of the equations is required. An analytic solution is possible on the assumption that the array is flat. In this case all $c_i = 0$.

The full solution of this simple analytic case is given as an example of the method.

The least squares equations in matrix form are

$$\underline{A}\underline{u} = \underline{b}$$

$$A = \begin{pmatrix} \sum a_i^2 & \sum a_i b_i \\ \sum a_i b_i & \sum b_i^2 \end{pmatrix}$$

$$\underline{u} = \begin{pmatrix} l \\ m \end{pmatrix} \quad \text{and} \quad \underline{b} = -v \begin{pmatrix} \sum a_i t_i \\ \sum b_i t_i \end{pmatrix}$$

The solution to this provides a first guess to the iterative solution, which is found by using Taylor's theorem to linearize the least squares equations. Rarely more than two iterations are required. The analytic and iterated solutions usually differ by less than 1%.

For the case N>3, the timing variance can be estimated from the fitted plane by

$$\sigma^2 = \frac{S}{v^2(N-3)}$$

If N=3, a value of $\sigma^2 = 68 \times 68 = 4624$ nsec^2 is used. This is based on the results of spherical fits to 171 showers which triggered more than four stations.

The variances in l and m are assumed to be independent and normally distributed and are estimated from the diagonal elements of the inverse matrix of coefficients and the timing variance

e.g. in the analytic plane case,

$$\sigma_l^2 = A^{-1}_{11}\,\sigma^2 \quad \text{and} \quad \sigma_m^2 = A^{-1}_{22}\,\sigma^2$$

(2) Spherical Fit.

The spherical analysis is almost identical to the plane fit analysis, except in this case a four parameter fit is required. The four parameters are l, m, n and ρ. l, m and n approximate to the direction cosines and ρ is the radius of curvature. All parameters are assumed to be independent and normally distributed. A point soure of origin (x_o, y_o, z_o) is assumed for the sphere.

$$l = \frac{x_o}{r}, \quad m = \frac{y_o}{r}, \quad n = \frac{z_o}{r} \text{ and } \rho = \frac{1}{r}$$

where r is the radius.

The set of least squares equations is found by minimizing

$$S = \sum \left(vt_i + \frac{1}{\rho} - \{(a_i - \frac{l}{\rho})^2 + (b_i - \frac{m}{\rho})^2 + (c_i - \frac{n}{\rho})^2\}^{\frac{1}{2}} \right)^2$$

with respect to ρ, l, m and n.

For N=4, the fit is exact and for N>4 an iterative solution such as used in the plane fitting, is required.

Also as in the plane analysis, an analytic solution can be made on the assumption that the array is flat. This provides a first guess to the iteration.

An estimate of the timing variance is made when N>4

$$\sigma^2 = \frac{S}{v^2(N-4)}$$

The errors in ρ, l, m and n are found from the inverse matrix of coefficients used in the least squares analysis. These errors are assumed to be normally distributed and independent.

Knowing the core position, the corrected direction cosines can be evaluated.

CHAPTER 3

RADIO FREQUENCY TIMING LINK.

3.1 INTRODUCTION.

The vast extent of the SUGAR array eliminates any economical use of coaxial cables to interconnect individual stations. In the early stages of the design of the array, the use of microwave links was considered as an alternative to cables for relaying real time coincidence information. A system such as this however involves many difficulties and is very expensive.

The system finally settled on is the use of a central transmitter to radiate continous timing information to each station in the array, and to record each event locally. In this way the extent of the array is limited only by the distance over which the transmitter can successfully radiate.

To obtain reasonable pulse risetimes requires a wide bandwidth system. This together with the requirement that no-one else will radiate on the same frequency and thus produce interference, limited us to the U.H.F. end of the radio spectrum for a carrier frequency. The frequency band allocated by the Post Master General's Department was 397.25 ± 2.5 MHZ.

In this chapter the design and construction along with problems encountered in this radio link, are discussed.

3.2 CARRIER WAVE TRANSMISSION.

The problems behind the propagation of radio waves in the region of 400 MHZ(λ = 75 cm)are quite considerable. The receiving and transmitting apparatus need to meet rigid tolerances in their construction, and for good transmission, as near to a line of sight path as possible is required.

3.2.1 SIGNAL TO NOISE RATIO.

The signal to noise ratio at each station determines whether or not that station can record event timing information effectively. Any radio frequency receiver has an inherent amount of noise generated by it. This noise is primarily due to thermal agitation of electrons in the first stage or stages of the receiver. If we consider the amplifying elements of the receiver to add no noise (i.e. zero *noise figure*), then the amount of noise generated at the input of the receiver is given by the familiar Nyquist formula

$$dP = 4kT\,df \qquad 3.1$$

where dp = R.M.S. noise power

k = Boltzmann's constant

T = temperature at the input

df = bandwidth of system

However all transistors and hence receivers have an inherent noise figure, N. This increases the noise as given by eqn. 3.1, the amount of noise actually generated at the input being

$$dP = 4NkT\ df \qquad 3.2$$

In a system such as that used for SUGAR

$$N \sim 6\ dB, \quad T \sim 20^{o}C \quad \text{and} \quad df \sim 3\ MHZ.$$

The noise power generated then being of the order of

$$dP \sim 2 \times 10^{-13} \text{watts}$$

The input resistance of each receiver is 50Ω and hence the R.M.S. noise voltage is

$$dV \sim 3\ \mu V.$$

To obtain good waveforms at the receiver output we require that the signal to noise ratio be quite large, otherwise noise pulses may appear as bits in the timing pattern. For reliable operation it is desirable for the signal to noise ratio to be approximately 10 : 1, requiring at least 30 μV input to each receiver over the extent of the array. This is determined by the transmission loss between transmitting and receiving antennas.

3.2.2 TRANSMISSION LOSS.

The operating power of the base transmitter varies between 10 watts and 100 watts (ref. section 3.5) R.M.S., and the total gain of the receiving and transmitting aerials is 10 to 20 dB. Hence the maximum allowable transmission loss is

$$L = 10\log_{10}\left(\frac{10}{2\times10^{-11}}\right) + 10 \quad dB$$

i.e. $L \sim 127$ dB

An approximate discussion of the way this transmission loss may occur, can be made if we assume line of sight transmission over flat ground (Bullington 1956). The effect on the propagation of radio waves is given approximately by

$$E = E_o + RE_o e^{j\Delta} \qquad 3.3$$

where E is the observed field strength and is comprised of a direct wave E_o and a reflected wave given by the second term of eqn. 3.3. R is the reflection coefficient, which can be set equal to -1 for perfectly reflecting ground (which is almost the case for low grazing angle reflection).

$$\Delta = \frac{4\pi h_T h_r}{\lambda d}$$

where h_T and h_r are the heights of the transmitting and

receiving aerials respectively, λ is the wavelength of the radiation and d is the aerial separation.

Eqn. 3.3 reduces to

$$\left|\frac{E}{E_o}\right| = 2\sin\frac{2\pi h_T h_r}{\lambda d} \qquad 3.4$$

and if $\lambda d >> 2\pi h_T h_r$ as is the case in the SUGAR array, the eqn. 3.4 becomes

$$\left|\frac{E}{E_o}\right| = \left(\frac{P_r}{P_o}\right)^{\frac{1}{2}} = \frac{4\pi h_T h_r}{\lambda d} \qquad 3.5$$

P_r is the received power and P_o is the power which would have been received had there been no reflection (i.e. in free space).

The free space transmission ratio is given by

$$\frac{P_o}{P_T} = \left(\frac{\lambda}{4\pi d}\right)^2 g_T\, g_r \qquad 3.6$$

P_T is the transmitted power and g_T and g_r are the gains of the transmission and receiving aerials respectively.

Eqns. 3.5 and 3.6 give the transmission loss over a plane perfectly reflecting surface

$$\frac{P_r}{P_T} = \left(\frac{h_T h_r}{d^2}\right)^2 g_T\, g_r \qquad 3.7$$

From eqn. 3.7 it can be seen that the received power at a station varies inversely as the fourth power of its distance from the transmitter, and in this approximation is frequency independent.

If we insert the values h_r = 25 ft, h_T = 150 ft and d = 10 miles, which are typical for the SUGAR array, then the expected transmission loss is about 107 dB (including antenna gain). An extra loss of 3 dB due to Earth curvature can be included (Bullington 1956), giving a total loss of 110 dB. This leaves a margin of $\sim$ 20 dB if the propagation is in accordance with this simple theory.

3.3 FIELD TESTING OF TIMING LINK.

In early 1966, two main field tests of the timing link were made, to ascertain under what conditions the radio system would best work. The two possibilities of transmitting the timing signal were

(a) Transmission from an aerial mast located near the array.

(b) Transmission from a mountain some 40 miles from the array.

Option (a) being the preference, since it enables easy servicing and checking of the transmission system at regular intervals. On the other hand, due

to the increased equivalent height of the transmitting mast on a mountain, some 4000 ft, a better coverage of the array could be expected.

In order to test these options, a 10 watt transmitter, which now is the basic modulator in the final array and a prototype receiver, were taken firstly to Mt. Kurrajong, a mountain of height 2000 ft and located in reasonably flat (to within 50 ft over most localities) country about 40 miles from Sydney. Secondly the same assembly was used in the flat land about 20 miles from the base of Mt. Kurrajong and the transmitting aerial attached to the top of a 150 ft mast owned by the Department of Civil Aviation. In both cases, the transmitting aerial was a 9 element Yagi and the receiving aerial, a 3 element Yagi mounted on an adjustable 40 ft aerial mast connected to the rear of a utility truck. Field strength measurements were taken at varying distances from the transmitter by recording the automatic gain control voltage of the receiver, and knowing the transfer function, converting this voltage to an equivalent input signal strength. In most instances, measurements were made in reasonably open terrain.

The results of these two tests are given in table 3.1. In calculating the predicted transmission loss, the varying height of the land was included in

the height of the receiving aerial where necessary.

TABLE 3.1

Separation (miles)	L_{obs}(dB)	L_{pred}(dB)	h_r(ft)	h_T(ft)
	D.C.A. Measurements.			
2.5	87	90	38	150
3.4	97	95	38	150
4.9	103	101	38	150
5.3	114	103	38	150
5.5	104	103	38	150
7.2	116	108	38	150
8.0	119	110	38	150
	Kurrajong Measurements.			
11.5	101	94	40	1913
17.0	90	93	90	1913
24.5	105	93	190	1913
26.3	112	111	40	1913
31.0	94	89	340	1913

Reasonable agreement between the observed results and this simple theory were obtained. According to Bullington (1956), terrain irregularities of approximately 50 ft at 400 MHZ should produce an attenuation of approximately 6 dB.

On the basis of these results, and allowing for a margin of about 20 dB error due to attenuation, it was decided to use a 150 ft mast located 2 miles from the array at the base station, to radiate power from a one hundred watt transmitter. The height chosen for the receiving aerials was 25 ft, making construction easy since they would be self supporting and have no need for guy wires. Fig. 3.1 shows the theoretical transmission loss, L, across the array for radiation both from a 150 ft mast 2 miles from the array, and for radiation from a 4000 ft mountain 40 miles from the array. Curves for two receiving aerial mast heights, 25 ft and 50 ft, are shown.

3.3.1 PILOT ARRAY.

A pilot array of 3 station operating on the campus of the University of Sydney (Ryan 1968, Drownlee et al 1968b) successfully tested the feasability of receiving and recording transmitted timing information and extracting coincidence information at a later date using a digital computer. The longest transmitter receiver separation being about 2000 ft, and the transmitted power being about 10 watts.

FIGURE 3.1

Predicted transmission loss (assuming a flat perfectly reflecting earth) across the array for line of sight transmission between two dipoles (unity gain).

The transmitter aerial being

(a) Located on a 4000 ft mountain 40 miles from the array

(b) Located on a 150 ft mast 2 miles from the array.

Results for receiving aerial heights of 25 ft and 50 ft are shown.

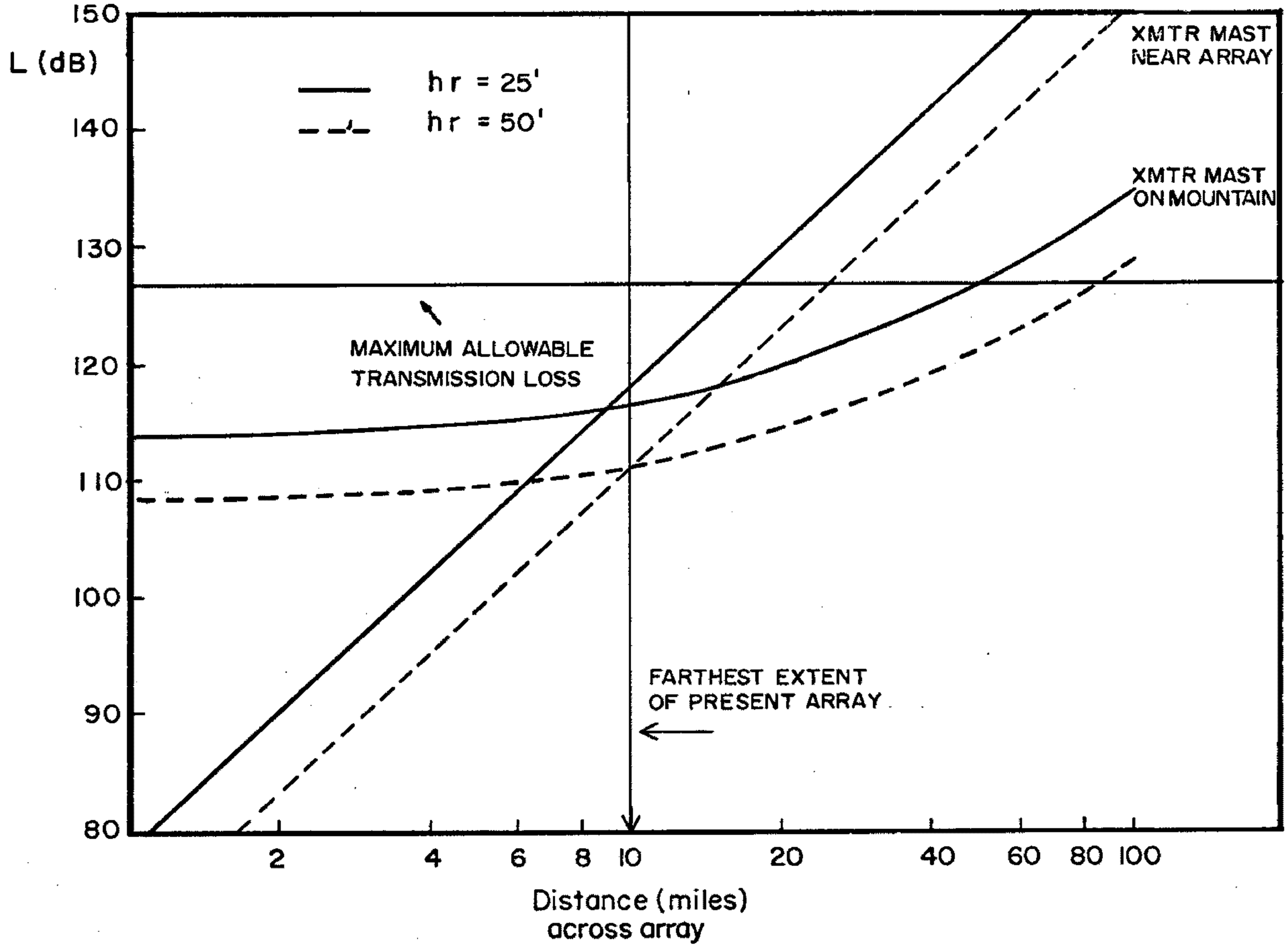
150
L (dB)
140
130
120
110
100
90
80
hr = 25'
hr = 50'
MAXIMUM ALLOWABLE
TRANSMISSION LOSS
XMTR MAST
NEAR ARRAY
XMTR MAST
ON MOUNTAIN
FARTHEST EXTENT
OF PRESENT ARRAY
2
4
6
8
10
20
40
60
80
100
Distance (miles)
across array

3.4 ATTENUATION OF TIMING SIGNAL.

Several distant stations in the array were operating marginally close to the allowed limit, and quite often owing to fluctuations in transmitted power (section 3.5) and adverse weather conditions such as rain and wind in the forest, the received signal strength dropped below the acceptable limit. These stations could then record invalid patterns (i.e. patterns containing noise pulses and hence not conforming to a given format), which meant subsequent rejection of these events in later analysis.

To cure this problem, it was decided to try raising the receiver aerials to a height of 50 ft in an attempt to gain line of sight transmission over the trees in the forest. The average height of the trees is forty feet.

3.4.1 EFFECT OF FOREST.

Trees at 400 MHZ are quite absorbent (Head, 1960), an attenuation of 0.15 dB m^{-1} being expected on the average. Figure 3.2a shows a typical transmission path of the timing signal to a SUGAR station. According to Head the signal should increase approximately in proportion to the logarithm of the clearing depth (defined as the distance of cleared land between the

receiving antenna and the forest, in the direction of the transmitting antenna), for clearing depths greater than a critical value, D. For clearing depths less than D, the signal remains constantly about 30 dB below the prediction of the simple flat earth theory. The signal in this region is that due to the leakage field, i.e. signal which has diffused through the foliage in the forest. As the clearing depth is increased the signal rises due to diffraction over the tree tops (fig. 3.2b).

3.4.2 DIFFRACTION EFFECTS.

If we consider the trees at the edge of the clearing to represent a sharp edge, an estimate of the effect of diffraction can be made (Bullington 1956). For our situation of near horizontal transmission, the first Fresnel zone clearance H_o, is given by

$$H_o = \left(\frac{\lambda d_1 d_2}{d_1 + d_2}\right)^{\frac{1}{2}} \qquad 3.8$$

which reduces to $H_o = \sqrt{(\lambda d_2)}$ for large d_1 (d_1 and d_2 are defined in fig. 3.2a). According to Head, the received field starts to increase above leakage level for clearances where $H/H_o > -\frac{1}{2}$. H is the separation of the receiving aerial from the obstructing edge. The critical clearing depth is then given by

FIGURE 3.2

(a) Direct transmission path between transmitting and receiving antennae.

(b) Attenuation of signal through forest and in clearing (Head, 1960, Proc. I.R.E. 48 p1016).

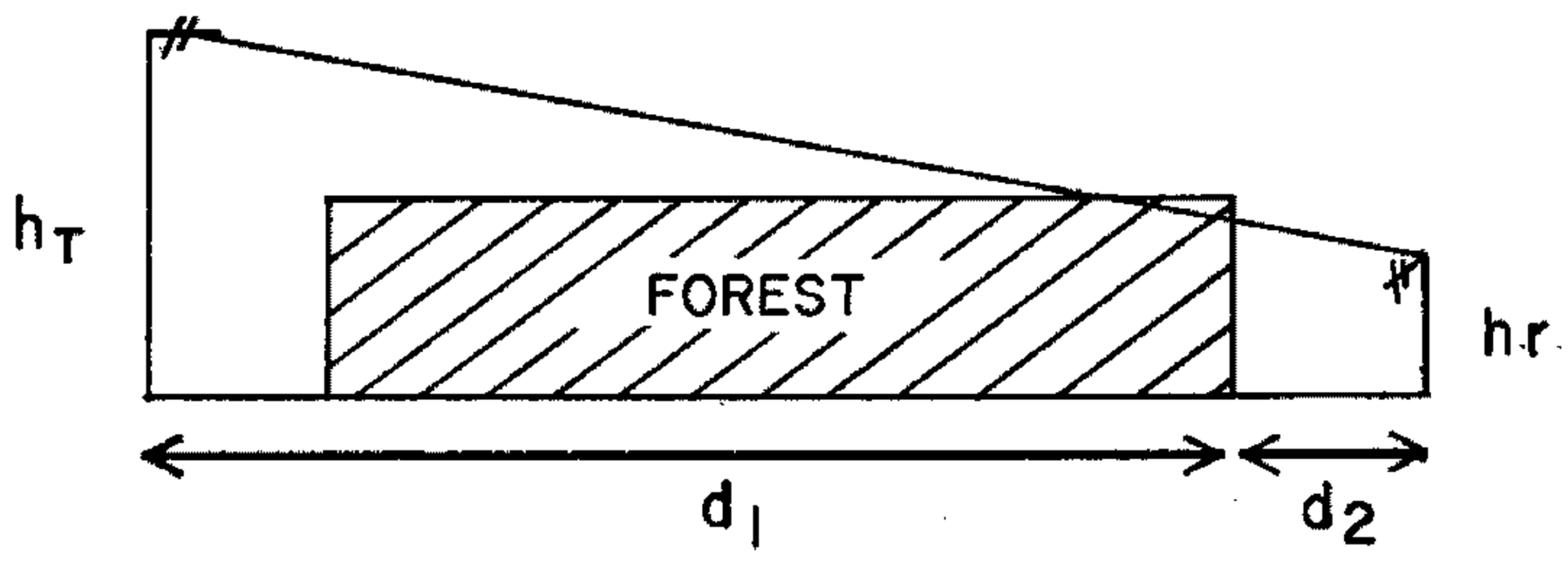

$d_1 \sim$ 10 Miles $\quad d_2 \sim$ 100 ft

(a)

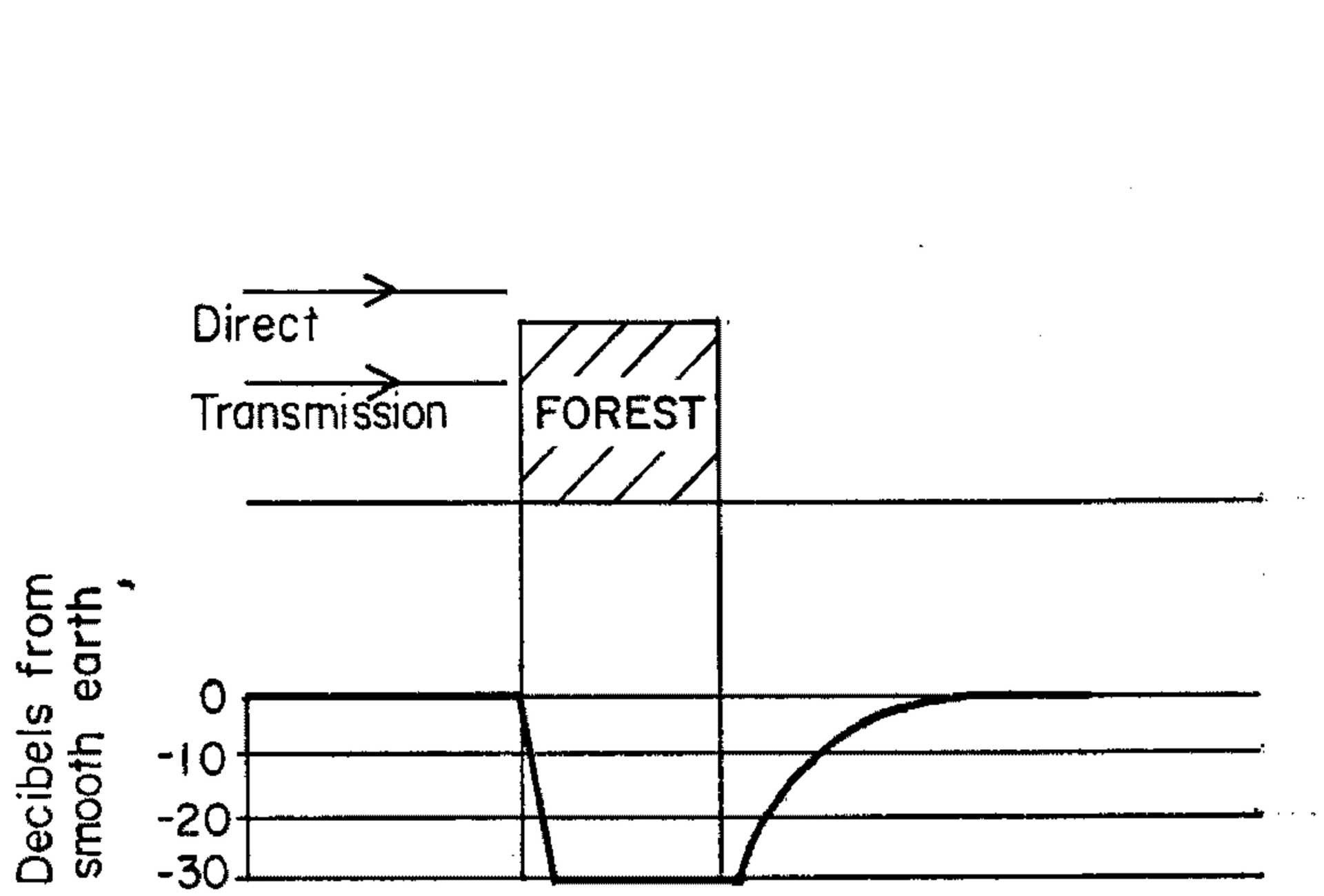

(b)

$$D \approx \frac{4H^2}{\lambda}$$

If the receiver mast height is 25 ft and $\lambda \sim 2.5$ ft, then for a tree height of 40 ft, D is approximately 350 ft.

Each station in the forest is cleared for about 50 ft to 100 ft around each tank. Stations with receiving aerials situated at the northern tank have a clearing depth of about 100 ft, while stations which have their receiving aerials mounted at the southern tank have a clearing depth of about 250 ft. Hence with 25 ft receiving masts, it is likely that it is the leakage field that is received. By raising the receiving aerials to 50 ft, diffraction loss should reduce to approximately zero and an increase of upto 30 dB in received signal strength should arise.

3.4.3 EFFECT OF INCREASING RECEIVING ANTENNA HEIGHT.

To test the effect of raising the receiving aerials' heights to 50 ft, an aerial was erected section by section at station 32. This station is one of the furthest stations in the array, (fig. 2.1), and the received signal strength was marginal. The clearance depth was 250 ft.

Measurements of signal gain were made for each height increase of one foot, upto the limit of 58 ft.

The results are shown in fig. 3.3. The increase in gain was measured by inserting a variable attenuation in the aerial cable such that the gain control voltage at the output of the station receiver remained constant for varying aerial height.

The gain increase with height was immediate, indicating that the signal being received by the 25 ft mast was above or just near the leakage level. The increase of 13 dB in signal strength that resulted for full aerial height, is 17 dB less than that based on the results of Head. Two possible reasons are firstly that the received signal was well above the leakage level to start with and secondly that owing to the diffuse, spread out nature of the foliage in the Pilliga forest (mostly cyprus pines and ironbark trees), the leakage field may be considerably greater than expected. The correct answer is probably a mixture of the two possibilities.

3.4.4 CONCLUSION.

On the strength of these results, the receiving antennae on all stations were raised to approximately 50 ft. A substantial increase in signal strength and a decrease in the number of invalid patterns recorded, were noticed at each station.

FIGURE 3.3

Increase of received signal strength at station 32 with increasing aerial height.

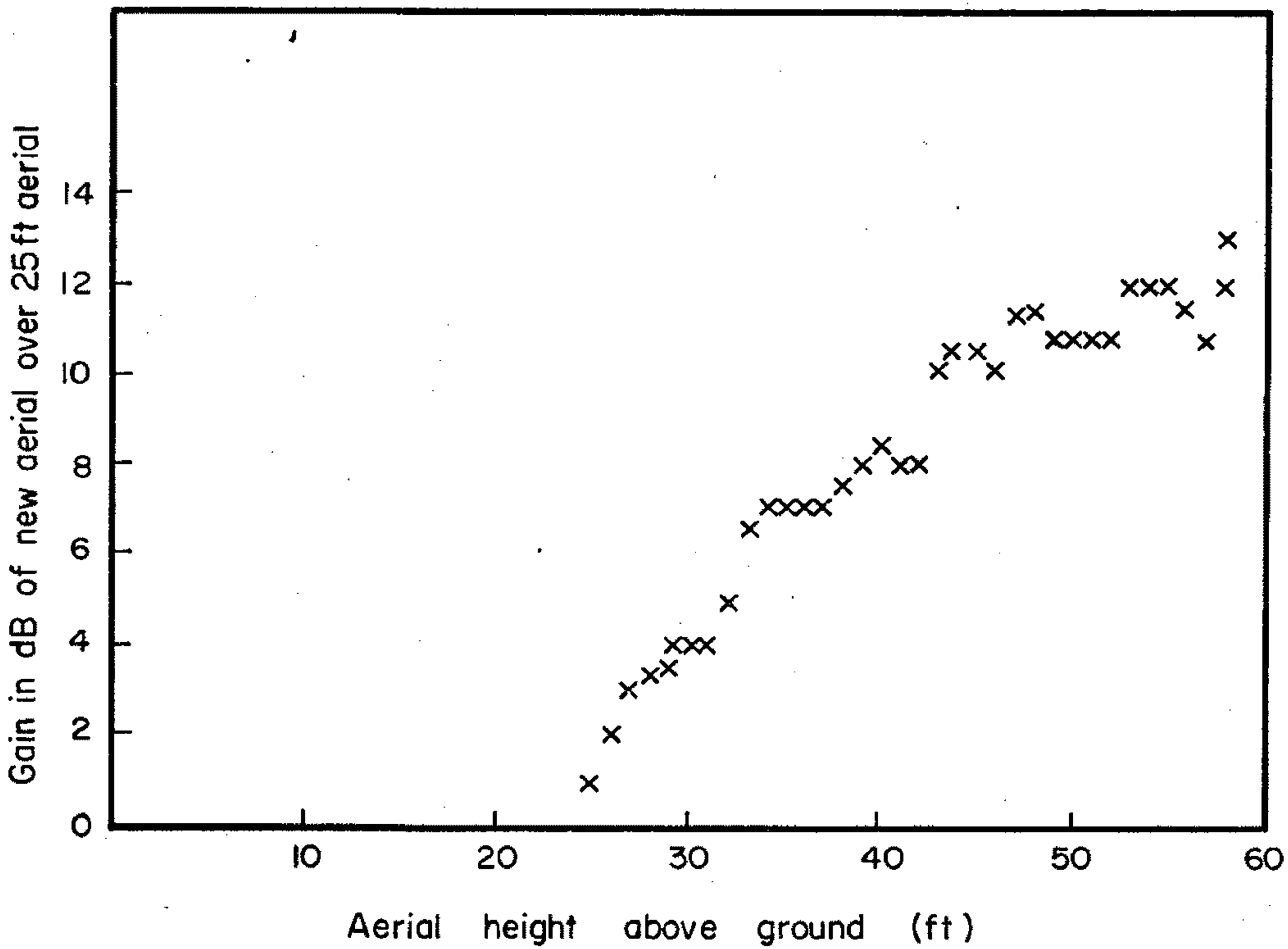
Gain in dB of new aerial over 25 ft aerial
0
2
4
6
8
10
12
14
10
20
30
40
50
60
Aerial height above ground (ft)

The increase in gain of 13 dB means that if the 100 watt central timing transmitter should only radiate 10 watts, as happens during power failures, the received signal strength at each station is still 3 dB above the maximum attainable signal strength at that station when using a 25 ft receiving mast.

3.5 TRANSMISSION SYSTEM.

The basic transmission system (plate 1) consists of a digital clock which keys a low power 397.25 MHZ transmitter. This is turn drives a high power amplifier (fig. 3.4 and 3.5). The low power transmitter, which delivers 10 watts R.M.S. power and the digital clock, can both run off storage batteries whilst the power amplifier, which radiates 100 watts R.M.S. power, can run only from the main supply.

This system is duplicated to minimize the risk of electrical failure turning off the transmitted timing signal, and demobilising the whole array. Individual elements may be interchanged readily via a system of coaxial relays.

3.5.1 LOW POWER TRANSMITTER.

During mains power failures, the low power drive transmitter is automatically switched into the transmitting aerial, continuing to radiate the timing signal at

PLATE 1 SUGAR CENTRAL TIMING UNIT.

Shown are:-

Left hand rack

Unit 1	Driver transmitter.
Unit 2	Driver transmitter.fig.3.5a.
Unit 3	Clock crystal oscillator.
Unit 4	Clock I.
Unit 5	Clock II.
Unit 6	Changeover switches for clocks and drivers. Power supplies occupy the rest.

Right hand rack

Units 1,2,3	Power supplies.
Unit 4	Power amplifier changeover switches.
Unit 5	Power amplifier. fig.3.5b.
Unit 6	Power supply.
Unit 7	(Just visible) Power amplifier.

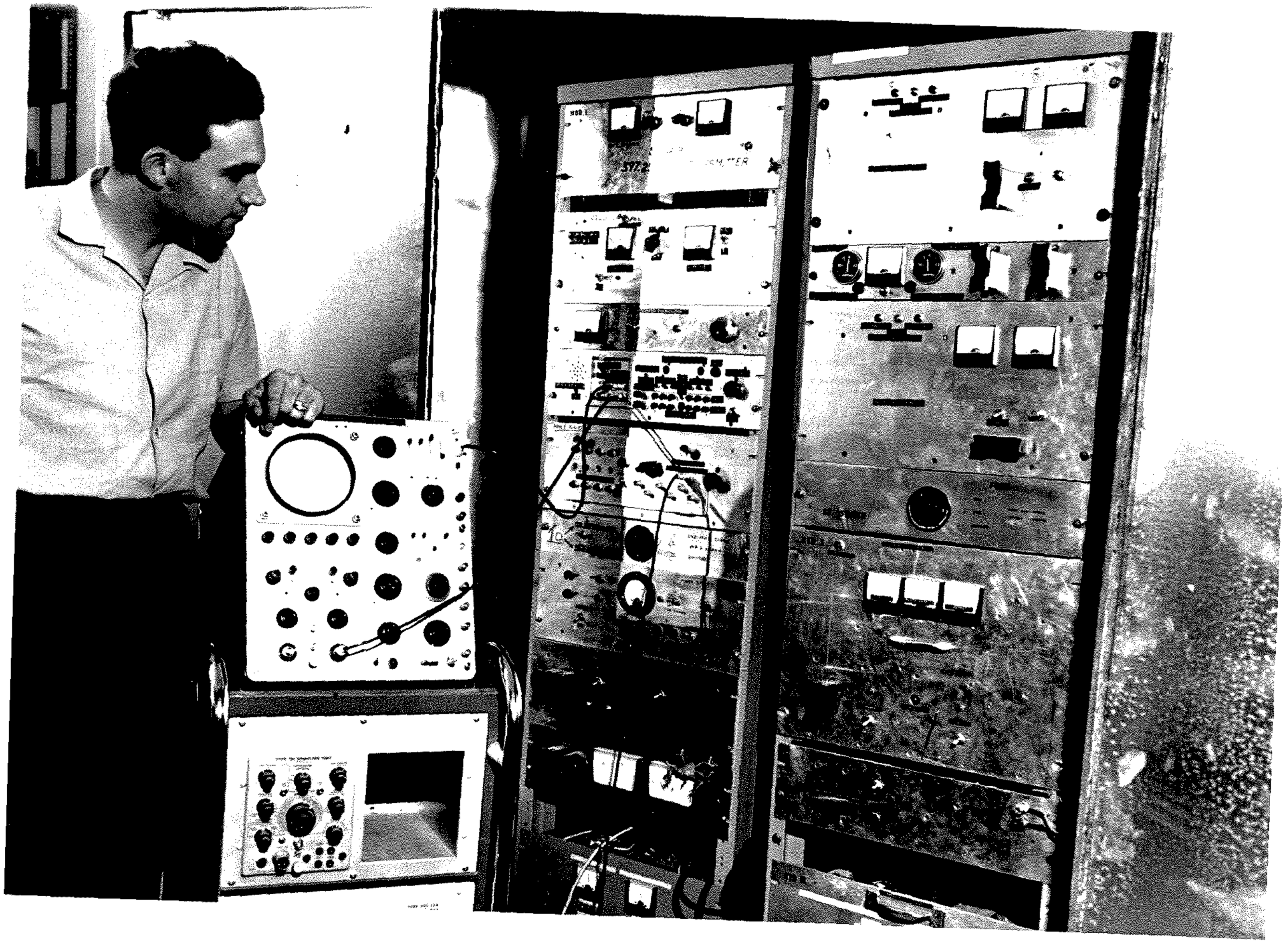

a reduced level.

Both drivers are basically crystal controlled oscillators, stable to 0.005%, and which are frequency multiplied and then amplified using convential vacuum tubes. Modulation is accomplished by keying the output stages from completely on to completely off with a fast rise time, high current transistor. The modulation is applied at the output rather than at the crystal oscillator to give better risetimes to the keyed pulses. The clock pattern, which provides the modulation, consists of pulses of height 6 volts and with risetimes of better than 10 nsecs.

3.5.2 HIGH POWER TRANSMITTER.

The driver output is used to drive the high power stage amplifier. This unit consists of an air cooled power tetrode valve type 4CX-250B, which is mounted in a coaxial cavity. The plate supply is 1500 volts and the plate efficiency ∿ 50%. The output signal is coupled via a loop in the plate circuit into a 50Ω coaxial cable. The output power is continuously monitored on a Bird thru-line wattmeter.

3.5.3 RADIATION OF THE TIMING SIGNAL.

The output of the transmitter system is radiated from a horizontally polarised *bedstead* array of eight

FIGURE 3.4

Basic unit of the transmission system. This unit is duplicated, and the various members of both units are readily interchangeable.

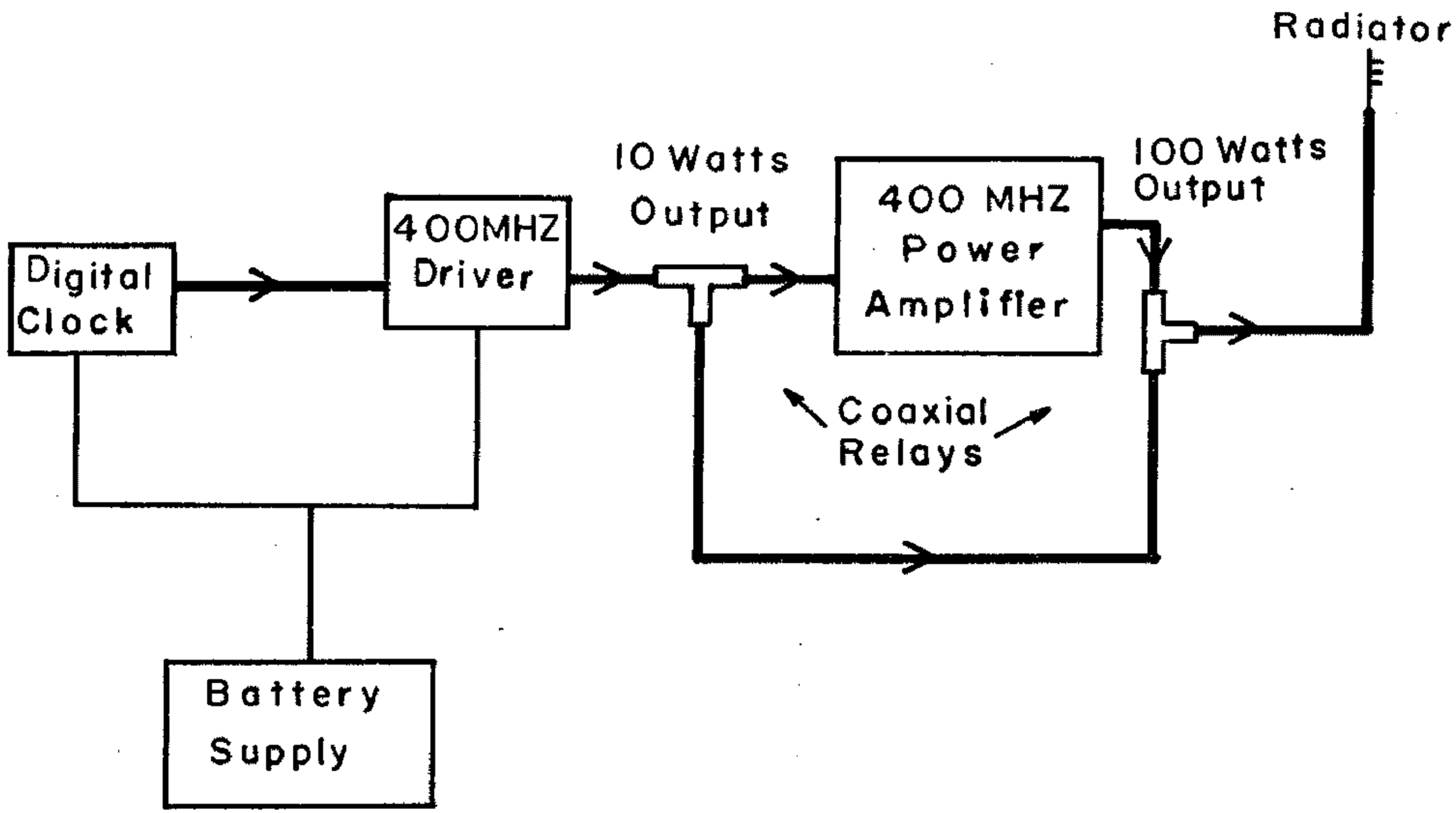
Radiator
10 Watts
Output
400MHZ
Driver
400 MHZ
Power
Amplifier
100 Watts
Output
Digital
Clock
Coaxial
Relays
Battery
Supply

FIGURE 3.5

TRANSMITTER CIRCUITRY.

(a) One of the low power driver stages.

A ten watt R.M.S. carrier is keyed by a fast 2N3051 transistor.

(b) One of the power amplifiers.

L_1 is a coaxial tuned cavity in the plate of a forced air cooled 4CX-250B power tetrode.

L_2 is a coaxial tuned grid line.

Output power is ~100 watts R.M.S.

(a) **DRIVER TRANSMITTER**

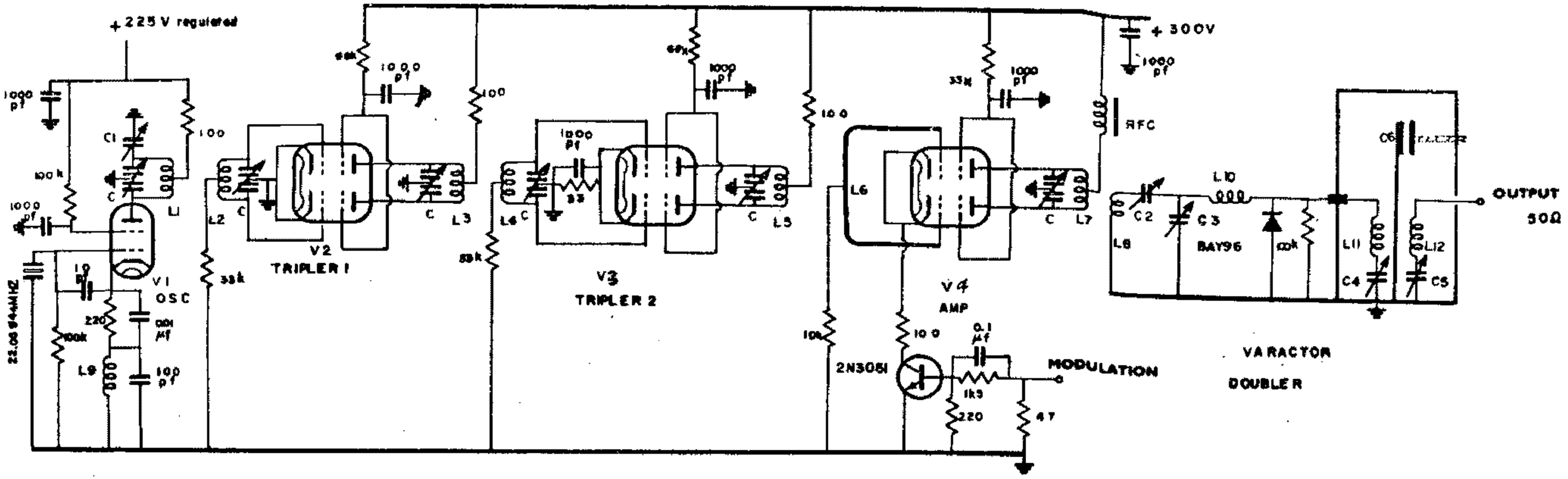

(b) **POWER AMPLIFIER**

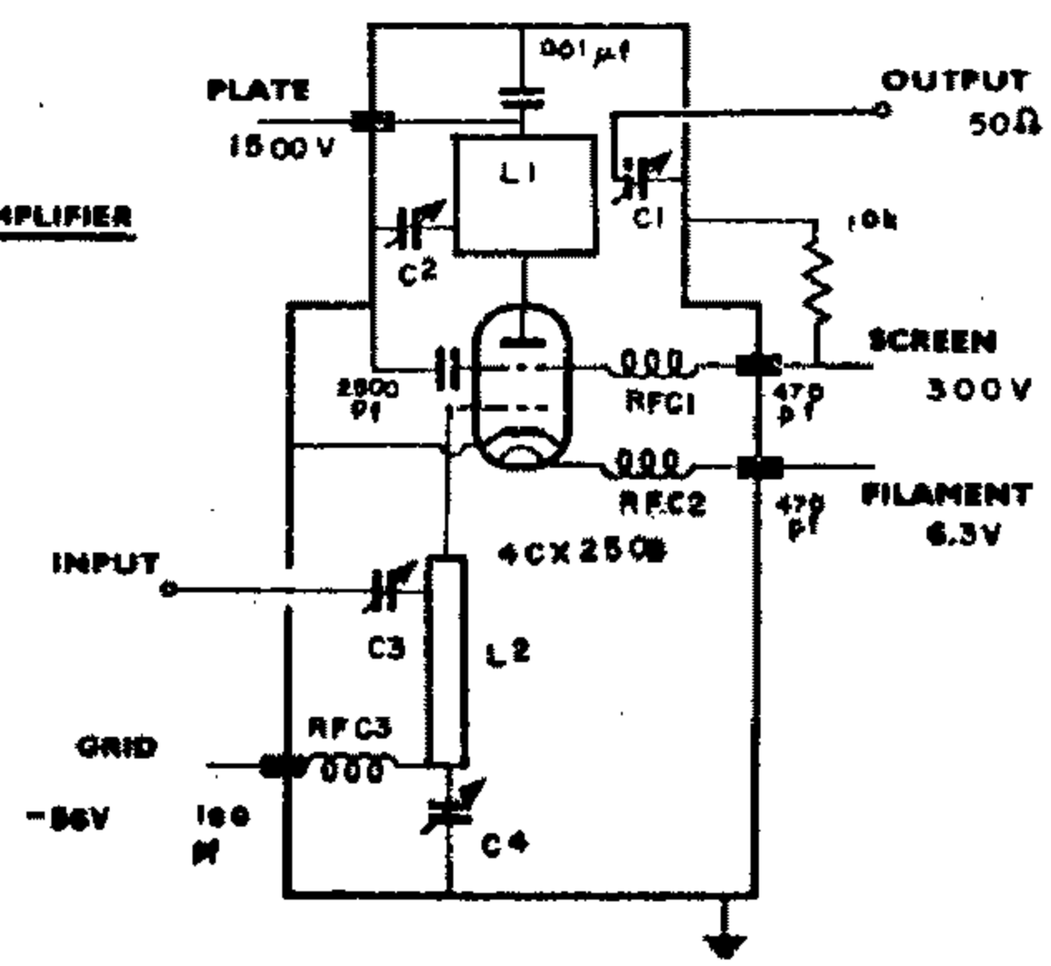

dipoles, mounted on top of a 150 ft mast. The loss in the coaxial cable leading to the radiator is less than 2 dB and the gain of the system of dipoles comprising the radiator is 14 dB. The radiation is transmitted in a fan beam just sufficiently wide to cover the array and hence save on radiated power.

The overall risetime of the transmitted pulses varies slightly with the tuning of the transmitter (ref. section 4.3). The average risetime is 150 nsecs and the width of one pulse (or bit) is ∿ 800 nsecs (ref. section 2.6).

3.6 RECEIVER SYSTEM.

The receiver system consists of a three element horizontally polarised Yagi antenna mounted on a 50 ft mast (ref. section 3.4) (plate 2). The received signal in some cases is amplified at the mast by a wideband transistor preamplifier tuned to 397.25 MHZ and having 20 dB gain and 6 dB noise figure. Before entering an all transistor superheterodyne receiver, the signal has to traverse upto 200 ft of UR67 coaxial cable which has an attenuation of 4.5 dB/100 ft at this frequency.

3.6.1 SUGAR RECEIVER.

The basic receiver, the latest version of which

FIGURE 3.6

Block diagram of the Receiver System.

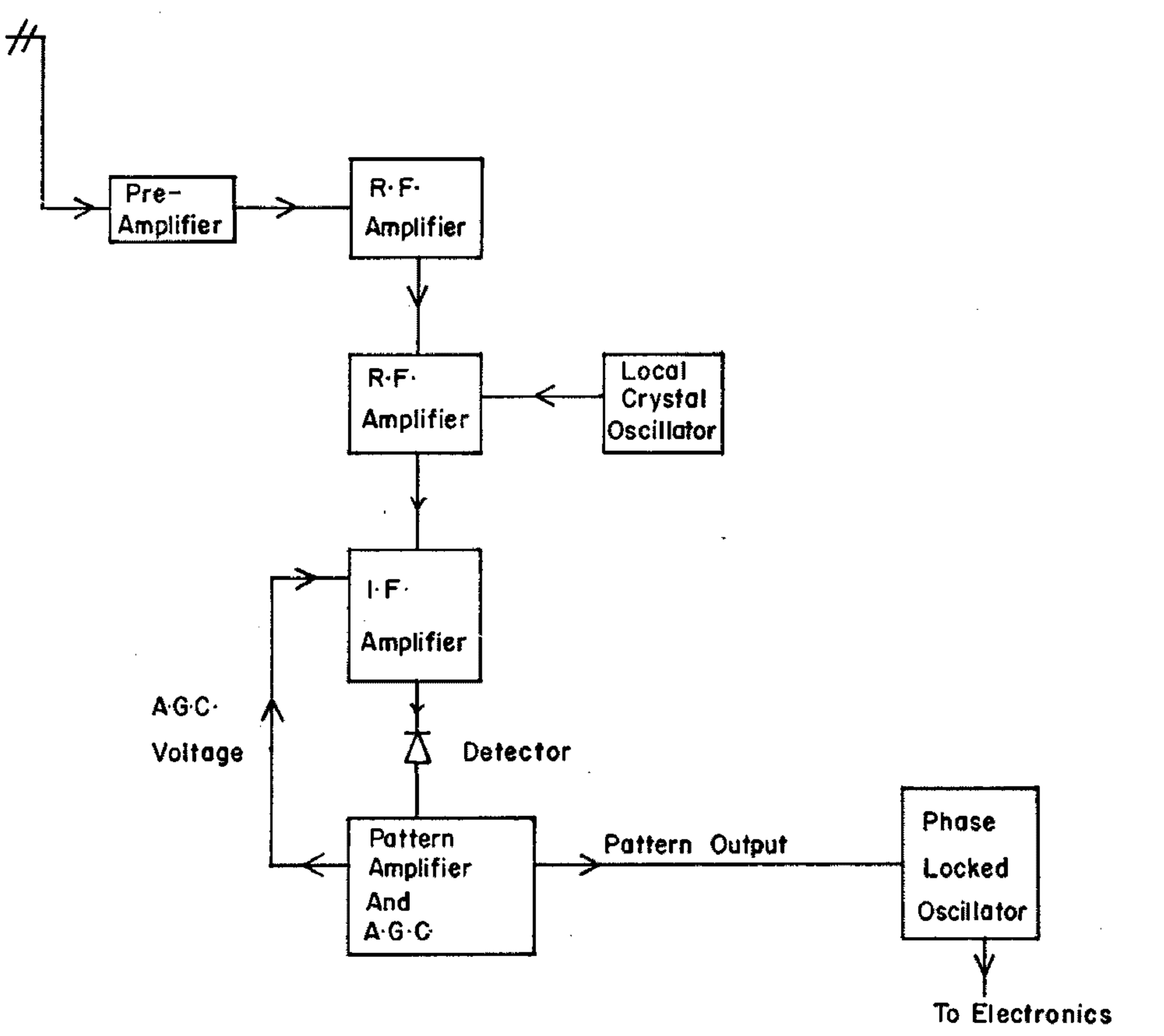
Pre-
Amplifier
R·F·
Amplifier
R·F·
Amplifier
Local
Crystal
Oscillator
I·F·
Amplifier
A·G·C·
Voltage
Detector
Pattern
Amplifier
And
A·G·C
Pattern Output
Phase
Locked
Oscillator
To Electronics

is shown in fig. 3.7, consists of two R.F. stages which feed together with the signal from a local crystal oscillator (stable to 0.005%) into a mixer which produces an I.F. frequency of 32.25 MHZ. The I.F. frequency is amplified by an automatic gain controlled three stage amplifier. The signal after detection (now the clock pattern), is amplified to + 6V and held constant by the automatic gain control, independent of fluctuations of the input signal.

3.6.2 AUTOMATIC GAIN CONTROL (A.G.C.).

The gain control system has to be able to handle fluctuations of upto 10 dB in input signal due to

(a) variations in radiated power and

(b) changing conditions along the transmission path of the signal (e.g. wind and rain in the forest).

In addition, it has to average out the fluctuations in voltage level at the output caused by the constantly changing number of bits in the timing pattern. A value of about $\bar{5}$ msec is used as the A.G.C. time constant. In this way, pattern jitter has been kept to ± 10 nsec for a reasonable level of input signal. The dynamic range of the A.G.C. is such that the output signal level remains constant without clipping, over a range of at least 40 dB. The A.G.C. ceases to function for signal

FIGURE 3.7

CIRCUIT DIAGRAM OF A SUGAR RECEIVER.

L_1 to L_6 are 1" by ¼" brass rods.

The R.F. transistors are low noise

type BF180.

The I.F. integrated circuits are wide-

band operational amplifiers type CA3028A

Noise figure ∿ 6 dB

Bandwidth ∿ 5 MHZ

OSC

5 X MULTIPLIER

RF AMPLIFIERS

MIXER

IF STAGES

DETECTOR

PATTERN AMP

AGC

INPUT

OUTPUT

−12 V

+12V

−6 V

32 MHZ

385 MHZ

levels less than 10 μV.

The circuit depicted by fig. 3.7 represents the latest version of the SUGAR receiver, the major improvements being better gain, bandwidth and stability. For its predecessor, the gain was ∿ 120 dB with fluctuations of upto 10 dB between individual receivers. The bandwidth of the entire system was about 3 MHZ, which corresponds to a risetime of ∿ 200 nsecs for bits comprising the clock pattern. The bandwidth of the system is now ∿ 5 MHZ, giving better risetimes.

The received timing pattern is squared by feeding it into a transistor switch circuit, then fed into the phase locked crystal oscillator (section 2.6).

PLATE 2

A typical SUGAR station showing the 50 ft receiving mast with a three element horizontally polarised Yagi antenna on top.

At the base of the aerial are the bottles of propane gas used to fuel the thermoelectric generator above them. This supplies power for charging the station's batteries.

In the foreground is the servicing truck.

CHAPTER 4

SHOWER FRONT TIMING ERRORS.

4.1 INTRODUCTION.

The angular resolution of the SUGAR array is limited only by the accuracy with which each individual station can register the relative arrival time of an incident shower of muons. The principal sources of error in this time arise from the transmission and reception of the timing signal, the registering of the coincidence pulse, the structure of the shower front and the limitations imposed by the electronics. In the following sections each source of error is investigated and the total timing error is compared with that derived from experimental results.

4.2 STABILITY OF CRYSTAL CONTROLLED OSCILLATOR.

All analysis of shower front arrival directions and curvatures rely on relative time. Absolute time is needed only to determine the celestial co-ordinates of individual showers. As we shall see, the accuracy with which the local co-ordinates of a shower can be determined is approximately 5^{o}, or 20 minutes of time. A crystal controlled oscillator, such as is used to provide the timing signal for the SUGAR array, typically has a long term stability of one part in 10^{6}. This amounts to a drift of about 30 seconds in one year of operation, not allowing for resetting. The maximum error

in the solar and hence the sidereal time is therefore about 30 sec which corresponds to an uncertainty in the celestial co-ordinates of a shower to be less than $\frac{1}{8}^{0}$ due to this effect.

Local coincidence times are measured over a period no greater than 80 μsec, which corresponds to one pattern period (section 2.6), hence assuming a short term stability even as low as one part in 10^{6}, the drift in resolving relative time is much less than 1 nsec. However the major limitation in this respect is set by the station electronics. This being discussed later in this chapter (section 4.7).

It can be concluded that drift in the local crystal oscillator providing the basic timing pattern, contributes a negligble amount to the total timing error.

4.3 ERROR IN TRANSMISSION SYSTEM.

The transmitted timing pattern has a small amount of inherent jitter, incurred in the modulation of the R.F. carrier. The extent of this jitter is less than 10 nsecs. However, a more serious effect on the timing error due to the transmission system occurs after the station receiver.

If any element of the transmission system is

interchanged, which invariably happens during power failures or electrical breakdowns, the overall bandwidth of the transmission system can change. The change in bandwidth results in a change in risetime of the transmitted and hence received pulse. This in turn causes a change in signal delay through the electronics due to the fact that the electronics is set to trigger at a preset voltage level. The overall variation in signal delay time varies from station to station and must be allowed for in further computation.

4.4 PHASE MEASUREMENT.

It is not necessary to know the absolute timing signal delay through each set of station electronics. What is required is a measurement of the relative delay between individual stations. This relative delay is referred to as the *phase* of that station. Undetected variations in phase can lead to a large error in timing measurement.

The factors which contribute to the phase of a station are:-

(a) Delay through the receiver system.

(b) Delay through the phase locked oscillator.

(c) Delay through the aerial cable.

Factors (a) and (b) are discussed separately in section 4.5 and section 4.6 respectively.

Typical delays in each case are:-

(a) ∿ 500 nsec.

(b) ∿ 100 nsec

(c) ∿ 50 nsec depending on cable length.

The range of variation in relative delay between all stations is approximately -200 nsecs to 100 nsecs.

Any change involving replacement or retuning of a station's receiver or phase locked crystal oscillator, will alter that station's phase. Should such a change occur, then the phase of the affected station is remeasured and the new value used in further computation. Any change in the transmission system will alter the phases of all stations. Ideally a list of phase measurements should be kept relating to each possible transmitter configuration. This is however uneconomical in terms of available staff and time. Instead a complete set of phases is kept corresponding to transmission from either of the two high power amplifiers. This is the most common state of transmission, any other state occurring for only a small percentage of time. During this small time, an uncertainty of phase of ± 20 nsec may occur, thus

introducing a moderate timing error.

A portable standard clock, consisting of a superheterodyne receiver coupled to a phase locked crystal oscillator, is used to measure the phase of a station. To make this measurement, the received timing signal is divided into two parts by a 50Ω strip-line power divider, such that the station receiver and the standard receiver each obtain half of the received power. The 596.5 KHZ clock signals obtained from the two phase locked crystal oscillators are displayed on a twin beam oscilloscope, and the time difference in their leading edges is, after correcting for antenna cable length, the phase of that station.

Jitter of the displayed clock patterns during phase measurement lead to an unavoidable error in its determination. The extent of this jitter increases with decreasing signal strength (section 4.6). For a receiving antenna height of 25 ft, the average error in phase determination is ± 15 nsecs, whereas for a 50 ft mast the average error is ± 5 nsecs. The drift in phase for a station which has been left untouched for several weeks, is ± 10 nsecs.

4.5 ERROR IN RECEIVER SYSTEM.

The source of signal delay in a receiver is due

to the reduction of group velocity in the tuning elements. The major delay occurs typically in the bandwidth limited I.F. stages. In the receivers employed in the SUGAR system over the past two years, this delay is of the order of 500 nsecs. Any variation of this delay leads to a source of timing error. The most likely sources of variation are due to:-

(a) Input signal fluctuations.

(b) Battery voltage variation.

(c) Temperature variation

Table 4.1 gives the maximum timing errors to be expected under normal operating conditions.

TABLE 4.1

Signal Strength	Voltage	Temperature
± 10 nsec over a range of 20 dB.	<±5 nsec for a ±2V change.	± 10 nsec for a change of 20°C.

Signal level will vary whenever the transmitted power changes, or the transmission properties of the surrounding country change (i.e. during windy, rainy etc. weather conditions). To compensate for signal variation, the automatic gain control system of the receiver varies the overall gain of the receiver.

Two typical receivers were checked for delay variations over a range of 20 dB about the normal operating signal strength and a maximum delay change of 10 nsecs was observed.

The delay change suffered due to varying supply voltage, is less than 5 nsec over a range of ± 2V about each supply line.

The change of delay with respect to temperature variations is 0.5 nsec/^{o}C for the receivers, and for the aerial cables it is 0.2 nsec/^{o}C/15 ft of UR67 cable.

As each receiver is contained with the rest of the electronics inside the buried scintillator tank (section 2.4), the temperature fluctuations are reduced below ambient variations and hence temperature dependent delay changes are negligible. The antenna cable which is exposed to ambient temperature variations of upto 20^{o}C over about 50 ft of its length, can introduce delay variations of upto 15 nsecs.

The change in total delay between receivers is of the order of 50 nsec, but this effect is eliminated by the measuring of a station's phase.

4.6 PHASE LOCKED CRYSTAL OSCILLATOR.

The phase locked crystal oscillator generates

a clock signal of period 1.6 μsec, and is locked in phase to the receiver output. The shape and hence risetime of the receiver output pulse determines the point at which the oscillator locks. Variation of risetime due to any cause, will introduce an uncertainty in the locking and hence introduce a timing uncertainty. The maximum error due to locking is measured as jitter during phase measurements and is ± 10 nsecs for typical reception, however in the case of a noisy receiver pulse the jitter in locking may increase to ± 50 nsecs. Variations in the risetime of the receiver pulse due to changes in the transmission system, can introduce a change of delay through the phase locked crystal oscillator of upto 20 nsecs. However this is in general compensated for by remeasuring the phase of that station.

4.7 VERNIER TIME MEASUREMENT.

The timing resolution at the output of the phase locked crystal oscillator is approximately plus or minus one clock pulse or ± 800 nsec. However, whenever a station registers a coincidence an unsynchronised 20 MHZ vernier oscillator is gated into a scaler (section 2.6). The form of the vernier output is a continous train of square pulses of period 50 nsecs.

The error in timing introduced whenever the vernier oscillator is gated, therefore follows a rectangular distribution of width 100 nsecs. Since the vernier is gated twice during each coincidence time measurement, the resultant distribution of the vernier timing error is a symmetrical triangular distribution of base width 100 nsec, mean 0 nsecs and standard deviation 20 nsecs. The timing error introduced by the use of 20 MHZ vernier oscillator is therefore ± 20 nsec.

In the event of no other error, it is the vernier oscillator that sets the lower limit to the timing resolution of the SUGAR array.

4.8 MINOR TIMING ERRORS.

Minor timing errors arise due to:-

(a) Refractive Index Of Air.

If the refractive index of the air varies across the array, then the signal propagation time will vary. Across the SUGAR array, the error involved is only ± 3 nsec (Parkinson 1969).

(b) Curvature Of Earth.

All calculations assume a flat earth, the effect of curvature introduces a difference of only 10 picosecs.

(c) Reflection From The Ground Plane.

This introduces an error of less than 1 nsec.

(d) Surveying.

The accurate positions of both transmitter and receiver masts must be known to calculate the total transmission time of the timing signal to each station. A maximum error in surveying of ± 6 ft is involved at each point. This leads to a total error in transmission distance of 8 ft which corresponds to a timing error of ± 8 nsecs.

(e) Diffusion Of Timing Signal.

In section 3.4, the affect of absorption by the forest of the R.F. field which carries the timing signal, was investigated. To check for signal delay due to diffusion through the trees of the forest, the relative arrival time of the timing signal was measured for two receiver mast heights. A mast height of 50 ft allowed for line of sight transmission and a mast height of 25 ft gave transmission through about 1 mile of forest.

The signals from both aerials were fed into two separate receivers, the outputs being displayed on a twin beam oscilloscope. The time difference between the leading edges of two equivalent pulses then gave the time delay. The receivers were interchanged and the same reading taken, in this way the inherent delay through both receivers was eliminated.

Within the limits of reading, the maximum delay introduced by the forest, is less than 10 nsecs.

The total timing error due to these minor effects is less than ± 10 nsecs.

4.9 GHOSTING OF TIMING SIGNAL.

An inherent difficulty associated with the reception of U.H.F. radiation is spurious reflection. In television, because of the appearance of a usually weaker, superimposed but delayed picture, this is known as *ghosting*. A similar effect is observable for the SUGAR timing pattern when it is displayed on an oscilloscope, in weak signal areas.

The affect of ghosting on the timing signal is to increase the risetime of the received pulses. This occurs because the resultant pulse is the sum of the direct pulse and its ghosts. The delay in nanoseconds between the ghosted and direct signals varies in magnitude between once and twice the distance away in feet of the reflecting object (speed of light = 1 ft $nsec^{-1}$).

Reflections of the signal from trees in the nearby forest are the primary cause of ghosting. In one instance the reflected signal was stronger than the direct, requiring the receiver antenna to be rotated

about 70^{0} away from the direction of the transmitter for best reception. On removal of a large tree near the aerial, the situation became normal, a resultant change of phase of -60 nsecs occuring.

As a test to determine the variation in jitter involved in phase measurement over a period of several hours, the clock pulses from both the standard clock and the station clock were fed into an integrated circuit *and* gate. The resultant overlap pulse being proportional in width to the phase of that station. This overlap pulse when integrated, provided a D.C. voltage proportional to the phase, which was displayed on a chart recorder. A change of phase of 1.5 nsec produced a pen deflection of 1 cm.

A direct phase measurement at midday yielded a phase of + 30 ± 5 nsec, two hours later the phase had changed to 35 ± 5 nsec. From the chart recorder, a drift of 6 nsec and an average jitter of about ± 2 nsec with maximum jitter ± 5 nsec was observed. This was in good agreement with direct observation on the oscilloscope screen. During periods of high gusty winds, where the tree branches would swing several feet, the jitter increased to more than ± 10 nsecs and subsided as the wind subsided. This is in direct agreement with the proposal that the jitter of the phase locked oscillator

is due to the changing risetime of the received pulses and that in this case, the changing risetime is due to varying ghosting at the receiver.

Pattern variations due to the periodic emptying and filling of the 48 bit timing pattern, caused jumps in phase (via the receiver A.G.C.) of upto 3 nsecs and appeared to be responsible for 6 nsec drift observed.

4.10 TIMING ERROR IN SHOWER DETECTION.

The coincidence pulse, which registers the time of arrival of an air shower front at a station, is measured with respect to the second scintillator tank to be hit. A small time delay is introduced by the scintillator and a large variable delay is introduced by the risetime of the photomultiplier pulse. Cables and amplifiers also contribute to the spread in delay times. The error due to the decay time of the luminescence of the scintillator fluid, and the spread in the photon transit time to the photomultiplier is estimated at ± 5 nsecs. The spread of transit times of the low energy photo-electrons in the photomultiplier tube gives rise to current pulses which follow approximately a normal distribution with standard deviation ∿ 30 nsec (Ryan 1968).

The current pulse is integrated before being

discriminated at a level corresponding to 3 vertical particles (section 2.5). Large pulse heights trigger the station earlier than small pulse heights, and in principle a three particle pulse would take an infinite time to register a coincidence. For this reason, low pulse heights are too inaccurate for fast timing measurements, and events with pulse height less than 1.2 times the discrimination level (equivalent to 3.6 vertical particles) are rejected in the direction and curvature analysis of chapters 5 and 6. For events with pulse height greater than 1.2 times the threshold, a timing correction is estimated.

The difference involved in timing between a 1.2 times threshold pulse and a 100 times threshold pulse, amounts to 100 nsec. For the assumed normal distribution, this rises to infinity which is unrealistic, as the pulse must start from a zero level. For computational reasons a triangular distribution is assumed for the current pulse, and over the above range of pulse heights, agrees to within 5 nsec with the normal distribution (Parkinson 1969).

The triangular current distribution is taken to be symmetrical with a constant width of 120 nsecs, which corresponds to a standard deviation of 25 nsecs. This is

in agreement with a direct measurement by Ryan (1968). The timing correction cannot exceed 120 nsecs and the height of the distribution is proportional to the pulse height. If r is the ratio of the pulse height to the threshold, the timing correction is given by adding

$$t = 25\sqrt{6}\left(\left[\frac{2(r-1)}{r}\right]^{\frac{1}{2}} - 1\right) \qquad 1.2<r\leq 2$$

and

$$t = 25\sqrt{6}\left(1 - \left(\frac{2}{r}\right)^{\frac{1}{2}}\right) \qquad r>2$$

to the recorded triggering time. Zero correction has been normalised to r=2.

An empirical fit to more than 4000 pulse shapes from an individual photomultiplier by Fisher (1969) gave a relationship

$$T = \left(\frac{3}{N} - 0.5\right)x200 \quad \text{nsecs}$$

for the pulse height timing correction. N is the number of particles, and higher orders of N in the fit are small and have been neglected.

This gives a maximum delay with respect to a 6 particle pulse of ± 100 nsec for N varying from 3 to infinity. This is larger than the above quoted estimate of ± 60 nsecs and is probably a slight overestimate. However in principle it is possible to continuously

check each station's current pulse shapes and apply individual timing corrections for each photomultiplier, thus helping to eliminate any variation between individual photomultipliers.

4.11 ESTIMATE OF TIMING ERROR.

An approximate estimate of the timing error due to instrumental and signal transmission variations can now be made. Since the errors are assumed to be independent and normally distributed, the total error is the quadratic sum of the individual errors, any timing measurement is also a normally distributed variable.

Since as we have seen, the individual errors may change from day to day, a precise estimate of the total timing error cannot be made. However, between best and worst conditions a value between 55 nsecs and 75 nsecs is an average estimate of the instrumental timing error.

Assuming a shower model, in this case one with a spherical shower front, it is possible to determine an experimental estimate of the timing error. This estimate is proportional to the square root of the sum of the squares of the residuals as calculated in the appendix of chapter 2. This is an unbiassed estimate,

and the mean variance based on 347 events gives a value of σ = 79 nsecs. The distribution of σ is given in fig. 4.1a. The mean of σ as opposed to the square root of the mean of the variance is 66 nsecs.

The estimate of the variance is taken over all zenith angles. As a function of zenith angle it is marginally better as zenith angle increases. This is because at low zenith angle, fewer stations in an event of given energy are triggered than at high zenith angle.

A smaller sample of 171 showers (Parkinson 1969) gave a value of σ = 68 nsecs. The higher value of 79 nsecs may be due to a period of several weeks when the array was badly serviced due to rain. A statistical fluctuation of the true mean could also explain part of the difference.

This value of σ not only includes instrumental timing errors, but model dependent errors and errors due to the delay of the critical triggering particle at tanks just above threshold. The difference between 79 nsecs and the estimated 55 nsecs to 75 nsecs instrumental error, allows for a muon spread of 25 to 55 nsecs. This is consistent with known muon spreads (Baxter 1969), and indicates that the instrumental error is consistent with results of the fast timing measurements.

FIGURE 4.1

(a) Estimated timing deviations of 347 showers which triggered 5 or more stations.

(b) Distribution of error angle for the showers in (a).

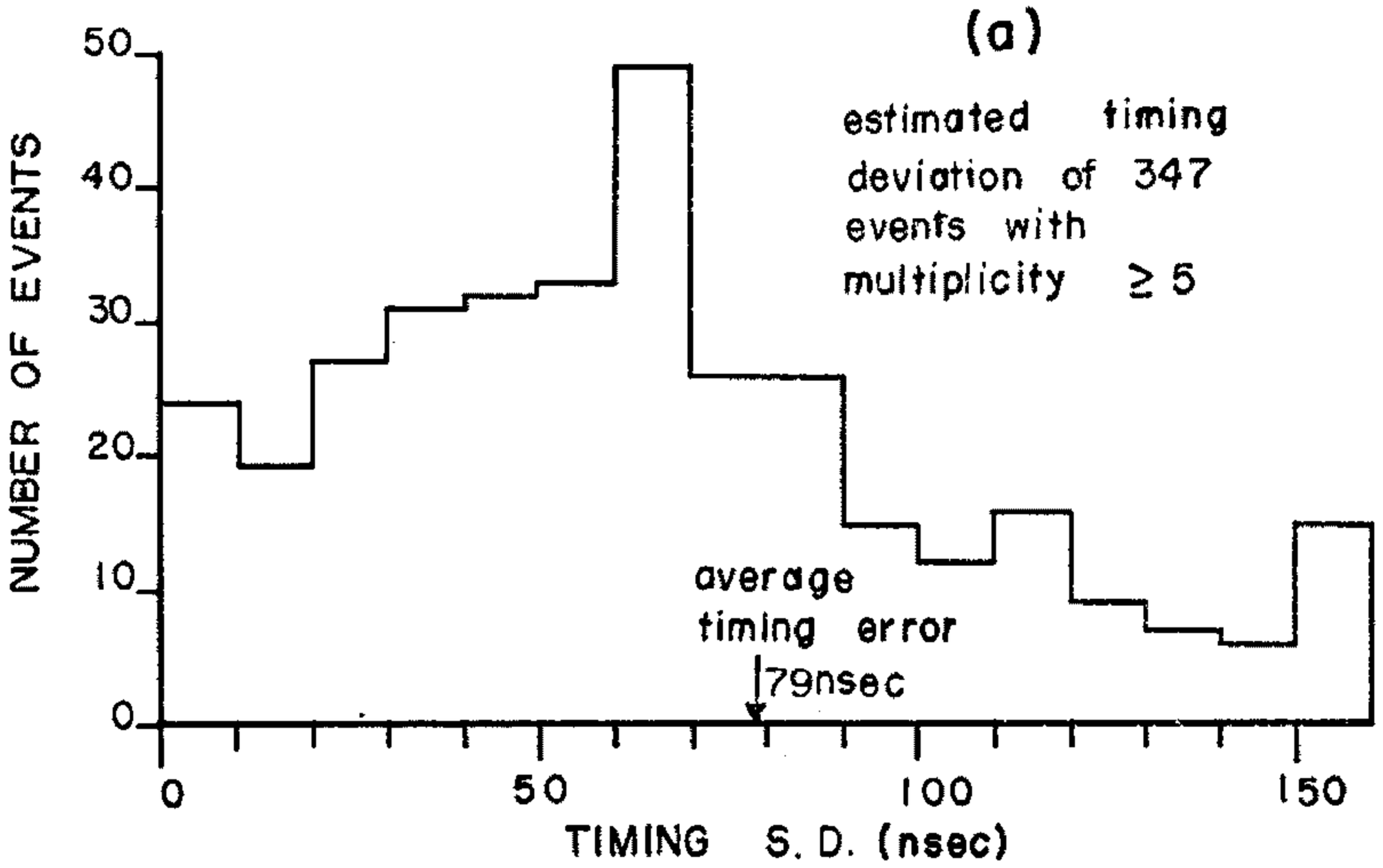
(a)
estimated timing deviation of 347 events with multiplicity ≥ 5
NUMBER OF EVENTS
50
40
30
20
10
0
average timing error
79nsec
0
50
100
150
TIMING S. D. (nsec)

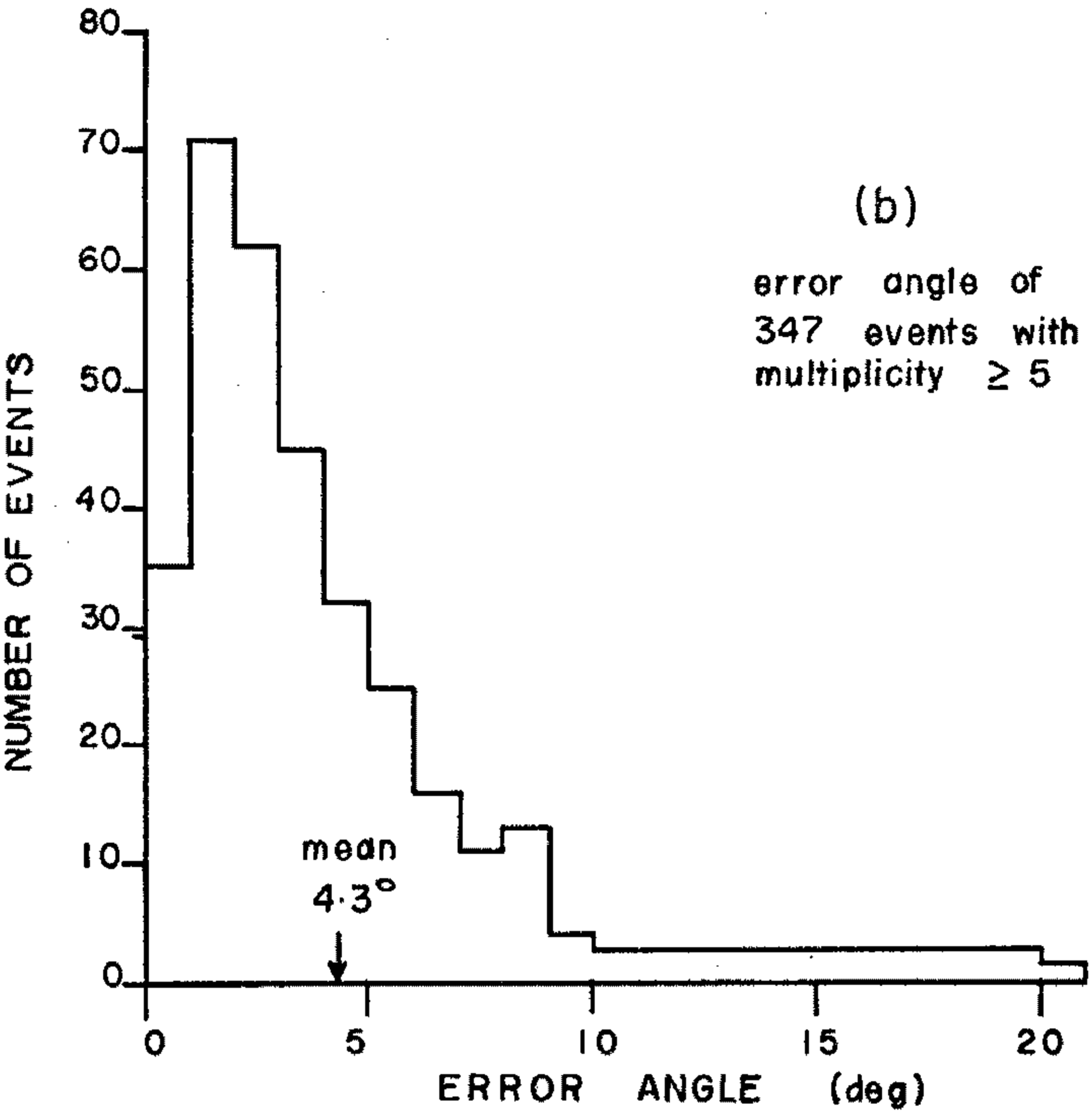
(b)
error angle of 347 events with multiplicity ≥ 5
NUMBER OF EVENTS
80
70
60
50
40
30
20
10
0
mean
4.3°
0
5
10
15
20
ERROR ANGLE (deg)

For all events triggering five or more stations on the quarter mile array, the timing delays have been plotted as histograms (fig. 4.2). The distributions are all approximately normal. If σ is the timing error at each station, and N is the number of stations triggered, then the standard deviations of the distributions should be given by

$$s = \sigma \left(1 - \frac{4}{N}\right)^{1/2}$$

if N = 5 s = 35 nsec

if N = 6 s = 46 nsec

Table 4.2 gives the means and spreads of each distribution. Since most of the events used are 5-folds with a few greater than 5-folds, the results are consistent with σ = 79 nsec.

The means of the distributions are not all zero, station 20 in particular is negatively biased. Similar biasing for all stations was also evident using the same analysis in half the number of events (Parkinson 1969). The most likely explanation is a systematic reflection or ghosting of the timing signal, adding a fixed time to each event involving the station in question.

FIGURE 4.2

Delays with respect to fitted spherical shower fronts for all showers with multiplicity $\geq$ 5 which triggered the quarter mile array.

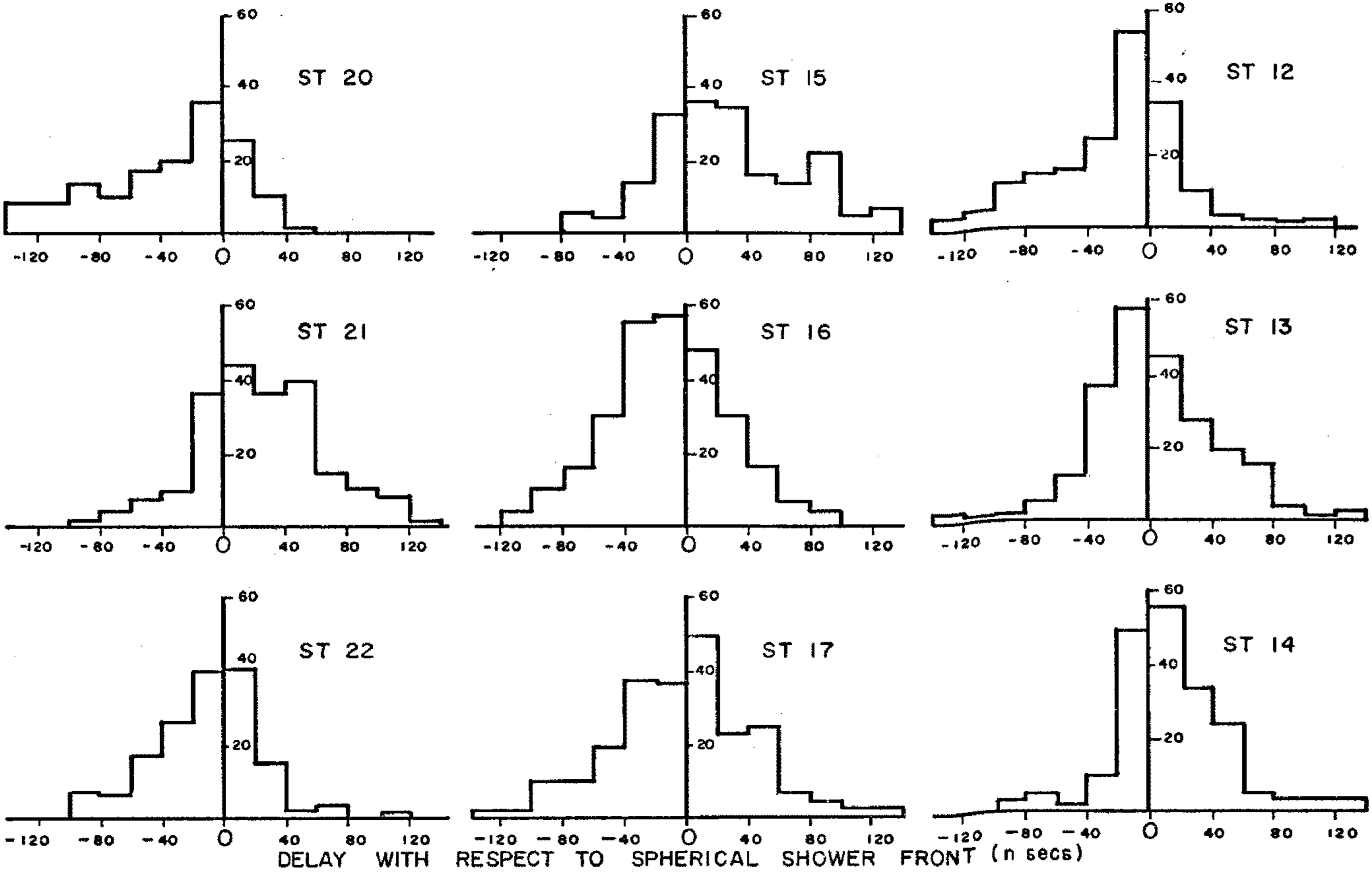
ST 20
ST 15
ST 12
ST 21
ST 16
ST 13
ST 22
ST 17
ST 14
60
40
20
-120
-80
-40
O
40
80
120
DELAY WITH RESPECT TO SPHERICAL SHOWER FRONT (n secs)

TABLE 4.2

Station	No. of Events	Mean (nsec)	S.D. (nsec)
12	187	-22.0±3.2	43.5
13	230	3.0±2.7	40.8
14	197	13.4±2.6	36.7
15	193	28.1±3.5	46.4
16	279	-11.9±2.4	39.8
17	230	- 2.8±3.0	45.4
20	152	-34.4±3.6	44.9
21	211	24.6±2.8	40.3
22	158	-11.3±2.7	34.3

The extent of the bias is not likely to seriously affect the curvature distributions of chapter 6, since stations occur randomly in each event, instead the spread of errors may increase. If the bias is due to reflection, then since increasing the height of the receiving aerials the bias should have disappeared. The complete results of this will not be available until many more events have been analysed, however based on a small sample of about 500 showers, the results do indicate that the bias has disappeared.

4.12 ERROR IN SHOWER ARRIVAL DIRECTIONS.

For all showers with multiplicity $\geq$ 4 the

errors in zenith and azimuth angles are calculated from the estimated timing standard deviation. For events with multiplicity < 4 a value of σ = 68 nsec is used. The actual error is dependent on the value of the measured angle and also on the geometric arrangement of the stations involved. The error in zenith angle increases towards the horizontal and the error in azimuth increases for small zenith angles.

A more sensible angle to use when discussing errors, is the solid angle containing the one standard deviations of the directions cosines. The use of individual timing fits can in some circumstances underestimate the error. However, during periods of poor timing accuracy, a fixed value for σ would also underestimate the error. Fig. 4.1b shows the error angle distribution based on spherical shower fits to 347 showers with multiplicity $\geq$ 5. A comparison can be made between the timing standard deviation and error angle, fig. 4.1a and 4.1b. The mean of the error angle distribution is 4.3^{o}.

4.13 ANGULAR SYMMETRY OF ARRAY.

The array is slightly tilted towards the north by 15m in 8 km. Departures of individual detectors from this general slope are less than ± 3m except for

station 33 in the south east corner, which is 13m below. If this tilt was neglected in computation, it would amount to an error of $\sim 0.1^{o}$ in zenith angle.

It is also conceivable that a *tilt* due to delay of the timing signal in the forest may exist. To check for this and any other irregularity, a sample of 767 showers representing all usable events between events numbers 1000 and 2000, were plotted in terms of their zenith and azimuth angles (fig.4.3). Zenith being plotted radially and azimuth plotted anti-clockwise from the direction of the timing transmitter. The number of showers when divided into four quadrants, are given below

↑

Direction of Transmitter.

195	177
207	188

A chi-squared estimate of 2 is consistent with there being no tilt.

4.14 EVENTS WITH UNPHYSICAL TIMING.

A small percentage of showers yield no directional information due to the fact that the triggering times of individual stations imply that the speed of the shower particles is faster than that of light. Such a shower

FIGURE 4.3

Plot of local co-ordinates for 767 showers.

Zenith angle is plotted radially in degrees.

Azimuth angle is plotted clockwise from the direction of the timing transmitter (marked T).

T is $39^{o}21'$ east of north.

EVENTS 1000 TO 2000

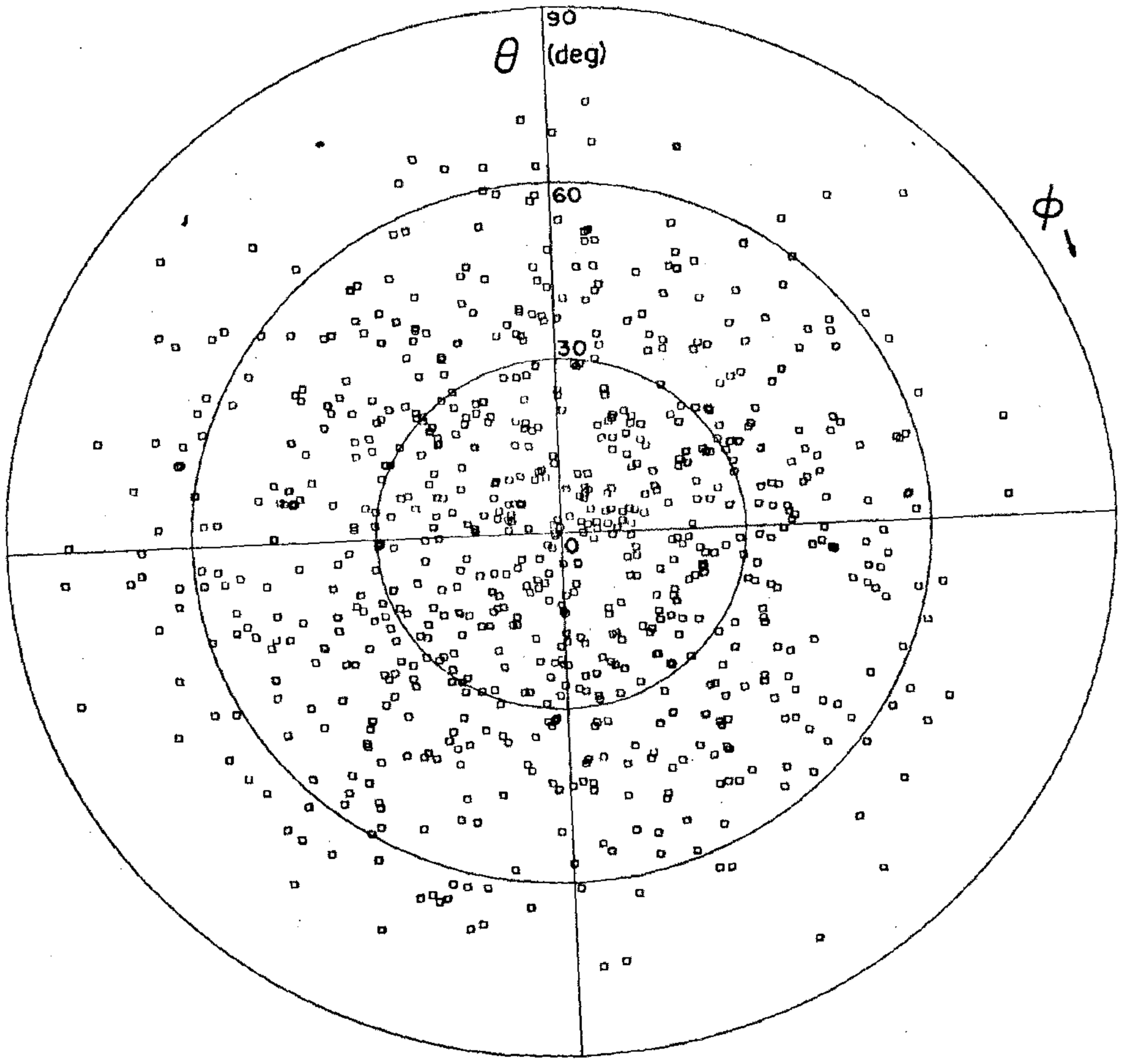

is called *unphysical*. An unphysical shower shows up in the analysis during the calculation of its direction cosines, since it gives an imaginary value of $n = \cos\theta$ where $n = \sqrt{(1 - l^2 - m^2)}$, θ = zenith angle and l and m are two of the direction cosines.

Out of just over 3400 showers, 36 were unphysical. Eleven of these could be traced to electronic faults in which the station's clock was not operating correctly. The remaining 25 events constitute 0.7% of all events. On substituting different phase information, four of the above events became physical and all were highly inclined to the zenith. The zenith angles of these showers are:-

Event Number.	Zenith Angle (deg).
2593	81.7
2607	65.9
2837	84.6
3094	58.5

One further event, a threefold in which the stations were greatly separated, almost certainly corresponds to the three stations recording noisy receiver patterns and hence registering a false coincidence. The final 20 showers are shown plotted against event number in fig. 4.4a. Before event

FIGURE 4.4

(a) Times unphysical events plotted against event number.

(b) Estimated timing fluctuation of 14 unphysical showers, on the assumption that they are near horizontal.

(a)

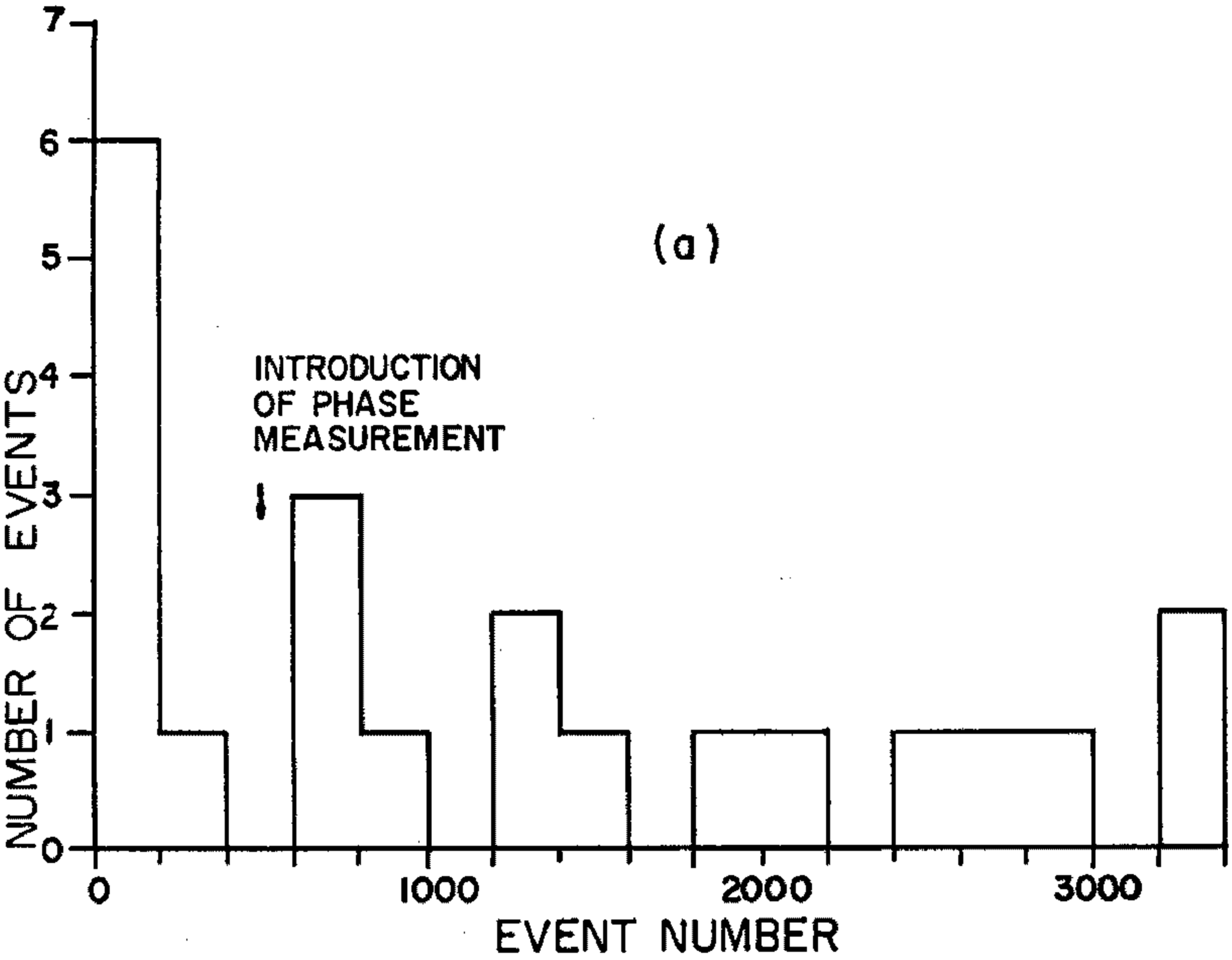
INTRODUCTION
OF PHASE
MEASUREMENT
NUMBER OF EVENTS
0
1
2
3
4
5
6
0
1000
2000
3000
EVENT NUMBER

(b)

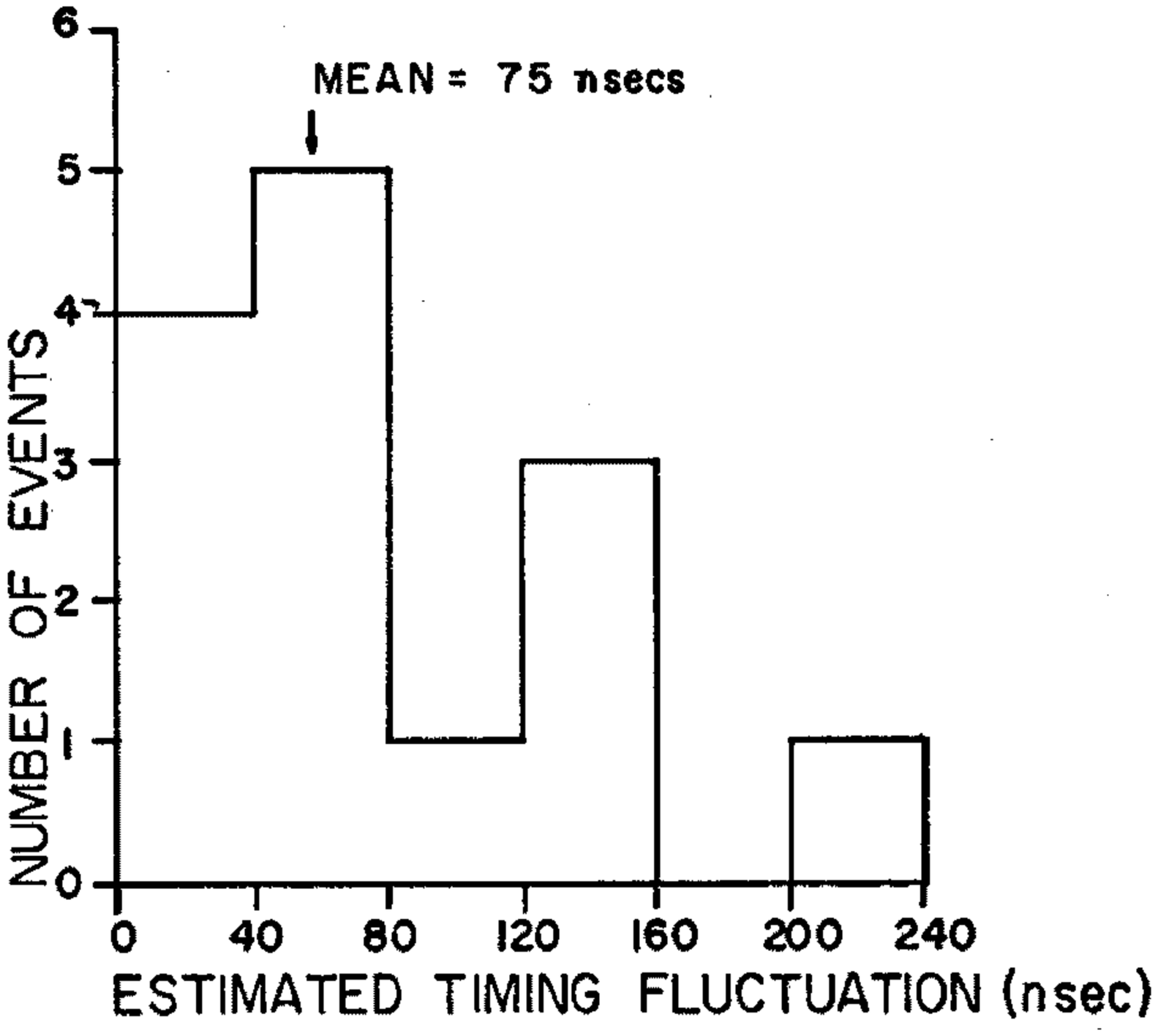
MEAN = 75 nsecs
NUMBER OF EVENTS
0
1
2
3
4
5
6
0
40
80
120
160
200
240
ESTIMATED TIMING FLUCTUATION (nsec)

number 400, no phase information was used and hence more unphysical showers should be expected.

The 14 unphysical showers after event number 400 are more than likely to be low energy highly inclined showers. Such a highly inclined shower will produce a relative triggering time between stations, which is very close to the limit imposed by the station's separation. Any timing fluctuation in the wrong direction, can render the shower unphysical.

Triggering times for each station in each of the 14 remaining unphysical events, were calculated on the assumption that the showers were horizontal. These times were compared with the measured triggering times, and for each event a root mean square timing deviation was calculated. These deviations are plotted in fig. 4.4b. The mean of this distribution is 75 nsecs which is in close agreement with the experimentally determined timing standard deviation of 79 nsecs.

4.15 ARTIFICIALLY TRIGGERED SHOWERS.

In order to check our technique of phase measurement and at the same time generate some artificial near vertical showers to determine the error in zenith angle measurement, three stations on the quarter mile array were connected by UR67 coaxial cable. In the first

case, clock pulses were sent directly from one station to another and after correcting for cable length, the relative phase was measured from an oscilloscope screen. In most cases the direct phase measurement agreed well with the conventional technique, however some discrepancies did exist. These discrepancies were probably due to ghosting affecting the conventional method of phase measurement.

Dr. L.S. Peak using a pulsing circuit designed by himself, artifically triggered six showers by sending a coincidence pulse along almost identical lengths of cable to each of the three above stations. The tapes from these three stations were then processed in the normal way (section 2.10), and the local co-ordinates for each event were obtained from the CHUNK III output. The results for the 6 showers were:-

Zenith (deg)	Azimuth (deg)
20.4	87.7
21.6	93.5
21.8	82.1
21.7	84.7
19.3	90.5
19.8	77.8

The main source of error in a measurement of this type is that due to the vernier oscillator. The mean of the fluctuations in the relative triggering times of each station for each of the events is 55 nsecs which is in agreement with the vernier period being 50 nsecs. The errors in zenith angle and azimuth angle are within the expected possible error.

4.16 SIMULATED SHOWERS.

Mr. S. David has generated a number of simulated showers using the Physics Department's KDF9 computer. For each shower, the azimuth angle is chosen randomly, and the zenith angle is chosen from a $\cos^{n}\theta\sin\theta$ distribution (n=2.5). The shower front is plane. A primary energy is randomly selected from the Sydney energy spectrum, and the muon number is sampled with fluctuationsfrom our energy to muon number conversion. (McCusker et al 1969b). The co-ordinates of the core are randomly chosen within set boundaries. Fluctuations are added to the responses of each tank in the coincidence, and timing deviations sampled from a normal distribution of mean 68 nsecs are added to the relative triggering times.

The raw data now generated is analysed in the usual way and new estimates of the original parameters

are obtained. The error angle of a sample of 485 simulated showers is 3^{o}, slightly less than the measured value of 4.3^{o} based on individual real shower fits. An interesting feature is that some *times unphysical* showers, 0.6% altogether, are found amongst the highly inclined simulated showers.

Since the generated shower front is planar with built in timing deviations, any measure of curvature should be normally distributed with mean zero. The curvature analysis program was run using the simulated showers. The results were exactly as expected, indicating no bias in our method of curvature estimation. With a timing standard deviation of 68 nsecs, the standard error in curvature measurement appears to be 0.3 km^{-1}.

4.17 CONCLUSION.

The average timing error of 79 nsecs is in general agreement with the estimated instrumental error. The fact that this is greater than the earlier value of 68 nsecs is probably due partly to statistical fluctuation and partly to a period of running of the array when little accurate phase information was available. The average error in angle measurement is less than 5^{o}, becoming less over longer baselines on the array. Unphysical showers are most likely highly inclined small

showers which have been made unphysical by timing fluctuations.

With the present inherent errors in transmission and reception of the timing signal there would be no major gain in accuracy by increasing the frequency of the vernier oscillator. The results of simulated showers are in good agreement with actual observation.

CHAPTER 5

THE ARRIVAL DIRECTIONS OF HIGH ENERGY COSMIC RADIATION.

5.1 INTRODUCTION.

The identification of source regions of high energy cosmic radiation has long been a problem facing the cosmic ray physicist. The fact that the majority of cosmic ray primaries are charged particles and that space is permeated with random magnetic fields, means that the primaries do not travel in straight lines. This makes the identification of distant sources virtually impossible.

The recent prediction that pulsars may create cosmic rays with energies upto 10^{21}ev (Gunn and Ostriker 1969) leads us possibly to expect anisotropies in the arrival directions of very high energy primaries. The large acceptance angle, three steradians, and the latitude of the SUGAR array, enable all but a few of the now known pulsars to be observed.

5.2 RESULTS OF OTHER LARGE ARRAYS.

Other large air shower groups which have made a study of the arrival directions of cosmic rays, have mostly been confined to observations of the northern half of the sky. The SUGAR array is the first very large array capable of observing the directions of high energy primaries over the whole southern sky.

Early results from both the both the Cornell

(latitude N43^{o}) and Agassiz arrays (latitude N49^{o}) showed some sign of anisotropy for showers with total number N > 10^{8} particles (Delvaille et al 1962, Clark et al 1962). For the combined data of 100 showers from the Cornell array and 32 showers from the Agassiz array, a chi-squared test gave a confidence of 2% in favour of an isotropic distribution. The major factor contributing to this result was an absence of showers between 15 hr and 16 hr in right ascension.

The Volcano Ranch (latitude N35^{o}) results (Linsley et al 1962b) also showed a similar trend towards anisotropy. These results based on 306 showers with N > 10^{8} particles at 5800 ft elevation had the same phase for the anisotropy but attributed less significance to it. The results of the El Alto array (latitude S16^{o}) based on 195 showers with N > 10^{8} showed no trend towards anisotropy (Hersil et al 1962).

Later results on a small group of showers from the Cornell array still gave some evidence of anisotropy, while the directions of 1034 showers from the Volcano Ranch array showed no signs of anisotropy (Linsley 1963). The average primary energy for these showers was greater than 10^{18}ev. Fig. 5.1 shows the grouped distribution in right ascension for the 1962 Agassiz and El Alto results, combined with the 1963 Volcano Ranch and Cornell results.

The results are tabulated in table 5.1. A chi-squared test gives a confidence of 1% for isotropy.

TABLE 5.1

RIGHT ASCENSION DISTRIBUTIONS.

R.A.(hr)	AGASSIZ	EL ALTO	CORNELL	VOLCANO	TOTAL
0 - 2	5	20	15	69	109
2 - 4	2	15	24	82	123
4 - 6	4	9	21	83	117
6 - 8	1	18	11	81	111
8 - 10	3	16	10	58	87
10 - 12	6	17	9	91	123
12 - 14	0	22	15	104	141
14 - 16	0	12	4	89	105
16 - 18	3	25	12	109	149
18 - 20	0	16	15	91	122
20 - 22	4	10	15	85	114
22 - 24	4	14	13	92	123
TOTAL	32	194	164	1034	1424

The Haverah Park Stage 1 array (latitude N54^{o}) recorded no anisotropy in the arrival directions of 6000 showers with primary energy $\sim 10^{17}$ev (Dennis and Wilson, 1963). Analysis of 22,000 selected showers with mean energy 5 x 10^{17}ev recorded by the larger Stage 2

GURE 5.1

Right ascension distribution for the combined results of:-

El Alto (1962)

Agassiz (1962)

Cornell (1963)

Volcano Ranch (1963)

The middle dotted line represents the mean and the upper and lower dotted lines are plus and minus one standard deviation.

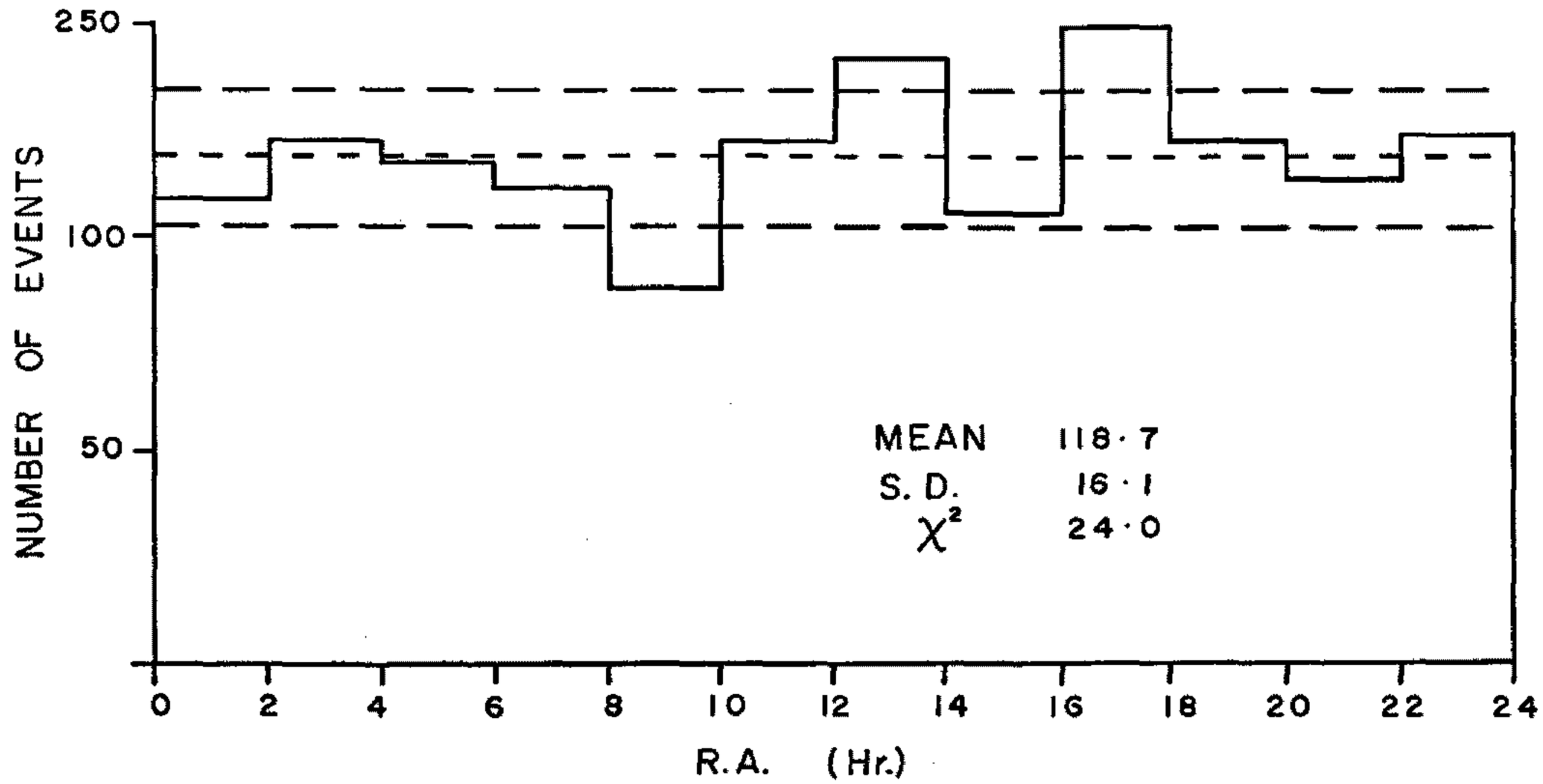
1962 AGASSIZ
EL ALTO
1963 CORNELL
VOLCANO RANCH
250
100
50
NUMBER OF EVENTS
MEAN 118·7
S. D. 16·1
χ^2 24·0
0
2
4
6
8
10
12
14
16
18
20
22
24
R.A. (Hr.)

array firmly establish that the deviation from isotropy in right ascension in the northern hemisphere is no more than 3% (Blake et al 1968) for primaries with energy of the order of 5×10^{17}ev.

Early results of the SUGAR array (Brownlee et al 1969b) showed no significant anisotropy for 626 showers with $E_p \geq 10^{18}$ev and 54 showers with $E_p \geq 10^{19}$ev.

5.3 DIRECTIONAL ANALYSIS OF SUGAR SHOWERS.

As described in the appendix of chapter 2, the direction cosines of a shower front and their associated errors, are obtained by a least squares analysis. From the direction cosines, the local co-ordinates for the primary cosmic ray are determined in the usual way. The zenith angle is designated as θ and the azimuth angle as ϕ in future context. For a vertical shower, θ is 0^{o}. The azimuth angle is measured clockwise from north. Since the error in zenith angle increases as sec(θ), all showers with $\theta > 87^{o}$ have been dropped from the analysis.

From the local co-ordinates and knowing the sidereal time of arrival of a shower front, the celestial co-ordinates, α and δ are evaluated. The right ascension is α and the declination is δ. These co-ordinates in

turn enable the galactic co-ordinates of the primary particle to be calculated. The new system of galactic co-ordinates is used wherein the galactic north pole is at α = 12hr 49m and $\delta = 27.4^{o}$, the origin (galactic centre) is at α = 17hr 39m and $\delta = -28.9^{o}$. Galactic latitude is referred to as b, and galactic lontitude is l. The galactic centre then has co-ordinates $l = 0^{o}$, $b = 0^{o}$.

Errors in all co-ordinates are evaluated from the variances of the direction cosines l and m. The average error angle is $< 5^{o}$ (section 4.12).

The serial number of the last event used in the subsequent analysis is 3503, of these events 944 needed to be dropped from the analysis. A small number of these showers were unphysical (section 4.14). The remaining were showers which only triggered collinear stations and showers in which, after rejecting any stations for having low pulse heights (section 4.10), the number of stations left was less than three.

The following analysis is based on 2659 showers which were recorded by the SUGAR array between January 1968 and March 1970.

5.4. ARRIVAL DIRECTION DISTRIBUTIONS.

5.4.1 LOCAL CO-ORDINATES.

The distribution of azimuth angles for all events is as would be expected from fig. 4.3, isotropic. A harmonic analysis yields a figure of 7 ± 3% as the amplitude of the largest harmonic. Similarly there is no significant variation of intensity with solar time. The amplitude of the largest harmonic of solar time is 8 ± 2%.

On the assumption of an isotropic azimuth distribution, a differential zenith distribution of the form

$$dN = (n+1)N\cos^{n}\theta\sin\theta d\theta$$

has been assumed.

For an isotropic zenith distribution and for no atmospheric attenuation of the muon component of the air showers, the exponent n should equal one. Early results of the SUGAR array (Brownlee et al 1969b) indicate an exponent value of n = 2, over all shower sizes.

The 2659 showers in the present analysis, have been divided into three energy ranges; $E_p \geq 10^{17}$ev, 10^{18}ev $\leq E_p \leq 10^{19}$ev and $E_p \geq 5 \times 10^{18}$ev. The observed distributions along with their fitted functions of the

above form are depicted in fig. 5.2. The parameters of each distribution are:-

E_p	N	n
$E_p \geq 10^{17}$ev	2659	2.2 ± 0.3
10^{18}ev$\leq E_p \leq 10^{19}$ev	719	2.2 ± 0.5
$E_p \geq 5 \times 10^{18}$ev	167	1.0 ± 1.0

N = number of showers in each energy range

The value of n ∿ 2 is low when compared to the value n ∿ 10 obtained from the electron component of air showers. For a muon triggered array, the detection efficiency at large zenith angles is greater than that for an electron triggered array, since the muon component is absorbed very slowly by the atmosphere while the electron component is rapidly absorbed, when past the shower maximum.

The value of n is expected to decrease with increasing energy, since these showers can penetrate deeper into the atmosphere. In all further analysis a value n = 2 is assumed for the exponent of the differential zenith angle distribution, which then becomes

$$dN = 3N\cos^2\theta\sin\theta d\theta$$

FIGURE 5.2

Zenith Angle Distributions for:-

(a) 2659 showers $E_p \geq 10^{17}$ev

(b) 719 showers 10^{18}ev $\leq E_p \leq 10^{19}$ev

(c) 167 showers $E_p \geq 5 \times 10^{19}$ev

Curves of best fit of the form $\cos^n\theta\sin\theta d\theta$ are also shown.

Cell size is 5^o.

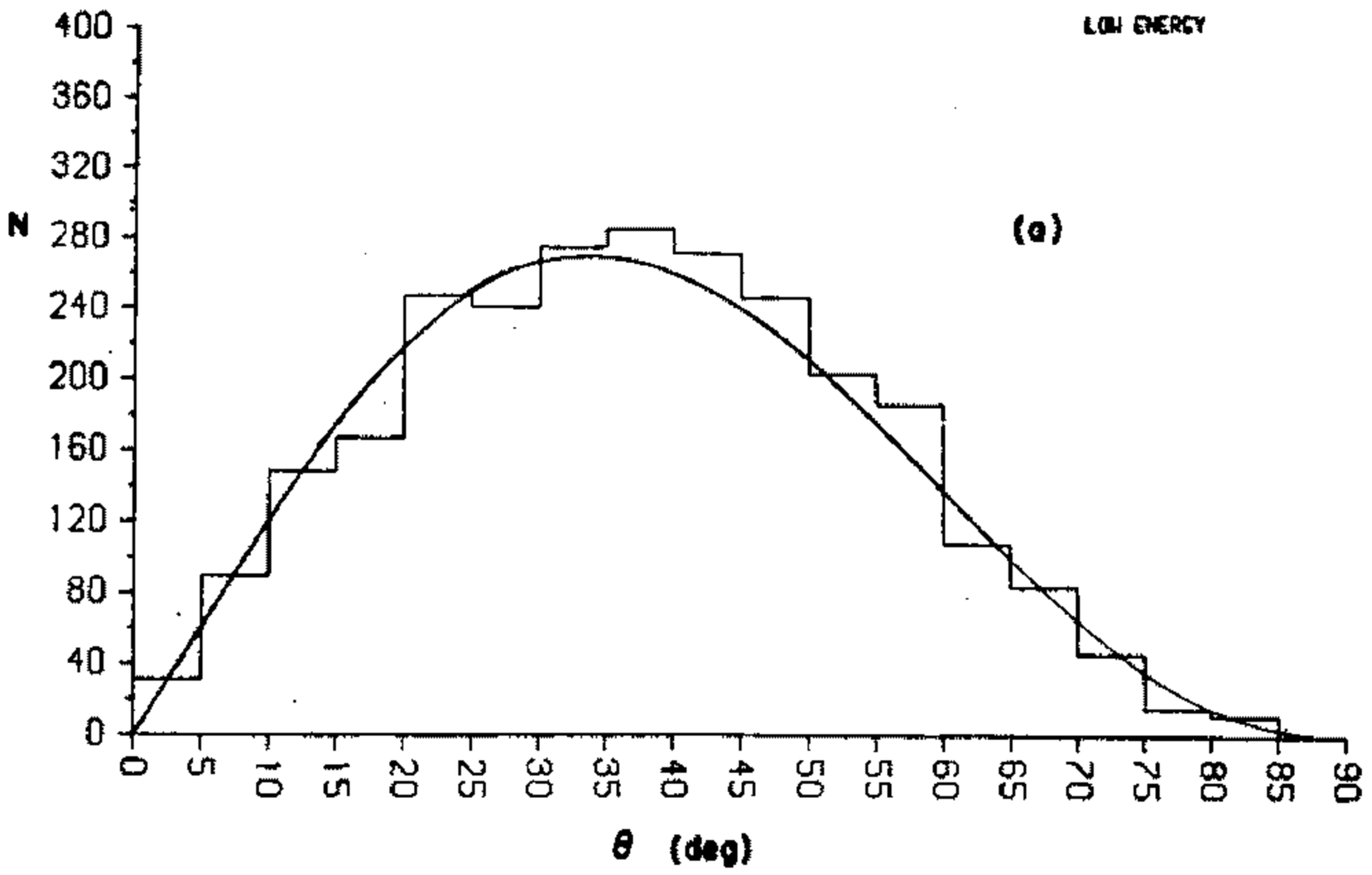
LOW ENERGY
(a)
N
θ (deg)

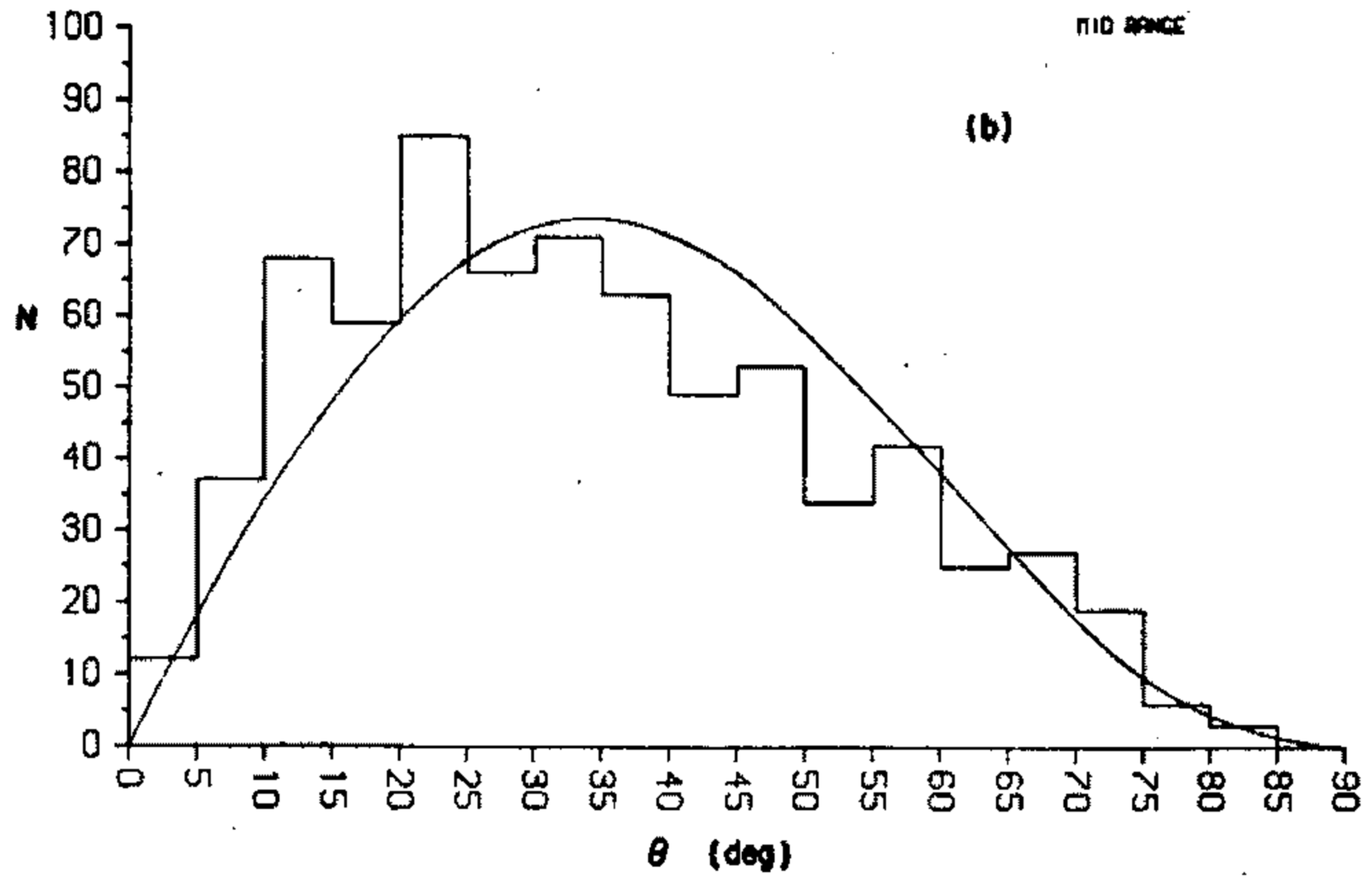
MID RANGE
(b)
N
θ (deg)

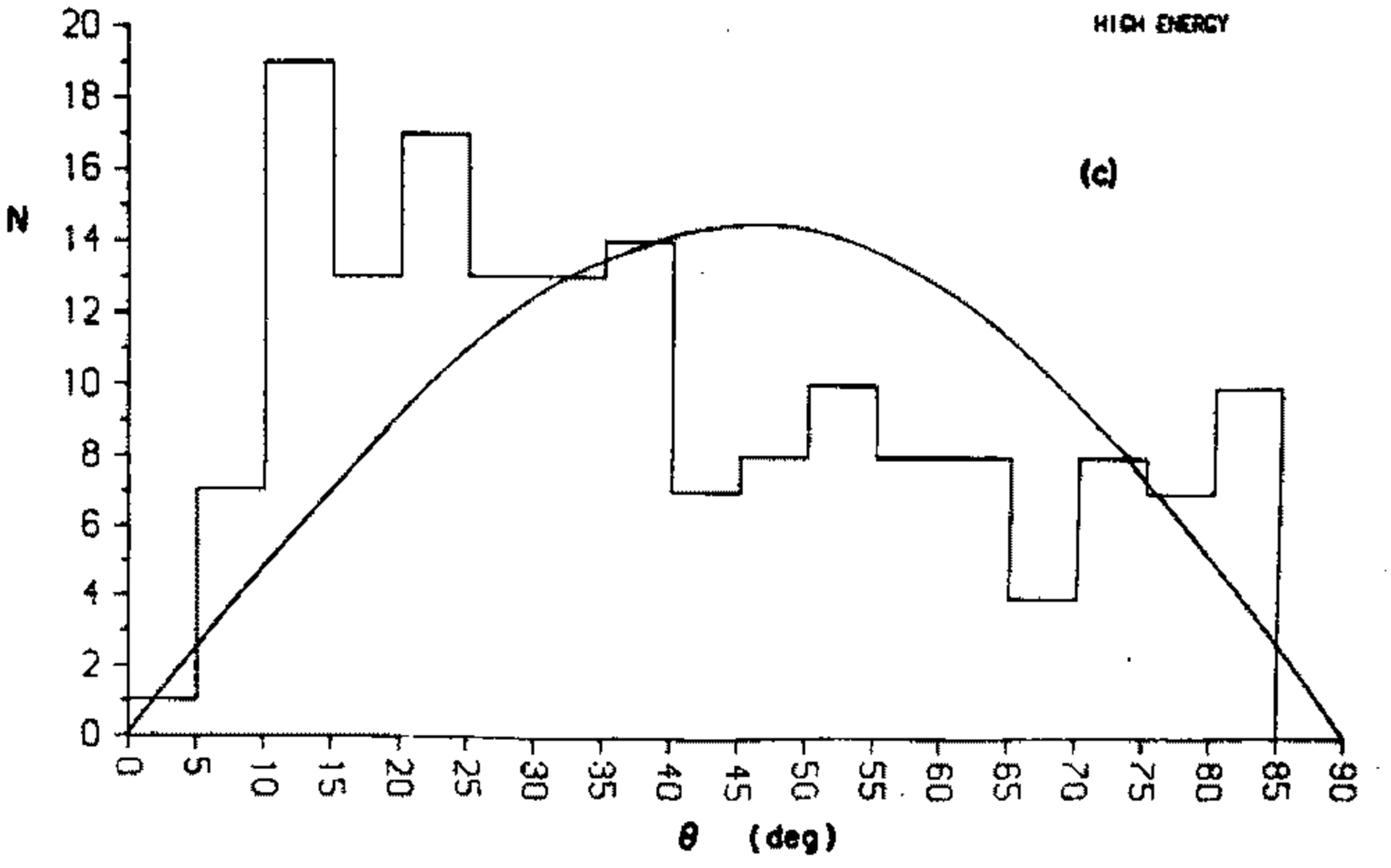
HIGH ENERGY
(c)
N
θ (deg)

5.4.2 CELESTIAL CO-ORDINATES.

The latitude of the SUGAR array is $-30^{o}28'$. This enables us to see the sky from the south celestial pole upto about $\delta \sim 60^{o}$, with the most sensitive region being at $\delta \sim -30^{o}$. Our most northerly shower has $\delta = +47^{o}$. This 150^{o} wide strip of the sky contains potentially the most interesting part of the celestial sphere, namely the major part of the galactic plane which includes the galactic centre and the outward and inward local spiral arms. The nearest extragalactic objects, the Large and Small Magellanic Clouds are also in the southern sky.

On the assumption of an isotropic azimuth distribution and a zenith distribution proportional to $\cos^{2}\theta$, we can predict a declination distribution. Both the observed and predicted distributions for all showers with $E_p \geq 10^{17}$ev are shown in fig. 5.3b. A chi-squared test gives a confidence of 96% for isotropy, which is excellent agreement. For showers with $E_p \geq 10^{18}$ev (fig. 5.4a), a chi-squared test gives a confidence level of 11% for an isotropic distribution. This results from an excess of events, amounting to 3.4 standard deviations above the mean, in the range $-45^{o} < \delta < -20^{o}$. This however is not inconsistent with an isotropic distribution.

FIGURE 5.3

(a) Sidereal viewing time for all events upto event 3503

Mean 111.4

S.D. 11.6

The dotted line represents the mean.

Cell size is 1 hr.

(b) Observed and predicted declination distribution for all events

$E_p \geq 10^{17}$ev.

Cell size is 5^{o}.

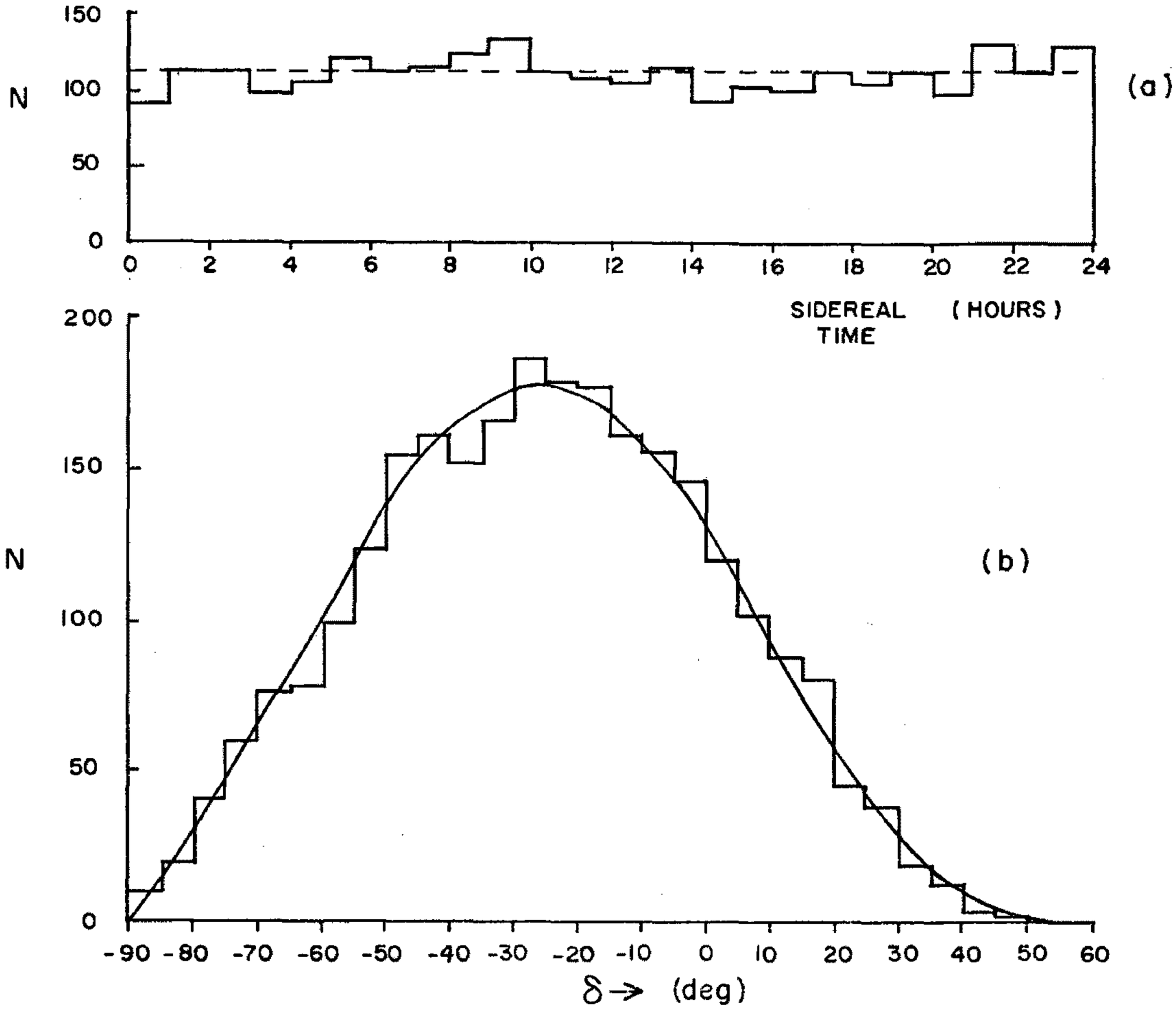
150
N
100
50
0
0
2
4
6
8
10
12
14
16
18
20
22
24
(a)
SIDEREAL TIME (HOURS)
200
150
N
100
50
0
-90
-80
-70
-60
-50
-40
-30
-20
-10
0
10
20
30
40
50
60
δ→ (deg)
(b)

FIGURE 5.4

(a) Declination distribution for

808 events with $E_p \geq 10^{18}$ev

(b) Galactic latitude distribution for

808 events with $E_p \geq 10^{18}$ev

For both (a) and (b) cell size is 5^o.

Also shown are the predicted distributions.

(a)

DECLINATION DISTRIBUTION FOR 808 EVENTS

$E_p \geq 10^{18}$ ev

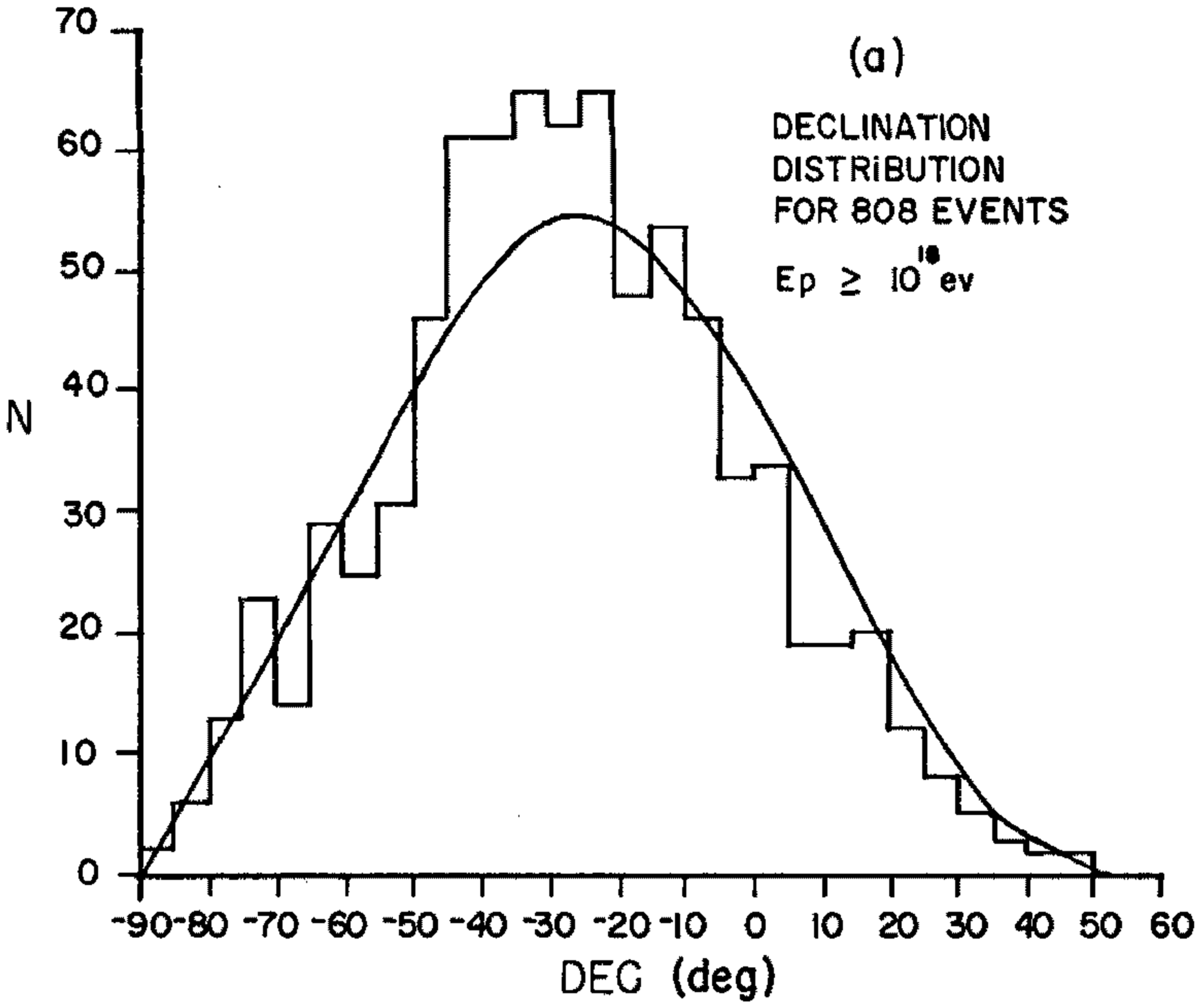

(b)

GALACATIC LATITUDE DISTRIBUTION FOR 808 EVENTS

$E_p \geq 10^{18}$ ev

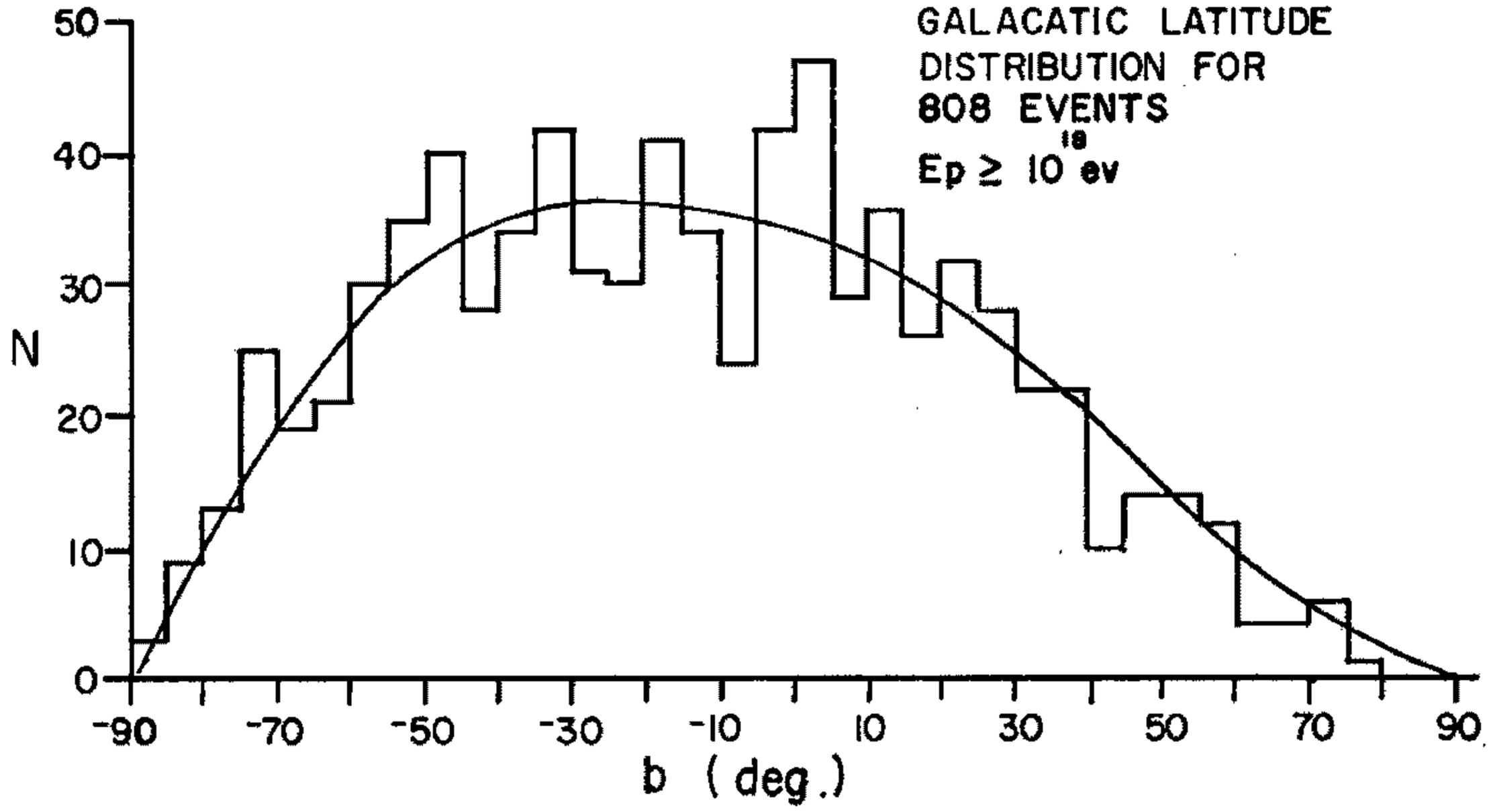

Owing to the relatively small number of showers recorded, none have been randomly rejected to equalise sidereal viewing time. Fig. 5.3a shows the distribution in sidereal time of every event upto and including event 3503 (this includes 16 events with $E_p < 10^{17}$). The mean of this distribution is 111.4 ± 11.6. At a confidence level of 22%, no significant deviation from isotropy is observable.

A convenient way of displaying shower arrival directions in celestial and galactic co-ordinates, is on a Mercator Projection of the celestial sphere. Analysis in right ascension is simplified by the uniform scanning of the sky in each declination band. The mean number of showers in each bin and the standard deviation can easily be calculated. The celestial sphere has been divided into bins 10^{o} wide in declination and 1 hr wide in right ascension. In this way we have 24 bands in right ascension. A chi-squared test on these bands then has 23 degrees of freedom. This bin size easily encompasses the average error angle per event. All events have been divided into four energy ranges; 2659 events with $E_p \geq 10^{17}$ev, 808 events with $E_p \geq 10^{18}$ev, 87 events with $E_p \geq 10^{19}$ev and 8 events with $E_p \geq 10^{20}$ev.

The distribution in right ascension of all events with $E_p \geq 10^{17}$ev is shown in fig. 5.5. The results of

FIGURE 5.5

Distribution in Right Ascension

of all 2659 showers with $E_p \geq 10^{17}$ev

The middle dotted line represents

the mean.

The upper and lower dotted lines are

plus and minus one standard deviation

Mean	110.8
S.D.	10.5
χ^2	24.0

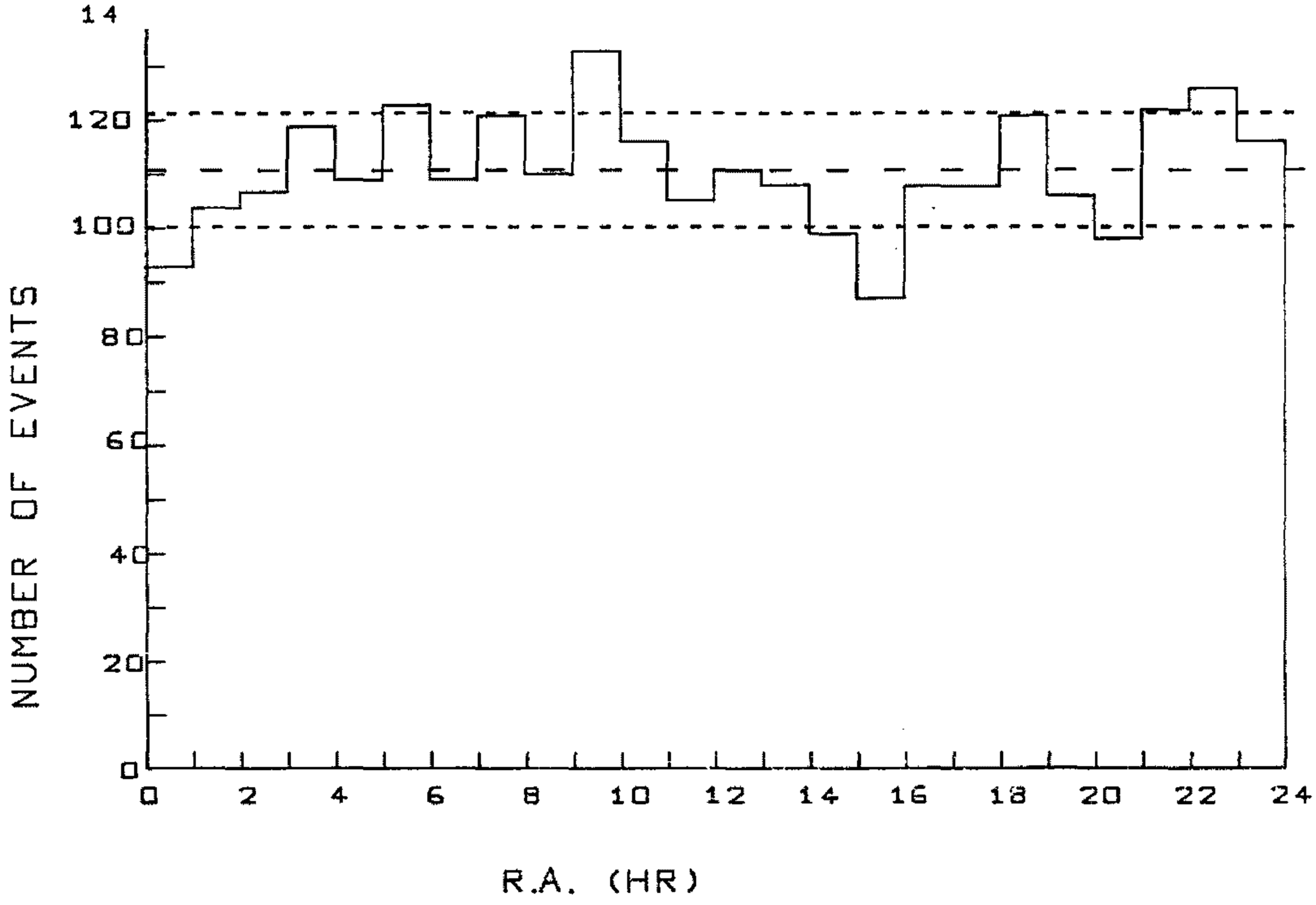
14
120
100
80
60
40
20
0
NUMBER OF EVENTS
0
2
4
6
8
10
12
14
16
18
20
22
24
R.A. (HR)

a chi-squared test give a value of $\chi^2 = 24.0$ which is consistent with an isotropic distribution. The distributions in right ascension of the other ranges are shown in fig. 5.6. The parameters of these distributions are given in table 5.2 and a list of the eight showers with suspected primary energy greater than 10^{20}ev is given in table 5.3. Figs. 5.7 and 5.8 are Mercator projections for events with $E_p \geq 10^{17}$ev and $E_p \geq 10^{18}$ev respectively.

TABLE 5.2

E_p Range (ev)	Mean	S.D.	χ^2	Confidence for Isotropy
$E_p \geq 10^{17}$	110.8	10.5	24.0	40%
$E_p \geq 10^{18}$	33.7	5.8	23.7	42%
$E_p \geq 10^{19}$	3.6	2.0	-	-
$E_p \geq 10^{20}$	0.3	0.6	-	-

An accurate estimate of chi-squared is not possible in the cases $E_p \geq 10^{19}$ev and $E_p \geq 10^{20}$ev owing to the small expected number of events in each bin.

The fact that we and others (Andrews et al 1968, Linsley, 1963b) do see cosmic radiation above the predicted blackbody cutoff implies that if the primaries are protons then

(a) there is no cutoff at 3×10^{19}ev, or

(b) the sources are closer than 10 Mpc.

TABLE 5.3

Event	$E_p x10^{20}$(ev)	$N_\mu x10^8$	Zenith(deg)	R.A.(hr)	Dec(deg)
70	1.02	3.05	39.9±3.4	0.5±0.3	-24.4±3.7
1696	1.26	3.14	32.1±2.7	21.8±0.2	-32.8±2.4
848	1.35	2.48	11.1±0.6	6.7±0.1	-30.3±0.6
1704	1.46	3.28	27.7±1.9	16.3±0.1	- 3.7±1.8
1740	2.02	1.68	76.9±4.3	8.5±0.1	41.1±4.4
1810	2.35	4.31	19.8±3.4	9.3±0.2	-47.0±4.7
1705	4.74	7.84	20.6±2.5	12.3±0.5	-51.1±2.8
3031	230.00*	1.66	84.4±6.7	19.7±0.1	18.8±3.1

* Event 3031 is discussed in section 6.7.

FIGURE 5.6

Distributions of Showers in Right Ascension for:-

(a) 808 showers with $E_p \geq 10^{18}$ev

(b) 87 showers with $E_p \geq 10^{19}$ev

(c) 8 showers with $E_p \geq 10^{20}$ev.

Where drawn, the dotted line represents the mean.

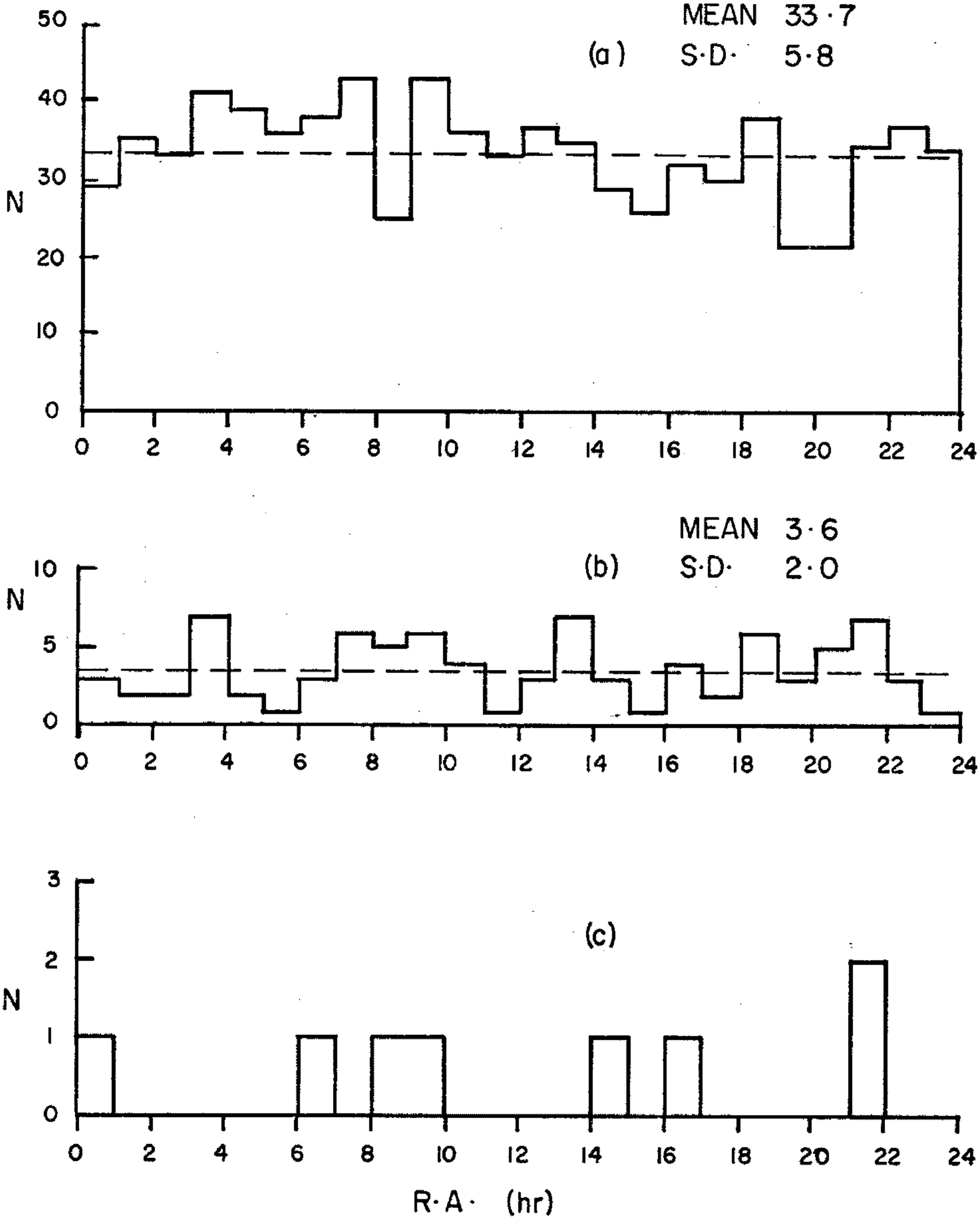
MEAN 33·7
(a) S·D· 5·8
N
50
40
30
20
10
0
0 2 4 6 8 10 12 14 16 18 20 22 24
MEAN 3·6
(b) S·D· 2·0
N
10
5
0
0 2 4 6 8 10 12 14 16 18 20 22 24
(c)
N
3
2
1
0
0 2 4 6 8 10 12 14 16 18 20 22 24
R·A· (hr)

fig. 5.9 is a celestial map of 87 showers with $E_p \geq 10^{19}$ev; 8 showers marked with a cross on the latter map have $E_p \geq 10^{20}$ev. Figs. 5.10 to 5.12 show the numbers of showers in each celestial bin for each of the energy ranges. Bins marked with an asterisk in fig. 5.12 contain one shower with $E_p \geq 10^{20}$ev.

All distributions appear to support the hypothesis of isotropic arrival directions for cosmic radiation, no deviation being more than three standard deviations from the mean.

5.4.3 GALACTIC CO-ORDINATES.

Predicted distributions in galactic latitude and galactic longtitude have been evaluated on the assumption of an isotropic right ascension distribution of cosmic rays and a zenith distribution proportional to $\cos^2\theta$. The standard deviation of the mean for each cell has been evaluated assuming Poisson fluctuations. These distributions for all events with $E_p \geq 10^{17}$ev are shown in figs. 5.13a and 5.14, also plotted are the observed distributions. Fig. 5.13b is the galactic latitude distribution for a smaller sample of 1328 events with $E_p \geq 10^{17}$ev, based on earlier work, (Parkinson 1969).

Parkinson remarked on two possible anisotropies, an excess of 3.8 standard deviations over all longtitudes

FIGURE 5.7

Mercator Projection of the Celestial Sphere.

2659 events with $E_p \geq 10^{17}$ev.

The galactic plane is shown and G marks the galactic centre.

CELESTIAL

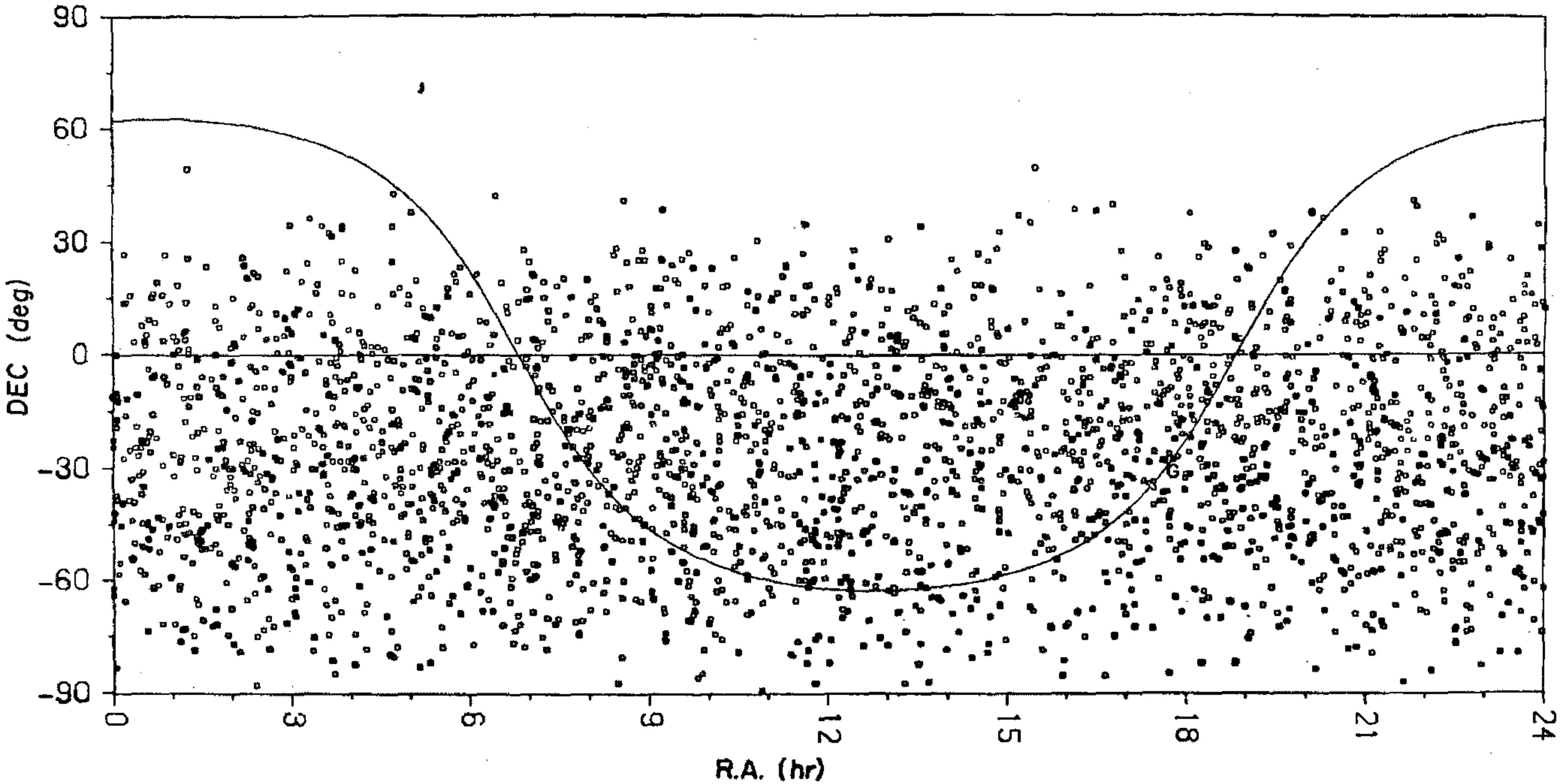

LOG MIN.ENERGY=17

EVENTS 1 TO 3503

FIGURE 5.8

Mercator Projection of Celestial Sphere.

808 events with $E_p \geq 10^{18}$ev.

The galactic plane is shown and G marks the galactic centre.

The points marked as a triangle on the overlay represent the positions of 48 pulsars. The positions of CP 0950+8 and NP 0531+21 are shown separately.

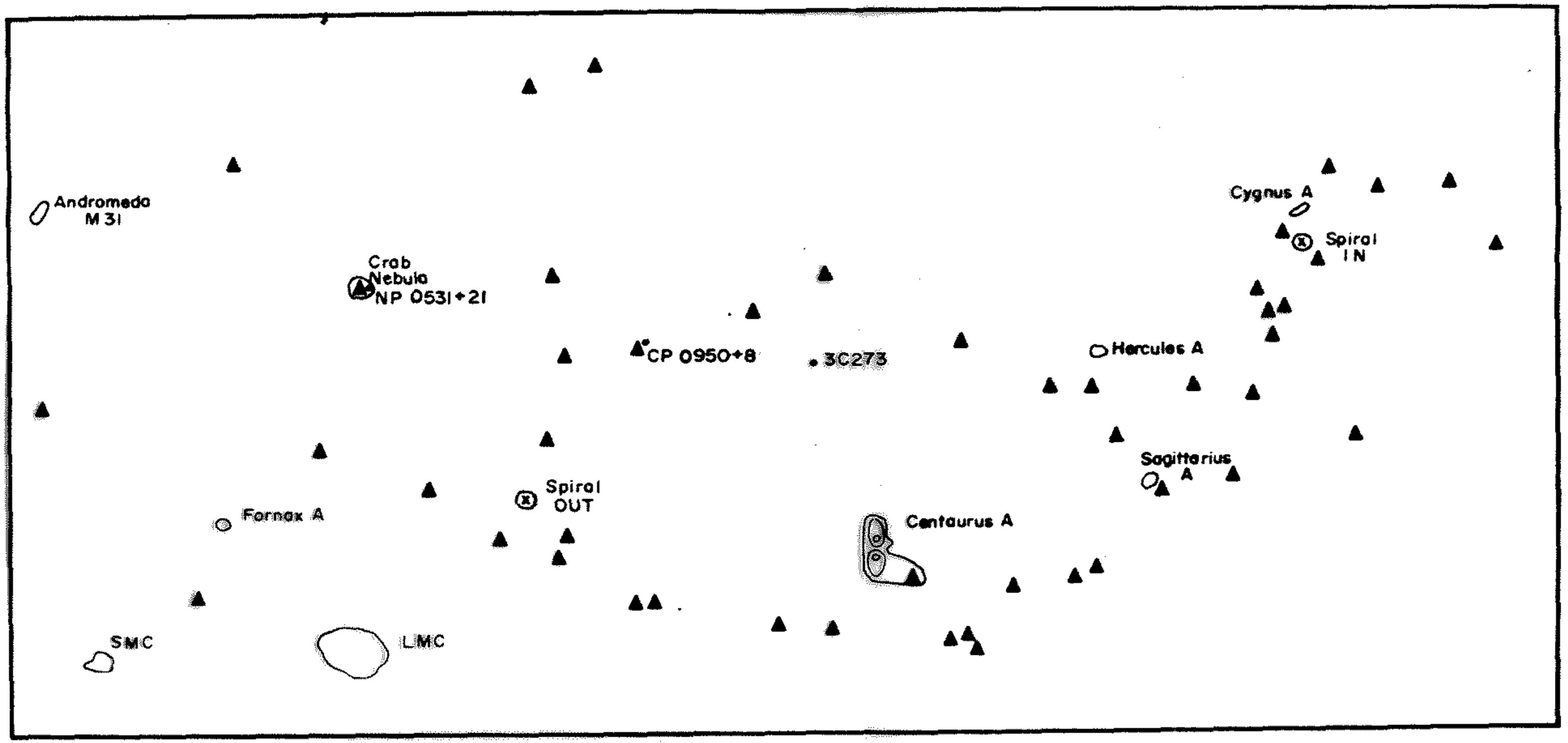
Andromeda
M 31
Crab
Nebula
NP 0531+21
CP 0950+8
3C273
Hercules A
Cygnus A
Spiral
I N
Sagittarius
A
Spiral
OUT
Fornax A
Centaurus A
SMC
LMC

CELESTIAL

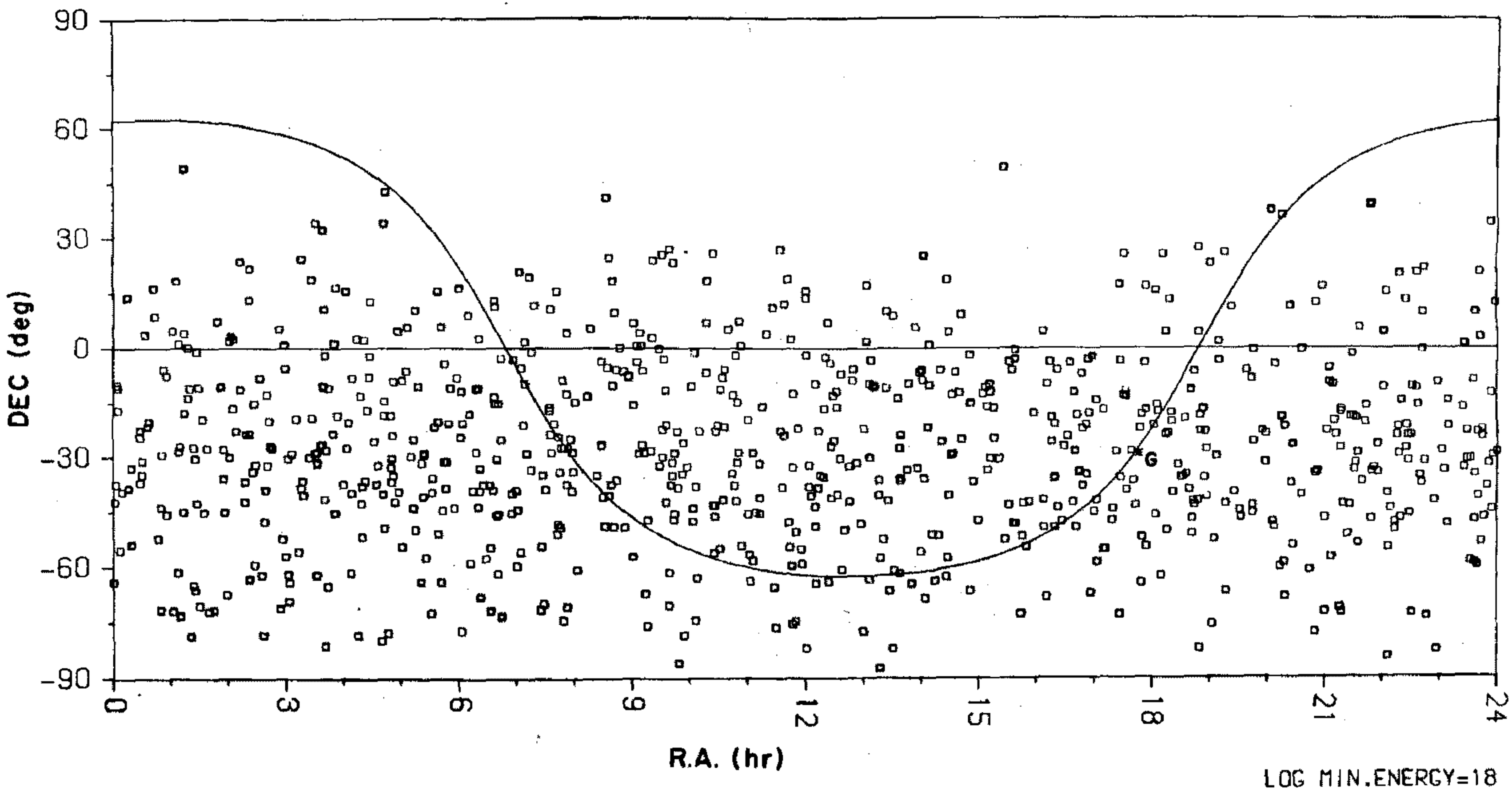

LOG MIN.ENERGY=18

EVENTS 1 TO 3503

FIGURE 5.9

Mercator Projection of Celestial Sphere.

87 events with $E_p \geq 10^{19}$ev

8 events marked with a cross have $E_p \geq 10^{20}$ev

Error bars are one standard deviation in both directions.

The galactic plane is shown and G marks the galactic centre.

CELESTIAL

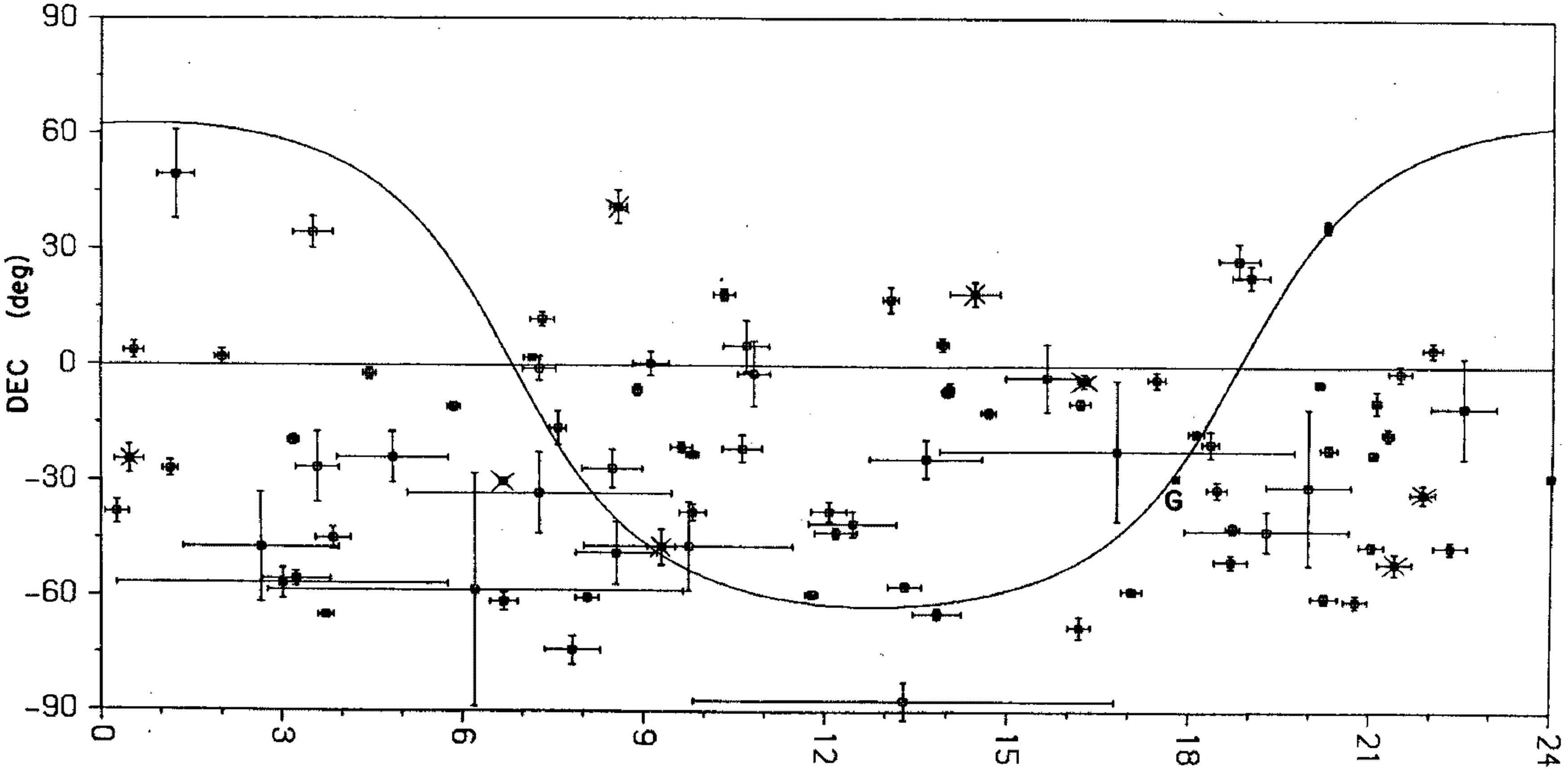

LOG MIN.ENERGY=19

EVENTS 1 TO 3503

FIGURE 5.10

Cellular Division of Mercator

Projection of Celestial Sphere

for 2659 events with $E_p \geq 10^{17}$ev

CELESTIAL

DEC (DEG)	0	1	2	3	4	5	6	7	8	9	10	11	12	13	14	15	16	17	18	19	20	21	22	23	MEAN	S.D.	CHIS
60	0	0	0	0	0	0	0	0	0	0	0	0	0	0	0	0	0	0	0	0	0	0	0	0	0		
50	0	1	0	0	1	0	1	0	1	0	0	0	0	0	0	1	0	0	0	0	0	1	0	0	0.3	0.4	18.0
40	0	0	1	6	1	1	0	0	0	1	1	1	0	2	1	2	3	0	1	1	3	2	3	1	1.3	1.4	34.8
30	2	2	7	2	2	3	3	4	6	7	2	4	4	0	5	0	2	2	5	4	1	6	5	5	3.5	2.0	27.2
20	8	3	5	8	6	9	6	7	5	10	6	9	8	8	5	2	3	11	8	8	9	8	8	8	7.0	2.2	16.9
10	9	12	12	7	9	11	5	10	12	8	11	3	8	14	9	6	6	8	14	8	9	6	13	13	9.3	2.9	21.8
0	5	9	12	15	13	14	9	11	19	20	14	13	12	12	10	15	19	13	13	12	10	11	12	9	12.6	3.4	21.4
-10	11	10	7	14	13	12	15	16	17	11	16	14	13	15	15	15	17	17	16	21	8	19	14	12	14.1	3.2	17.5
-20	14	14	17	22	15	19	14	18	12	20	15	8	13	8	12	10	20	15	20	9	13	18	20	20	15.2	4.1	26.1
-30	12	7	14	9	18	19	20	14	11	18	13	8	14	13	13	12	11	14	15	11	12	15	12	13	13.2	3.2	18.0
-40	14	22	10	13	13	13	11	17	12	10	15	17	18	9	7	9	15	11	13	16	12	12	12	15	13.2	3.3	19.5
-50	10	7	10	7	7	9	12	12	6	11	11	16	7	9	9	7	3	10	6	8	11	14	12	9	9.3	2.8	20.3
-60	5	7	4	11	4	9	7	6	7	9	7	4	9	11	8	2	5	4	8	4	6	4	6	7	6.4	2.3	19.9
-70	2	10	7	3	5	2	6	6	0	6	4	6	4	4	4	4	3	2	0	4	3	5	7	4	4.2	2.2	28.0
-80	1	0	1	2	2	2	0	0	2	2	1	2	1	3	1	2	1	1	2	0	1	1	2	0	1.2	0.8	13.2
-90																											
R.A. (HR)	0	1	2	3	4	5	6	7	8	9	10	11	12	13	14	15	16	17	18	19	20	21	22	23			
TOTAL	93	104	107	119	109	128	109	121	110	133	116	105	111	108	99	87	108	108	121	106	98	122	126	116	110.8	10.5	24.0
																							SUM	2659			

FIGURE 5.11

Cellular Division of Mercator Projection of Celestial Sphere for 808 events with $E_p \geq 10^{18}$ev.

CELESTIAL

DEC (DEG)	0	1	2	3	4	5	6	7	8	9	10	11	12	13	14	15	16	17	18	19	20	21	22	23	MEAN	S.D.	CHIS
60	0	0	0	0	0	0	0	0	0	0	0	0	0	0	0	0	0	0	0	0	0	0	0	0	0		
50	0	1	0	0	1	0	0	0	1	0	0	0	0	0	0	1	0	0	0	0	0	0	0	0	0.2	0.4	20.0
40	0	0	0	2	1	0	0	0	0	0	0	0	0	0	0	0	0	0	0	0	2	1	0	1	0.3	0.6	30.7
30	0	0	2	1	0	0	0	1	1	4	1	1	0	0	1	0	0	1	2	2	0	0	3	1	0.9	1.1	30.4
20	2	1	1	3	2	3	2	4	1	0	1	3	2	2	1	0	0	2	2	1	3	0	2	1	1.6	1.1	17.0
10	2	5	5	1	3	2	2	2	3	5	4	2	1	3	3	0	1	0	2	1	0	1	2	3	2.2	1.5	23.5
0	2	1	1	2	4	4	2	4	6	4	5	0	7	4	5	5	7	2	1	4	2	4	2	1	3.3	1.9	27.0
-10	3	6	5	6	5	3	7	3	3	2	4	3	4	4	4	6	4	7	7	0	1	7	5	3	4.2	1.9	27.0
-20	5	5	6	8	4	7	4	11	1	10	5	4	3	4	5	1	7	3	7	4	2	6	7	8	5.3	2.5	28.1
-30	7	2	5	6	11	6	9	7	3	7	4	3	9	5	2	3	4	3	7	2	3	6	5	7	5.2	2.4	26.4
-40	3	4	2	4	3	5	4	3	5	4	7	5	7	2	1	6	7	5	7	5	3	4	6	5	4.5	1.7	14.8
-50	3	0	2	2	1	3	3	4	0	1	3	7	0	3	3	3	0	5	1	1	3	3	1	4	2.3	1.7	29.7
-60	1	4	2	5	1	2	2	1	1	2	1	2	3	5	4	0	2	1	1	1	2	0	0	0	1.8	1.4	27.9
-70	1	6	2	0	3	1	3	3	0	3	1	3	0	1	0	1	0	1	0	1	1	3	2	0	1.5	1.5	34.7
-80	0	0	0	1	0	0	0	0	0	1	0	0	1	2	0	0	0	0	1	0	0	0	2	0	0.3	0.6	28.0
-90																											
	0	1	2	3	4	5	6	7	8	9	10	11	12	13	14	15	16	17	18	19	20	21	22	23			
R.A. (HR)																											
TOTAL	29	35	33	41	39	36	38	49	25	48	36	38	37	35	29	26	32	30	38	22	22	35	37	34	33.7	5.8	29.7
																							SUM	808			

FIGURE 5.12

Cellular Division of Mercator Projection of Celestial Sphere for 87 events with $E_p \geq 10^{19}$ev.

Cells marked with an asterisk contain ONE shower with $E_p \geq 10^{20}$ev.

CELESTIAL

DEC	0	1	2	3	4	5	6	7	8	9	10	11	12	13	14	15	16	17	18	19	20	21	22	23	24	MEAN	S.D.	CHIS
60	0	0	0	0	0	0	0	0	0	0	0	0	0	0	0	0	0	0	0	0	0	0	0	0	0	0		
50	0	1	0	0	0	0	0	0	*1	0	0	0	0	0	0	0	0	0	0	0	0	0	0	0	0	0.1	0.3	22.0
40	0	0	0	1	0	0	0	0	0	0	0	0	0	0	0	0	0	0	0	0	0	1	0	0	0	0.1	0.3	22.0
30	0	0	0	0	0	0	0	0	0	0	0	0	0	0	*1	0	0	0	1	1	0	0	0	0		0.1	0.3	21.0
20	0	0	0	0	0	0	0	1	0	0	1	0	0	1	0	0	0	0	0	0	0	0	0	0	0	0.1	0.3	21.0
10	1	0	1	0	0	0	0	1	0	1	1	0	0	1	0	0	0	0	0	0	0	0	0	1	0	0.3	0.5	17.0
0	0	0	0	0	1	0	0	1	1	0	1	0	0	1	1	1	*2	1	0	0	1	2	0	0		0.5	0.6	18.4
-10	0	0	0	1	0	1	0	1	0	0	0	0	0	0	1	0	0	0	1	0	0	1	1	0		0.3	0.5	17.0
-20	*1	1	0	1	1	0	0	0	1	2	1	0	0	1	0	0	1	0	1	0	1	1	0	1		0.6	0.6	13.4
-30	1	0	0	0	0	0	*1	1	0	1	0	0	1	0	0	0	0	0	1	1	0	*1	0	0		0.3	0.5	16.0
-40	0	0	1	1	0	0	0	0	1	*2	0	0	2	0	0	0	0	0	1	1	0	1	1	0		0.5	0.6	21.7
-50	0	0	0	2	0	0	1	0	0	0	0	1	0	1	0	0	0	1	1	0	1	*1	0	0		0.4	0.6	20.3
-60	0	0	0	1	0	0	1	0	1	0	0	0	0	1	0	0	1	0	0	0	1	0	0	0		0.3	0.4	18.0
-70	0	0	0	0	0	0	0	1	0	0	0	0	0	0	0	0	0	0	0	0	0	0	0	0		0.0	0.2	23.0
-80	0	0	0	0	0	0	0	0	0	0	0	0	0	1	0	0	0	0	0	0	0	0	0	0		0.0	0.2	23.0
-90	0	1	2	3	4	5	6	7	8	9	10	11	12	13	14	15	16	17	18	19	20	21	22	23	24			
R.A. (HR)																												
TOTAL	3	2	2	7	2	1	3	6	5	6	4	1	3	7	3	1	4	2	6	3	5	7	3	1		8.6	2.0	28.4
																							SUM	87				

in the latitude range b(-50^{o},-45^{o}) and a deficiency of 2.4 standard deviations in the range b(-5^{o},0^{o}). These results together with the present results based on twice the number of showers are tabulated below (table 5.4). Also included are the ranges b(-10^{o},5^{o}) and b(0^{o},5^{o}).

TABLE 5.4

GALACTIC LATITUDE DEVIATIONS.

	1328 Events		2659 Events	
b	N	n_o/n_e	N	n_o/n_e
(-50^{o},-45^{o})	3.8	1.52	2.4	1.23
(-10^{o},-5^{o})	-1.0	0.88	-1.5	0.86
(-5^{o}, 0^{o})	-2.4	0.68	-1.5	0.86
(0^{o}, 5^{o})	1.7	1.23	2.3	1.22

N = number of standard deviations from mean.

n_o = observed number of events

n_e = expected number of events

The earlier predictions of Parkinson appear to be only statistical fluctuations from the mean. The cell b(0^{o},5^{o}), which is the region just north of the

galactic plane, appears to be consistently 1.2 times the background flux. Many more events are required to verify whether this effect is real or not.

The results of a chi-squared test on the galactic latitude distribution (fig. 5.13a) for all events with $E_p \geq 10^{17}$ev, gives a 7% confidence in an isotropic distribution. The same test on all showers with $E_p \geq 10^{18}$ev (fig.5.4b) gives a confidence of 44% in favour of an isotropic distribution.

The predicted and observed distributions in galactic longtitude for all events with $E_p \geq 10^{17}$ev, are shown in fig. 5.14. No anisotropy is observable, a chi-squared test with 35 degrees of freedom yields a value of 37.1 which implies a 40% probability in favour of the distribution being isotropic.

Figs. 5.16 to 5.18 are Mercator projections of the galactic co-ordinates for showers with $E_p \geq 10^{17}$ev, $E_p \geq 10^{18}$ev and $E_p \geq 10^{19}$ev, respectively. The points marked with a cross in fig. 5.18, correspond to showers with $E_p \geq 10^{20}$ev. The cellular division of all events with $E_p \geq 10^{17}$ev is tabulated in fig. 5.15. The cell size is 10^0 x 15^0 and in each cell the large print refers to the observed number of showers in that cell. The smaller print is the expected number of showers in that cell, based on combining the predicted latitude and

FIGURE 5.13

Galactic latitude distributions for

(a) 2659 events with $E_p \geq 10^{17}$ev.

(b) 1328 events with $E_p \geq 10^{17}$ev.

Predicted distributions are also shown.

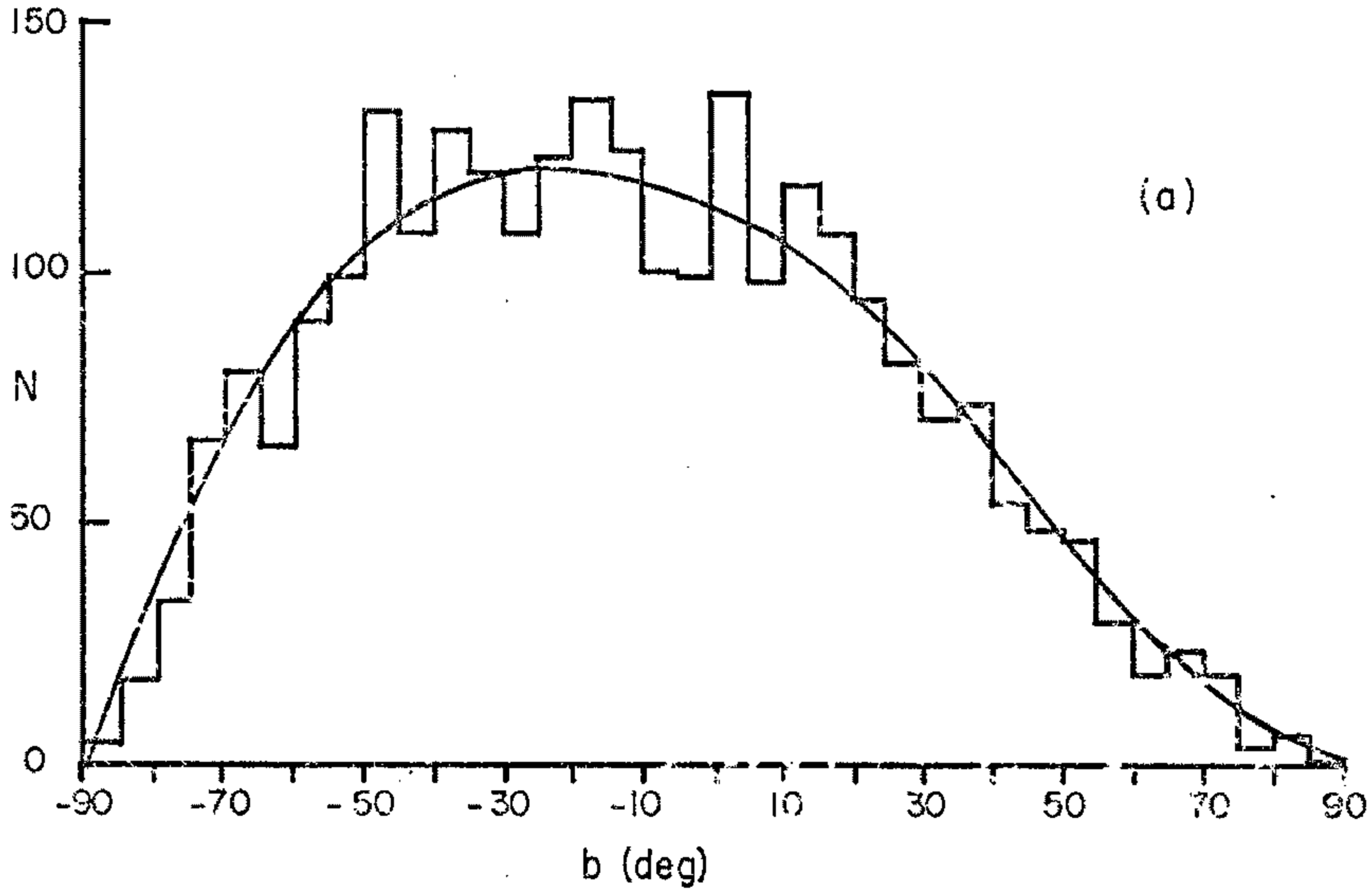
150
100
N
50
0
-90
-70
-50
-30
-10
10
30
50
70
90
b (deg)
(a)

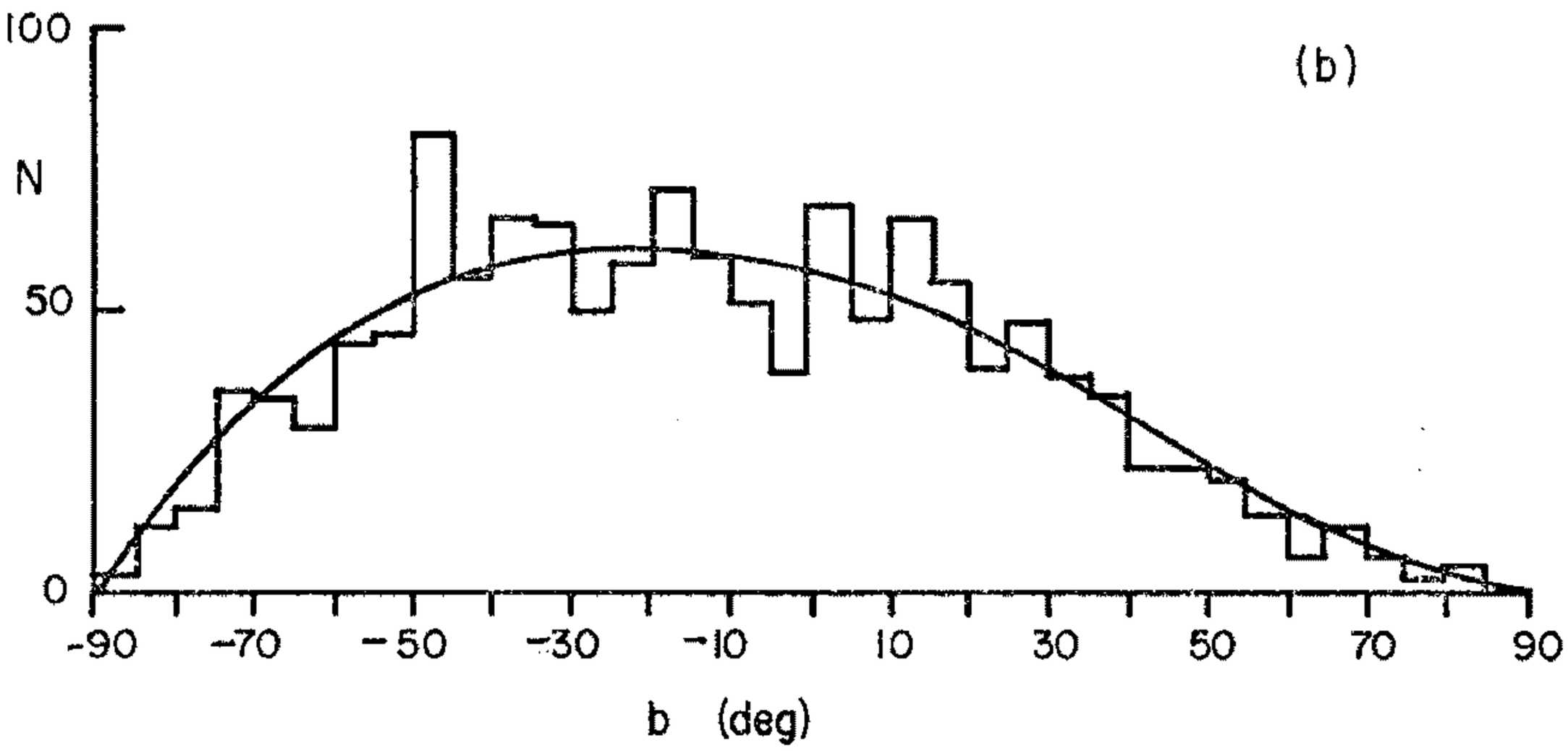
100
N
50
0
-90
-70
-50
-30
-10
10
30
50
70
90
b (deg)
(b)

FIGURE 5.14

Galactic longtitude distribution for 2659 events with $E_p \geq 10^{17}$ev.

$l = 0^o$ is at the galactic centre.

The predicted distribution is also shown.

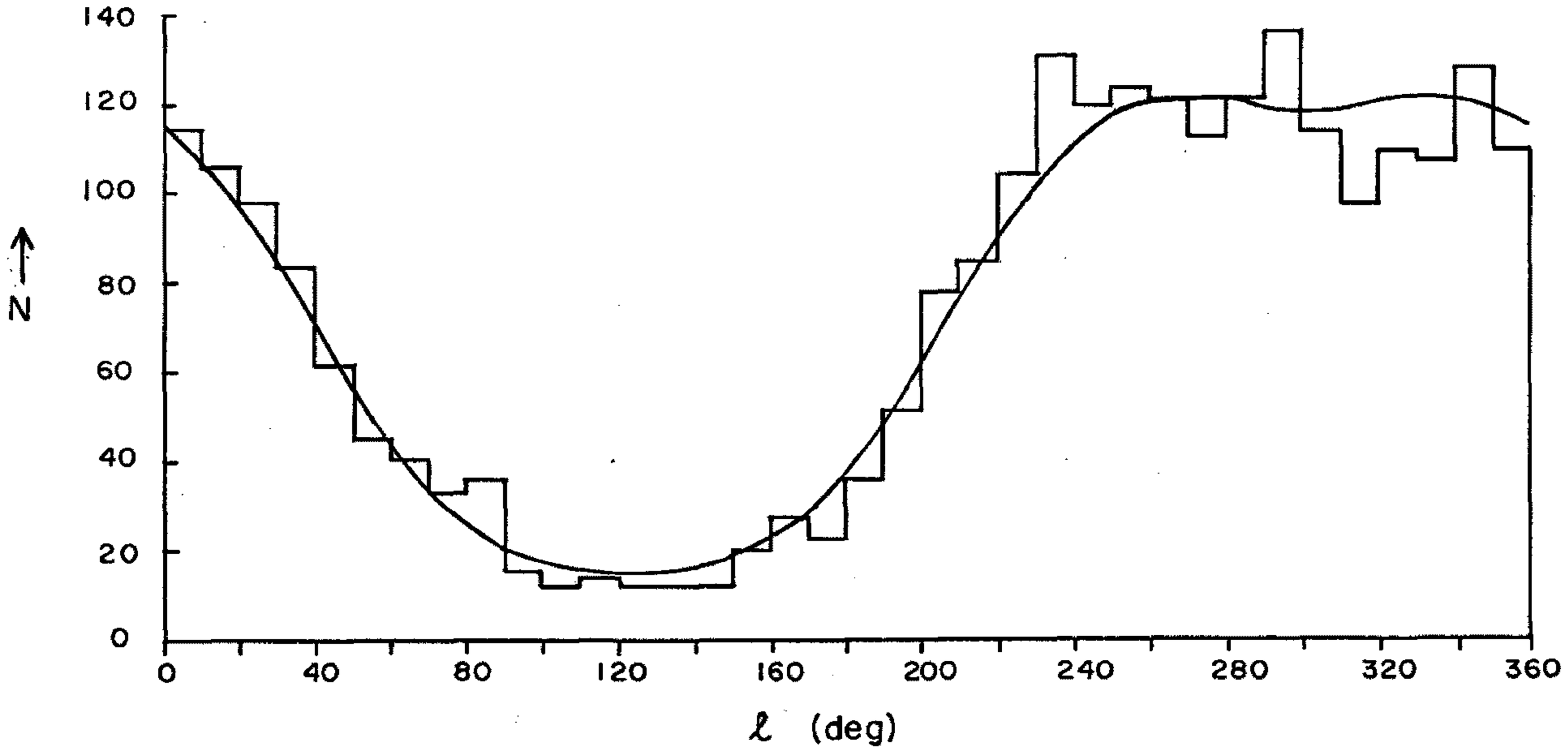
140
120
100
80
60
40
20
0
N
0
40
80
120
160
200
240
280
320
360
ℓ (deg)

FIGURE. 5.15

Cellular division of 2659 events in galactic co-ordinates.

In each cell the larger top number is the observed number of showers, the smaller bottom number is the expected number of showers.

GALACTIC

LAT (DEG)	0	1	2	3	4	5	6	7	8	9	10	11	12	13	14	15	16	17	18	19	20	21	22	23	24
90	0 0.4	0 0.4	0 0.3	0 0.2	0 0.1	1 0.1	0 0.1	0 0.1	0 0.1	0 0.1	0 0.1	0 0.1	0 0.1	0 0.2	1 0.8	0 0.4	0 0.4	1 0.5	1 0.5	0 0.5	2 0.5	1 0.5	0 0.5	0 0.5	0 0.5
80	1 1.5	1 1.3	1 1.0	0 0.7	1 0.5	0 0.3	0 0.2	0 0.2	0 0.2	0 0.2	0 0.3	0 0.4	1 0.6	1 0.9	0 1.2	2 1.4	1 1.6	4 1.6	1 1.6	0 1.6	2 1.6	2 1.6	2 1.6	1 1.6	
70	1 2.8	4 2.4	3 1.9	1 1.4	0 0.9	0 0.8	0 0.5	0 0.4	0 0.4	0 0.4	0 0.5	0 0.8	0 1.2	1 1.7	3 2.8	3 2.7	3 3.0	1 3.2	2 3.2	4 3.1	4 3.1	5 3.2	5 3.2	2 3.1	
60	6 4.6	1 4.0	0 3.2	1 2.2	1 1.5	1 1.0	0 0.8	0 0.6	0 0.6	0 0.7	0 0.9	0 1.3	0 1.9	2 2.8	2 3.7	5 4.4	5 4.9	6 5.2	6 5.2	8 5.1	9 5.0	10 5.2	8 5.2	4 5.0	
50	3 6.7	4 5.8	1 4.6	0 3.2	3 2.2	0 1.4	0 1.1	0 0.9	0 0.9	0 1.0	0 1.3	0 1.9	1 2.8	6 4.1	5 5.4	6 8.4	10 7.2	5 7.5	13 7.5	7 7.4	9 7.3	13 7.5	7 7.5	7 7.3	
40	9 8.9	5 7.6	1 6.0	1 4.2	0 2.9	0 1.9	0 1.5	0 1.2	0 1.2	0 1.3	0 1.7	0 2.5	1 3.7	7 5.4	9 7.1	12 8.4	12 9.5	18 9.9	10 9.9	13 9.7	7 9.6	10 9.9	11 9.9	18 9.6	
30	15 10.9	10 9.3	10 7.4	1 5.2	1 3.5	0 2.3	0 1.8	0 1.5	0 1.5	0 1.6	0 2.1	0 3.0	0 4.5	4 6.6	9 8.7	22 10.9	12 11.6	9 12.1	13 12.1	16 11.9	12 11.8	16 12.1	12 12.1	14 11.8	
20	20 12.5	13 10.7	15 8.5	4 6.0	0 4.0	0 2.6	0 2.1	0 1.7	0 1.7	0 1.8	0 2.4	1 3.4	2 5.2	10 7.6	10 10.0	13 11.8	14 13.3	28 13.9	17 13.9	25 13.6	15 13.5	8 13.9	12 13.9	17 13.5	
10	18 13.6	16 11.6	11 9.2	6 6.5	4 4.4	0 2.9	0 2.2	0 1.9	0 1.9	0 2.0	0 2.6	0 3.7	2 5.6	7 8.2	12 10.8	19 12.8	18 14.5	15 15.1	19 15.1	22 14.8	16 14.7	15 15.1	17 15.1	17 14.7	
0	20 14.2	11 12.1	8 9.7	9 6.8	1 4.6	1 3.0	0 2.4	0 2.0	0 2.0	0 2.1	1 2.7	2 3.9	6 5.9	6 8.6	7 11.4	10 13.5	20 15.2	15 15.8	13 15.8	15 15.5	17 15.4	19 15.8	14 15.8	14 15.4	
-10	21 14.6	16 12.4	10 9.9	6 7.0	8 4.7	3 3.1	1 2.4	0 2.0	1 2.0	0 2.1	6 2.8	1 4.0	10 6.0	13 8.8	12 11.6	17 13.8	18 15.5	19 16.2	15 16.2	19 15.9	16 15.8	14 16.2	13 16.2	19 15.8	
-20	8 14.7	15 12.5	5 10.0	11 7.0	7 4.7	6 3.1	2 2.4	1 2.0	0 2.0	0 2.2	2 2.8	4 4.0	4 6.1	14 8.9	13 11.7	19 13.9	18 15.6	20 16.3	18 16.3	9 16.0	11 15.9	11 16.3	8 16.3	21 15.9	
-30	12 14.4	16 12.3	16 9.8	5 6.9	11 4.6	7 3.0	2 2.4	2 2.0	2 2.0	5 2.1	4 2.8	8 4.0	12 6.0	9 8.7	15 11.5	16 13.6	19 15.4	13 16.0	10 16.0	18 15.8	9 15.6	12 16.0	14 16.0	18 15.6	
-40	10 13.6	12 11.6	14 9.2	6 6.5	11 4.4	8 2.9	9 2.2	3 1.9	7 1.9	2 2.0	5 2.6	9 3.7	9 5.6	11 8.2	15 10.9	12 12.9	14 14.5	9 15.1	11 15.1	14 14.9	13 14.7	13 15.1	12 15.1	12 14.7	
-50	10 12.0	8 10.3	13 8.2	8 5.7	3 3.9	9 2.5	4 2.0	6 1.7	6 1.7	3 1.8	7 2.3	4 3.3	6 5.0	5 7.3	15 9.6	8 11.4	9 12.8	6 13.4	11 13.4	6 13.1	10 13.0	10 13.4	13 13.4	10 13.0	
-60	5 9.6	13 8.2	6 6.5	6 4.6	5 3.1	4 2.0	2 1.6	3 1.3	4 1.3	5 1.4	4 1.8	5 2.6	4 3.9	6 5.8	7 7.6	8 9.0	7 10.2	6 10.6	9 10.6	13 10.4	7 10.3	4 10.6	10 10.6	2 10.3	
-70	6 6.2	8 5.3	5 4.2	3 2.9	2 2.0	8 1.3	2 1.0	1 0.9	1 0.9	3 0.9	4 1.2	2 1.7	1 2.6	4 3.7	5 4.9	7 5.8	4 6.6	3 6.9	4 6.9	6 6.7	5 6.7	4 6.9	10 6.9	2 6.7	
-80	3 2.1	0 1.8	2 1.5	1 1.0	3 0.7	2 0.5	2 0.4	1 0.3	0 0.3	0 0.3	0 0.4	1 0.6	1 0.9	1 1.3	2 1.7	1 2.0	0 2.3	0 2.4	1 2.4	1 2.3	0 2.3	0 2.4	1 2.4	3 2.3	
-90																									

LONG (HR)

FIGURE 5.16

Mercator Projection in New Galactic Co-ordinates of 2659 events with $E_p \geq 10^{17}$ev.

GALACTIC

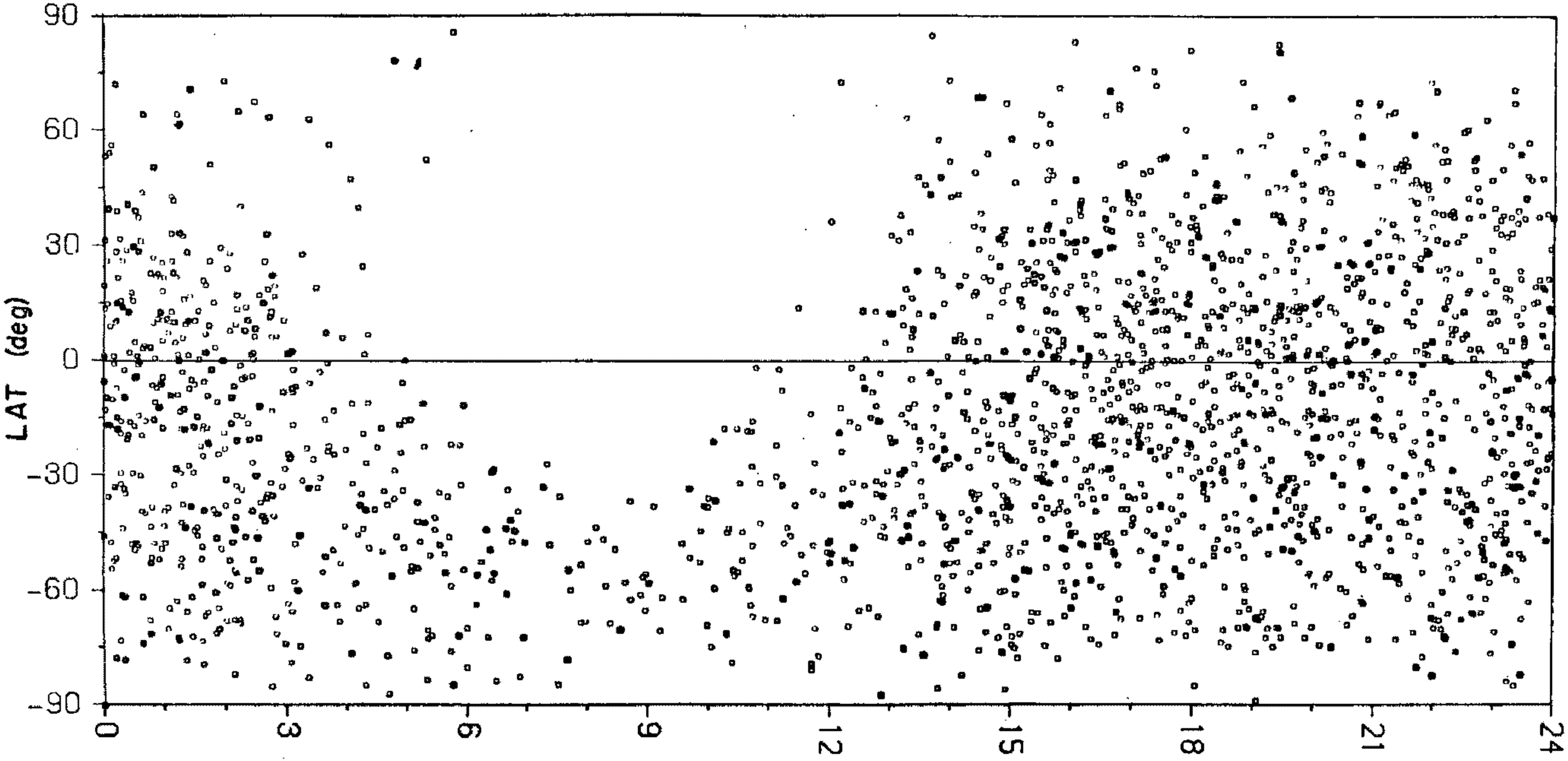

LOG MIN.ENERGY=17

EVENTS 1 TO 3503

FIGURE 5.17

Mercator Projection in New Galactic Co-ordinates of 808 events with $E_p \geq 10^{18}$ev.

GALACTIC

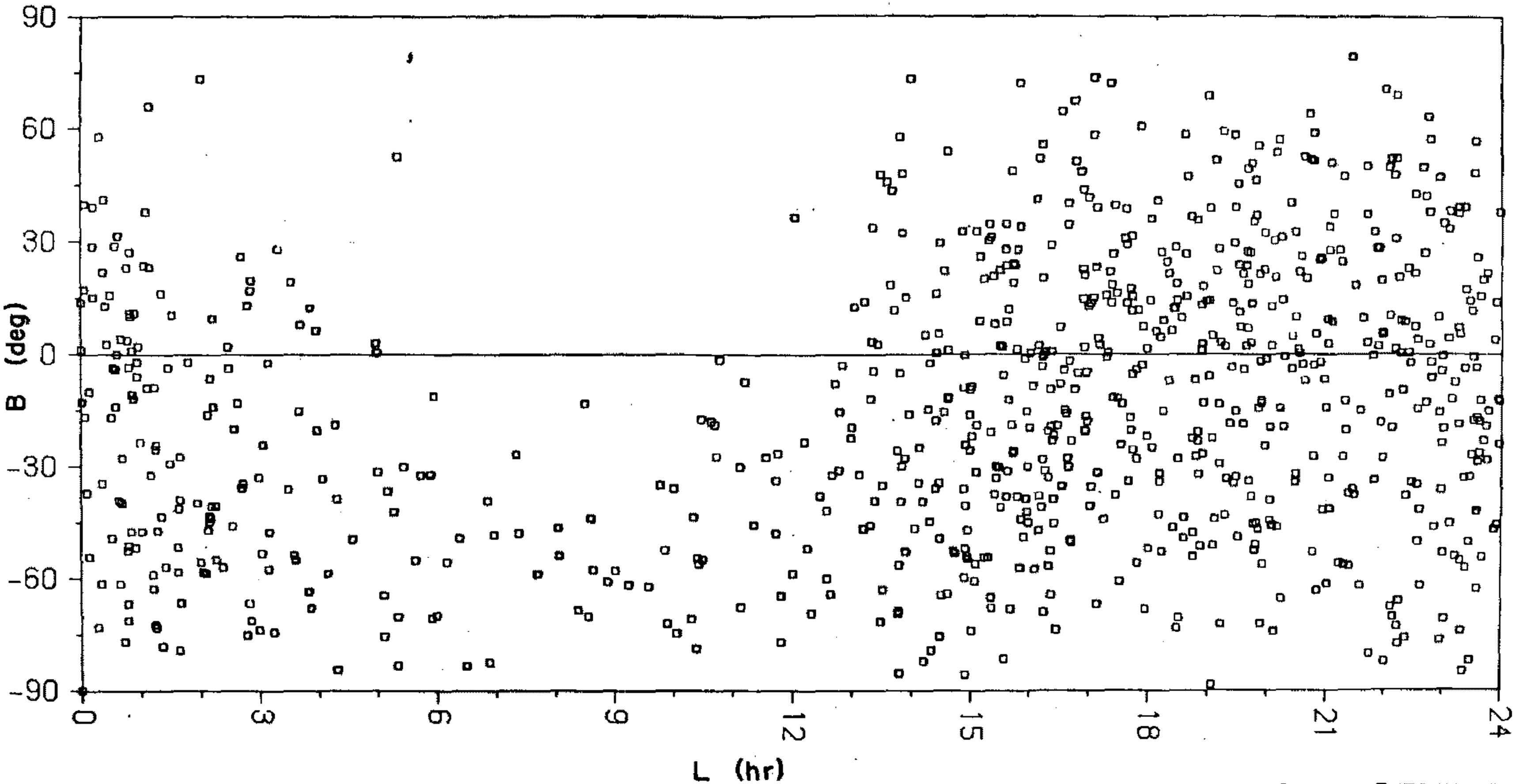

LOG MIN.ENERGY=18

EVENTS 1 TO 3503

FIGURE 5.18

Mercator Projection in New Galactic

Co-ordinates of 87 events with

$E_P \geq 10^{19}$ev.

8 events marked with a cross have

$E_P \geq 10^{20}$ev.

Error bars are one standard deviation

in both directions.

GALACTIC

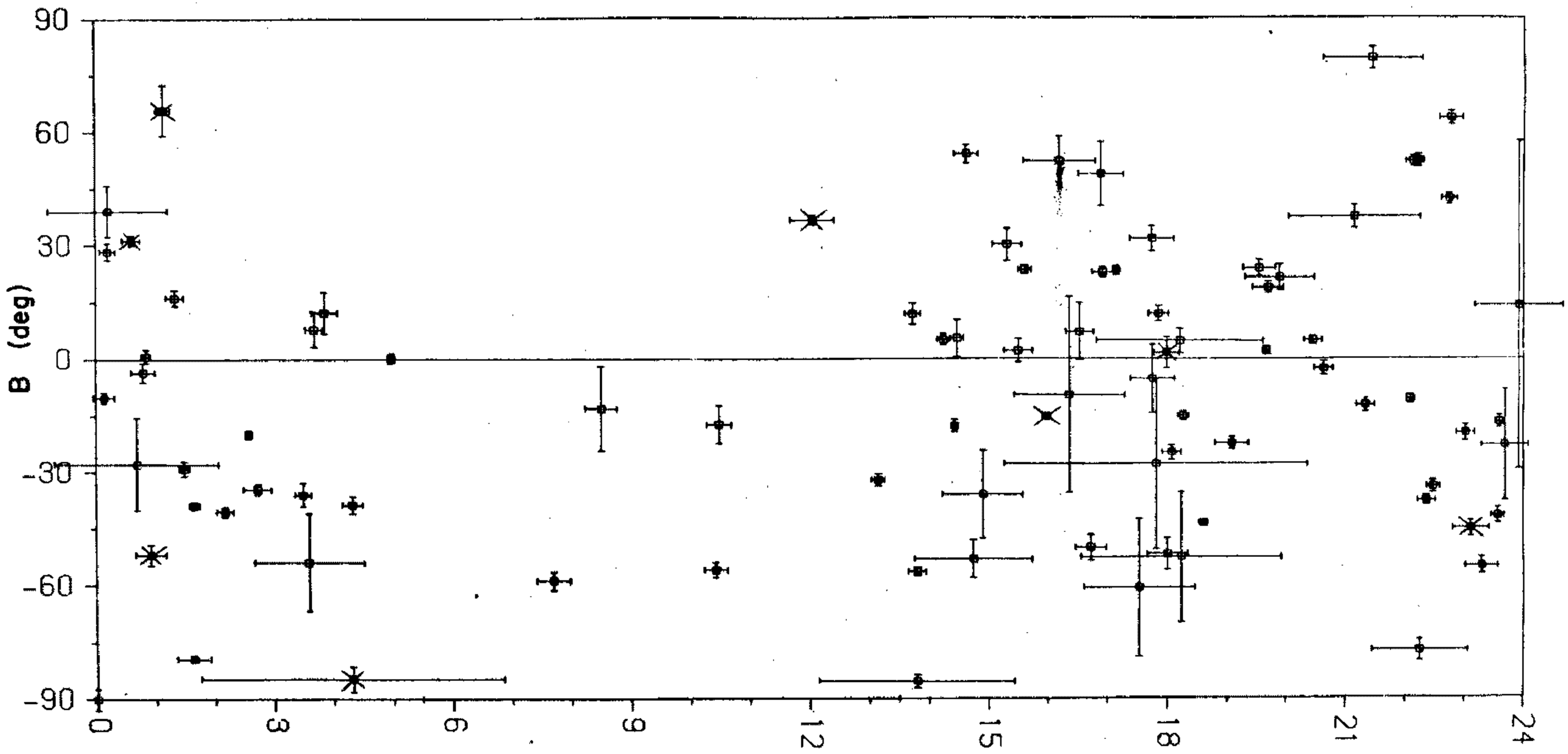

LOG MIN.ENERGY=19

EVENTS 1 TO 3503

longtitude distributions and integrating over the cell.

5.5 POSSIBLE SOURCE REGIONS.

The probability of detecting point sources of cosmic rays is very low. This is basically due to two effects. Firstly, the flux of charged particles from distant objects is *stirred up* by galactic and extra-galactic magnetic fields, and secondly, the absolute flux from any normal object would not stand out appreciably above the background cosmic radiation. Should a point source exist and be close enough not to be diffused, it would take many events for the identification of such a source to become statistically significant. This is evidenced by the random firing of about 2500 events onto a Mercator projection of the celestial sphere, where excesses of upto three standard deviations above the mean in various declination bands were produced.

Fig. 5.8 is a Mercator projection of the celestial co-ordinates of the 808 events with energy greater than 10^{18}ev, which have been recorded by the SUGAR array. An overlay, picturing objects of astrophysical interest, indicates no correlation between these objects and the arrival directions of the cosmic radiation.

It is likely that cosmic radiation is a random relativistic gas, in which case no sources will ever be

found. The following sections however, investigate several possible regions where cosmic rays, if they are produced, possibly should have been detected.

5.5.1 THE MAGELLANIC CLOUDS.

The nearest extragalactic objects to us are the large and small Magellanic Clouds. These objects, referred to as the L.M.C. and the S.M.C., are dwarf irregular systems typical of many galaxies. The diameter of the L.M.C. is 12 kpc and the diameter of the S.M.C. is 4.5 kpc. Both are situated to within 20% of 60 kpc from the centre of our galaxy. They are situated below the plane of the galaxy and close to the south celestial pole. The centroid of the S.M.C. is α = 0hr 55m, $\delta = -73^{o}$ and the centroid of the L.M.C. is α = 5hr 22m, $\delta = -69^{o}$.

Both systems, and in particular the L.M.C., appear to contain regions of ionised hydrogen, indicating the presence and formation of young stars (Robinson 1963). The radio output from each is $\sim 10^{30}$ watts which is relatively small when compared to the strong radio source Cygnus A which has a radio output of 10^{38} watts. It seems reasonable to believe that, if cosmic ray sources exist in the Magellanic Clouds, they will be typical of other sources.

Assuming that sources of cosmic radiation with energy > 10^{17}ev exist in the Magellanic Clouds, then a factor hindering our observation of the radiation, if it is charged, is the magnetic deflection of the primaries. Typical estimates of the intergalactic magnetic field strength based on radio observations, are of the order of 10^{-7} gauss. A particle of energy E ev and unit charge travelling a distance d cm in a uniform magnetic field of strength B gauss, will suffer a deflection θ radians (for small θ) given by

$$\theta = \frac{300dB}{E}$$

However magnetic fields in intergalactic and galactic space although having a fairly constant magnitude, are likely to be randomly orientated and possibly confined to various regions. Using a simple model where the magnetic field strength is constant in magnitude and restricted to regions (scattering centres) of extent d and each centre separated by 2d, a 2 - dimensional Monte-Carlo calculation of the total scattering of several primaries in transit between the Magellanic Clouds and us was made. The direction of the magnetic field at each centre was determined by selecting a random number between -1 and +1. Using a value of B = 10^{-7} gauss and assuming the scattering

centres are of width d = 1 kpc, then at each centre a 10^{18}ev proton will have a radius of curvature of 11 kpc and will suffer a deflection of 5^{o}. Firing 35 protons of energy 10^{18}ev into this system gave a total angular deviation on reaching us of 3.3^{o}. The standard deviation was 10^{o} and the average number of scatters suffered by each primary was thirty.

In order to be observable, the flux received from the Magellanic Clouds must be of the order of or greater than the background flux. The integral energy spectrum (fig. 1.2) gives an intensity of $\sim 10^{-10}$ showers m^{-2} sr^{-1} sec^{-1} for showers with energy > 10^{17}ev. For the Magellanic Clouds to produce this flux, requires an isotropic output of $\sim 3 \times 10^{29}$ watts in cosmic radiation with energy > 10^{17}ev. This energy is comparable to the radio output of either cloud.

Figure 5.19 is an equal area polar plot of the south celestial pole region below declination -60^{o}. The positions of all showers in this region with $E_p \geq 10^{17}$ev are shown. The celestial cellular plot (fig. 5.10) yields a value of 28.0 for chi-squared with 23 degrees of freedom for the declination band $\delta(-70^{o},-80^{o})$. The confidence for isotropy is 22%. The main region contributing to the value of chi-squared is the cell α(1hr,2hr) where the observed count is 10, 2.6 standard

FIGURE 5.19

Equal Area Polar Plot of the South Celestial Sky below $\delta = -60^{0}$.

All showers have $E_p \geq 10^{17}$ev.

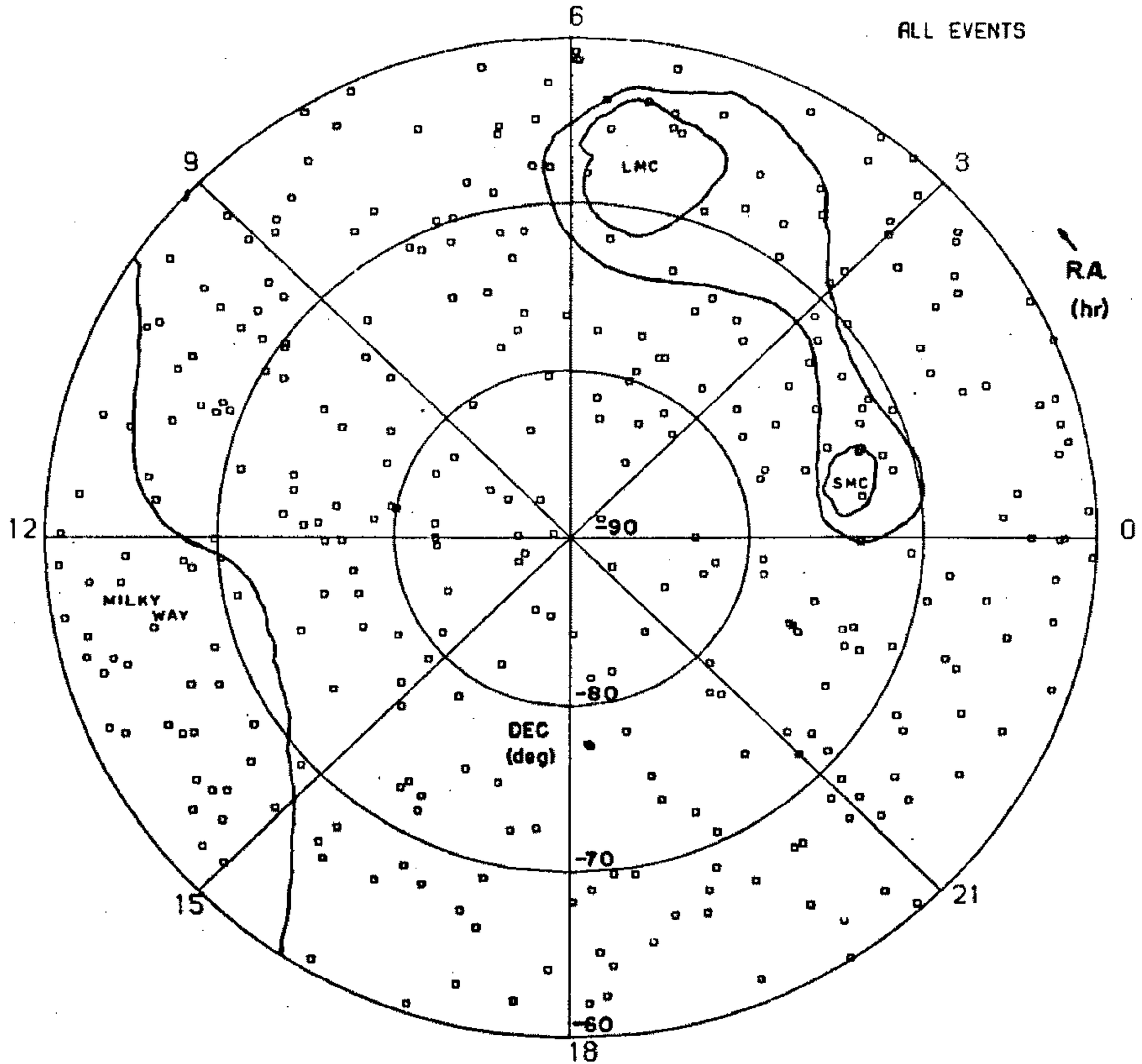
ALL EVENTS
6
9
3
12
0
15
21
18
LMC
SMC
MILKY WAY
-90
-80
-70
-60
R.A. (hr)
DEC (deg)

deviations above the mean of 4.2 The same cell for showers with $E_p \geq 10^{18}$ev (fig. 5.11) contains 6 showers, which is 3 standard deviations above the mean of 1.5. The high value of $\chi^2 = 34.7$ in this case is not reliable owing to the small expected number of showers. However combining these cells enables us to calculate a usable value of chi-squared. The combined cells (3 hr bins) in the declination band $\delta(-70^o,-80^o)$ for showers with $E_p \geq 10^{18}$ev are

R.A.(hr)	0-3	3-6	6-9	9-12	12-15	15-18	18-21	21-24
Observed	9	4	6	7	1	2	2	5

The mean of this distribution is 4.5 with a standard deviation of 2.8. There appears to be an excess of events over the regions covered by the Magellanic Clouds. However no significant anisotropy can be claimed. A chi-squared test gives a value of $\chi^2 = 12.0$ (with 7 degress of freedom) which gives a confidence for isotropy of 10%.

5.5.2 THE GALACTIC DISC.

The galaxy as we know it consists of a disc of width a few hundred parsecs and diameter 30 kpc. At the centre is a nucleus of diameter 1 to 1.5 kpc. Surrounding the galaxy there is believed to be a

spherical halo of diameter 30 kpc. The internal structure of the galaxy is made up of spiral arms, our solar system being situated in one of these spiral arms (the local arm) and is 15 pc north of the galactic plane. Radio observations of the constellation Sagittarius A have placed the galactic centre at α = 17hr 43m, $\delta = -29^{o}$. The magnetic field in the galaxy is believed to be of the order of 10^{-5} gauss and probably confined mainly to the spiral arms (Thielheim and Langhoff 1968). However some modern measurements (Smith 1968b) give a much lower value. Assuming a total energy content of cosmic rays in the galaxy of 10^{56}ergs and a cosmic ray lifetime of 10^{16}secs, requires an input of 10^{40}ergs sec^{-1} to maintain equilibrium (Ginzburg and Syrovatskii 1964).

The approximate galactic longtitude of the outward local or Orion arm is $l \sim 250^{o}$, and for the inwards direction $l \sim 70^{o}$. In celestial co-ordinates, these directions roughly correspond to α = 8hr, $\delta = -30^{o}$ and α = 20hr, $\delta = 30^{o}$.

The radius of curvature of a 10^{18}ev proton in a magnetic field of 10^{-5} gauss is 100 pc and that of an iron nucleus is 4 pc. If this value of magnetic field is representative of the magnetic field within a spiral arm, then it is conceivable that some high energy cosmic

radiation and in particular heavy nuclei, could become trapped and confined to move within the spiral arms. The cross-sectional diameter of a spiral arm also being of the order $\sim$ 100 pc (or more).

If there is a net flux of cosmic radiation along the spiral arm, possibly from the galactic centre, then we should see an enhancement in the number of showers arriving from the direction of the spiral arm as opposed to a direction at right angles to it.

As a check on this, the declination bands containing the spiral arms (fig. 5.10) were investigated. In both cases, the four cells (each 10^{o} x 15^{o} in size) in the vicinity of the arm and the direction perpendicular to it in the same declination band, were totalled and compared to the mean. In this way an area of sky 20^{o} x 30^{o} was covered at each point. In the case of the spiral outward direction, the direction perpendicular to the arm and in the same declination band, is at galactic latitude b $\sim 20^{o}$ (fig. 5.20).

The outward spiral arm is at α = 8hr and $\delta = -30^{o}$, the direction perpendicular to this for the same declination is $\alpha \sim$ 16hr. The expected number of showers in a 20^{o} x 30^{o} bin centred on $\delta = -30^{o}$ is from fig. 5.10, 57. The observed number along the outward arm is 55 and

FIGURE 5.20

A section of the local spiral arm showing the outwards direction and the direction perpendicular to this in the same declination band.

The projected area in each case is 20^{o}(dec) x 30^{o}(r.a.).

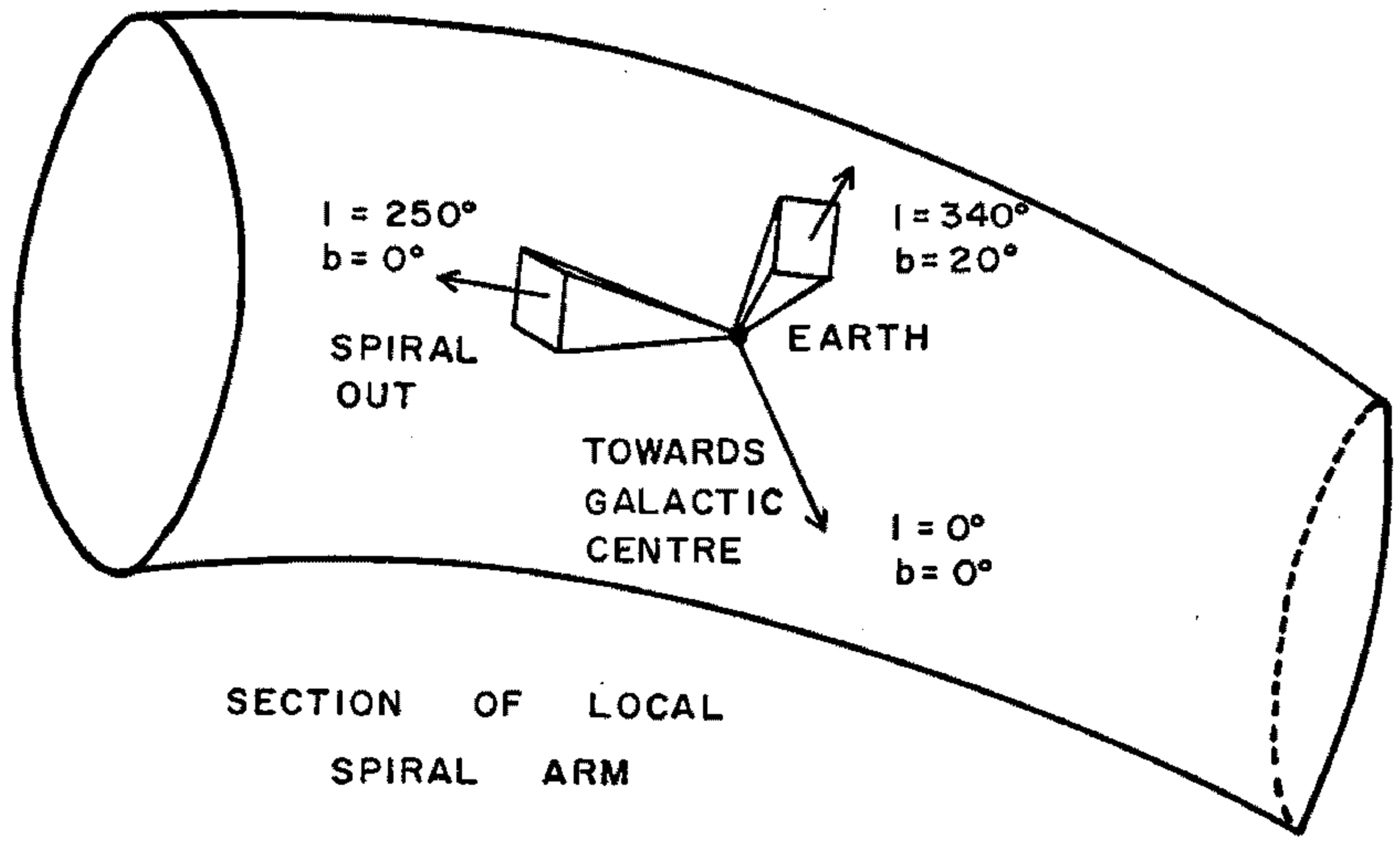

SECTION OF LOCAL
SPIRAL ARM

at right angles is 53. The inward spiral arm is at α = 20hr, $\delta = 30^{o}$ and the direction perpendicular to this for the same declination is $\alpha \sim$ 4hr. The expected number of showers in a $20^{o} \times 30^{o}$ bin centred on $\delta = 30^{o}$ once again from fig 5.10, is 10. The observed number along the inward arm is 9 and at right angles is 11.

Clearly no anisotropy exists in either case.

To further investigate the affect of the galactic plane on the right ascension distribution, the region $-40^{o} < \delta < -10^{o}$ for showers with $E_p \geq 10^{17}$ev, has been plotted separately. This strip is cut twice by the galactic plane and also contains the galactic centre.

The events have been broken into three categories, 2659 events recorded between event numbers 1 and 3503 (fig. 5.21a), 1362 events recorded between event numbers 1753 and 3503 (fig. 5.21b) and 1297 events recorded between event numbers 1 and 1752 (fig. 5.21c).

Only in the first few hundred events (fig. 5.21c) does the distribution appear to deviate from isotropy, yielding a value of 35 for a chi-squared with 23 degrees of freedom. With increasing numbers, the value of chi-squared drops to 22.0 (fig. 5.21a).

The same scan for all showers with $E_p \geq 10^{18}$ev, derived from fig. 5.11, yields a value of chi-squared (23 degrees of freedom) equal to 34, implying a 6%

FIGURE 5.21

Right ascension scan of the declination band $-40^{o} < \delta < -10^{o}$ for events with $E_p \geq 10^{17}$ev.

(a) 2659 events from serial numbers 1 to 3503.

(b) 1362 events from serial numbers 1753 to 3503.

(c) 1297 events from serial numbers 1 to 1752.

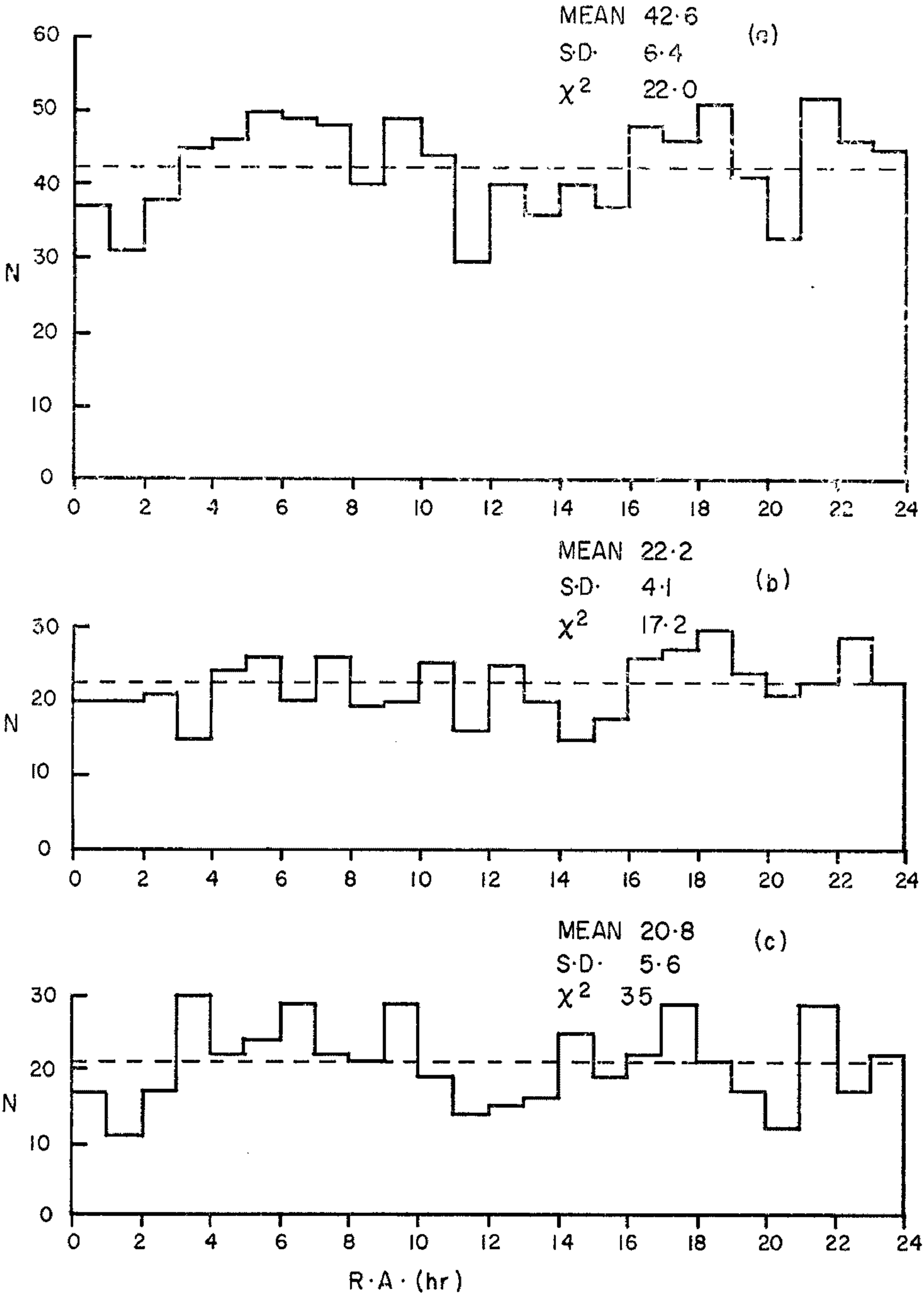
MEAN 42·6
S·D· 6·4
χ² 22·0
(a)
60
50
40
30
20
10
0
N
0 2 4 6 8 10 12 14 16 18 20 22 24
MEAN 22·2
S·D· 4·1
(b)
χ² 17·2
30
20
10
0
N
0 2 4 6 8 10 12 14 16 18 20 22 24
MEAN 20·8
S·D· 5·6
(c)
χ² 35
30
20
10
0
N
0 2 4 6 8 10 12 14 16 18 20 22 24
R·A·(hr)

confidence in isotropy.

5.5.3 PULSARS ?

As we have already seen (ref. section 1.2.2), pulsars have been proposed as a source of high energy cosmic radiation. The energy of the emitted radiation is proportional to the angular velocity of the pulsar and the charge of the emitted particles, an iron nucleus receiving 34 times more energy than a proton.

At the time of writing, 50 pulsars have been observed. The positions of these pulsars in celestial co-ordinates are shown in fig. 5.22 (and also the overlay for fig. 5.8). The distances of these pulsars, based on dispersion measurements, range from 30 pc to 2.7 kpc and their periods range from 0.033 secs to 3.745 secs. Twenty one of these pulsars are closer than 0.2 kpc, the closest being CP 0950+8 which is distant 30 pc and has a period of 0.25 secs. Twenty four pulsars have periods less than 0.5 seconds, the fastest being NP 0531+21, which is associated with the Crab Nebula and is distant $\sim$ 2 kpc. Its period is 0.033 secs.

The initial flux from the Crab pulsar, according to Gunn and Ostriker (1969) is believed to have been 3×10^{37} particles sec^{-1} following a differential spectrum of slope -2.5. If the Crab is radiating

FIGURE 5.22

A Mercator Projection of the Celestial Sphere showing the positions of 50 known pulsars.

P indicates one pulsar in the cell.

nP indicates n pulsars in the cell.

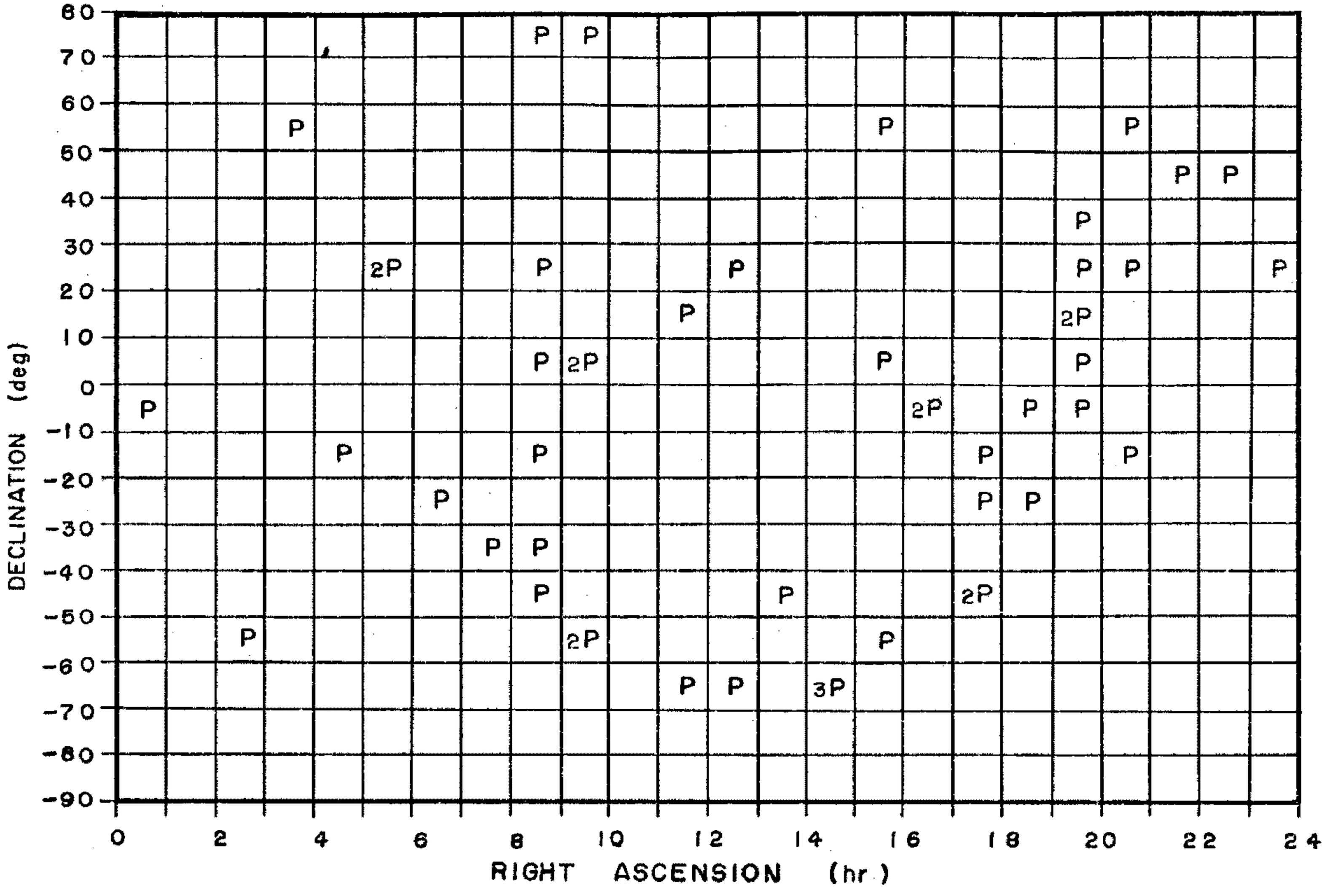
80
70
60
50
40
30
20
10
0
-10
-20
-30
-40
-50
-60
-70
-80
-90
DECLINATION (deg)
0
2
4
6
8
10
12
14
16
18
20
22
24
RIGHT ASCENSION (hr)

isotropically, then this flux of high energy particles should produce an observed intensity at our array in the direction of the Crab of 6×10^{-8} particles m^{-2} sec^{-1}.

It is possible that magnetic deflection has delayed the flux of particles. The age of the Crab is 916 years and a magnetic field of 2.5×10^{-7} gauss between us and the Crab is sufficient to delay 3×10^{17}ev protons by 940 years. The same field would delay 10^{18}ev protons by 60 years and 10^{20}ev protons by 2 days.

If the flux from the Crab is 10^{34} particles m^{-2} sec^{-1} as it would be now, 916 years after its creation, the observed intensity at our array would still be 2×10^{-11} particles m^{-2} sec^{-1}. In two years or 6.3×10^{7} sec we should have seen at least 3000 showers in the direction of the Crab, if it is producing high energy ($> 10^{17}$ev) protons and they are reaching us. This is a thousand times greater than our experimental flux.

The Crab is situated in our neighbouring spiral arm and is at right angles to us. If magnetic field lines are confined to and are parallel to the spiral arms, then the flux of particles from the Crab pulsar would suffer maximum deflection before reaching us. For an average field of 2.5×10^{-7} gauss and a proton

primary energy of 3 x 10^{17}ev, the deflection amounts to about 60^{o} and the bending is 26 times greater if the primary is an iron nucleus.

The pulsar CP 0950+8 is very close to us and in our spiral arm such that if the magnetic field is confined parallel to the arm, any particles travelling towards the Earth from this pulsar will travel parallel to the magnetic field and receive very little deflection. Even assuming an average field component of 10^{-6} gauss, a 10^{18}ev proton would only suffer a deflection of 2^{o} and a 10^{17}ev proton a deflection of 20^{o}.

The electromagnetic radiation emitted by pulsar CP 0950+8 is very strong and almost completely linearly polarised. By measuring the Faraday rotation of this radiation allowing for the affect of the ionosphere, and knowing the integrated electron density along the line of sight and the distance of the pulsar, Smith (1968a) has estimated the mean value of the galactic magnetic field in the direction of this pulsar to be less than 2 x 10^{-7} gauss. Roger and Shuter (1968) claim that Smith did not take proper account of the affect of the ionosphere on the Faraday rotation. Their revised estimate for the component of the magnetic field in the direction of CP 0950+8 is $\sim 10^{-6}$ gauss, which is still reasonably small.

Further work on Faraday rotation by Smith (1968b, private communication 1970), has reaffirmed his previous estimate for CP 0950+8 and has given estimates of the magnetic field components in the directions of two other pulsars. One, the pulsar CP 0328 is at a distance greater than 4.3 kpc, beyond both the local and Perseus spiral galactic arms. The measured magnetic field in the direction of this pulsar is 3.5×10^{-6} gauss. The other, pulsar AP 2015+28 is closer, and the magnetic field in its direction is 2.0×10^{-6} gauss. The accuracy of Smith's determinations is ± 15%.

Staelin and Reifenstein (1969) have recently reported a lower value of 2.8×10^{-6} gauss for CP 0328 and also one of 9×10^{-7} gauss for NP 0527. Faraday rotation measurements on PSR 0833-45 (the Vela pulsar) yield a value of 8×10^{-7} gauss (Radhakrishnan et al 1969, Large et al 1968) for the line of sight component of the galactic field. For the Crab pulsar NP 0532, using observations of the rotation of the polarized nebular radiation combined with the dispersion measure for the pulsar, Verschuur calculates a line of sight estimate of 5.5×10^{-7} gauss (Radhakrishnan 1969).

The value obtained for magnetic field strengths

by observing Faraday rotation, relies on a knowledge of the distance of the pulsar. In most cases this is not known exactly, however in the case of the Crab pulsar and the Vela pulsar, the distance is well known.

An average value for the galactic magnetic field, within a few kiloparsecs of us and based on Faraday rotation of the polarised radiation from pulsars, is $\sim 1.2 \times 10^{-6}$ gauss.

If all primaries above 10^{18}ev are protons and are produced by pulsars, two conclusions can be drawn. If we can assume that the galactic magnetic field is $\sim 10^{-6}$ gauss, then cosmic rays from the pulsar CP 0950+8 should reach us virtually undeflected and with an intensity of the order of a thousand times what we do observe. If however, the protons of energy $> 10^{18}$ev are produced only within a short time after creation of a pulsar, then the magnetic field of the galaxy would not be able to contain them for a long period of time and we would thus not expect to observe the flux we do.

On the other hand, if primaries above 10^{18}ev are iron nuclei or heavier, then it is conceivable (depending on galactic magnetic fields) that they can be trapped and produce an isotropic direction distribution.

The slope of the integral energy spectrum is -1.5 if we assume the theory of Gunn and Ostriker (1969).

Based on the luminosity distribution and the local density of pulsars, one can estimate that there are at least 10^6 pulsars in the galaxy. To maintain the present energy density of cosmic rays in the galaxy then requires an average output of 10^{34} ergs/pulsar/sec, well within the range of the Gunn and Ostriker model.

Owing to the fact that a pulsar probably radiates electromagnetic energy into a cone of width $\sim 20^{\circ}$, we would expect that the pulsars we see (in the radio spectrum) would amount to less than a hundredth of the total number of local pulsars. Although we cannot see all pulsars, it is likely that their particle radiation would become well stirred up by galactic magnetic fields. With this increased number estimate, we require less than 10^{32} ergs/pulsar/sec to be radiated to maintain equilibrium of the cosmic ray energy density in the galaxy.

5.5.4 OTHER REGIONS.

In the hope of identifying source regions of cosmic rays other than those already considered, the cellular divisions of events in both celestial and galactic co-ordinates have been scanned. In the

following section, two interesting regions are considered.

(a) The region α(8hr,10hr), $\delta(-10^{o},10^{o})$.

This region of the sky contains three pulsars. One already mentioned is CP 0950+8, the other two are CP 0834+6 and PP 0943+8. The latter two pulsars are distant 130 pc and 175 pc respectively and have periods 1.3 secs and 1.1 secs respectively.

The observed number of showers n_o, the expected number n_e and the number of standard deviations from the mean for the cell α(8hr,10hr), $\delta(-10^{o},10^{o})$ are shown in table 5.5 for two energy ranges, $E_p \geq 10^{17}$ev and $E_p \geq 10^{18}$ev. Table 5.6 is the same data, but grouped differently. The cell in this case is α(8.8hr,9.6hr), $\delta(-7.5^{o},7.5^{o})$ and the results are shown only out of interest, no conclusions can be fairly drawn from results derived by rearranging data. The rearrangement was not made to improve the statistics of the results, but forms another mode of analysis not mentioned here.

TABLE 5.5

$\alpha(8hr,10hr)$, $\delta(-10^{o},10^{o})$

$E_p \geq 10^{17}ev$

Number of Events	1328				2659			
	n_o	n_e	n_o/n_e	N	n_o	n_e	n_o/n_e	N
	33	22.4	1.47	2.9	59	43.8	1.34	2.4

$E_p \geq 10^{18}ev$

Number of Events	808			
	n_o	n_e	n_o/n_e	N
	18	11	1.64	1.9

TABLE 5.6

$\alpha(8.8hr,9.6hr)$, $\delta(-7.5^{o},7.5^{o})$

$E_p \geq 10^{17}ev$

Number of Events	1328				2659			
	n_o	n_e	n_o/n_e	N	n_o	n_e	n_o/n_e	N
	15	6.4	2.35	3.4	29	12.8	2.26	4.5

$E_p \geq 10^{18}$ev

Number of Events	808			
	n_o	n_e	n_o/n_e	N
	10	3.9	2.56	3.1

This region when converted to galactic co-ordinates appears quite interesting. The galactic cell l(15hr,20hr), b(0^o,30^o) for showers with $E_p \geq 10^{17}$ev (fig. 5.17) overlaps the transformed region, and contains some large fluctuations from the mean.

The latitude band b(10^o,20^o) has an excess of twice the mean number of showers for l(17hr,18hr) and an excess of 1.8 times the mean for l(19hr,20hr). A chi-squared test on this band using only cells where the expected number of showers is greater than 5, yields a value of $\chi^2 = 41.9$ with fifteen degrees of freedom. The corresponding confidence for isotropy is 0.02%.

A chi-squared test on the fifteen 1 hr x 10^o cells contained within l(15hr,20hr), b(0^o,30^o) yields a value of $\chi^2 = 48.6$ for fourteen degrees of freedom, corresponding to a confidence for isotropy

of 0.001%. A random selection of fifteen other cells in a 5 hr x 30^{o} bin gives a value of $\chi^2 = 14.4$.

No significant optical or radio sources other than the already mentioned pulsars exist anywhere near this area. The significance of a chi-squared test on the relatively small number of showers may be suspect and before any anisotropy can be claimed, we would need to observe the same effect in as many showers again.

(b) The region $\alpha(3hr,4hr)$, $\delta(30^{o},40^{o})$

This region is just within our limit of observation. The expected number of showers with energy $\geq 10^{17}$ev, in this cell is 1.3 and the standard deviation is 0.4 (fig. 5.12), however 6 showers have been observed. The numbers involved are too small to do a chi-squared test on this declination band, however assuming Poisson fluctuations in each cell, the probability of observing six or more events while expecting 1.3 is easily calculated to be 0.002. Table 5.7 lists the parameters of the six showers.

The zenith angles of these events are all high due to the large declination. The showers all have relatively low energy except event 1638, which owing to its larger than normal zenith angle, is more than likely

an overestimate (the energy conversion is only valid for $\theta < 75^{o}$).

TABLE 5.7

Event	E_p(ev)	θ^{o}	R.A.(hr)	Dec(deg)
232	2.0×10^{17}	64	3.7±0.4	31.6± 4.8
1638	4.2×10^{19}	81	3.5±0.3	34.3± 4.1
1908	2.6×10^{17}	68	3.9±0.6	33.5±13.4
2089	1.5×10^{18}	66	3.6±0.2	32.5± 5.2
2478	2.4×10^{17}	67	3.3±0.3	36.2±10.9
3073	5.0×10^{17}	68	3.9±0.5	34.4±12.7

If in the directional analysis we include showers which would normally have not been used because the numbers of particles recorded by one or more stations were not sufficient to provide accurate timing (ref. section 4.10), then altogether in this cell we have eight showers. This number together with a mean of 1.5 corresponds to a Poisson probability of 2×10^{-4}.

If this region is a source of cosmic radiation, it should have been observed by other large arrays, such as the Haverah Park array in the Northern hemisphere. The fact that it has not points to it being a

statistical fluctuation of 3.4 standard deviations. Doubling the number of events will probably verify this.

5.6 CONCLUSION.

The results of two years observation of the southern sky have shown no definite trend towards anisotropy for cosmic rays with energy $\geq 10^{17}$ev. The absence of any significant clustering of events for any energy range, in particular for primaries with energy $>10^{20}$ev, make the chances of ever finding a point source of cosmic radiation very small.

The absence of a cutoff of the cosmic ray primary energy spectrum at 5×10^{19}ev indicates that if blackbody photons are universally abundant, then the sources of cosmic radiation may exist within 10 Mpc. The strong radio galaxy, Centaurus A which is 5 Mpc distant and has a radio output of 10^{35} watts, is a good candidate for the production of cosmic rays by a *quark-fusion* process (Bahcall et al 1970). Stirring up and further acceleration of ejected particles by a large scale Fermi process (Burbidge and Hoyle 1964) within the local supercluster is also possible.

If the blackbody radiation is not universal then objects like Fornax A ($d \sim 17$ Mpc, $P \sim 10^{35}$ watts),

Hercules A (d∿470 Mpc, P∿10^{37} watts), Cygnus A (d∿190 Mpc, P∿10^{38} watts) and the quasars (d>400 Mpc, P∿10^{39} watts) are also likely cosmic ray sources. In all cases, due to the distances involved, an isotropic arrival direction distribution would be expected.

Further observation in the region of the Magellanic Clouds may, although unlikely, reveal them as a source of cosmic radiation. However, with our present event rate many years of observation would be needed to supply adequate statistics. Increasing the number of stations in our quarter mile array is needed to increase our shower detection rate.

No direct correlation of cosmic rays with pulsars has been observed, contrary to what would be expected if they were producing very energetic protons. Present theories regarding cosmic ray acceleration by pulsars are at the moment very crude and little weight can be given to conclusions drawn from them. However, if one assumes a Gunn and Ostriker type theory and also assumes that all primaries above 10^{18}ev are iron nuclei or heavier and that galactic magnetic field strengths are of the order of 10^{-6} - 10^{-5} gauss, then pulsars can explain the observed flux of isotropic radiation. This taken together with the absence of a blackbody cutoff and the possible absence of an *ankle* in the energy

spectrum, makes the idea of a local uniform source of cosmic radiation tenable.

It is possible that our latest observed energy spectrum, corresponds to the region above the *ankle*, which may occur at a lower energy than expected and thus be on the threshold of the SUGAR array's detection capability. If this is the case, the primaries we observe above this ankle, may still represent a *metagalactic* flux of protons, as suggested by Linsley and Scarsi (1962).

An increase in the sensitivity of the SUGAR array to small showers ($E_p < 10^{17}$ev) and a comparative measure of the μ/e ratio, above and below the ankle, is required to elucidate the problem of primary composition.

CHAPTER 6

THE CURVATURE OF THE MUON SHOWER FRONT.

6.1 INTRODUCTION.

At each nuclear interaction as the primary particle descends through the atmosphere, secondary particles are emitted at small angles (determined by their transverse and longtitudinal momenta) to the core. It is this effect coupled with the straggling of low energy particles, that predominantly defines the curvature of the muon shower front.

The curvature of a muon shower front has been determined as a by-product of the means of refining the accuracy of arrival direction measurements. A simple plane fit does not take into account the position of the core. In this way, if the core is near the edge of the array and we only see one side of the shower, a fitted plane would not correspond to the *tangent plane* (i.e. the plane which is, at the core, tangent to the shower front produced by particles which have travelled furthest in the forward direction). The resulting arrival direction would then be in error by an amount determined by the delay of the shower front with respect to its tangent plane.

There are some showers which may be double cored (Brownlee et al 1969e), and are classed as *peculiar* showers. It is difficult to distinguish these events

from those that are due to large statistical fluctuations in the stations' responses.

By investigating muon shower front curvatures, it may be possible to gain some knowledge regarding the heights of primary interactions and the longtitudinal development of E.A.S.

Except in events with a favourable geometry and in which many stations have been triggered, little information regarding curvature can be gained from individual determinations. This is due to the moderately large intrinsic error in curvature determination, posed by detector timing limitations. What has been investigated in the following sections is the variation amongst groupings of many individual curvature measurements with respect to zenith angle and muon number.

6.2 Time Delayed Particles in E.A.S.

Early attempts to investigate arrival time differences for shower particles, yielded only upper limits for particle delays, independent of distance from the core. Using G-M detectors, McCusker et al (1950) found no particles delayed by more than 1.5 μsec. Mezzetti et al (1951) found penetrating particles with delays upto 1.2 μsec, the average delay being less than

0.5 μsec. The delay between shielded particles and particles able to penetrate 10 cm of lead was found by Officer (1951) to be about 20 nsec.

Jelley and Whitehouse (1953), using a liquid scintillation counter showed that ∿ 0.85% of shower particles were delayed by 30 - 700 nsec. The distribution having the form of an exponential function, with half of the delayed particles occuring within 100 ± 20 nsec. Using Geiger counters with fast reaction times and shielded by at least 15 cm of lead, Officer and Ecceles (1954) observed penetrating particles in air showers, delayed by more than 50 nsecs. These two experiments also attempted no core location.

Using three scintillation counters to provide fast timing measurements of the shower front, Bassi, Clark and Rossi (1953) were able to estimate the thickness of both the electromagnetic front and, by shielding one detector, the muon front. Their results showed that the muon component arrives in a disc 2m to 3m thick and delayed 3m behind the electromagnetic component, which forms a thinner disc of 1m to 2m. The results of Sugarman and DeBenedetti (1956), and a Monte Carlo calculation on the electromagnetic component of the shower front by Locci et al (1967), are in agreement with the above results. Typical energies

under consideration were of the order of 10^{15}ev, and the core distances involved were $\sim$ 30m.

Measurements made at large core distances ($\sim$ 500m) by the Cornell group (Bennett et al 1962), indicated that the shower front is not planar but has a positive curvature. Averaged over about 1000 showers of average size 3×10^7 particles, they obtained a mean radius of 2.8 km for the electron shower front.

Linsley and Scarsi (1962a), using the large M.I.T. Volcano Ranch array (1.8 km above sea level), were able to measure delayed particles at distances upto 1500m from the core. By measuring the delays of single particles with respect to the tangent plane defined at the core of the shower, they estimated that for muons, the height of origin is constant and corresponds to 320 ± 70 g cm^{-2} or $\sim$ 7 km.

Blake and Harris (1969) using a shielded liquid scintillator of area 10 m^2, have demonstrated the existence of delayed muons of energy greater than 1Gev in air showers of energy $\sim 10^{17}$ev. At core distances of 200m to 500m they obtained muons delayed by more than 100 nsecs. This they attribute to a path difference between the prompt and the delayed muons and not to velocity differences.

Using large area (34 m^2) water filled Cerenkov detectors, the Haverah Park 500m array has measured the radii of curvature for showers of energy $\sim 10^{17}$ev (Suri 1965, Tennent 1968). Divided into three zenith angle ranges, the mean curvatures are 0.25 km^{-1} for vertical showers, 0.2 km^{-1} for showers at 50^{o} and 0.13 km^{-1} for showers at $\theta > 60^{o}$. The distributions tend to broaden with increasing zenith angle. The standard deviation in their measurement of curvature is $\sim$ 0.08 km^{-1}. Owing to the large detector area, it is likely that the Haverah Park curvatures correspond to the *extreme front* of an air shower.

Also at Haverah Park, Baxter (1969) has determined the arrival time distributions for muons at two core distances. This he obtains, by subtracting the electron-photon component (based on a Monte Carlo calculation) from their experimental time delay distributions. By comparing his results with respect to a plane front, he is able to determine the delay of the first detected signal and the median delay of muons, at a given distance from the core. The form of the arrival time distribution is a negative exponential, with a tail extending out to at least 600 nsec. Table 6.1 lists his results.

TABLE 6.1

Core Distance	400m	600m
Delay of first signal (nsec)	45±12	90±40
Median muon delay (nsec)	67^{+14}_{-12}	126^{+66}_{-43}
Height of production (km)	$4.0^{+0.9}_{-0.7}$	$4.7^{+2.5}_{-1.6}$
Atmospheric depth (g cm^{-2})	650^{+50}_{-80}	580^{+140}_{-170}

The SUGAR array and the Haverah Park array are at approximately the same elevation (280m and 230m respectively). The area of a SUGAR detector is 6 m^2 and only the muon component is observed. Curvature determination is based on observations at 400m to 1000m from the core. It therefore appears reasonable to expect a correlation between the SUGAR and Haverah Park results.

Early results of the SUGAR array (Brownlee et al 1969d) indicate that such a correlation exists. However for small vertical showers, an apparent discrepancy exists. This effect is discussed in section 6.6.

6.3 CURVATURE ANALYSIS.

The determination of individual curvatures is

accomplished by a least squares method and has been shown elsewhere (appendix chapter 2, Parkinson 1969). The basic assumption of the method is that the muons originate from a point and travel radially with a velocity of 0.299m nsec^{-1}.

The error in each measurement has been based on an earlier timing standard deviation of 68 nsecs, and is also a function of array geometry and the number of triggered stations for that event. The latter two parameters vary for each event. About 25% of events trigger 4 or more stations while about 2% trigger 6 or more stations.

In order to form curvature distributions and hence determine an average curvature, it is necessary to give more *weight* to a well determined measurement than to a less well determined measurement. On the assumption that curvature is a normal variable each event is given a weight w_i, which is inversely proportional to the estimated variance of that event (Guest 1961).

$$w_i \propto \sigma_i^{-2} \qquad \sigma_i = \frac{68}{\sqrt{N}} f(G)$$

N is the number of triggered stations and f(G) is a geometrical factor obtained from the least squares analysis. The weight increases slowly with N. For

large area events f(G) is very small and for events tending towards being collinear, f(G) is large.

A SUGAR station registers the time of an event only for those events which produce the equivalent of three or more vertical particles in a tank. However, in such an event, the photomultiplier pulse and hence the timing, is iniated by the first particle to strike the scintillator. The total photomultiplier pulse is the integrated sum of all particles in the tank (integration time = 3 μsec).

For large particle densities in a tank, the timing will almost certainly always be with respect to the extreme front of the shower disc. In the case of tanks with low particle densities, the timing will often be with respect to a delayed particle in the air shower. Hence in these cases and averaged over many events, our measured curvature would correspond to delayed particles and not to the extreme front.

6.4 THE ERROR IN CURVATURE ESTIMATION.

The simulated showers referred to in section 4.16, provide an excellent means of testing the method of curvature analysis and of estimating the spreads in individual curvature measurements.

Each simulated shower is in fact a plane front

and the simulated timing responses generated when it triggers the array, correspond accordingly. Each response is allowed to vary plus or minus an amount determined by randomly selecting a timing error from a normal distribution with a mean 68 nsec. In this way a fitted curvature should ideally have mean zero and an error proportional to the actual array instrumental error.

An investigation of the spread of curvature measurements amongst a sample of simulated showers has been carried out, and the results are presented. Even though the affect of station dead time is used in the production of simulated responses, the proportion of large multiplicity events is considerably greater than in their real counterpart. This is due to the fact that stations in the actual array are often off the air because they have electronic faults or flat batteries. Out of 592 simulated showers, 315 or 53% had multiplicity $\geq$ 4 and 100 or 17% had multiplicity $\geq$ 6.

Figure 6.1 represents the weighted and unweighted distributions for the curvatures of simulated events. The events are grouped into three zenith angle ranges independent of muon number. The parameters of each distribution are listed in table 6.2 below. Also

FIGURE 6.1

Zenith angle groupings of the curvature distributions of simulated plane showers which have inherent timing fluctuations.

SIMULATED EVENTS (σ_t = 68 n secs)

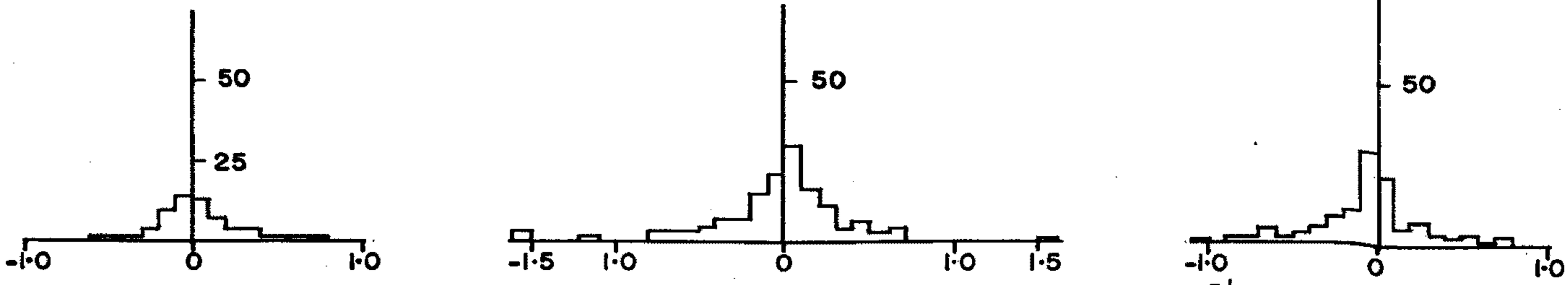

UNWEIGHTED DISTRIBUTIONS (CURVATURE Km^{-1})

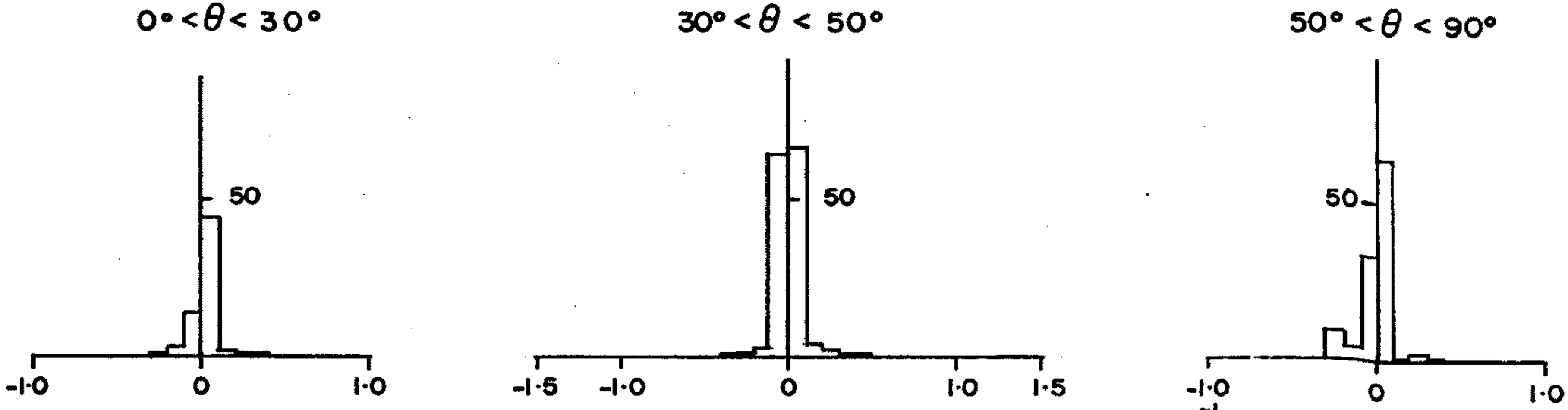

WEIGHTED DISTRIBUTIONS (CURVATURE Km^{-1})

listed are the parameters for the distribution of all simulated events over all zenith angles, as depicted in fig. 6.2.

TABLE 6.2

Zenith	No. of Events	Unweighted Curvature(km^{-1})	Weighted Curvature(km^{-1})
0^{o}-30^{o}	65	0.031±0.029	-0.002±0.010
30^{o}-50^{o}	139	-0.025±0.035	-0.002±0.006
50^{o}-90^{o}	111	-0.053±0.030	-0.026±0.008
0^{o}-90^{o}	315	-0.024±0.020	-0.012±0.005

The effect of weighting is particularly evident (fig. 6.2) when all events are considered together. As would be expected the distributions have means approximately zero and are normal in shape. The errors of the means are significantly reduced by weighting each event.

If σ_s is the standard deviation of the mean of the distribution of n events, each of which has standard deviation σ, then this standard deviation of each measurement is given by

$$\sigma = \sqrt{n}\ \sigma_s$$

To estimate σ, the unweighted distribution of

FIGURE 6.2

The distribution of curvature of all simulated plane showers which have inherent timing fluctuations.

ALL SIMULATED EVENTS

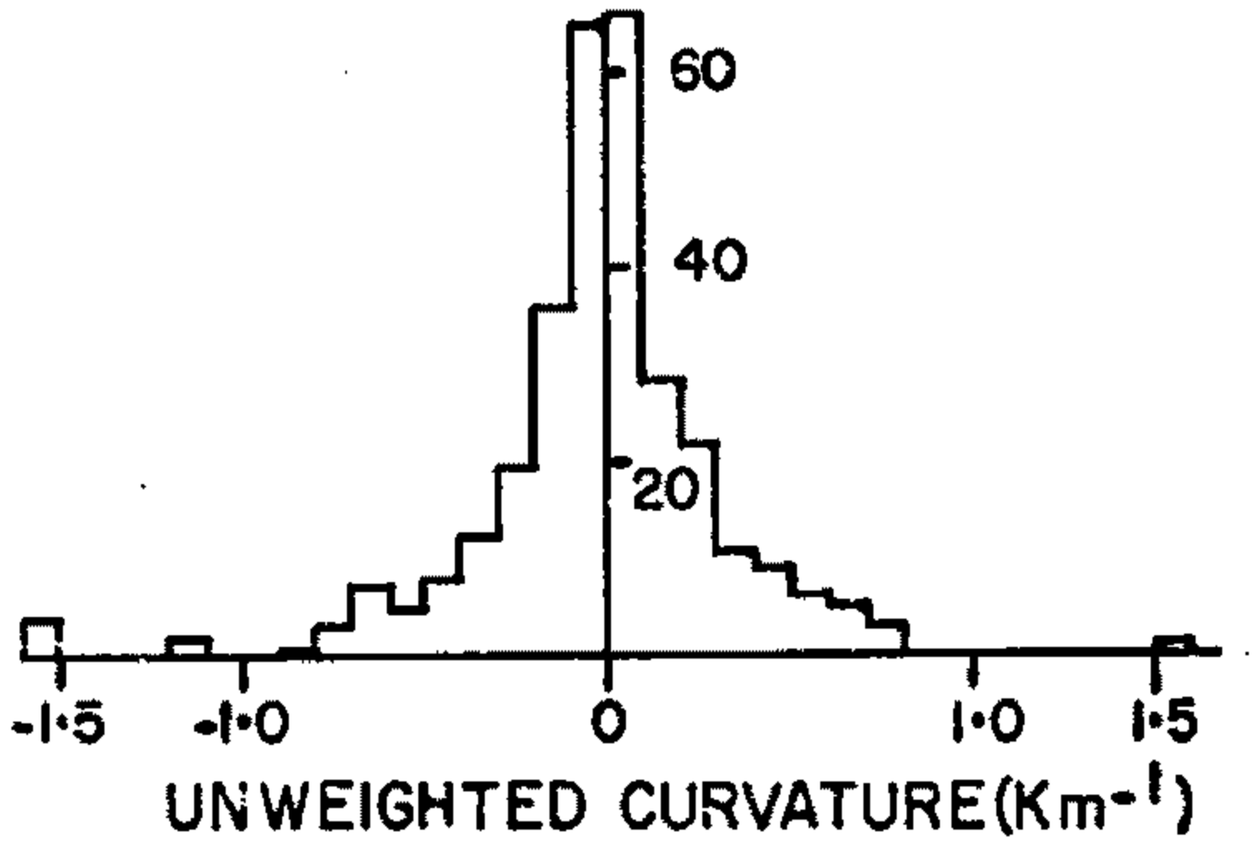

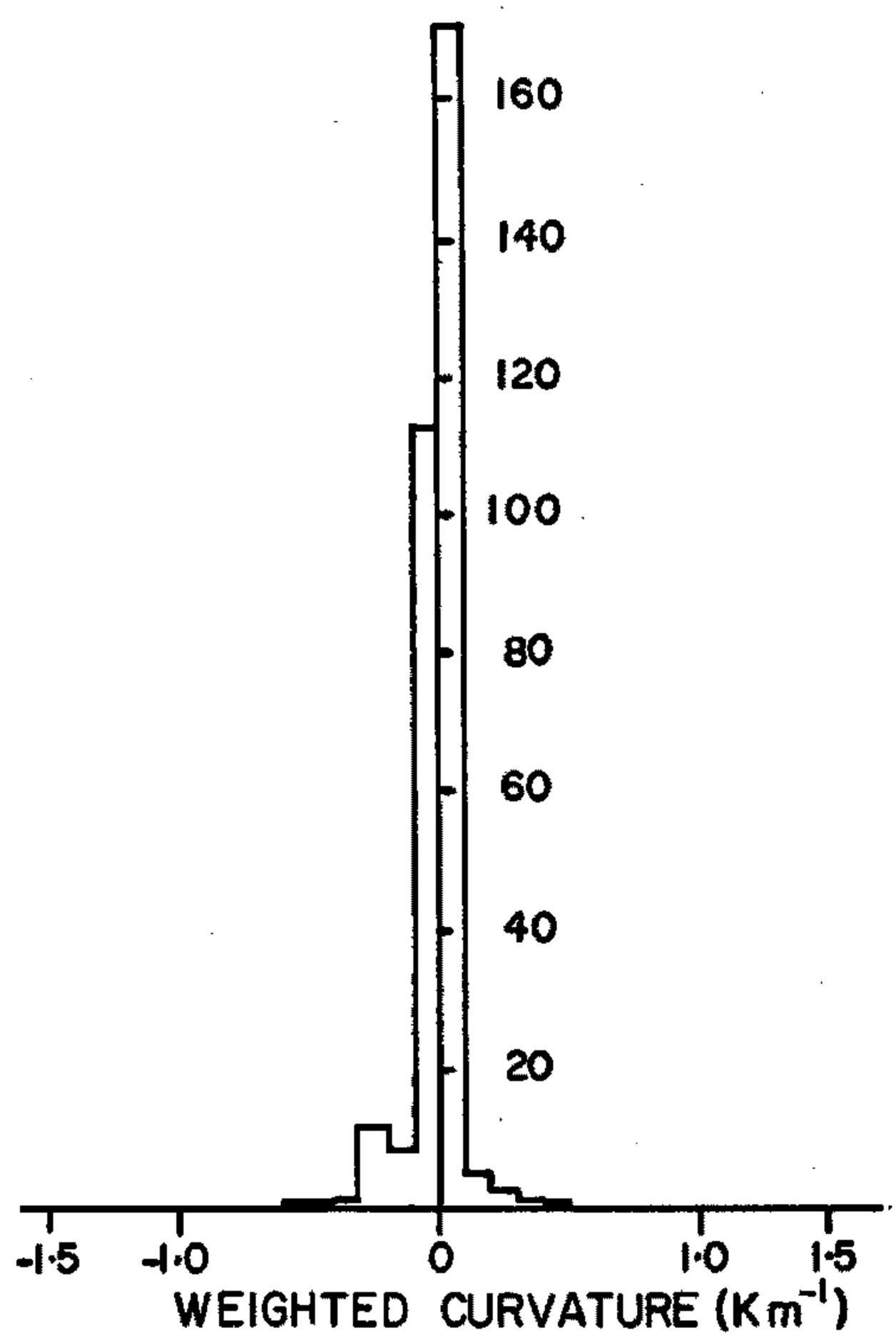

the total of 315 events is used, this then implies that, based on a timing standard deviation of 68 nsec, the standard deviation in the estimation of curvature is $\sim 0.35\ km^{-1}$.

6.5 GROUPED CURVATURE DISTRIBUTIONS.

A total of 723 events with multiplicity ≥ 4 have been used to estimate the curvature of the muon shower front. These events have been grouped with respect to both muon number and zenith angle. Three zenith angle ranges have been considered and in each zenith angle range, five muon number ranges have been used. Figures 6.3 to 6.5 inclusive depict these distributions, both for weighted and unweighted events. The weighted distributions have been normalised to the same number of events as the unweighted distributions. The parameters of the respective distributions are shown in tables 6.3 to 6.5 inclusive and are accompanying the diagrams.

The effect of *weighting* is apparent, the means of the weighted and unweighted distributions agreeing well to within their range of error. As in the simulated distributions (section 6.4) the spread in the weighted means is less than the spread in the unweighted means.

FIGURE 6.3

Unweighted (top row) and weighted (bottom row) curvature distributions of 206 events with zenith angles $0^{o} < \theta < 30^{o}$.

Units of curvature are km^{-1}.

TABLE 6.3

N_μ	No. of Events	Unweighted Curv. (km^{-1})	Weighted Curv. (km^{-1})
$N_\mu < 4\times10^6$	31	0.403±0.070	0.387±0.068
$4\times10^6 < N_\mu < 8\times10^6$	67	0.289±0.041	0.279±0.041
$8\times10^6 < N_\mu < 1.3\times10^7$	45	0.260±0.046	0.240±0.039
$1.3\times10^7 < N_\mu < 4\times10^7$	49	0.222±0.035	0.244±0.029
$N_\mu > 4\times10^7$	14	0.267±0.044	0.209±0.017

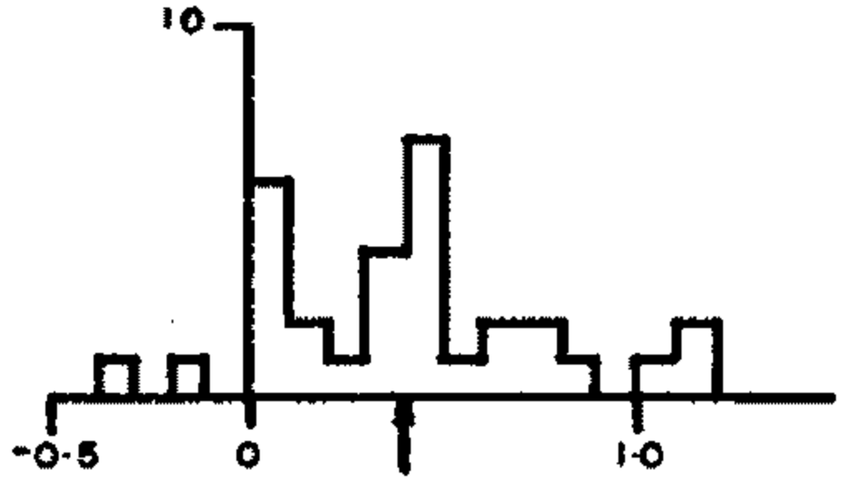
10
-0·5
0
1·0

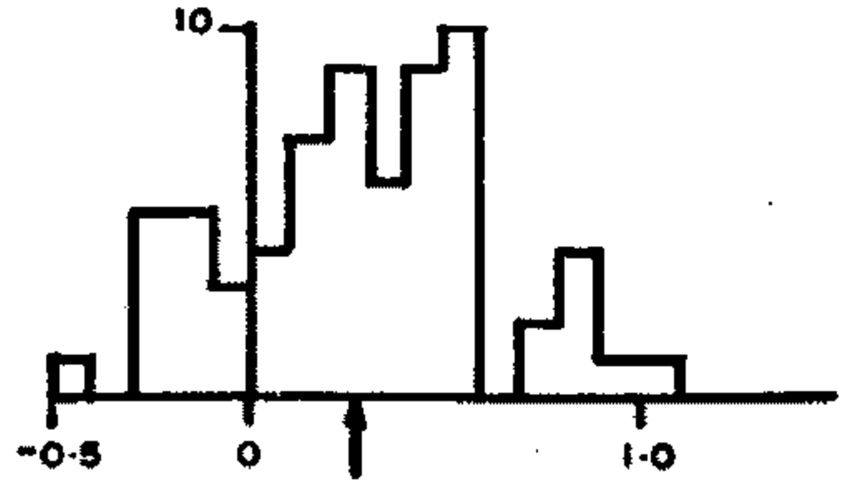
10
-0·5
0
1·0

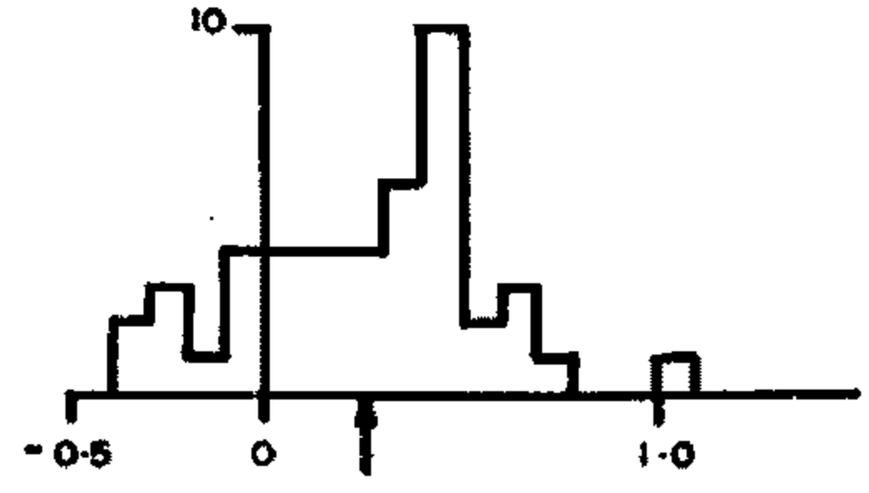
10
-0·5
0
1·0

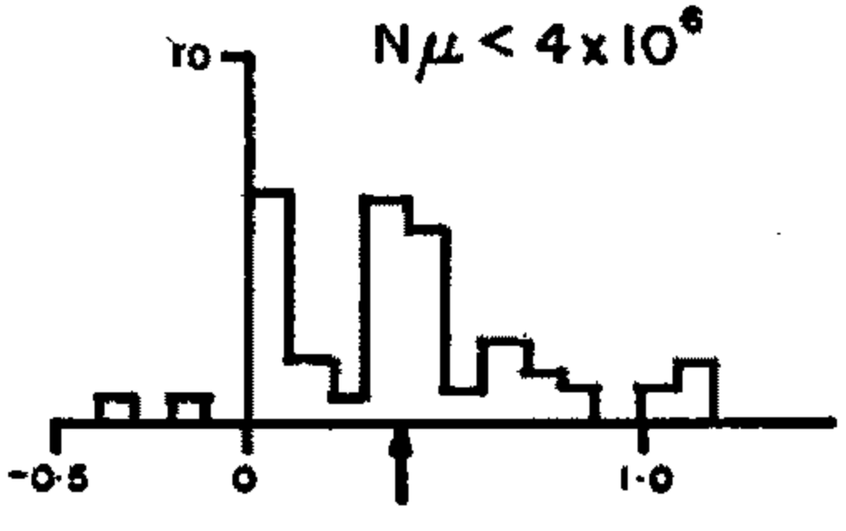
Nμ < 4x10⁶
10
-0·5
0
1·0

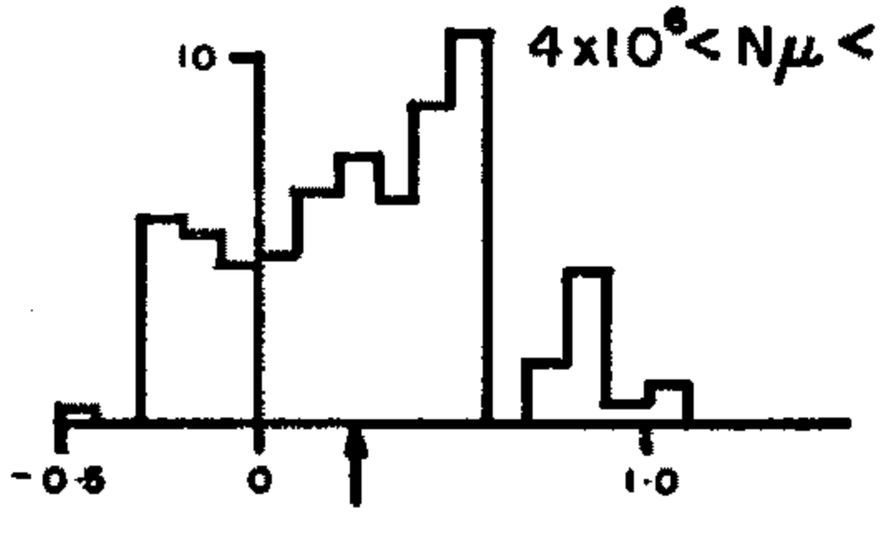
4x10⁶< Nμ <8x10⁶
10
-0·5
0
1·0

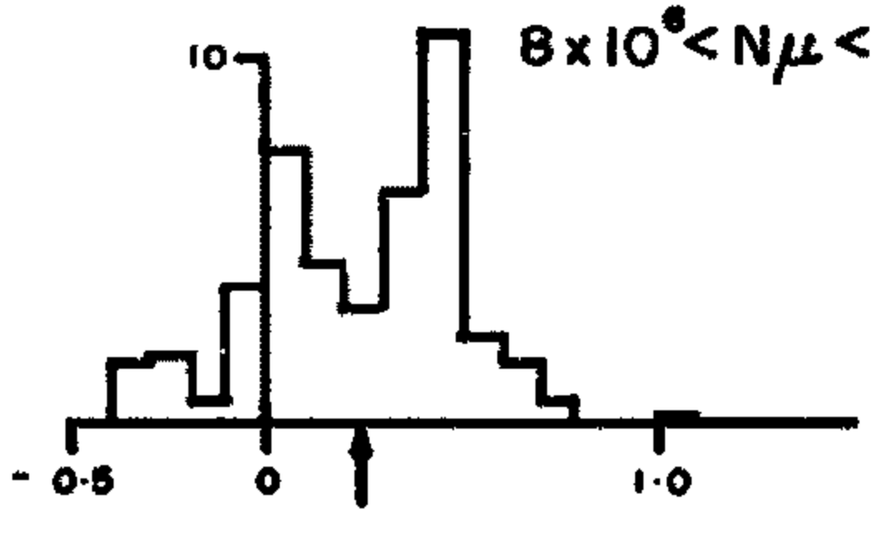
8x10⁶< Nμ <1·3x10⁷
10
-0·5
0
1·0

ZENITH 0° — 30°

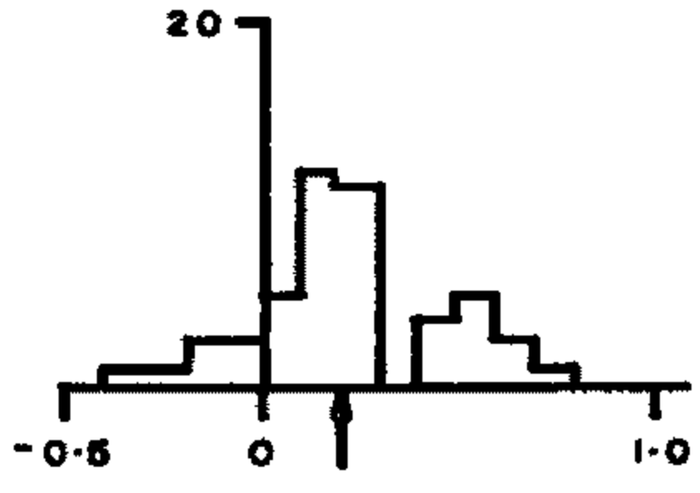
20
-0·5
0
1·0

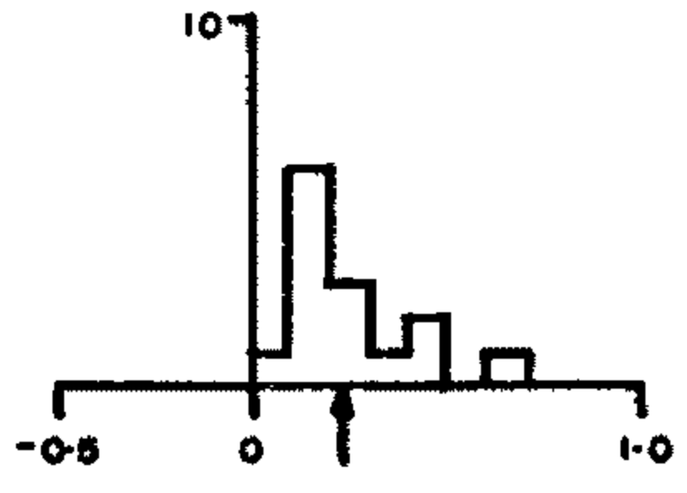
10
-0·5
0
1·0

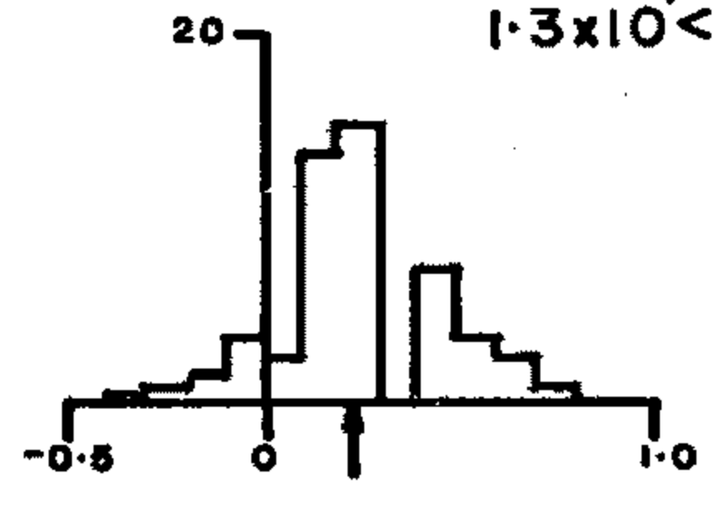
1·3x10⁷<Nμ<4x10⁷
20
-0·5
0
1·0

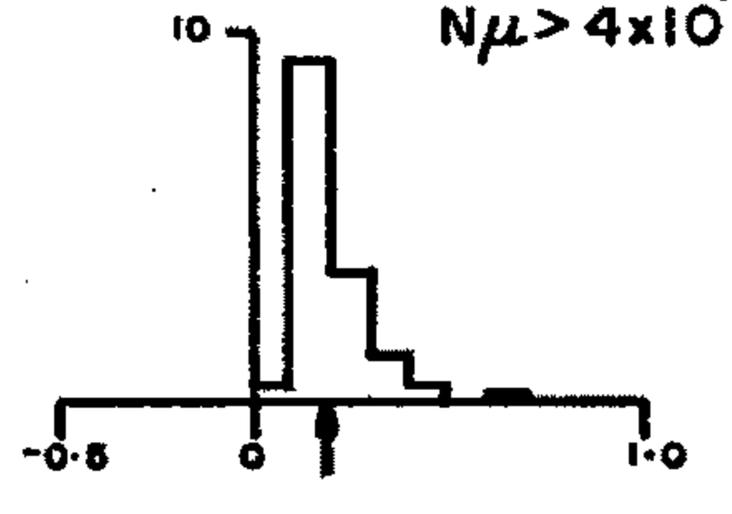
Nμ>4x10⁷
10
-0·5
0
1·0

FIGURE 6.4

Unweighted (top row) and weighted (bottom row) curvature distributions of 289 events with zenith angles $30^{0} < \theta < 50^{0}$.

Units of curvature are km^{-1}.

TABLE 6.4

N_μ	No. of Events	Unweighted Curv. (km^{-1})	Weighted Curv. (km^{-1})
$N_\mu < 4\times10^6$	101	0.162±0.049	0.223±0.042
$4\times10^6 < N_\mu < 8\times10^6$	82	0.159±0.037	0.204±0.032
$8\times10^6 < N_\mu < 1.3\times10^7$	44	0.156±0.060	0.177±0.031
$1.3\times10^7 < N_\mu < 4\times10^7$	44	0.193±0.038	0.179±0.029
$N_\mu > 4\times10^7$	18	0.207±0.035	0.143±0.016

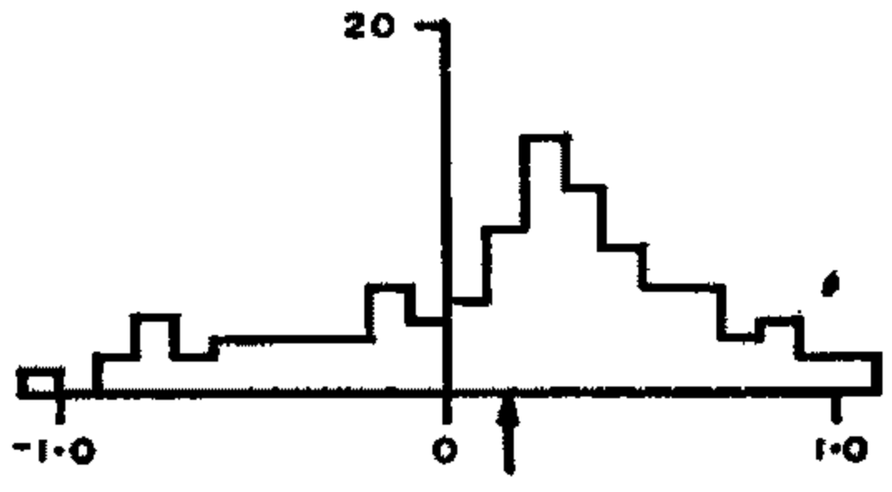

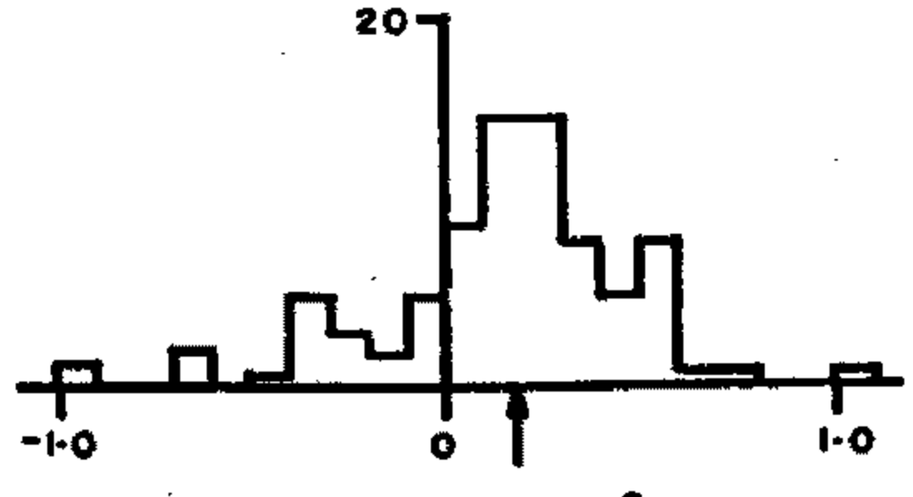

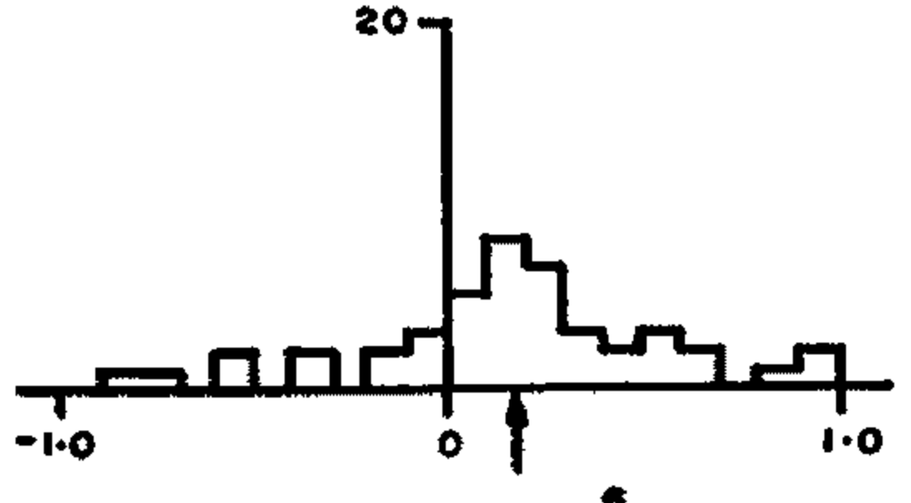

$N\mu < 4 \times 10^6$

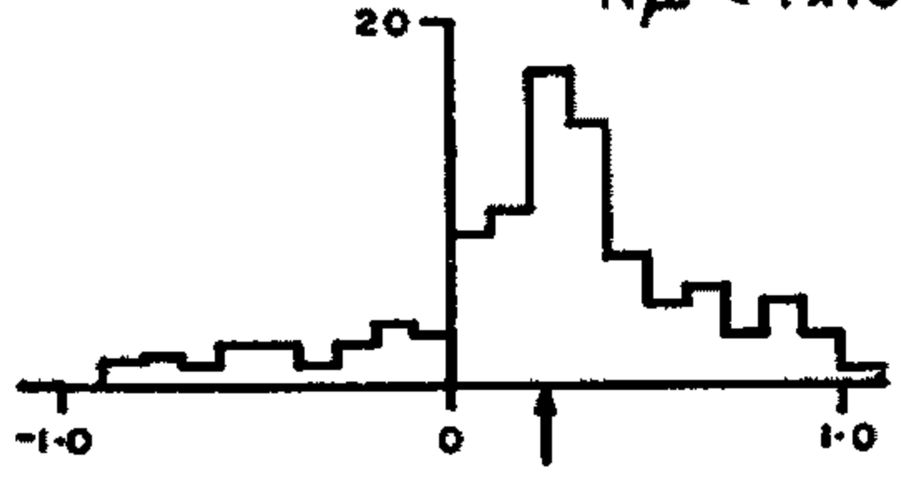

$4 \times 10^6 < N\mu < 8 \times 10^6$

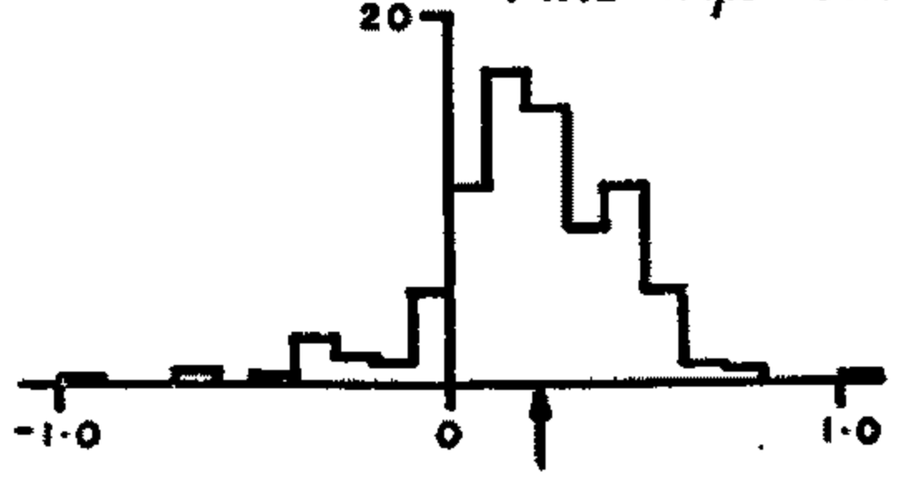

$8 \times 10^6 < N\mu < 1{\cdot}3 \times 10^7$

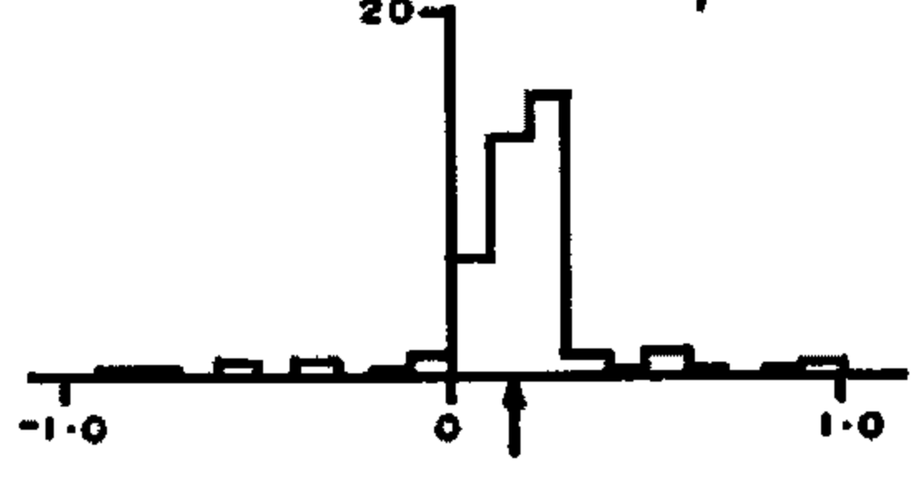

ZENITH $30^\circ - 50^\circ$

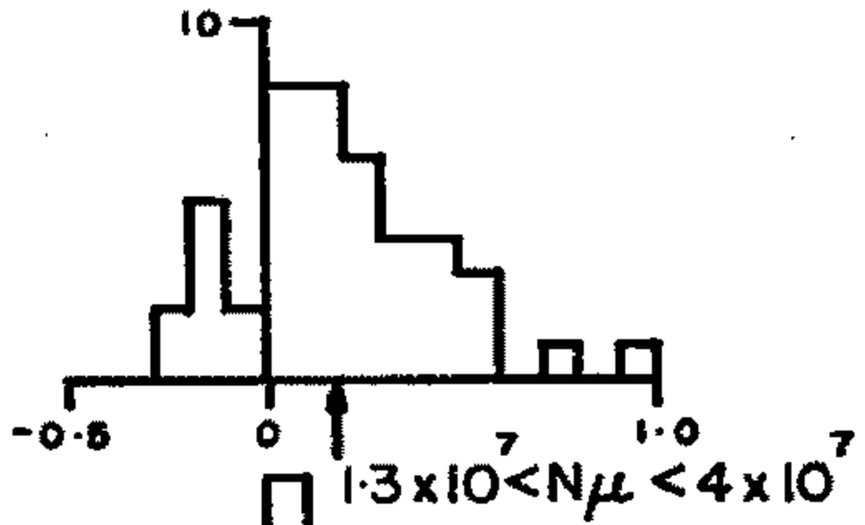

$1{\cdot}3 \times 10^7 < N\mu < 4 \times 10^7$

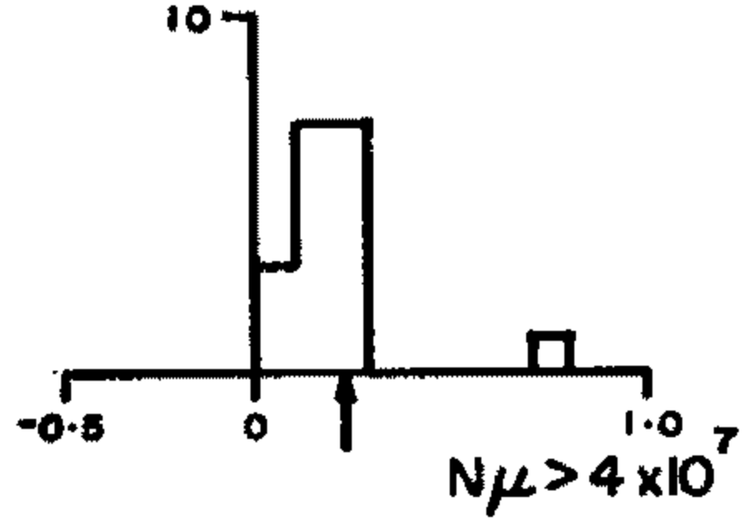

$N\mu > 4 \times 10^7$

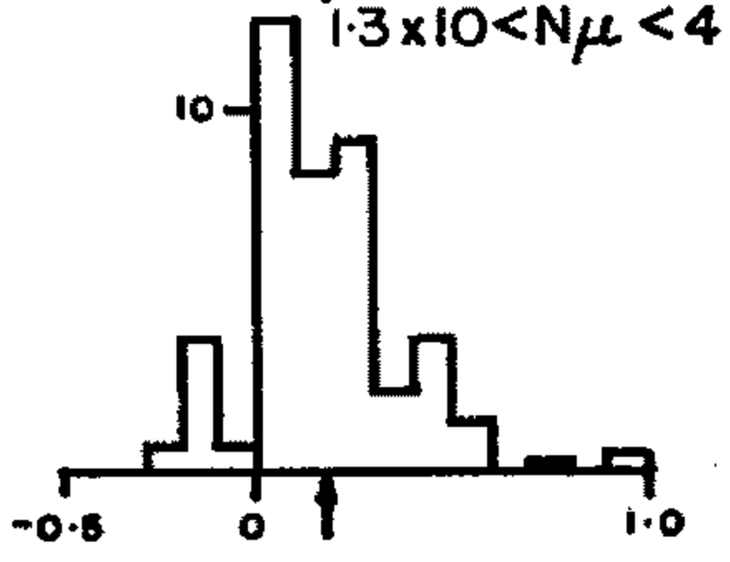

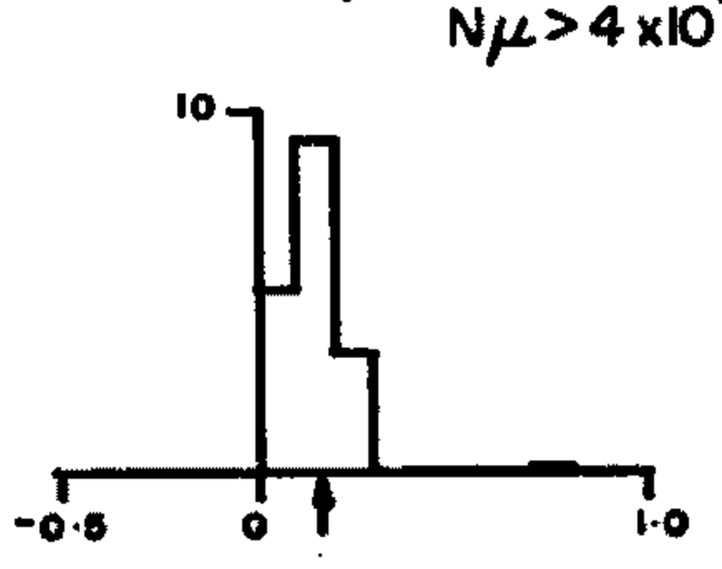

FIGURE 6.5

Unweighted (top row) and weighted (bottom row) curvature distributions of 228 events with zenith angles $50^{o} < \theta < 90^{o}$.

Units of curvature are km^{-1}.

TABLE 6.5

N_μ	No. of Events	Unweighted Curv. (km^{-1})	Weighted Curv. (km^{-1})
$N_\mu < 4\times10^6$	99	0.159±0.061	0.147±0.042
$4\times10^6 < N_\mu < 8\times10^6$	64	0.143±0.046	0.072±0.025
$8\times10^6 < N_\mu < 1.3\times10^7$	17	0.153±0.029	0.091±0.017
$1.3\times10^7 < N_\mu < 4\times10^7$	29	0.078±0.051	0.097±0.018
$N_\mu > 4\times10^7$	19	0.054±0.026	0.037±0.009

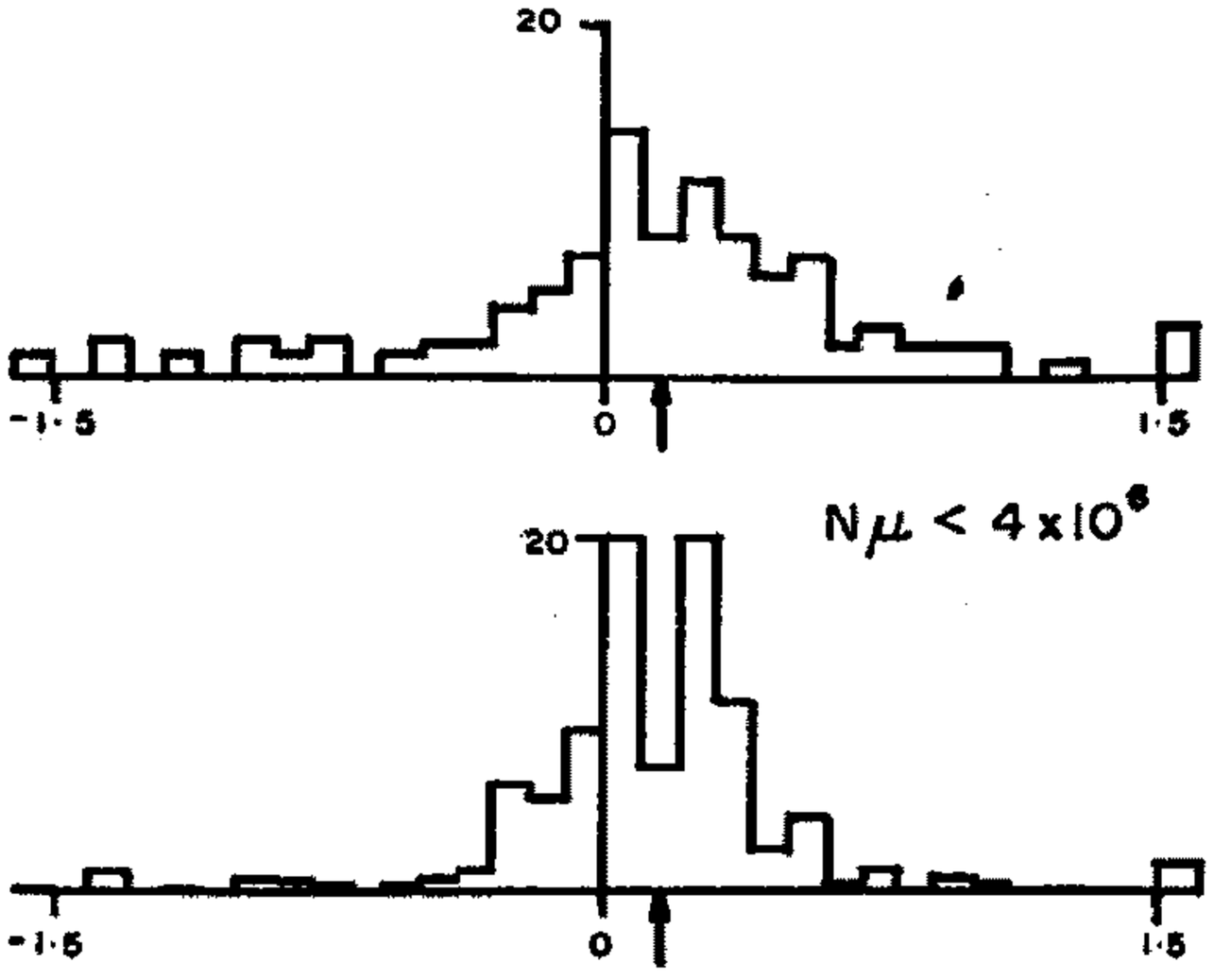
20
-1·5
0
1·5
Nμ < 4x10⁶
20
-1·5
0
1·5

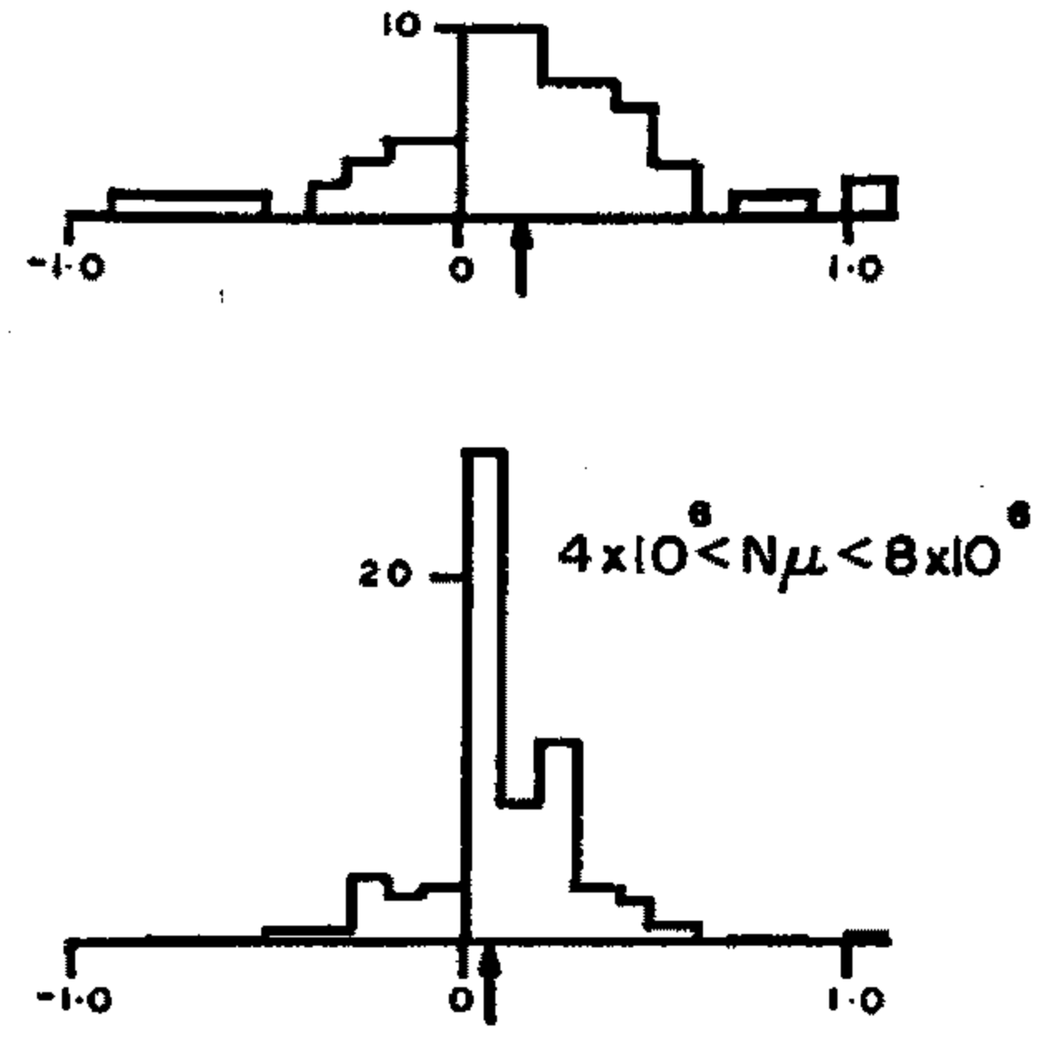
10
-1·0
0
1·0
4x10⁶<Nμ<8x10⁶
20
-1·0
0
1·0

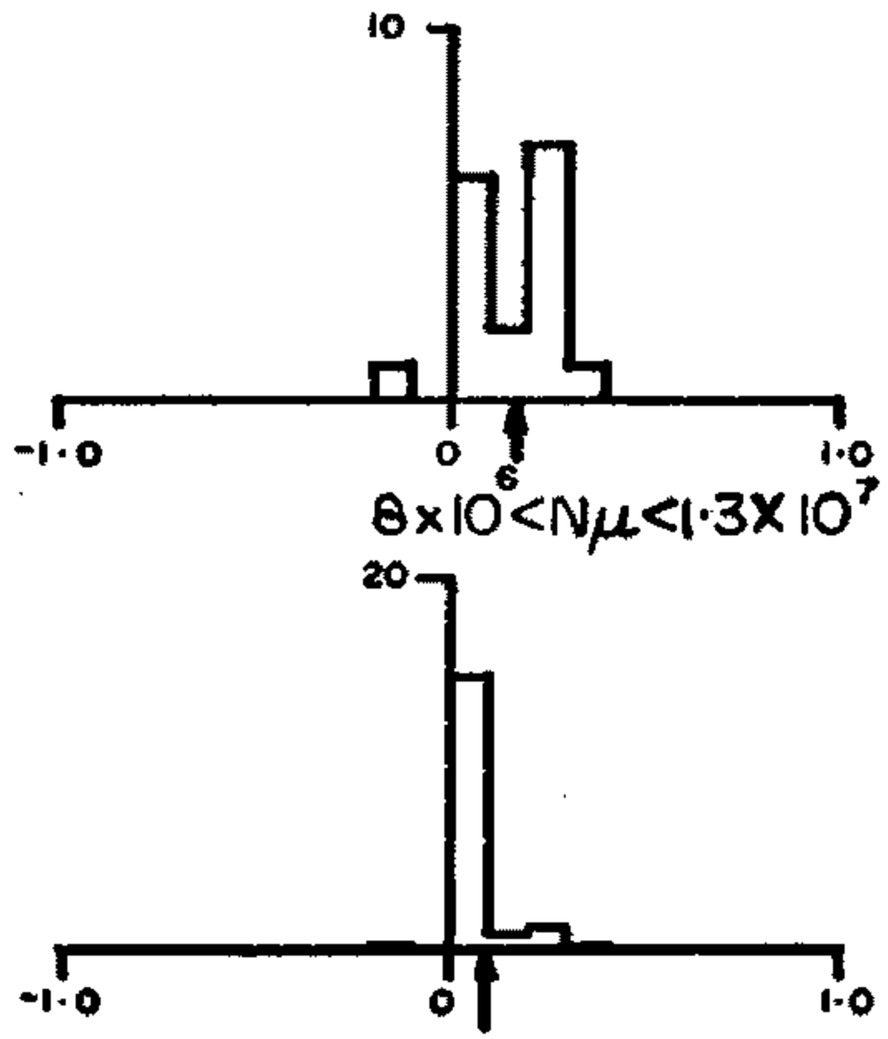
10
-1·0
0
1·0
8x10⁶<Nμ<1·3X10⁷
20
-1·0
0
1·0

ZENITH 50°— 90°

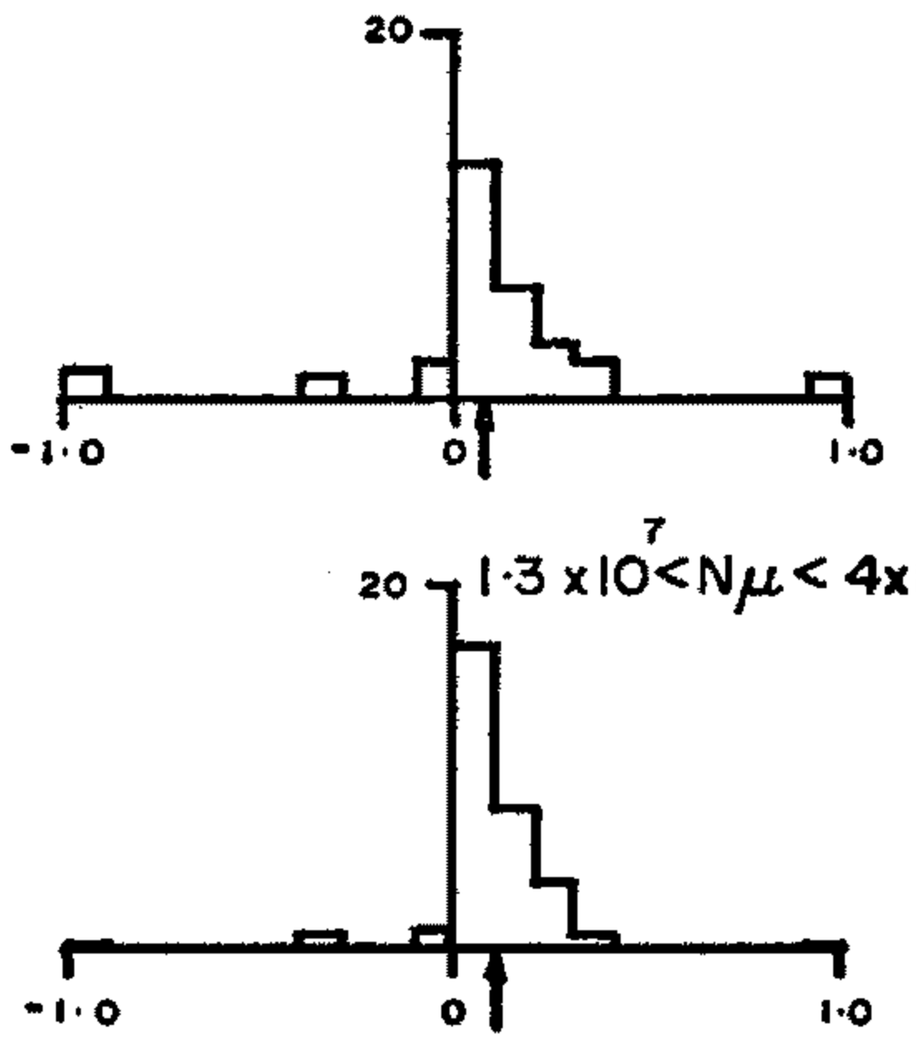
20
-1·0
0
1·0
1·3 x10⁷<Nμ< 4x10⁷
20
-1·0
0
1·0

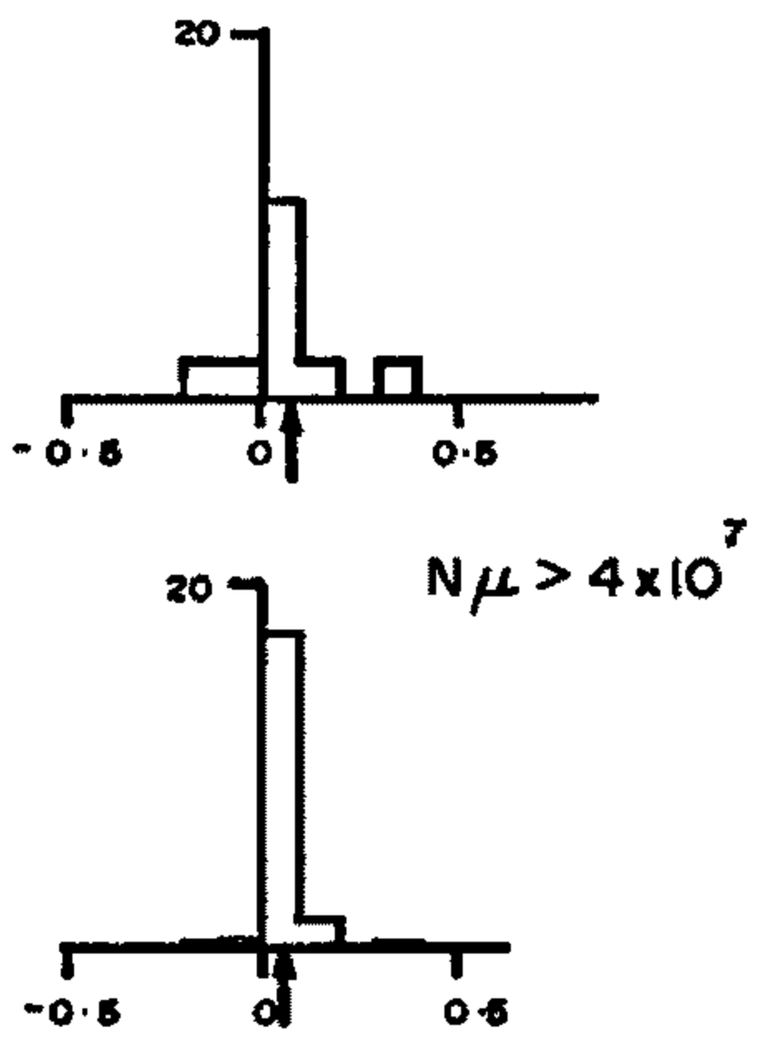
20
-0·5
0
0·5
Nμ > 4x10⁷
20
-0·5
0
0·5

From the spread of the unweighted means, it appears that the standard deviation in the measurement of curvature is $\sim$ 0.3 km^{-1}. This is in close agreement with the value 0.35 km^{-1} predicted for a timing standard deviation of 68 nsecs (section 6.4).

For showers in the range $0^{o} < \theta < 30^{o}$, the distributions appear uneven for small showers. For highly inclined small showers, the distributions appear to broaden, and tend to be more uniform. Large showers appear to be well behaved in all ranges.

6.6 INTERPRETATION OF RESULTS.

To investigate the variation of the curvature of the muon shower front with respect to zenith angle and muon shower size, the distributions of section 6.5 have been further divided such that there are now 9 muon number ranges in each of the 3 zenith angle bins. The weighted means of the curvature distributions, together with their one standard deviation error bars, are plotted as a function of N_{μ}, for each zenith angle bin in figs. 6.6 to 6.8 respectively. Each zenith angle bin will now be considered separately.

(a) $0^{o} < \theta < 30^{o}$

As noted in section 6.5, the curvature distributions in this range are uneven for low muon

shower size. The variation of the weighted mean with shower size is such that for $N_\mu < 8 \times 10^6$, curvature increases rapidly. Above $N_\mu = 8 \times 10^6$, the curvature appears to remain constant with increasing shower size and a mean value of 0.24 km^{-1} agrees well with the Haverah Park results (Tennent 1968).

For near vertical showers, station separation in the shower plane is approximately the same as in the ground plane. In this way, the timing information which determines the measurement of the shower front curvature, is derived in most cases, approximately 400m from the core.

Using our observed structure function (section 2.12.1), the number of particles expected in a tank for vertical showers at 200m, 400m and 600m from the core is shown, for the muon showers sizes under consideration, in table 6.6 below

TABLE 6.6

N_μ	Muons per detector at core distances		
	200m	400m	600m
1.5×10^6	6.0	2.4	0.6
2.5×10^6	19.2	4.2	1.2
3.5×10^6	27.0	5.4	1.8
5.0×10^6	39.0	7.8	2.4
7.0×10^6	54.6	10.8	3.6

FIGURE 6.6

Curvatures in the range $0^{o} < \theta < 30^{o}$

as a function of Nμ

Error bars are one standard deviation.

The numbers in brackets are the number of events determining each point.

The point H.P. is determined from the Haverah Park array.

Tennant (1968).

ZENITH 0°–30°

$\rho(km^{-1})$

0
0·1
0·2
0·3
0·4
0·5
0·6

H.P.

(4) (11) (16) (38) (29) (45) (49) (11) (3)

10^6 $1{\cdot}3\times10^6$ 2×10^6 3×10^6 4×10^6 6×10^6 8×10^6 10^7 $1{\cdot}3\times10^7$ 4×10^7 10^8 $1{\cdot}5\times10^8$

$N\mu$

As can be seen from the table, the number of muons in the tanks of the stations that determine the shower front curvature, is quite low. At least three particles are required to register an event.

Since the muons in the shower front, at these core distances, have an inherent time-delay distribution, it is obvious that in many instances, the first particle to arrive at a station, will be a delayed particle. In this way, the averaged curvature will correspond to a *delayed shower front* and not to the actual extreme front. Also due to the diffuseness of the front, the first particle recorded (which determines the arrival time) will occur randomly from the extreme front of the shower to the tail, and hence explain the *uneveness* of the distributions in fig. 6.3.

From fig. 6.6, the difference in average curvature between showers with muon size $\sim 2 \times 10^6$ and showers with $N_\mu > 8 \times 10^6$, is $\Delta\rho \sim 0.25$ km^{-1}. The time delay with respect to the extreme front, at 400m from the core, required to produce this difference is $\Delta t \sim 70$ nsecs. This result is in good agreement with the results of Baxter (1969) as shown in table 6.1, and also calculations by Hillas (1965).

FIGURE 6.7

Curvatures in the range $30^{o} < \theta < 50^{o}$

as a function of Nμ

Error bars are one standard deviation.

The numbers in brackets are the number of events determining each point.

The point H.P. is determined from the Haverah Park array.

Tennent (1968).

ZENITH 30°—50°

(20) (41) (40) (52) (30) (44) (44) (14) (4)

0 0·1 0·2 0·3 0·4 0·5 0·6

$\rho(km^{-1})$

H·P·

10^6 $1{\cdot}5\times10^6$ 2×10^6 3×10^6 4×10^6 6×10^6 8×10^6 10^7 $1{\cdot}3\times10^7$ 4×10^7 10^8 $1{\cdot}5\times10^8$

$N\mu$

(b) $30^{o} < \theta < 50^{o}$.

Fig. 6.7 depicts the variation of weighted curvature as a function of N_{μ}, and in the range $30^{o} < \theta < 50^{o}$.

The projection of the array into the shower plane for inclined showers, has the effect of decreasing inter-station separations. The decrease is proportional to $\cos\theta$. In this way, curvature determination is made closer to the core for inclined showers and is not as badly affected by delayed particles as is the case for vertical showers.

The observed curvatures in the range $30^{o} < \theta < 50^{o}$, tend to increase slightly with muon shower size, but at the same time are not inconsistent with being constant and having an average value of $\sim 0.19\ km^{-1}$. This is once again in close agreement with Haverah Park results.

(c) $50^{o} < \theta < 90^{o}$.

Since the line of interactions which produce an E.A.S. is further away for very inclined showers, the radius of curvature should approach zero, corresponding to an almost plane front. This is evidenced in fig. 6.8. There appears to be little or no variation with N_{μ}.

The curvature distribution for the bin $3 \times 10^{6} < N_{\mu} < 4 \times 10^{6}$, has been plotted separately in

FIGURE 6.8

Curvatures in the range $50^{o} < \theta < 90^{o}$

as a function of N_{μ}.

Error bars are one standard deviation.

The numbers in brackets are the number of events determining each point.

The point H.P. is determined from the Haverah Park array.

Tennent (1968)

The point marked with an asterisk in the range $3x10^{6} < N_{\mu} < 4x10^{6}$ is discussed in the text.

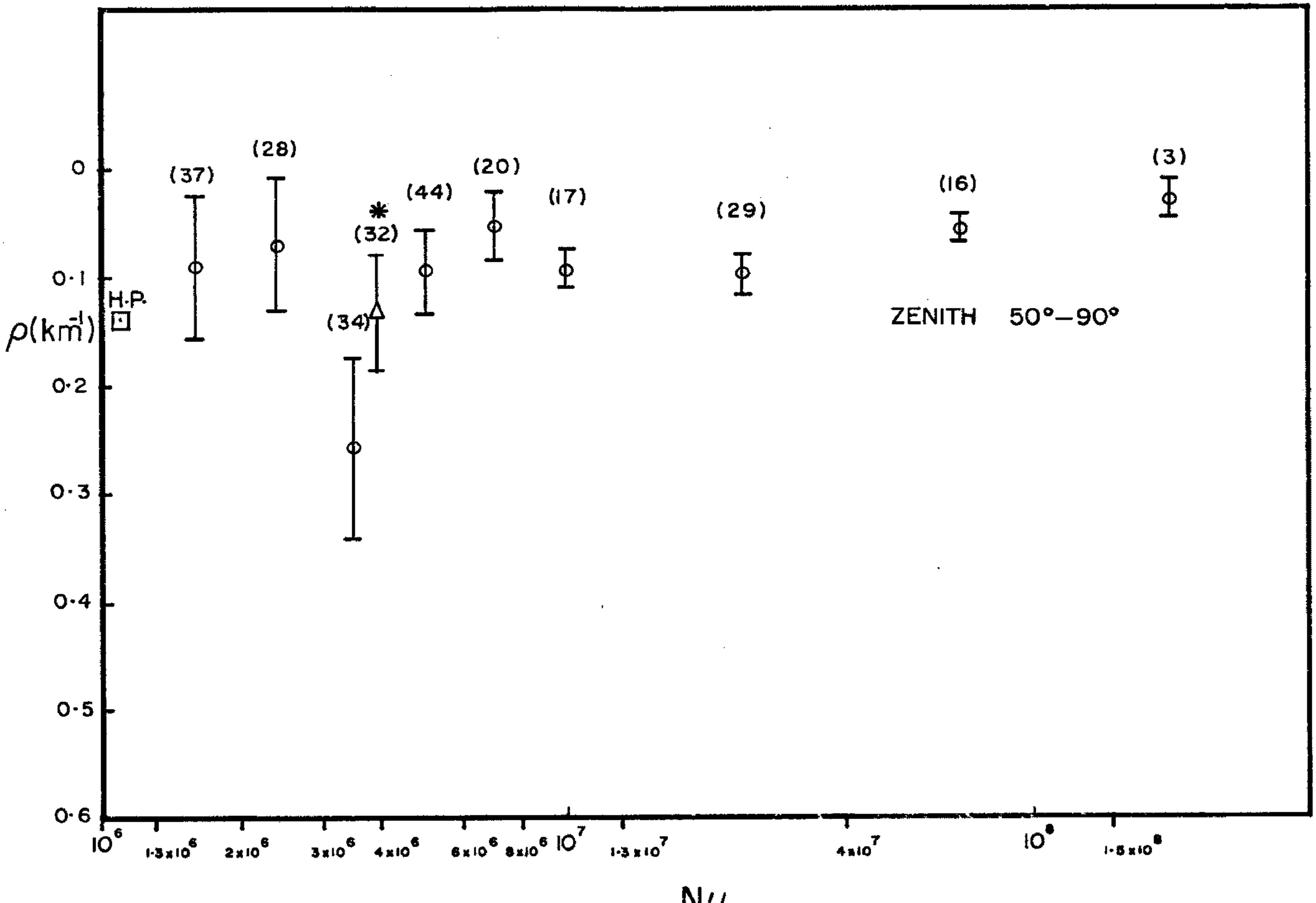
0
0·1
0·2
0·3
0·4
0·5
0·6
ρ(km⁻¹)
H.P.
(37)
(28)
(34)
*
(32)
(44)
(20)
(17)
(29)
(16)
(3)
ZENITH 50°–90°
10⁶
1·3x10⁶
2x10⁶
3x10⁶
4x10⁶
6x10⁶
8x10⁶
10⁷
1·3x10⁷
4x10⁷
10⁸
1·5x10⁸
Nμ

FIGURE 6.9

Weighted and unweighted curvature distributions for events with $3x10^6 < N_\mu < 4x10^6$ and $50^o < \theta < 90^o$

The distributions including the cross hatched sections, correspond to 34 showers and have means

$m_{uw} = 0.238 \pm 0.089\ km^{-1}$

$m_w = 0.256 \pm 0.084\ km^{-1}$

The distributions minus the cross hatched sections, correspond to the removal of 2 suspect events (see text), leaving 32 events. The adjusted means are

$m'_{uw} = 0.183 \pm 0.076\ km^{-1}$

$m'_w = 0.159 \pm 0.050\ km^{-1}$

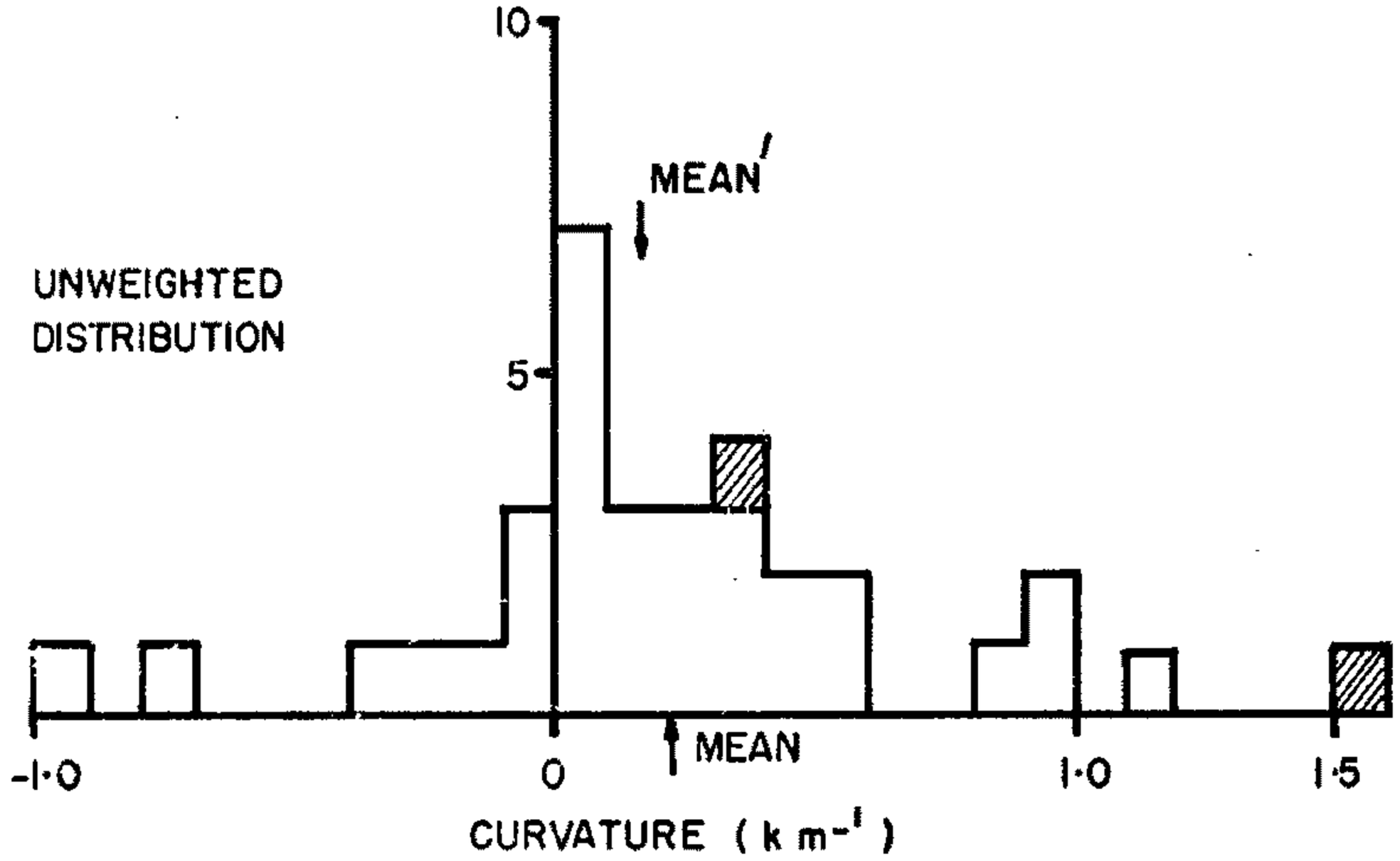

$3 \times 10^6 < N\mu < 4 \times 10^6$

$50° < \theta < 90°$

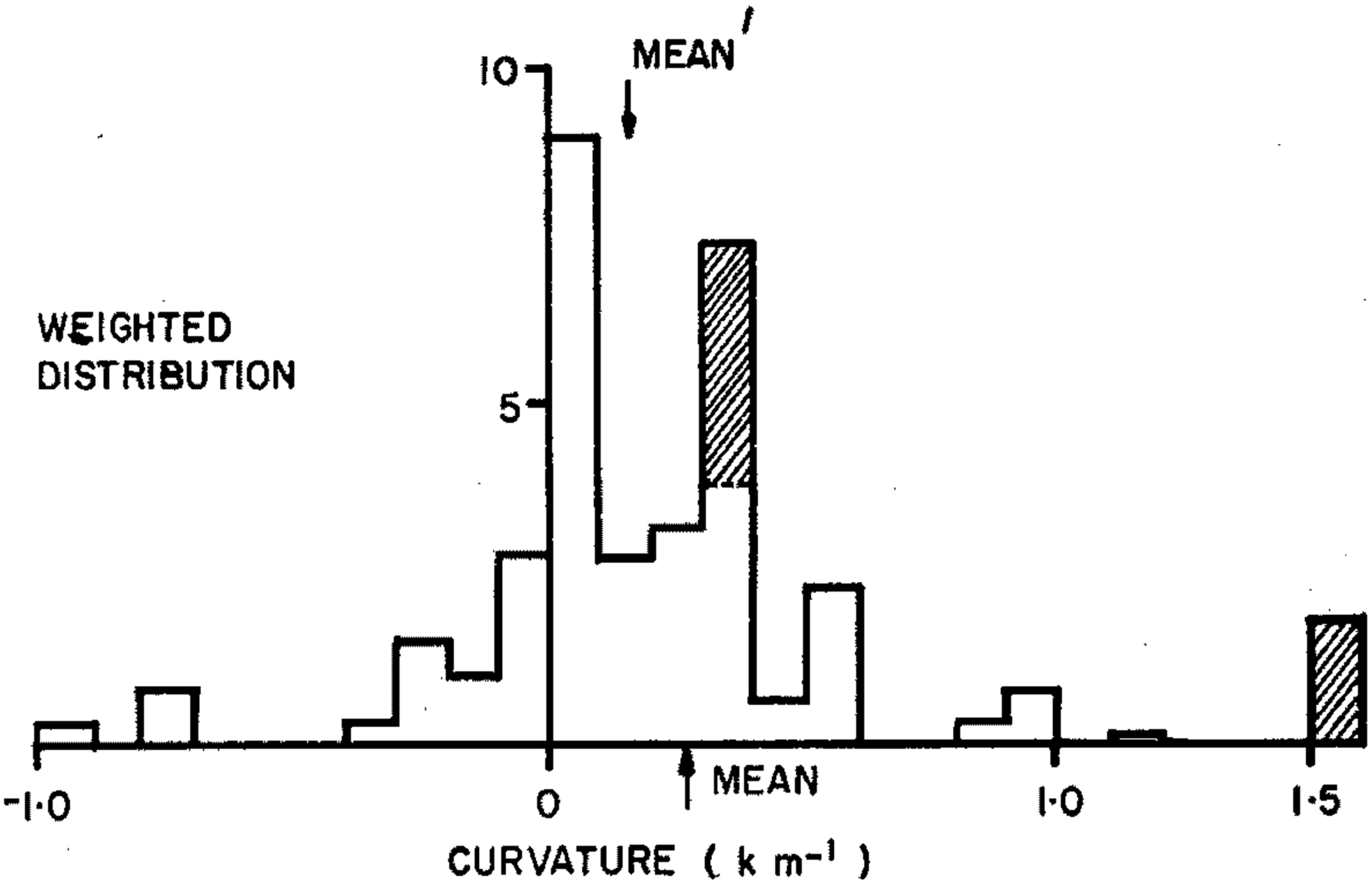

fig. 6.9. Originally this bin contained 34 events, however two of these events were later found to be suspect.

The inclusion of these events gives a larger than average curvature of 0.256±0.084 km^{-1}. On removal of these events, one of which was an early event, number 402, and very likely had bad timing information and the other was event number 2610 which had a large curvature of 1.9 km^{-1} and was also a poor timing suspect, the new weighted curvature became 0.159±0.050 km^{-1}.

The average curvature in the range $50^{o} < \theta < 90^{o}$ is $\sim$ 0.07 km^{-1}. This is a little lower than the curvatures measured for $\theta > 60^{o}$ by Haverah Park. However this may be due to the fact that we have included some relatively high zenith angle events. Out of the 226 good events with $\theta > 50^{o}$, 25 had $\theta > 70^{o}$, and in particular, 2 of the 3 events with $N_{\mu} > 1.5 \times 10^{8}$ had $\theta > 75^{o}$.

For the three zenith angle bins, the heights of origin are approximately constant and equal to 4 km.

6.7 A CANDIDATE FOR GEOMAGNETIC SPLITTING.

One event recorded by the SUGAR array, event number 3031, had a *best fit* zenith angle of 84.4^{o} and triggered 16 stations. The map of the triggered stations in both the ground plane and shower plane, is

FIGURE 6.10

(a) Map of event number 3031 in the plane of the array.

o Station Not Triggered

x Station Dead

Numbers are the average number of particles in a tank for each station triggered.

(b) Map of event number 3031 projected in the shower plane.

o and x as above

T = Triggered Station

Particle numbers are listed as they appear in map.

C = Core Position.

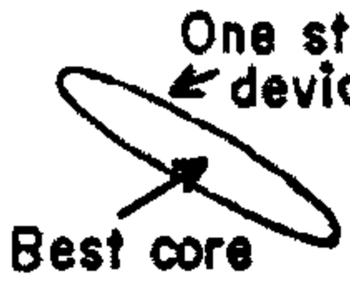

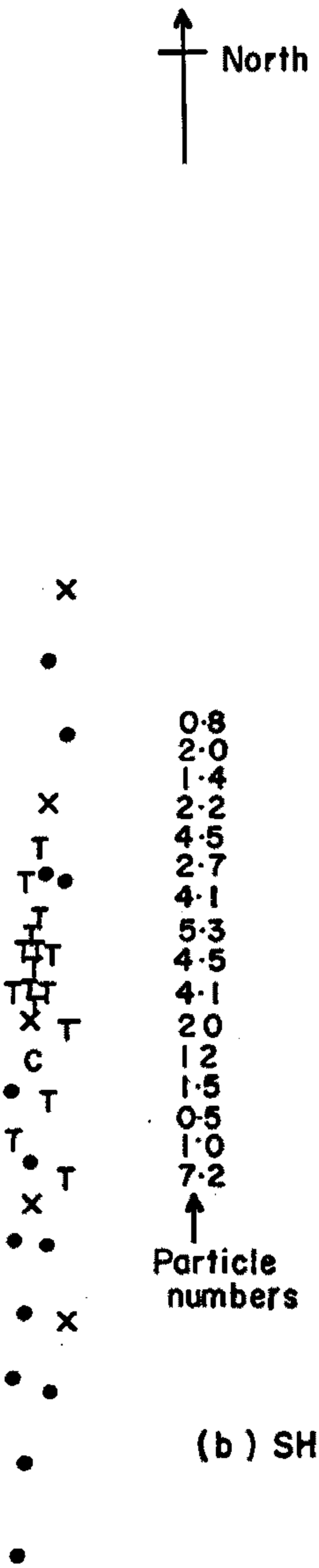

(a) GROUND PLANE

Scale 1cm = 0·8 km

(b) SHOWER PLANE

FIGURE 6.11

Envisaged geomagnetic splitting of event snumber 3031.

Zenith $\sim 84^{o}$

Splitting $\geq$ 4km

Dip angle of magnetic field at Narrabri is -60^{o}. The field is in a direction 10^{o} east of north.

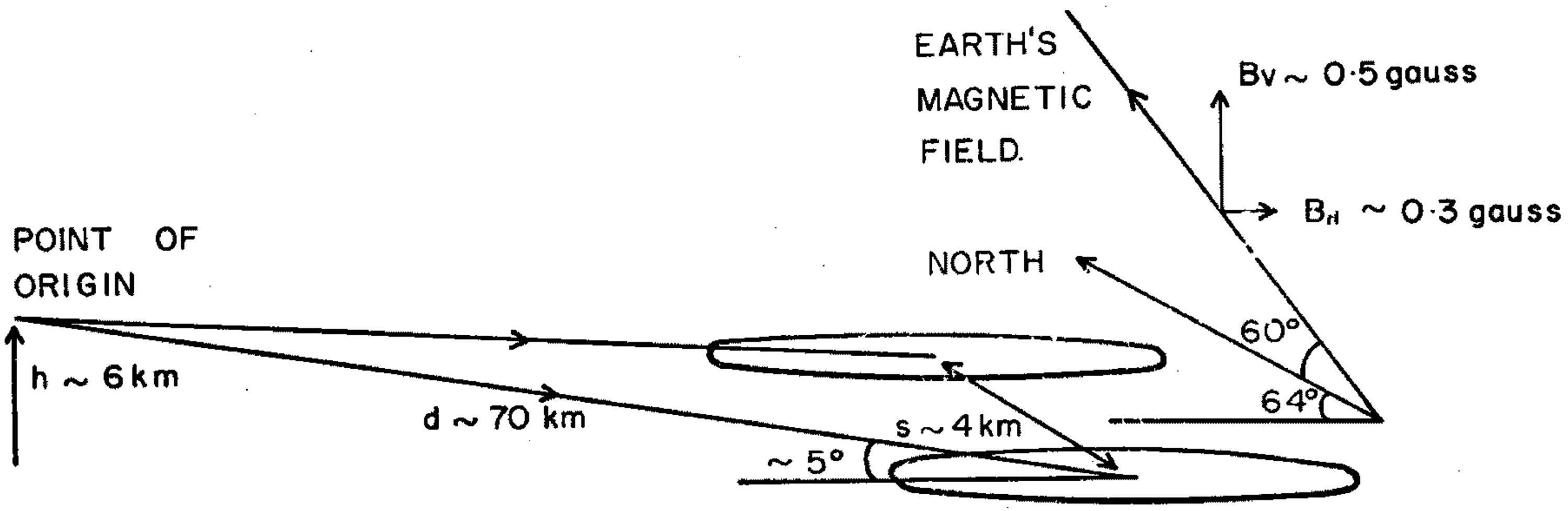

POSSIBLE GEOMAGNETIC SPLITTING OF SN 3031

shown in fig. 6.10.

The dip angle of the Earth's magnetic field at Narrabri is -60^{o} and the direction of the field is 10^{o} east of true north. The vertical component of the field is 0.49 gauss and the horizontal component is 0.29 gauss. The azimuth of the shower was 154.3^{o} measured anti-clockwise from east.

Under these conditions, the charged shower particles would have suffered a large geomagnetic deflection, possibly large enough to separate the two oppositely charged columns such that only one wing of the shower hit the array. Fig. 6.11 depicts a possible splitting of this event.

Since the value of the zenith angle is critical in determining the extent of the possible splitting, its error was calculated in a more detailed manner than usual. By stepping plus or minus steps of one degree on either side of the *best fit* zenith and azimuth angle, new estimates of the goodness of fit (expressed in nsecs) were determined (fig. 6.12). Based on a timing variance of 79 nsecs, contours containing deviations of one and two standard deviations from the mean were drawn. As can be seen in fig. 6.12, the azimuth, as would be expected, is quite well determined, having a value $\phi = 154^{o} \pm 3^{o}$ to within

FIGURE 6.12

Error in arrival direction of shower event number 3031.

The changes in timing fit (in nsecs) for steps of 1^{0} about the mean direction are shown.

Contours corresponding to one and two standard deviations from the mean are also shown where $\sigma \sim 79$ nsecs.

AZIMUTH

ZENITH	-7	-6	-5	-4	-3	-2	-1	+0	+1	+2	+3	+4	+5	+6	+7
-10	259	228	202	186	181	190	213	247	288	335	387	441	499	559	621
-9	266	232	202	179	167	171	190	221	262	309	360	415	473	533	596
-8	276	240	206	177	159	156	170	199	238	285	336	391	449	510	573
-7	288	249	213	180	155	145	153	179	217	263	314	369	427	488	551
-6	301	260	222	186	156	139	140	162	198	243	294	349	408	468	532
-5	313	272	232	193	160	137	132	148	181	225	276	331	390	451	514
-4	326	284	243	202	166	138	126	137	167	210	260	315	373	435	498
-3	338	296	253	212	173	142	124	129	155	197	246	301	359	420	484
-2	349	307	264	221	181	147	124	124	146	185	234	289	347	408	471
-1	359	317	273	230	189	152	126	120	139	176	224	278	336	397	461
+0	368	325	282	238	196	158	129	119	134	169	216	269	327	388	451
+1	376	333	289	246	203	164	133	119	130	163	209	262	319	380	444
+2	383	339	295	251	208	168	136	119	128	159	204	256	313	374	438
+3	387	344	300	256	213	172	138	120	126	156	200	252	309	370	433
+4	391	347	303	259	216	175	140	121	125	154	197	249	306	367	430
+5	393	349	305	261	217	176	141	121	125	153	196	247	304	365	428

BEST FIT ARRIVAL DIRECTION $\theta = 84.4^{\circ}$

$\phi = 154.3^{\circ}$

one standard deviation. However, the zenith is poorly determined. To within one standard deviation it is equal to $\theta = 84^{o} \, {}^{+6^{o}}_{-8^{o}}$.

Before estimating the affect of the Earth's magnetic field on the muons in the shower, an estimate of their average energy must be made.

On the assumption of an exponential atmosphere in static and thermal equilibrium and assuming a uniform density for the ground around each station, the threshold energy versus zenith angle for four different heights of origin has been calculated (fig. 6.13). A constant energy loss of 2 Mev g^{-1} cm^{2} has been assumed and one atmosphere has been taken to correspond to 1010 g cm^{-2}. The radius, or approximate distance to the point of origin for this event, was $65 \, {}^{+\infty}_{-34}$ km.

For d $\sim$ 70 km and $\theta \sim 84^{o}$, muons require 20 Gev energy to enter our detectors. The muons must traverse 4.4 atmospheres of air and 5 atmospheres of soil. The variation of threshold energy with respect to distance travelled and zenith angle can be seen in fig. 6.13.

The value of 70 km is probably an underestimate for the total path length of the muons from their point of origin. If we assume that the interaction mean free path of the primary is less than 80 g cm^{-2}, and take

FIGURE 6.13

Threshold energy for muons in highly inclined showers.

Curves are representative of a point origin at distances of

(1) 100 km

(2) 70 km

(3) 30 km

(4) 10 km

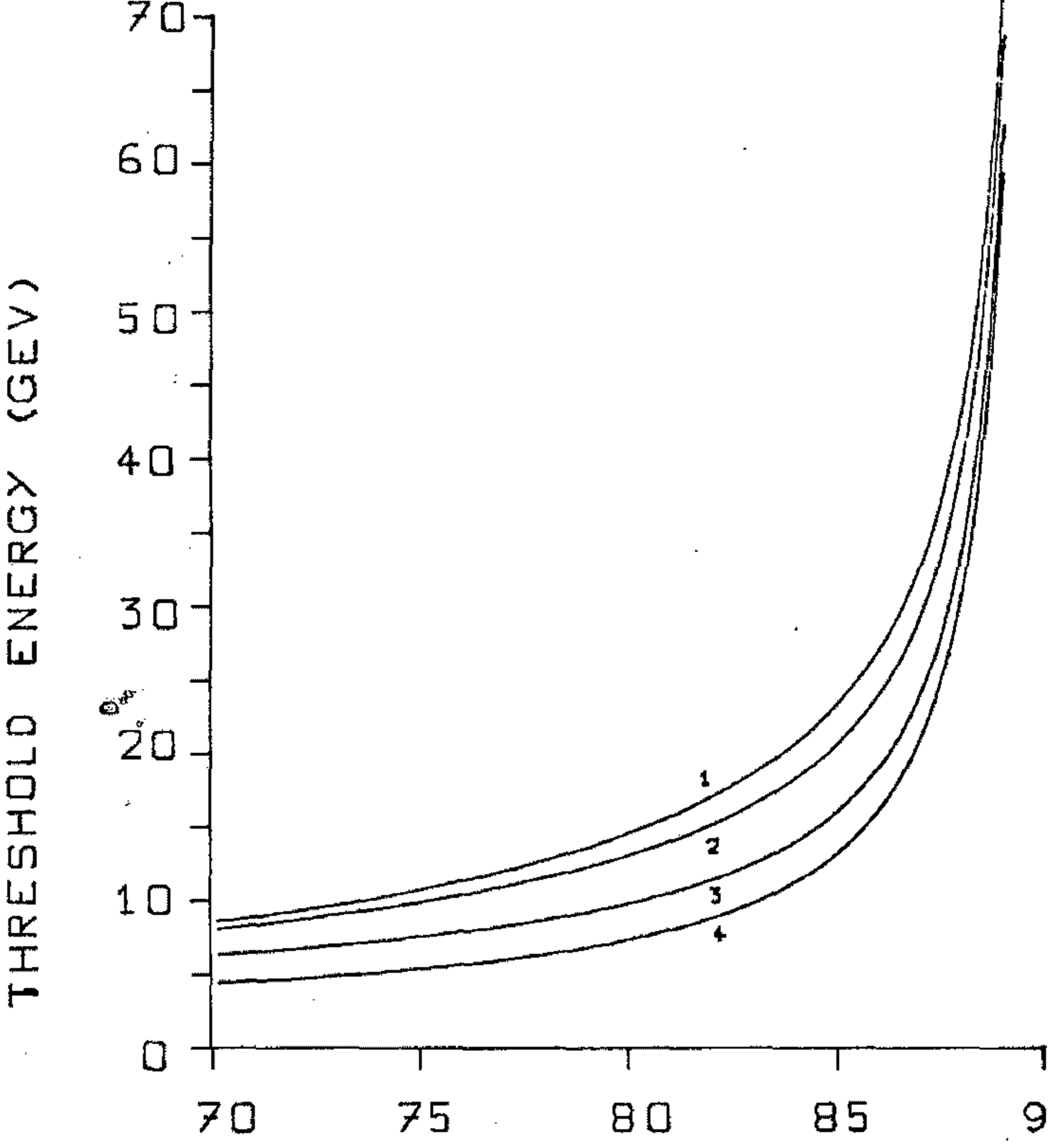
THRESHOLD ENERGY (GEV)
70
60
50
40
30
20
10
0
1
2
3
4
70
75
80
85
90
ZENITH ANGLE (DEG)

into account the curvature of the Earth, then for a shower with zenith angle $\sim 85^{o}$, the first interaction occurs at a height of about 30 km above sea level and about 300 km from the array. By the time the shower gets to 10 km above sea level, it is still about 100 km from the array and has traversed more than 2 atmospheres and is therefore past maximum development. On reaching the array the shower would have traversed more than 10 atmospheres of air and since the scale height of the atmosphere is 8 km, it still has another atmosphere to go in crossing the array. Altogether the shower may have traversed upto 16 or 17 atmospheres of matter, corresponding to a threshold energy of about 35 Gev for the muons. The path length being greater than 200 km.

To evaluate the extent of the geomagnetic splitting, a rigorous treatment including rate of energy loss over the path length (Bonnevier 1959), is required. However, a rough estimate can be made by assuming that muons are created with the calculated threshold energy, and this remains constant along the path of travel.

The extent of splitting for muons at an angle of 84.4^{o} to the zenith and with various threshold energies, is shown with respect to the total path length in

FIGURE 6.14

Geomagnetic deflection of muons at a zenith angle of 84.4^{o} as a function of total path traversed.

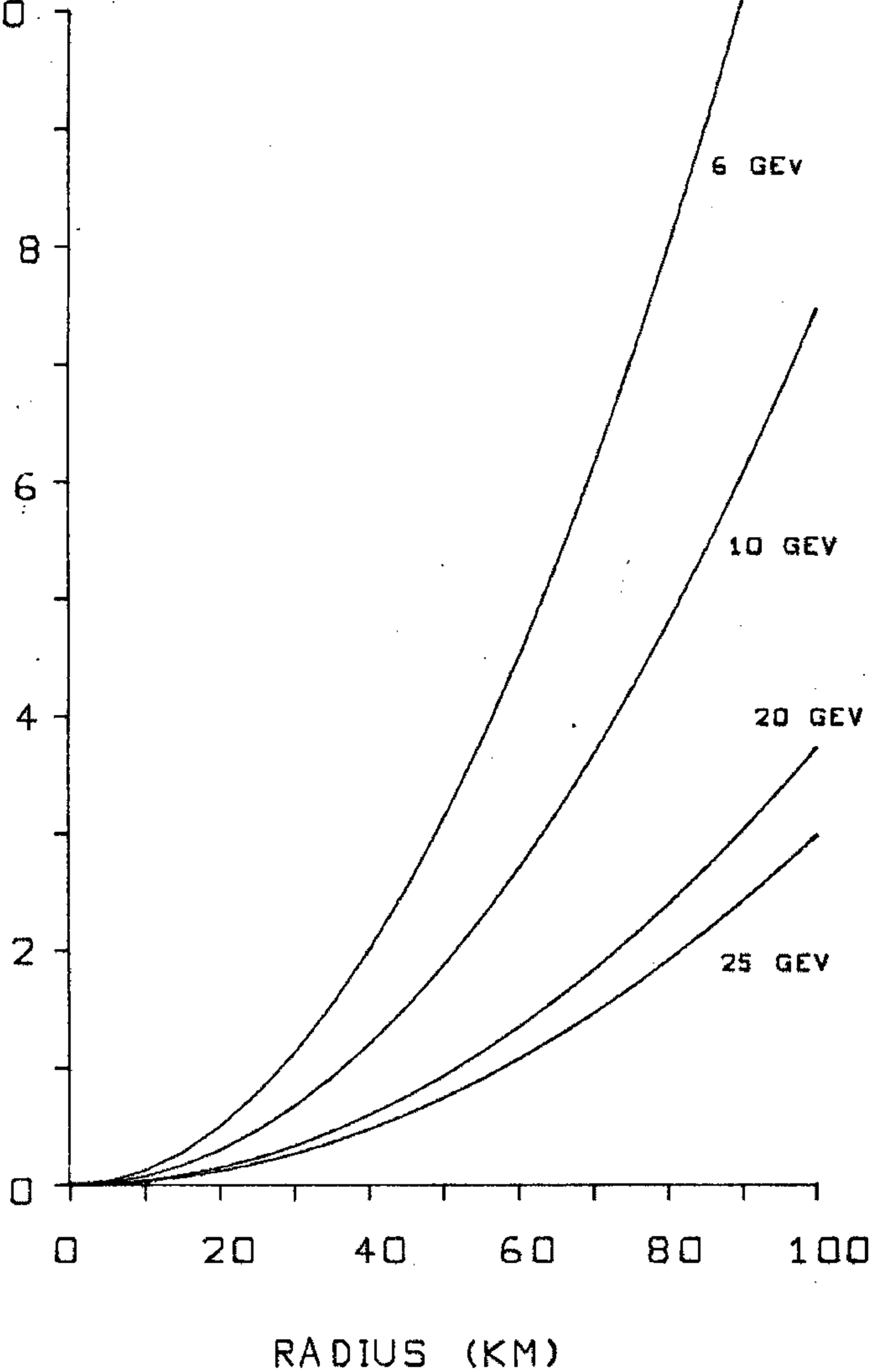
10
8
6
4
2
0
SPLITTING (KM)
6 GEV
10 GEV
20 GEV
25 GEV
0
20
40
60
80
100
RADIUS (KM)

fig. 6.14. For muons with energy 20 Gev, this splitting amounts to ∿ 2 km for d = 70 km. The splitting between the two wings of the shower would be twice this and equal to 4 km.

Since the splitting is proportional to the square of the total path length and only inversely proportional to the muon energy, the splitting is much greater for muons originating far away. If the threshold is 35 Gev and the length is 200 km, then the total splitting between the two wings of the shower at the array would be approximately 10 to 20 km.

An energy estimate as in section 2.12.2, for showers with $\theta > 75^{o}$ is unreliable, the estimate for this event being 2×10^{22}ev. The muon shower size is 1.7×10^{8} muons. If the shower is split then our muon number is a factor of 2 too low, since we only see half of the shower. If each muon has energy greater than 20 Gev and there are 3.4×10^{8} of them, then the minimum primary energy is probably well in excess of 10^{19}ev.

A theoretical analysis of the muon component of highly inclined extensive air showers, has been made by de Beer et al (1969). They have derived a relation-ship between average muon number and primary energy in

FIGURE 6.15

Average muon number to primary energy conversion for showers inclined at 84^{o} to the zenith.

Solid lines are according to de Beer et al (1969).

Broken lines are extrapolations to larger shower sizes.

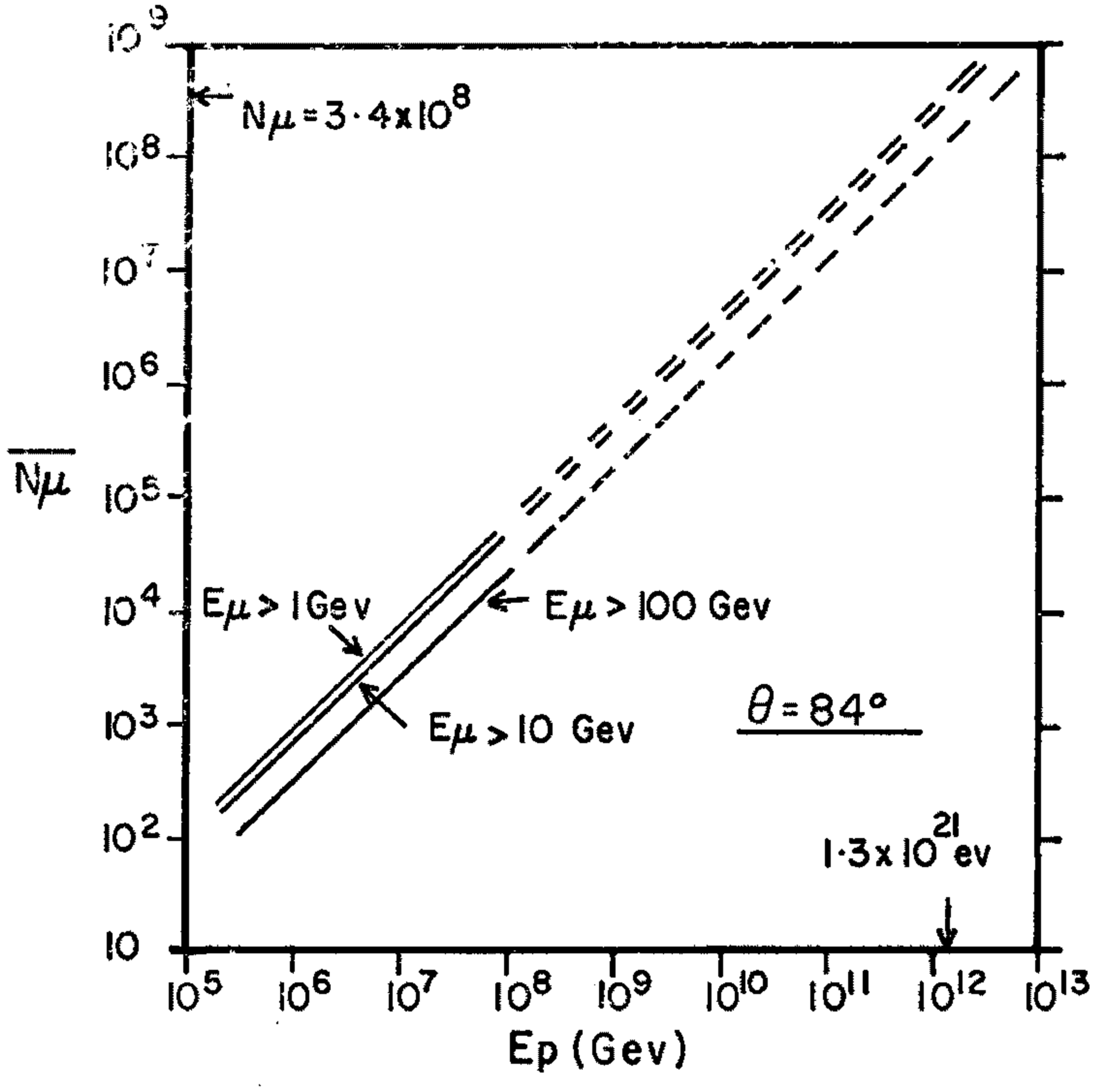
10^9
$N\mu = 3\cdot4\times10^8$
10^8
10^7
10^6
$\overline{N\mu}$
10^5
10^4
$E\mu > 1$ Gev
$E\mu > 100$ Gev
10^3
$E\mu > 10$ Gev
$\theta = 84°$
10^2
$1\cdot3\times10^{21}$ ev
10
10^5 10^6 10^7 10^8 10^9 10^{10} 10^{11} 10^{12} 10^{13}
Ep (Gev)

the range 10^{14}ev to 10^{17}ev. This they have done for two zenith angles, one of which is $\theta = 84^{o}$, and for three muon energy thresholds. The results are shown, with extrapolation to $N_{\mu} \sim 10^{8}$, in fig. 6.15.

If it is valid to extrapolate these graphs (which are linear on a log-log plot) to $N_{\mu} = 3.4 \times 10^{8}$ev, then it appears that the energy of event number 3031 is of the order of 1.3×10^{21}ev, making it the highest energy event recorded by the SUGAR array.

6.8 CONCLUSION.

Based on the results derived from simulated showers, the method used for determining and weighting curvature measurements is acceptable. A timing variance of 68 nsecs corresponds to an uncertainty in curvature determination of ~ 0.3 km^{-1}.

The curvatures recorded by the SUGAR array imply that for small vertical showers, the delayed component at 400m from the core, contributes most to the curvature determination. The amount of delay needed agreeing well with the results of Baxter (1969).

For other showers, curvature appears to be independent of shower size and a constant height of origin of ~ 4 km is observed.

Using the results of curvature analysis on a single, large, highly inclined shower, an estimation of the amount of geomagnetic splitting has been made and shown to be at least 4 km between the two halves of the shower. On the assumption that we only detected one half of the shower and based on an extrapolation of the muon number to energy conversion of de Beer et al (1969), the energy of this event appears to be of the order of 1.3×10^{21}ev.

REFERENCES.

Abell, G.O., (1962) Astronomical Union Symp. No. 15, Problems of Extragalactic Research, ed. G.C, McVittie (London:MacMillan), 213.

Allan, H.R., Clay, R.W., and Jones, J.K., (1970) Nature 227, 1116.

Andrews, D., Evans, A.C. Reid, R.J.O., Tennent, R.M., Watson, A.A., and Wilson, J.G., (1968) Nature 219, 343.

Bahcall, J.N., Callan, C.G.Jr., and Dashen, R., (1970) Orange Aid Preprint, No. 213.

Bakich, A., McCusker, C.B.A., and Winn, M.M., (1970) J. Phys. A. (Gen. Phys.) 3, 662.

Bassi, P., Clark, G., and Rossi, B., (1953) Phys. Rev. 92 441.

Baxter, A.J., (1969) J. Phys. A. (Gen. Phys.) 2, 50.

Bennetts, S., Delvaille, J., Greisen, K., and Kendziorski, F., (1962) J. Phys. Soc. Japan, Suppl A-III 17, 196.

Blake, P.R., Hollows, J.D., Hunter, H.W., Reid, R.J.O., Tennent, R.M., Watson, A.A., and Wilson, J.G., (1968) Canad. Jnl. Phys. 46, 578.

Blake, P.R., and Harris, D.M., (1969) Proc. Int. Conf. Cosmic Rays, Budapest. (EAS 54/1) (to be published in Acta. Phys. Hungarica).

Bonnevier, B., (1959) Arkiv För Fysik 14, 225.

Bosia, G., Castagnoli, C., Dando, M., and Marangoni, G., (1970) Nature 225, 532.

Bothe, W., and Kolhörster, W., (1929) Z.f. Phys. 56, 751.

Bradt, H., Rappaport, S., Mayer, W., Nather, R.E., Warner, B., McFarlane, M., and Kristian, J., (1969).
Nature 222, 728.

Bray, A.D., Crawford, D.F., Jauncy, D.L., McCusker, C.B.A., Melley, D., Nelson, D., Poole, P.C., Rathgeber, M.H., Seet, S.H., Ulrichs, J., Wand, R.H., and Winn, M.M., (1965)
Proc. Int. Conf. Cosmic Rays London 2, 668.

Brownlee, R.G., Fisher, A.J., Goorevich, L., Kohn, P.C., McCusker, C.B.A., Ogelman, H.B., Parkinson, A.F., Peak, L.S., Rathgeber, M.H., Ryan, M.J., and Winn, M.M.,
(1968a) Canad. J. Phys. 46 S259
(1968b) Canad. J. Phys. 46 S263.

Brownlee, R.G., Chapman, G.J., David, S.A., Fisher, A.J., Goorevich, L., Horton, L., Kohn, P.C., McCusker, C.B.A., Outhred, A., Parkinson, A.F., Peak, L.S., Rathgeber, M.H., Ryan, M.J., and Winn, M.M.,
(1969a) Proc. Int. Conf. Cosmic Rays, Budapest (EAS-5) (to be published in Acta Phys. Hungarica).

Brownlee, R.G., David, S.A., Fisher, A.J., Goorevich, L., Horton, L., Kohn, P.C., McCusker, C.B.A., Outhred, A., Page, D.E., Parkinson, A.F., Peak, L.S., Rathgeber, M.H., Reid, R.J.O., Ryan, M.J., and Winn, M.M.,
(1969b) Proc. Int. Conf. Cosmic Rays, Budapest (EAS-6) (to be published in Acta Phys. Hungarica).

Brownlee, R.G., David, S.A., Fisher, A.J., Goorevich, L., Horton, L., Kohn, P.C., McCusker, C.B.A., Outhred, A., Parkinson, A.F., Peak, L.S., Rathgeber, M.H., Ryan, M.J., and Winn, M.M.,
(1969c) Proc. Int. Conf. Cosmic Rays, Budapest (EAS-55/2) (to be published in Acta Phys. Hungarica).
(1969d) Proc. Int. Conf. Cosmic Rays, Budapest (EAS-55/1) (to be published in Acta Phys. Hungarica)
(1969e) Proc. Int. Conf. Cosmic Rays, Budapest (EAS-26) (to be published in Acta Phys. Hungarica).

Bullington, K., (1957)
The Bell System Tech. Jnl. 36, 593.

Bunner, A.N., Greisen, K., and Landecker, P.B., (1968)
Canad. J. Phys. 46, S266.

Burbidge, G.R., and Hoyle, F., (1964)
Proc. Phys. Soc. 84, 141.

Cairns, I., McCusker, C.B.A., Peak, L.S., and Woolcott, R.L.S., (1969)
Phys. Rev. 186, 1394.

Chatterjee, B.K., Gopalakrishnan, N.V., Murthy, G.T., Naranan, S., Skreekantan, B.V., Srinivasa Rao, M.V., Tonwar, S.C., and Vatcha, R.H., (1968)
Canad. J. Phys. 46, S131.

Chu, W.T., Kim Young, S., Beam, W.J., and Kwak Nawhan, (1970)
Phys. Rev. Letters 24, 917.

Clark, G.W., Earl, J., Kraushaar, W.L., Linsley, J., Rossi, B.B., Scherb, F., and Scott, D.W., (1962)
Phys. Rev. 122, 537.

Cole, T.W., (1970)
Nature 227, 788.

Colgate, S.A., and White, R.H., (1963)
Proc. Int. Conf. Cosmic Rays, Jaipur 3, 335.

Cranshaw, T.E., and Galbraith, W., (1957)
Phil. Mag. 2, 804.

Crawshaw, J.K., and Elliot, H., (1955)
Proc. Phys. Soc. 69, 102.

Davies, K.H., Fall, S.M., and Stenerson, R.O., (1970)
Preprint.

de Beer, J.F., Holyoak, B., Turner, M.J.L., Wdowczyk, J., and Wolfendale, A.W., (1969)
J. Phys. A. (Gen. Phys.) 2, 354.

Delvaille, J., Kendziorski, F., and Greisen, K., (1962)
J. Phys. Soc. Japan, Suppl III-A 17, 76.

Dennis, B.R., and Wilson, J.G., (1963)
Proc. Int. Conf. Cosmic Rays, Jaipur 4, 258.

Dicke, R.H., Peebles, P.J.E., Roll, P.G., and
Wilkinson, D.T., (1965)
Astrophys. J. 142, 414.

Efimov, N.N., Krasilnikov, D.D., Nikolsky, S.I., and
Shamsutdinova, F.K., (1968)
Canad. J. Phys. 46, S84.

Fermi, E., (1949)
Phys. Rev. 2nd Series 75, 1169.

Fisher, A.J., (1970)
Ph.D. thesis. University of Sydney.

Fowler, P.H., Adams, R.A., Cowen, V.G., and Kidd, J.M.,
(1967)
Proc. Roy. Soc. A. 301, 39.

Frye, G.M.Jr., Staib, J.A., Zych, A.D., Hopper, V.D.,
Rawlinson, W.R., and Thomas, J.A., (1969)
Nature 223, 1320.

Galbraith, W., and Jelley, J.V., (1953)
Nature 171, 349.

Gell-Mann, (1964)
Phys. Letters 8, 214.

Ginzburg, V.L., and Syrovatskii, S.I., (1964)
The Origin of Cosmic Rays, Permagon Press.

Gold, T., (1968) Nature 218, 731.

Gold, T., (1969) Nature 221, 25.

Gold, T., (1970)
Invited Paper, Proc. Int. Conf. Cosmic Rays,
Budapest. p.163.

Goldreich, P., (1969)
Proc. Ast. Soc. Aust. 1, 227.

Goorevich, L., (1969)
Ph.D. thesis. University of Sydney.

Greisen, K., (1965)
Invited Paper, Proc. Int. Conf. Cosmic Rays, London. 2, 609.

Greisen, K., (1966)
Phys. Rev. Letters 16, 750.

Guest, P.G., (1961)
Numerical Methods of Curve Fitting, Cambridge Univ. Press.

Gunn, J.E., and Ostriker, J.P., (1969)
Phys. Rev. Letters 22, 728.

Halliday, E.C., (1941)
Phys. Rev. 2nd Series 60, 101.

Hayakawa, S., (1967)
Invited Paper 10th Int. Conf. Cosmic Rays, Calgary. p.82.

Head, H.T., (1960)
Proc. I.R.E. 48, No.6(1) 1016

Hersil, J., Escobar, I., Clark, G., Olbert, S., Moore, S., and Scott, D., (1962)
J. Phys. Soc. Japan, Suppl A-III 17, 243

Hess, V.F., (1912)
Wien Ber. 121, 2001.

Hewish, A., Bell, S.J., Pilkington, J.D.H., Scott, P.F., and Collins, R.A., (1968)
Nature 217, 209.

Hillas, A.M., (1965)
Proc. Int. Conf. Cosmic Rays, London. 2, 758.

Hillas, A.M., (1968)
Canad. J. Phys. 46, S623.

Hoffmann, G., (1925)
Phys. Z. 26, 40 and 669.

Holmes, M.C., (1937)
Jnl. of the Franklin Institute 223, 495.

Hopper, V.D., Rawlinson, W.R., and Thomas J.A., (1969)
Nature 223, 1320.

Jeans, J.H., (1931)
Nature 127, 594.

Jelley, J.V., and Whitehouse, W.J., (1953)
Proc. Phys. Soc. 66, 454.

Kolhörster, W., (1923)
Berlin Ber. Nr. 34.

Kolhörster, W., (1925)
Berlin Ber. Nr. 7.

Komesaroff, M.M., (1970)
Nature 225, 612.

Large, M.I., Vaughan, A.E., and Mills, B.Y., (1968)
Nature 220, 340.

Linsley, J., (1963a)
Proc. Int. Conf. Cosmic Rays, Jaipur 4, 77.

Linsley, J., (1963b)
Phys. Rev. Letters 10, 146.

Linsley, J., and Scarsi, L., (1962)
Phys. Rev. Letters 9, 123.

Linsley, J., and Scarsi, L., (1962a)
Phys. Rev. 128, 2384.

Linsley, J., Scarsi, L., Eccles, P.J., and Rossi, B.B.
(1962a)
Phys. Rev. Letters 8, 286.

Linsley, J., Scarsi, L., and Rossi, B.B., (1962b)
J. Phys. Soc. Japan, Suppl III-A 17, 91

Locci, M.A., Picchi, P., and Verri, G., (1967)
Nuovo Cim. 50B, 384.

Matano, T., Miura, I., Nagano, M., Shibata, S.,
Suga, K., and Hasegawa, H., (1965)
Proc. Int. Conf. Cosmic Rays, London 2, 637.

McCusker, C.B.A., Ritson, D.M., and Nevin, T.E., (1950)
Nature 166, 400.

McCusker, C.B.A., and Winn, M.M., (1963)
Nuovo Cim. 28, 175.

McCusker, C.B.A., (1965)
Rapporteur Paper, Proc. Int. Conf. Cosmic Rays, London, 2, 810.

McCusker, C.B.A., and Cairns, I., (1969)
Phys. Rev. Letters 23, 658.

McCusker, C.B.A., Peak, L.S., and Rathgeber, M.H., (1969a)
Phys. Rev. 177, 1902.

McCusker, C.B.A., Peak, L.S., and Rathgeber, M.H., (1969b)
Proc. Int. Conf. Cosmic Rays, Budapest. (EAS-34) (to be published in Acta Phys. Hungarica).

Mezzetti, E., Pancinini, E., and Stoppini, G., (1950)
Phys. Rev. 81, 629.

Millikan, R.A., and Cameron, G.H., (1928)
Phys. Rev. 31, 163.

Officer, V.C., (1951)
Phys. Rev. 83, 458.

Officer, V.C., and Eccles, P.J., (1954)
Aust. J. Phys. 7, 410.

Parkinson, A.F., (1969)
Ph.D. thesis. University of Sydney.

Penzias, A.A., and Wilson, R.W., (1965)
Astrophys. J. 142, 419.

Piddington, J.H., (1970)
Monthly Not. R. Astr. Soc. 148, 131.

Prescott, J.R., and Hough, J.H., (1970)
Nature 227, 590.

Radhakrishnan, V., (1969)
Invited Paper, Proc. Astr. Soc. Aust. 1, 254.

Radhakrishnan, V., Cooke, D.J., Komesaroff, M.M., and Morris, D., (1969)
Nature 221, 443.

Richards, D., (1968)
I.A.U. Astron. Telegram Circular No. 2114.

Robinson, B.J., (1963)
Nature 199, 322.

Roger, R.S., and Shuter, W.L.H., (1968)
Nature 218, 1036.

Roll, P.G., and Wilkinson, D.T., (1966)
Phys. Rev. Letters 16, 405.

Rothwell, P., Wade, B., and Goodings, A., (1956)
Proc. Phys. Soc. A. 69, 902.

Ryan, M.J., (1968)
Ph.D. thesis. University of Sydney.

Skivanandan, K., Houck, J., and Harwit, M., (1968)
Phys. Rev. Letters 21, 1460.

Smith, F.G., (1968a)
Nature 218, 325.

Smith, F.G., (1968b)
Nature 220, 691.

Spitzer, L.Jr., (1950)
Phys. Rev. 74, 583.

Staelin, D.H., and Reifenstein, E.C., (1968)
Science (U.S.A.) 162, 1481.

Staelin, D.H., and Reifenstein, E.C., (1969)
Ap. J. 156, L121.

Stecker, F.W., (1969)
Phys. Rev. 180, 1264.

Suga, K., Clark, G., and Escobar, I., (1961)
Rev. Sci. Instr. 32, 1187.

Sugarman, R., and DeBenedetti, S., (1956)
Phys. Rev. 102, 857.

Suri, A.N., (1965)
Proc. Int. Conf. Cosmic Rays, London,
2, 751.

Tennent, R.M., (1968)
Canad. J. Phys. 46, S1.

Thielheim, K.O., and Langhoff, W., (1968)
J. Phys. A. (Proc. Phys. Soc.) 1, 694.

Vasseur, J., Paul, J., Parlier, B., Leray, J.P., Forichan, M., Agrinier, B., Boella, G., Maraschi, L., Treves, A., Bucchani, R., and Scarsi, L., (1970)
Nature 226, 535.

Waddington, C.J., (1960)
Prog. Nuc. Phys. 8, 4.

DIRECTIONAL ANAI

F VERY HIGH ENE

EXTENSIVE AIR S